SYNTHESIS, MAGNETIC AND ELECTRICAL CHARACTERIZATIONS OF NANOPARTICLE FERRITES

by

Hafiz Mohammed Ibrahim Abdallah

BSc (Hons) (Al Fashir University, Sudan), MSc (El Neelain University, Sudan)

This thesis is submitted in fulfilment of the academic requirements for the degree Doctor of Philosophy

June 2012

Abstract

The synthesis, structure and physical properties of a series of $Mn_x(Co, Mg)_{1-x}Fe_2O_4$, $(Mg, Sr)_{0.2}$ $Mn_{0.1}Co_{0.7}Fe_2O_4$ and $Mg_{0.5}Mn_{0.5}(RE)_{0.1}Fe_{1.9}O_4$ (where RE are rare earth elements) nanoferrites have been studied. These compounds were synthesized at low reaction temperature of about 200 ^oC using the glycol-thermal method. The starting materials were high-purity metal chlorides or nitrates which were precipitated by NH_4OH and KOH respectively. In addition, $Mn_xCo_{1-x}Fe_2O_4$ (x = 0, 0.5 and 1) samples were produced directly from high-purity metal oxides by high-energy ball milling technique. Single-phase cubic spinel structure and nanoparticle structure of the synthesized samples were confirmed by X-ray diffraction (XRD) and transmission electron microscope (TEM). The results show that the produced powders of the as-prepared samples have average grain sizes ranging from 7 to 16 nm. Filtering the precipitates by Whatman glass microfiber filters (GF/F) appears to be important in obtaining the small particle sizes. We suspect higher stability of the $Mn_xCo_{1-x}Fe_2O_4$ at x = 0 and 0.5 where complete symmetry in the proportion of the atoms on tetrahedral (A) and octahedral (B) sites would tend to favour larger nanoparticles.

The evolutions of the magnetic properties as a function of composition, annealing temperature under air and argon atmospheres or measuring temperature have been investigated by ^{57}Fe Mössbauer spectroscopy, vibration sample magnetometer (VSM) and superconducting quantum interference device (SQUID). Significant changes in magnetic properties are observed across the composition ranges studied. The Mössbauer spectra indicate ferrimagnetic, superparamagnetic and paramagnetic behaviours of the compounds. The results show evidence of transformation from single-domain to multi-domain structure with thermal annealing in our samples. Temperature dependence of magnetization shows differences between field cooling (FC) and zero field cooling (ZFC) which we attribute to spin-freezing and thermal relaxation for typical nanoparticles. Significant increase in coercive field with reduction in measuring temperature is obtained in Co- based compounds. $Mn_{0.5}Co_{0.5}Fe_2O_4$, $Sr_{0.2}Mn_{0.1}Co_{0.7}Fe_2O_4$ and $Mg_{0.2}Mn_{0.1}Co_{0.7}Fe_2O_4$ have large coercive fields of 1.45, 3.02 and 10.70 kOe at 4 K compared to 0.17, 0.05 and 0.05 kOe at room temperature respectively. Variation of coercive fields (H_C) with measur-

ing temperature for $Mn_xCo_{1-x}Fe_2O_4$ ($x = 0.1$ and 0.05), $(Mg, Sr)_{0.2}Mn_{0.1}Co_{0.7}Fe_2O_4$ nanoferrites follow the Kneller's law for uniaxial non-interacting single domain particles of the form $H_C(T) = H_C(0)[1-(\frac{T}{T_B})^{\alpha}]$. The observed temperature dependences are consistent with $\alpha = 1/2$. We also find evidence of the departure from this law at lower temperature. The temperature dependence of the saturation magnetizations were observed to vary with temperature according to the modified Bloch's law $M_S(T) = M_S(0)[1-(\frac{T}{T_0})^{\beta}]$ where β is at least 1.5. This is attributed to the confinement effects of the spin-wave spectrum for magnetic clusters. The equation appears to fit the saturation magnetization data over the entire temperature range with values of β from 2.1 to 2.4 for the samples studied. These results are consistent with the nanoparticle nature of the compounds.

In $Mg_{0.5}Mn_{0.5}(RE)_{0.1}Fe_{1.9}O_4$ nanoferrites, the grain sizes, lattice parameters and saturation magnetizations increase with RE substitution which we attribute to larger RE ions substituting smaller Fe ions. The results show evidence of superparamagnetic behaviour of the nanoparticles. The highest grain size and magnetizations are obtained for the Gd substituted sample. We find strong correlation between the saturation magnetizations, grain sizes and microstrains with de Gennes factor G. The correlation with grain sizes and microstrains appear to be unique and characteristic of the nanoparticle nature of the compounds.

Bulk samples in the form of pellets were also produced from the as-prepared samples of $Mn_xCo_{1-x}Fe_2O_4$ for resistivity measurements. The temperature dependence of the electrical resistivity for samples sintered from 600 - 1100 ^oC under argon atmosphere were studied using the four-probe method from room temperature to about 110 ^oC. Two possible mechanisms for resistivity involving T^{-1} and $T^{-1/2}$ dependences were investigated which we associated with semiconducting and inter-grain conductivity respectively. The $T^{-1/2}$ dependence is found to fit the data better and predicts higher activation energies. The resistivity was observed to be sensitive to the surface of the pellet being probed and the annealing temperature.

Declaration 1

Plagiarism

I, Hafiz Mohammed Ibrahim Abdallah declare that

1. The research reported in this thesis, except where otherwise indicated, is my original research.

2. This thesis has not been submitted for any degree or examination at any other University.

3. This thesis does not contain other person's data, pictures, graphs or other information, unless specifically acknowledged as being sourced from other persons.

4. This thesis does not contain other person's writing, unless specifically acknowledged as being sourced from other researchers. Where other written source have been quoted, then:
   (i)- Their words have been re-written but the general information attributed to them has been referenced.
   (ii)- Where their exact words have been used, then their writing has been place in italics and inside quotation marks, and referenced.

5. This thesis does not contain text, graphics or tables copied and pasted from the internet, unless specifically acknowledged, and the source being detailed in the thesis and in the referenced sections.

Signed: ..... Date: 29/02/2012

Name: H. M. I. Abdallah

Declaration 2

Publications based on current work

1. Structural and Mössbauer studies of $Mn_{0.5}Co_{0.5}Fe_2O_4$ ferrites prepared by high energy ball milling and glycothermal methods, **H. M. I. Abdallah**, T. Moyo and J. Z. Msomi, J. Phys.: Conf. Ser., 217 (2010) 012141.

2. Structural and magnetic properties of $Mn_xCo_{1-x}Fe_2O_4$ ferrite nanoparticles, J. Z. Msomi, **H. M. I. Abdallah**, T. Moyo and A. Lančok, J. Magn. Magn. Mater., 323 (2011) 47.

3. Mössbauer and electrical studies of $Mn_xCo_{1-x}Fe_2O_4$ compounds prepared via glycothermal route, **H. M. I. Abdallah**, T. Moyo and J. Z. Msomi, J. Supercond. Nov. Magn., 24 (2011) 669.

4. Mössbauer and magnetic studies of $Mn_{0.5}Co_{0.5}Fe_2O_4$ and $Mn_{0.1}Mg_{0.2}Co_{0.7}$-Fe_2O_4 nanoferrites, **H. M. I. Abdallah**, J. Z. Msomi, T. Moyo and A. Lančok, J. Supercond. Nov. Magn., Accepted, published online first 05/08/2011 (DOI: 10.1007/s10948-011-1230-5).

5. The effect of annealing temperature on the magnetic properties of Mn_xCo_{1-x}-Fe_2O_4 ferrites nanoparticles, **H. M. I. Abdallah**, T. Moyo and J. Z. Msomi, J. Supercond. Nov. Magn., Accepted, published online first 09/08/2011 (DOI: 10.1007/s10948-011-1231-4).

6. Magnetic properties of $Mg_xMn_{1-x}Fe_2O_4$ nanoferrites, J. Z. Msomi, T. Moyo and **H. M. I. Abdallah**, J. Supercond. Nov. Magn., Accepted, published online first 09/08/2011 (DOI: 10.1007/s10948-011-1235-00).

7. Mössbauer and magnetic studies of $Mn_{0.1}Sr_{0.2}Co_{0.7}Fe_2O_4$ nanoferrite, **H. M. I. Abdallah**, J. Z. Msomi, T. Moyo, J. J. Dolo and A. Lančok, Hyperfine Interac., 203 (2011) 99.

8. XRD, magnetic and Mössbauer spectral studies of $Ag_xNi_{1-x}Fe_2O_4$ ferrite nanoparticles, J. Z. Msomi, T. Moyo, **H. M. I. Abdallah**, A. M. Strydom and D. Britz, J. Supercond. Nov. Magn., 24 (2011) 711.

9. Magnetic properties of nanosized $Mg_{0.5}Mn_{0.5}(RE)_{0.1}Fe_{1.9}O_4$ ferrites synthesized by glycol-thermal method, **H. M. I. Abdallah**, T. Moyo and J. Z. Msomi, IEEE Transac. Magn., submitted.

Signed: ..... Date: 29/02/2012

Name: H. M. I. Abdallah

Dedication

This thesis is dedicated to my father (Mohammed), mother (Fatna), wife (Mahassin), son (Basil) and the rest of my family for support and understanding.

Acknowledgements

An experimental research project requires several kinds of inputs such as support, assistance, advice, and experience of many people to ensure its success. Therefore, I am indebted to express my truthful appreciation to the following:

Firstly, I am duly indebted to my supervisor Dr T Moyo for giving me the opportunity to carry out research in Condensed Matter Physics. His endless support in various ways not to mention his guidance, mentor-ship, thoughtful suggestions, never ending discussion and good friendship has indeed led to the success of this project.

Secondly, throughout my expeditions in various conferences and laboratories, I met several distinguished persons who made fruitful suggestions and gave me invaluable advice. These include: Professor J M D Coey (Dublin University, Ireland), Dr M L Branham, Dr J Z Msomi, Dr J Wesley-Smith, Mrs P Maartens, and Ms S Eggers. Dr Msomi provided me with enormous support in carrying out magnetization measurements using SQUID magnetometers at the Institute of Inorganic Chemistry, Czech Republic, Karlsruhe Institute für Technologie, Germany and the Physics Department at the University of Johannesburg, South Africa. The members of the Electron Microscope Unit, Westville Campus, University of KwaZulu-Natal; especially Mrs Maartens and Ms Eggers guided me through the HRTEM and TEM measurements including carrying out the microanalysis of the samples. My colleagues in the School of Chemistry and Physics provided me with the appropriate working environment for carrying out my research. This work would not be possible without the financial support provided by Al-Fashir University, Sudan and the University of KwaZulu-Natal, South Africa. I am also grateful to the Al-Fashir University for the leave of absence.

Finally, the unwitting support from my parents not mentioning the words of encouragement, inspiration and support throughout my education chores have made me to aim beyond the sky; my wife (Mahassin Nemair) for her zeal to persevere with me throughout all the cuddles, and the blessing of our union my son, Basil. To all members of my family, your patience and understanding for the entire study period is highly appreciated. May Allah bless you all!

Contents

List of Figures

List of Tables

Chapter 1

General introduction to ferrites

Ferrites are commercially important materials because they have excellent magnetic properties and high electrical resistance [1, 2, 3, 4, 5, 6]. They are well known for their chemical stability and easy phase formation. These compounds have a wide range of applications in electronics, power applications and telecommunications [6, 7, 8]. Medical, data storage, high frequency and magneto-mechanical applications are examples of modern uses of ferrites [7, 9]. The design, synthesis and characterization of nanoscale ferrites now occupies the attention of many researchers. Significant improvements in the techniques for synthesis and characterization have been made in order to optimise the properties. Ferrites can also be used as model materials for the better understanding of the magnetic interactions in nanoparticle materials [7, 10]. Ferrites are ferrimagnetic materials which have the spinel structure [11, 12, 13]. The location of different magnetic ions in the structure gives interesting properties. The properties depend on the constituent atoms in the crystal structure which influence the different applications [14, 15].

Magnetite (Fe_3O_4) is an example of natural occurring ferrite. In the present work, the study of mixed ferrites has been undertaken in order to investigate the evolution of properties as a function of synthesis method, composition and temperature of the samples [16]. $Mn_xCo_{1-x}Fe_2O_4$, $Mg_xMn_{1-x}Fe_2O_4$, $(Mg, Sr)_{0.2}Mn_{0.1}Co_{0.7}Fe_2O_4$, and $Mg_{0.5}Mn_{0.5}(RE)_{0.1}Fe_{1.9}O_4$ (where RE are rare earth atoms) are examples of mixed ferrites which we have produced and studied [17, 18, 19, 20, 21, 22, 23, 24]. These ferrites have been produced by low temperature synthesis using a stirred pressure

reactor. High-energy ball milling has been used to reduce the particle sizes or as an alternative route for the synthesis of the compounds. Nanosized samples can also be produced directly from the above synthesis methods. These nanoferrites reveal interesting properties which are the subject of this thesis. In this chapter we discuss briefly the structure, synthesis techniques and basic properties of ferrites. In addition, a brief motivation for the current work is also given.

1.1 Structure

The ferrites are a group of oxides with spinel structure with space group $F\tilde{d}3m$ [13]. The large oxygen ions with radii of about 0.13 nm are packed close together in the face centred cubic arrangement. The smaller metal ions with radii of about 0.075 nm occupy the space between the oxygen ions. This leads to the formation of two kinds of oxygen polyhedra, namely tetrahedron (A site) and octahedron (B site) [12]. Figure 1.1 shows a sketch of the spinel structure. In this structure there are eight formula units which form a face centred cubic lattice. The 64 tetrahedral sites are surrounded by 4 oxygen ions and the 32 octahedral sites are surrounded by 6 oxygen ions [12, 26]. The general cationic distribution of spinel structure can be symbolically described by the chemical formula $(M^{2+}{}_{1-\lambda}\mathrm{Fe}^{3+}{}_{\lambda})(M^{2+}{}_{\lambda}\mathrm{Fe}^{3+}{}_{2-\lambda})\mathrm{O}_4$ where M is a divalent metallic ion such as Mn, Mg, Co, Sr, Ni or Cu [27, 28]. The first and second sets of brackets denote cation sites with tetrahedral and octahedral coordination respectively. λ is referred to as the degree of inversion which represents the fraction of the A sites occupied by trivalent Fe cations. In the ideal spinel structure the O^{2-} ions form a cubic close packed lattice which occupy $\frac{1}{8}$ of A site and $\frac{1}{2}$ of B site coordinated interstices [29]. At the vertices of sublattice A, the metallic ion is surrounded by four oxygen ions. On B site the metallic ion is surrounded by six oxygen ions. The occupation of A and B sites occurs in the ratio of 1:2. Therefore, ferrites contain two non-equivalent sites due to two different types of crystallographic sites [30]. There are two extreme types of spinels known as normal and inverse spinels. In the normal spinel $\lambda = 0$ where all the divalent M ions occupy tetrahedral sites and all the trivalent ions occupy octahedral sites. In the

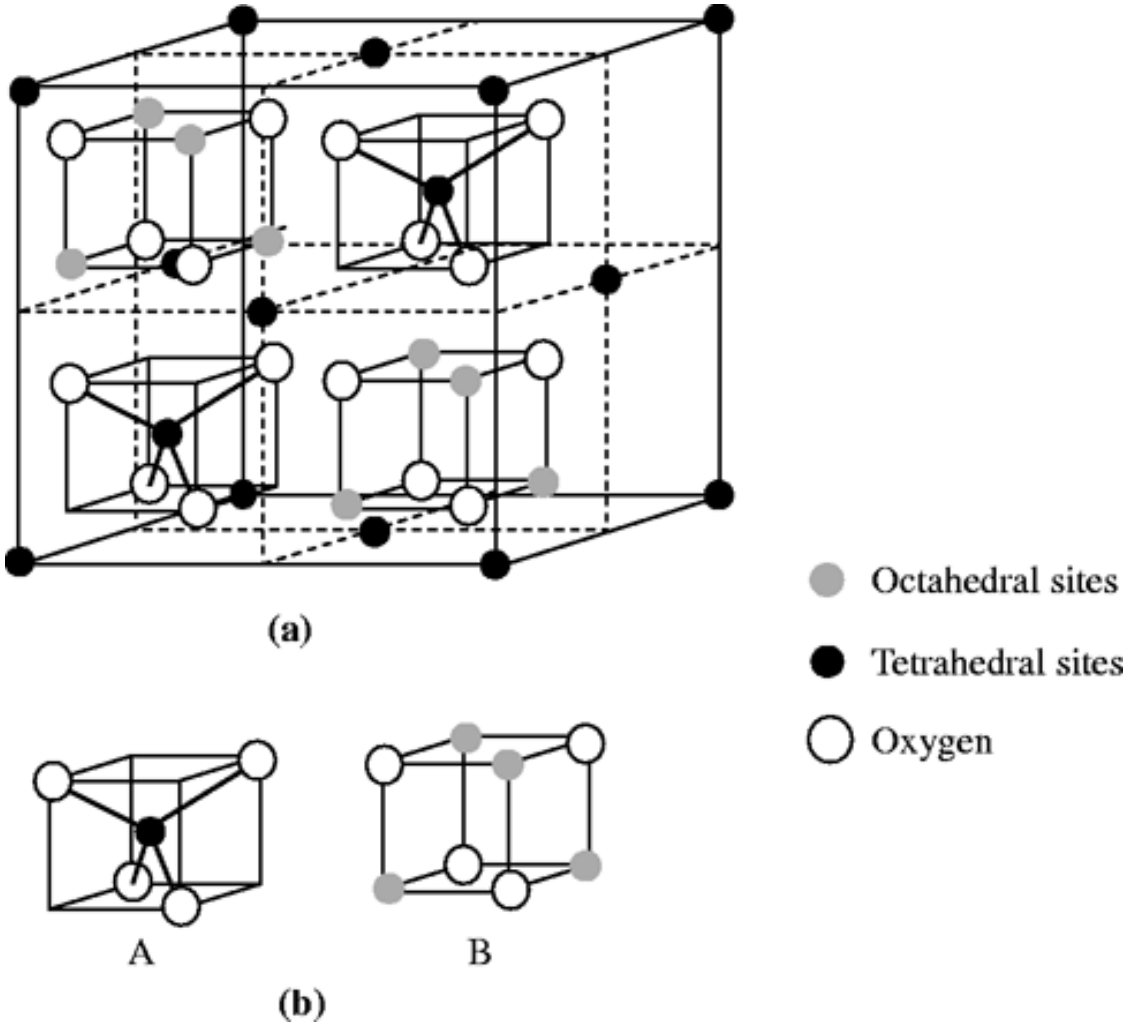

Figure 1.1: Schematic diagram of the spinel structure [25].

inverse spinel structure $\lambda = 1$. The divalent ions occupy half of the B sites and the trivalent ions are equally distributed between tetrahedral and octahedral sites. The normal and inverse spinels are sometimes designated as $(A)(B_2)O_4$ and $(B)(AB)O_4$ respectively [31].

Properties of ferrites are usually modified by chemical composition and cationic distribution in the spinel lattice that can be achieved by appropriate heat treatments [32]. Different ferrites can be synthesised with a range of possible distributions of the cations mixed by two or more kinds of divalent ions.

1.2 Synthesis

Bulk and nanosized ferrites can be produced by solid state reaction and wet chemistry methods. The ceramic method [33, 34, 35, 36, 37, 38, 39] and high-energy ball milling [27, 38, 40, 41] are examples of synthesis by solid state reaction. There are several wet chemistry methods which can be used to produce ferrites such as hydrothermal [42, 43, 44, 45, 46], glycol-thermal [47], sol-gel [8, 48, 49, 50], microwave refluxing [51], combustion process [2, 52, 53], microwave-induced combustion [54], co-precipitation [6, 54, 55, 56] and nitrate precursor [57, 58] methods.

The traditional method of producing ferrite materials is by the ceramic method. This requires two stages of grinding and double sintering in the temperature range of 900 – 1400 ^{o}C. The starting materials are pure metal oxides mixed in the correct proportion. This is a high temperature synthesis technique suited to the production of bulk samples. For high-energy ball milling the oxide mixture is milled for at least 50 hours in hardened steel or agate jars with an appropriate number of balls. The milling conditions depend strongly on the ball to sample mass ratio, the rotation speed of the jars and the atmosphere in the jars. This technique can produce nanoparticles directly. A little bit of sample can be removed from the jars at different time intervals in order to monitor the on-set of single phase formation. However, the grinding or milling techniques have an inherent disadvantage associated with mass losses due to adhesion of the sample to grinding surfaces. Furthermore, some erosion of the surfaces can take place leading to some contamination of the sample.

Metal oxides can also be produced by milling in oxygen atmosphere which cannot be avoided. Hence possible changes in stoichiometry of the final product can also occur due to the formation of metal oxides.

The combustion process can also be used to synthesize ferrites. Metal nitrates are mixed with a fuel such as urea and then heated up to generate an exothermic reaction from self-ignition of the mixture [52, 54].

The glycol-thermal process provides a powerful technique for synthesizing nano-sized compounds at low temperature with well controlled morphology and accurate stoichiometry. The starting materials are high-purity metal chlorides or nitrates mixed with a precipitating reagent such as ammonia. This is the primary technique that has been used to produced compounds studied in this thesis. A detailed discussion of the technique and the equipment used is given in chapter 3.

Other techniques for producing ferrites have also been innovated. These are intended to enhance the properties and improve single phase formation. These include plasma [59], micro-emulsion [60, 61], reverse mi-cell [62] and aerosol [63, 64] techniques.

1.3 Magnetic properties

There are several kinds of magnetic order that can be exist in solids [65]. This is attributed to the fact that magnetism is a structure sensitive phenomena. The magnetization of ferrites originates from the differences in the magnetic moments of the cations distributed at tetraheral (A) and octahedral (B) sites of the spinel cubic structure. This depends on the so-called superexchange magnetic interactions among A and B sites namely J_{AB} (A-O-B), J_{AA} (A-O-A) and J_{BB} (B-O-B). Ferrimagnetism prevails when J_{AB} becomes the strongest interaction. The interaction of the magnetic moments occurs through the intermediary O^{2-} ions to cause the magnetic order.

In bulk spinel ferrites the magnetic order is of long range with a net collinear spin structure. When the temperature of a sample decreases below the Curie temperature, the spontaneous magnetization increases. In some samples this may be

associated with remanent magnetization and coercive field due to freezing of the spins. Above the Curie temperature the paramagnetic order is observed.

In nanoparticle ferrites the interface spin canting occurs more strongly at the surface of a particle. For this reason the magnetic ground state may be influenced by the decreasing magnetization and ordering temperature. Nanoparticles tend to freeze into spin-glass-like phase at low temperatures [66]. The nanoferrite materials can be considered to consist of single-domain particles with magnetic moments of individual particles which act independently. The mechanism and strength of the interaction between nanoparticles is characterized by the instability of the magnetization due to thermal agitation. Each particle behaves like a paramagnetic atom with a magnetic moment [67]. This may result in the phenomenon of superparamagnetism which tends to be a unique feature of magnetic nanoparticles [68]. A more detailed discussion of magnetism in solids is given in chapter 2.

1.4 Electrical resistivity

Spinel ferrites have high electrical resistivity compared to other magnetic materials. Therefore, ferrites are widely used in several applications due to this combination of electrical and magnetic properties [6]. These properties depend on the chemical composition, cation distribution, grain size and preparation method. Ferrites with the compositions $M\mathrm{Fe_2O_4}$ where (M = Mn, Zn, Ni) are considered to be ideal materials for high frequency system passive components due to high resistivity, permeability and permittivity [4, 5, 6]. The substitution by different magnetic or non-magnetic cations at different sites in ferrite systems can provide different types of electrical and magnetic properties. In general, spinel ferrites behave like semiconductors with resistivity ranging between 10^{-2} and 10^{11} Ω cm. Singh [69] reported that the resistivity for $\mathrm{Mg}_x\mathrm{Mn}_{1-x}\mathrm{Fe_2O_4}$ bulk materials varies from 2×10^4 Ω cm to 9×10^5 Ω cm with increased magnesium concentration. The electrical resistivity appears to obey an exponential dependence of electrical resistivity with temperature. This also depends on the composition of the compound and the cation distribution. The resistivity is expected to be due to the presence of divalent Fe^{2+} and trivalent M^{3+}

ions. The extra electron from Fe^{2+} or the positive hole from M^{+3} can move through the crystal lattice. The existence of Fe^{2+} results in n-type behaviour and p-type behaviour from M^{3+}. The movement of a charge carrier is described on the basis of a hopping mechanism where the charge carrier jumps from one ionic site to another site as the temperature increases [26]. The hopping depends on the activation energy associated with energy barriers experienced by the electron during the hopping process.

The electrical conductivity can also be described on the basis of a granular tunnelling mechanism in which the charge carriers tunnel between neighbouring ferrite grains which are separated by grain boundaries [70].

1.5 Applications

The synthesis and study of magnetic nanoparticles with diameters of a few nanometers is important because of the possibility of enhancing the performance of existing materials [62]. The physical properties of ferrites depends strongly on their composition, synthesis conditions, crystallinity, shape, size and the distribution of nanoscale particles [8, 71]. The nanomagnetic particles have large volume fraction of the atoms in the grain boundary area with unusual properties like spin canting, surface anisotropy, dislocations and superparamagnetic behaviour [71].

Ferrites have a wide range of applications in the electronics industry based on their optical, electrical, magnetic and mechanical properties [6, 37, 72, 73]. Magnetic nanoparticles are used as the active components in ferrofluids, recording tape, flexible disk recording media, biomedical materials and catalysts. Cobalt ferrites ($CoFe_2O_4$) for example are important materials for high density magnetic and magneto-optic recording media [8, 50] becaues of their high magnetocrystalline anisotropy, high coercivity, moderate saturation magnetization, high chemical stability, strong wear resistance, good electrical insulation and significant mechanical hardness [8, 53, 74]. $CoFe_2O_4$ also has applications in drug delivery, colour imaging and biomolecule separation [75].

The Mn- substituted compounds have been found to be suitable for magnet-

optical, magnetomechanical [73], noncontact torque sensing, embedded stress-sensing and high magnetostriction applications [53]. Mn doped cobalt ferrites exhibit high magnetostriction, good mechanical properties and have low eddy current losses making them suitable in high frequency applications [57]. They also have high stress sensitivity and large magneto-mechanical effects and hence are suitable for application as stress sensors [72]. Mn doped Mg ferrites are used in high frequency applications because of their high initial permeability and low values of relative loss factor [58, 76]. Singh et al. [77] have also reported that a Mn-Mg ferrite is good candidate for magneto-electric applications. These ferrites have a rectangular hysteresis loop characteristics, making them highly suitable for use in memory and switching circuits of digital computers and as phase shifters [77].

1.6 Motivation for current work

Ferrites can therefore be considered to be strategic materials based on their interesting electronic, magnetic, optical, catalytic and mechanical properties. These materials tend to be synthesize by many different techniques. In the present work we aim to study the changes of some of the beneficial properties and to better understand the interesting Physics of mixed spinel ferrites. The nanosized compounds have become important because of the drastic changes in properties which occur when the particle sizes reduce from bulk samples. It is important to investigate how single phase formation is influenced by various factors such as synthesis method, conditions and route. In this respect, $Mn_xCo_{1-x}Fe_2O_4$ fine powders with $0 \leq x \leq 0.6$ have been synthesized by glycol-thermal reaction from pure metal chlorides at about 200 ^{o}C. Similar compounds with $x = 0$, 0.5 and 1.0 were synthesized by using high-energy ball milling from pure metal oxides. We also made single phase of $Mn_{0.5}Co_{0.5}Fe_2O_4$ from starting single phases of $CoFe_2O_4$ and $MnFe_2O_4$ powders by using high-energy ball milling. It has been observed that a pure and uniform form of a $Mn_{0.1}Co_{0.9}Fe_2O_4$ compound was difficult to obtain by high temperature synthesis using the ceramic technique [57]. We have therefore prepared related compounds with higher Mn content by different synthesis routes and at lower synthesis temperature in order to

investigate the single phase formation and associated properties.

The temperature dependence of resistivity in mixed ferrites is usually discussed on the basis of the Arrhenius equation which has T^{-1} dependence [4, 6, 78]. In the present case we have also investigated the $T^{-1/2}$ dependence associated with electrical conduction between grains [79, 80] which appear to proved better fits to the data.

Several efforts have been made to find the best substitutions to improve the properties of ferrites. Therefore, we have extended our studies to include substitutions by Mg, Sr and rare earth (RE) elements. In this respect we have produced and studied properties of $Mg_xMn_{1-x}(RE)_yFe_{2-y}O_4$ with $0 \leq x \leq 1.0$ and $0 \leq y \leq 0.1$ and $(Mg, Sr)_{0.2}Mn_{0.1}Co_{0.7}Fe_2O_4$ fine powders. We intend to investigate the temperature dependence of magnetization properties at different static magnetic fields.

We are also interested in the study of the onset of the single domain structure as a function of particle size and how it relates to the observed properties such as coercive fields. The particle size can be modified by milling and by thermal annealing of the as-prepared samples [72, 73]. Reliable values of the particle sizes are therefore necessary. We have obtained these from the measurements of X-ray diffraction (XRD), transmission electron microscopy (TEM) and high-resolution transmission electron microscopy (HRTEM).

In the next chapter a brief account of the basic magnetic interactions in solids are given. In chapter 3 we present the basic principles of Mössbauer spectroscopy. The experimental techniques relevant to the present study are discussed in chapter 4. The experimental results and discussions for different series of compounds are presented in chapters 5 – 8. Chapter 9 is devoted to the general conclusions and discussions derived from the thesis.

Chapter 2

Magnetic order in solids

In this chapter, we give a brief review of the most important concepts in magnetism. We define the magnetization, the susceptibility and the different types of magnetic order in solids. A summary of different models of micro-magnetism and magnetic interactions are also presented. These models are helpful in providing an explanation of the experimental data to be discussed in chapters 5 – 8.

2.1 Magnetization and susceptibility

The magnetization ($\overrightarrow{M}$) of a homogeneous isotropic material is defined as the total magnetic moment per unit volume which is expressed as

$$\overrightarrow{M} = \frac{1}{V}\sum_{i=1}^{N}\overrightarrow{\mu_i} \tag{2.1.1}$$

where V is the volume of a sample of mass m and $\overrightarrow{\mu_i}$ is the magnetic moment of each magnetic ion. This is usually measured under the influence of an external magnetic field, which affects the arrangement of the moments in the field direction. For a non-homogeneous compound, the magnetization can also be defined as

$$\overrightarrow{M} = \sum_{i=1}^{N}\frac{d\overrightarrow{\mu_i}}{dV}. \tag{2.1.2}$$

The magnetization depends on the magnetic coupling between magnetic moments and the temperature of the sample. Thermal expansion and magneto-striction affects the volume of a sample. This renders the use of $\overrightarrow{M}$ to be unsuitable in practice. In

experimental measurements, it is better to monitor the state of the magnetization per unit mass defined as

$$\overrightarrow{\sigma} = \frac{1}{m}\sum_{i=1}^{N}\overrightarrow{\mu_i}. \tag{2.1.3}$$

The magnetic state of a material depends strongly on how it responds to an external magnetic field. The response is characterized by magnetization M as a function of the applied field H. The response function is called the magnetic susceptibility (χ) [30] which can be defined as

$$\chi = \frac{\mu_o M}{B_o} \tag{2.1.4}$$

where B_o is the local macroscopic field intensity and μ_o is the permeability of free space. The fields B_o and H are related by

$$B_o = \mu_o H. \tag{2.1.5}$$

Various types of magnetic materials can be classified in three groups according to their bulk susceptibility. The first group consists of diamagnetic materials which are characterized by small negative susceptibilities. In these materials, the magnetization response is opposite to the direction of the applied magnetic field. The induced magnetic dipoles produced by eddy currents due to the applied field are responsible for diamagnetism. The induced magnetic dipoles are oriented anti-parallel to the applied field and give rise to a temperature independent magnetic susceptibility as shown in Figure 2.1. All materials have a diamagnetic effect but this is usually neglected because it tends to be small. Water, nearly all organic compounds, Cu, Ag, Hg, NaCl, CuO, SiO_2 and superconductors are examples of diamagnetic materials [65, 81, 82]. The second group of materials for which the susceptibility is small and positive are the paramagnets. The third well-known group of magnetic materials include ferromagnetic solids for which the susceptibility is large and positive [83]. Figure 2.2 shows the typical temperature dependence for inverse magnetic susceptibility of paramagnetic, ferromagnetic, antiferromagnetic and ferrimagnetic materials.

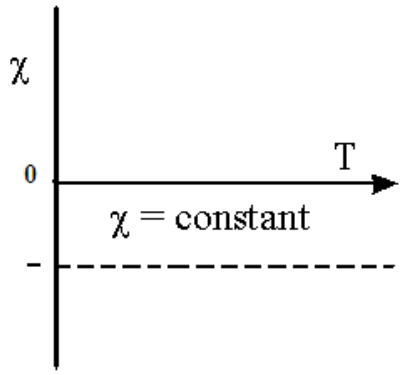

Figure 2.1: Graph of magnetic susceptibility versus temperature for a diamagnetic material [84].

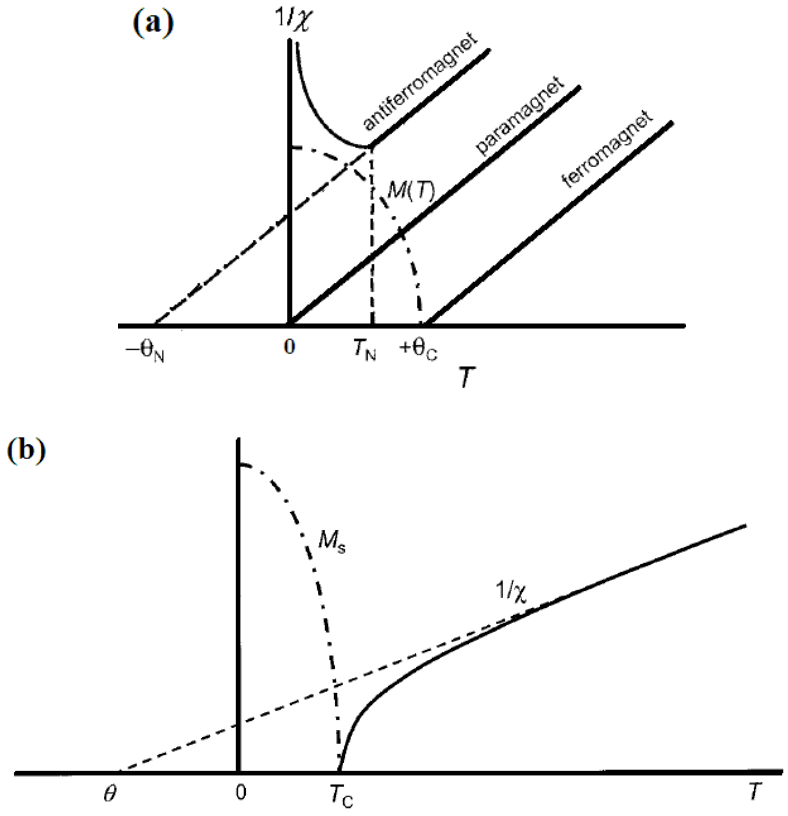

Figure 2.2: Variation of inverse magnetic susceptibilities with temperature for (a) paramagnetic, ferromagnetic, antiferromagnetic and (b) ferrimagnetic materials [81].

2.2 Paramagnetism

Paramagnetic materials consist of atoms and molecules with unpaired of electron spins, which give rise to permanent magnetic moments. These materials are characterized by a random orientation of magnetic moments as shown in Figure 2.3. Materials exhibiting paramagnetism have weakly interacting magnetic moments.

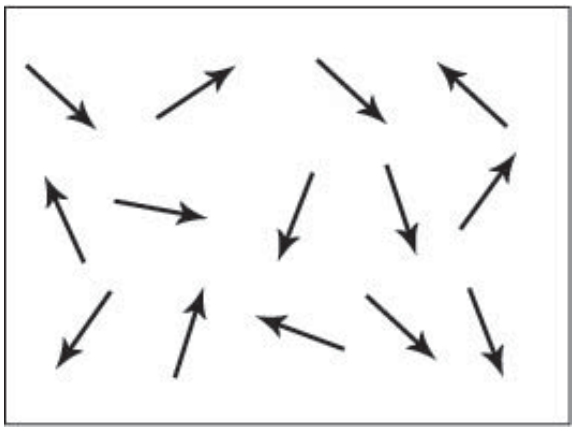

Figure 2.3: Magnetic structure in a paramagnet.

Their magnetic susceptibility is positive and temperature dependent. This is usually found in materials with atoms and ions with partially filled d and f shells in transition metals and rare earth elements respectively. In an applied magnetic field, the magnetic moments $\overrightarrow{\mu_i}$ re-orient towards the direction of the field. The corresponding splitting of the energy levels caused by the local field intensity B_o is given by

$$E_{m_J} = -\vec{\mu_i}.\vec{B_o} = -gm_J\mu_B B_o \tag{2.2.1}$$

where $\mu_B = eh/(4\pi m_e)$ is the Bohr magneton, J is the total angular momentum quantum number, m_J is the magnetic quantum number with values in range: $-J \leq m_J \leq J$, and g is the Lande's g- factor. The g- factor is given by the equation

$$g = 1 + \frac{J(J+1) + S(S+1) - L(L+1)}{2J(J+1)}. \tag{2.2.2}$$

The magnetic properties will mostly depend on the occupation of the $2J+1$ equally spaced energy levels under different experimental conditions. In equilibrium,

the probability for the occupation of each energy level E_{m_J} is given by the Maxwell-Boltzmann distribution [85]

$$P(E_{m_J}) = \frac{e^{-gm_J\mu_B B_o/k_B T}}{\sum_{m_J} e^{-gm_J\mu_B B_o/k_B T}} \tag{2.2.3}$$

where k_B is the Boltzmann constant. For a system consisting of n magnetic atoms or ions per unit volume, this leads to a magnetization which is given by

$$M = ng\mu_o\mu_B JB(J,x). \tag{2.2.4}$$

The parameter x is a dimensionless ratio of the Zeeman energy to the thermal energy [85] defined as

$$x = \frac{g\mu_B JB_o}{k_B T}. \tag{2.2.5}$$

$B(J,x)$ is called the Brillouin function which is defined by

$$B(J,x) = \frac{2J+1}{2J}\coth\left(\frac{(2J+1)x}{2J}\right) - \frac{1}{2J}\coth\left(\frac{x}{2J}\right). \tag{2.2.6}$$

When $J = 1/2$, equation (2.2.4) becomes

$$M = n\mu_B J\tanh x. \tag{2.2.7}$$

This is a special case for a two level system with $m_J = \pm 1/2$. Experimental measurements are usually conducted under conditions of $x \ll 1$ corresponding to high temperatures ($T \sim 300$ K) and low magnetic fields ($B_o \sim 1$ T). The Brillouin function can therefore be expanded into a Taylor series [85] where

$$B(J,x) \simeq \left(\frac{J+1}{3J}\right)x - \left(\frac{(J+1)[(J+1)^2+J^2]}{90J^2}\right)x^3 + O(x^5) + ... \tag{2.2.8}$$

Taking only the first order term in x, the magnetic moment per unit volume will be given by

$$M = \frac{ng^2\mu_B^2 J(J+1)B_o}{3k_B T}. \tag{2.2.9}$$

This leads to the Curie law for the susceptibility which can be expressed as

$$\chi = \frac{C}{T}. \tag{2.2.10}$$

The Curie constant C is given by

$$C = \frac{n\mu_o g^2\mu_B^2 J(J+1)}{3k_B}. \tag{2.2.11}$$

The Curie law is observed in dilute salts of transition metals, rare earth elements and actinides which have $3d$, $4f$ and $5f$ electrons in partially filled shells respectively. The agreement between theory and experimental results is better in rare earth and actinides where the magnetic electrons are in the inner shells. In this case, the picture of localised and non-interacting magnetic moments is more valid [86, 87]. In less dilute salts and crystals of pure elements, inter-ionic coupling of magnetic moments cannot be ignored [65]. This leads to the Curie-Weiss law which is expressed as

$$\chi = \frac{C}{T - \theta_p} \tag{2.2.12}$$

where θ_p is known as the paramagnetic Curie temperature.

2.3 Ferromagnetism

A ferromagnetic material consists of spins that are aligned-up spontaneously in more or less the same direction even in the absence of an applied magnetic field. Fe, Ni and Co are typical examples of the classical ferromagnetic materials. At absolute zero temperature, all magnetic moments are expected to be aligned parallel due to strong interaction as illustrated in Figure 2.4. With increasing thermal energy,

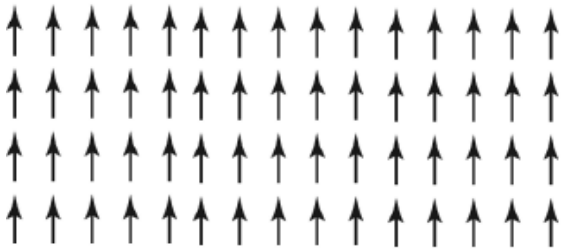

Figure 2.4: The magnetic structure of a ferromagnet [81].

the perfect alignment at $T = 0$ K declines and disappears completely at a critical temperature T_C called the Curie temperature. Above T_C, the magnetic moments point in random directions [65] and the material behaves like a paramagnet with a susceptibility that obeys the Curie-Weiss law. Below T_C the material is magnetically ordered [65, 81, 86, 87, 88, 89]. The Weiss mean-field theory has been used to study

the magnetization as a function of temperature in ferromagnetic materials. The theory is based on the assumption that magnetic moments order under the influence of an internal magnetic field B_{int}. This field is proportional to the local spontaneous magnetization (M_S) in the material given by

$$B_{int} = \lambda M_S \tag{2.3.1}$$

where λ is called the molecular field coefficient. The origin of this field is now known to be due to exchange interactions. We can estimate the size of the field by assuming the magnetic binding energy is $\mu_B B_{int}$. The thermal energy at T_C will be sufficient to destroy the perfect magnetic order that is assumed to exist at $T = 0$ K. Hence for a magnetic moment μ_B

$$\mu_B B_{int} \sim k_B T_C. \tag{2.3.2}$$

Typical values of T_C for many ferromagnetic materials are at least 100 K. For $T_C \sim$ 100 K, B_{int} is at least 100 T. This is a much larger field than can be obtained through the magnetic dipole interaction. This internal field is responsible for the splitting of the energy levels similar to equation (2.2.1). The effective field B_{eff} in a sample can therefore be attributed to additional external applied field B_o and the Weiss internal field B_{int} [30]. This can expressed as

$$\vec{B}_{eff} = \vec{B}_o + \lambda \vec{M}_S. \tag{2.3.3}$$

Similar to equation (2.2.4) the spontaneous magnetization of a ferromagnetic material can be written as

$$M_S(B_o, T) = ngJ\mu_B B(J, y) \tag{2.3.4}$$

where the parameter x is replaced by the parameter y defined as

$$y = \frac{gJ\mu_B(B_o + \lambda M_S)}{k_B T}. \tag{2.3.5}$$

The spontaneous magnetization $M_S(B_o, T)$ is still finite even for $B_o = 0$. In this case, the magnetic state of the sample will be described by two simultaneous equations

$$\frac{M_S(T)}{M_S(0)} = \frac{M_S(0, T)}{M(0, 0)} = B(J, y) \tag{2.3.6}$$

and

$$\frac{M_S(T)}{M_S(0)} = \frac{k_B T}{n\lambda g^2 J^2 \mu_B^2} y \tag{2.3.7}$$

derived from equations (2.3.4) and (2.3.7) respectively where $M_S(0) = ngJ\mu_B$ is the spontaneous magnetization at $T = 0$ K. The variation of the magnetization based on equations (2.3.6) and (2.3.7) is illustrated in Figure 2.5. The non-trivial intersection of equations of (2.3.6) and (2.3.7) corresponds to the possible magnetic state of the sample. The intersection point recedes to the state of zero spontaneous magnetization at $T = T_C$. At low temperatures as $T \longrightarrow 0$ K the parameter y becomes very large or $y \gg 1$. The Brillouin function can then be shown to be approximately

$$B(J, y) \simeq 1 - \frac{1}{J} exp(-\frac{y}{J}). \tag{2.3.8}$$

This leads to a spontaneous magnetization at low temperatures which is expected to vary as

$$\frac{M_S(T)}{M_S(0)} \simeq 1 - \frac{1}{J} exp(-\frac{\beta}{T}) \tag{2.3.9}$$

where β is a constant. Unfortunately this result is not observed experimentally [81]. What is observed is a temperature dependence of the form

$$\frac{M_S(T)}{M_S(0)} = 1 - AT^{3/2} + ... \tag{2.3.10}$$

which is known to be due to spin wave excitations. Near T_C and above, the parameter y tends to be much smaller than one ($y \ll 1$). Based on the first term in the Brillouin function approximation in equation (2.2.8) and from equations (2.3.4) and (2.3.7), we can deduce the molecular field coefficient (λ) from a known value of T_C to be

$$\lambda = \frac{3k_B T_C}{nJ(J+1)g^2\mu_B^2}. \tag{2.3.11}$$

Above T_C a ferromagnetic sample will be in a paramagnetic state for which any observed magnetization M will depend on the applied field B_o and the internal field λM. We can therefore replace B_o by $B_o + \lambda M$ in equation (2.3.9) to take into account interactions between magnetic moments. This leads to the Curie-Weiss law for the paramagnetic susceptibility

$$\chi = \frac{C}{T - \theta_p} \tag{2.3.12}$$

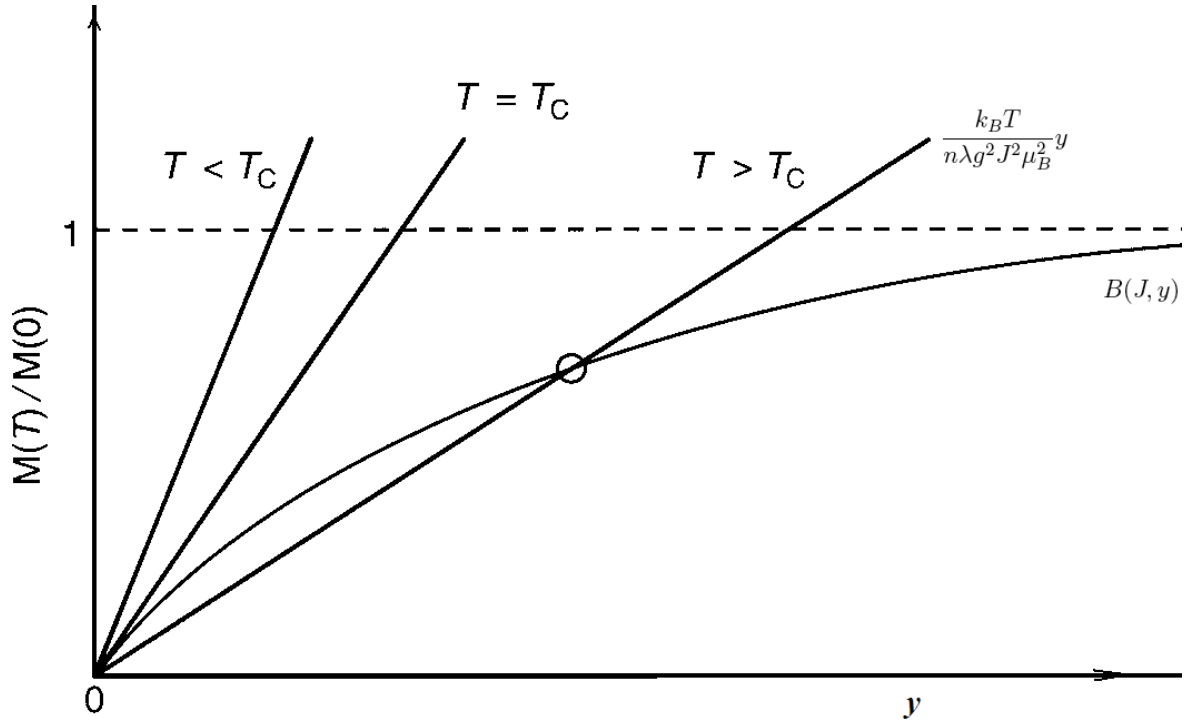

Figure 2.5: The point of the intersection between equations (2.3.6) and (2.3.7) defines the magnetic state of a sample. The spontaneous magnetization breaks down at $T = T_C$ where the linear curve is tangential to the Brillouin curve at the origin [84].

where C is the Curie constant defined in equation (2.2.11). θ_P is the paramagnetic Curie point for which

$$\theta_P = \lambda C. \tag{2.3.13}$$

For many materials, $\theta_P \gtrsim T_C$. The spontaneous magnetization of a ferromagnetic material can also be studied just below the Curie temperature T_C. Here the parameter y is still small but we need to include the first two terms of the Taylor expansion of $B(J, y)$ in our calculations (see equation (2.2.8)). This results in

$$\left(\frac{M_S(T)}{M(0)}\right)^2 = \frac{10(J+1)^2}{3(J^2+(J+1)^2)}.\left(1-\frac{T}{T_C}\right)\left(\frac{T}{T_C}\right)^2. \tag{2.3.14}$$

Just below T_C the reduced magnetization will be more sensitive to

$$\frac{M_S(T)}{M(0)} \propto \left(1-\frac{T}{T_C}\right)^{1/2}. \tag{2.3.15}$$

2.4 Antiferromagnetism

The lattice structure of magnetic atoms in an antiferromagnetic material is divided into two equivalent interpenetrating sublattices A and B such that A atoms have only B atoms as nearest-neighbours and vice versa. In most calculations it is assumed that the dominant interaction is between the nearest neighbours. This alignment occurs because of the negative exchange interaction. Typical spin alignments in an antiferromagnetic material are shown in Figure 2.6. Antiferromagnetism in-

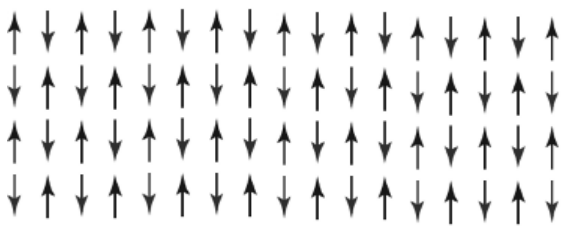

Figure 2.6: Magnetic structure in an antiferromagnet [81].

volves long-range order mechanism between identical magnetic moments on the two sublattices. At absolute zero, each sublattice has its maximum saturation magnetization and as the temperature increases, thermal excitation reduces the sublattice

spontaneous magnetization in a way similar to a ferromagnet. The spontaneous magnetization in a sublattice goes to zero at a critical temperature (T_N) called the Néel temperature. However, the net spontaneous magnetization of an antiferromagnet is zero at all temperatures $T \leq T_N$ as a result of the exact cancellation of the spontaneous magnetization of the two identical sublattices. Above T_N, the moments in each sublattice are randomly oriented and paramagnetic behaviour is observed. At $T = 0$ K spontaneous magnetization of the sublattices will be saturated but in opposite orientation [65, 86].

In order to study the magnetic properties of antiferromagnetic materials we use the same concepts as for ferromagnetism and mean-field theory that we have used before. However, the molecular field caused by the moments within the same sublattice will be different from that caused by moments of the other neighbouring sublattices. We can consider an antiferromagnet with an arrangement of magnetic moments as in Figure 2.6. We assume that the magnetic order is mediated by an internal magnetic field at each sublattice due to the interaction with the first and second nearest-neighbours. Hence, at each sublattice A and B, the internal magnetic fields are

$$\vec{B}^{A}_{int} = \lambda_{AA}\vec{M}_A + \lambda_{AB}\vec{M}_B \tag{2.4.1}$$

and

$$\vec{B}^{B}_{int} = \lambda_{BA}\vec{M}_A + \lambda_{BB}\vec{M}_B \tag{2.4.2}$$

where $\vec{M}_A$ and $\vec{M}_B$ are magnetizations at sublattices A and B respectively. λ_{ij} ($i, j =$ A, B) are the molecular field coefficients corresponding to first and second neighbours. The interaction between the first nearest-neighbours is antiferromagnetic and ferromagnetic between the second neighbours. Hence

$$\lambda_{AB} = \lambda_{BA} = -\lambda_1 \tag{2.4.3}$$

and

$$\lambda_{AA} = \lambda_{BB} = \lambda_2 \tag{2.4.4}$$

where $\lambda_1,\ \lambda_2 > 0$. The variation of the magnetization at each sublattice with temperature can be expressed as before as

$$M_i(T) = \frac{n}{2} g J \mu_B B(J, y_i) \tag{2.4.5}$$

where

$$y_i = \frac{Jg\mu_B B^i_{int}}{k_B T}. \tag{2.4.6}$$

In an antiferromagnet the net magnetization is effectively equal to zero below T_N. Hence

$$\vec{M}_A + \vec{M}_B = 0. \tag{2.4.7}$$

We can easily show that

$$y_i = \frac{Jg\mu_B}{k_B T}(\lambda_1 - \lambda_2)\vec{M}_i. \tag{2.4.8}$$

Clearly for each sublattice

$$M_i(T) = \frac{n}{2} gJ\mu_B B(J, y) \tag{2.4.9}$$

where

$$y = \frac{Jg\mu_B}{k_B T}\lambda M \tag{2.4.10}$$

and

$$\lambda = \lambda_1 - \lambda_2. \tag{2.4.11}$$

Equations (2.4.9) and (2.4.10) are similar to the ferromagnetic case. Here the magnetization in a sublattice will become zero at a T_N which is analogous to the magnetization at the Curie temperature T_C. Similarly T_N can be expressed as

$$T_N = (\lambda_1 - \lambda_2)\frac{n}{2}\frac{J(J+1)g^2\mu_B^2\mu_o}{k_B\mu_o} \tag{2.4.12}$$

or

$$T_N = \frac{(\lambda_1 - \lambda_2)}{2\mu_o} C \tag{2.4.13}$$

where C is the Curie constant.

Above T_N, the magnetization will depend on the applied field B_o. Hence, the effective fields (B_{eff}) at sublattices A and B will be given by

$$\vec{B}^A_{eff} = \vec{B}_o + \vec{B}^A_{int} = \vec{B}_o - \lambda_2\vec{M}_A - \lambda_1\vec{M}_B \tag{2.4.14}$$

and

$$\vec{B}^B_{eff} = \vec{B}_o + \vec{B}^B_{int} = \vec{B}_o - \lambda_1\vec{M}_A - \lambda_2\vec{M}_B. \tag{2.4.15}$$

The magnetization in each sublattice will be given by

$$\vec{M}_A = \frac{C}{T}(\vec{B}_o - \lambda_2\vec{M}_A - \lambda_1\vec{M}_B) \tag{2.4.16}$$

and

$$\vec{M}_B = \frac{C}{T}(\vec{B}_o - \lambda_1\vec{M}_A - \lambda_2\vec{M}_B). \tag{2.4.17}$$

Adding the two equations (2.4.16) and (2.4.17) gives

$$\vec{M}_A + \vec{M}_B = \frac{C}{T}[2\vec{B}_o - \lambda_1(\vec{M}_A + \vec{M}_B) + \lambda_2(\vec{M}_A + \vec{M}_B)]. \tag{2.4.18}$$

Since the magnetization $\vec{M}$ is given by

$$\vec{M} = \vec{M}_A + \vec{M}_B, \tag{2.4.19}$$

we can easily show that the susceptibility in an antiferromagnet follows Curie-Weiss law

$$\chi = \frac{C}{T - \theta_p} \tag{2.4.20}$$

where the paramagnetic Curie temperature θ_p is now defined as

$$\theta_p = -\frac{1}{2}(\lambda_1 + \lambda_2)\frac{C}{\mu_o}. \tag{2.4.21}$$

From equations (2.4.13) and (2.4.21) we can show that

$$T_N = \frac{(\lambda_1 - \lambda_2)}{2\mu_o}C. \tag{2.4.22}$$

The two characteristic temperatures T_N and θ_p are related [81] as follows

$$\theta_p = -\frac{(\lambda_1 + \lambda_2)}{(\lambda_1 - \lambda_2)}T_N. \tag{2.4.23}$$

The susceptibility of an antiferromagnetic material below the Néel temperature depends critically on the direction of the external applied magnetic field with respect to the direction of orientation of the spins [85]. The susceptibility will depend on whether the applied field (B_o) is perpendicular to the spins ($\chi_\perp$) or the applied field and the spins are along the same line ($\chi_\parallel$). The average antiferromagnetic susceptibility for a polycrystalline material can therefore be defined [85] as

$$\chi_{av} = \frac{1}{3}\chi_\parallel + \frac{2}{3}\chi_\perp. \tag{2.4.24}$$

2.5 Ferrimagnetism

Crystalline materials with non-equivalent magnetic atoms on different sublattices are known as ferrimagnets which were predicted by Néel in 1948 [65, 89]. Ferrimagnetism occurs in most oxides [85]. It is an intermediate magnetic state between ferromagnetism and antiferromagnetism [81]. The magnetic moments are arranged as in antiferromagnets but opposing moments on the sublattices are unequal. Therefore, the net spontaneous magnetization will be nonzero below a critical temperature. Figure 2.7 shows the simplest form of spin alignments in a ferrimagnetic crystal. The total magnetization is therefore given by

$$\vec{M} = \vec{M}_A + \vec{M}_B. \tag{2.5.1}$$

Above T_C the susceptibility follows the Curie-Weiss law but with a negative para-

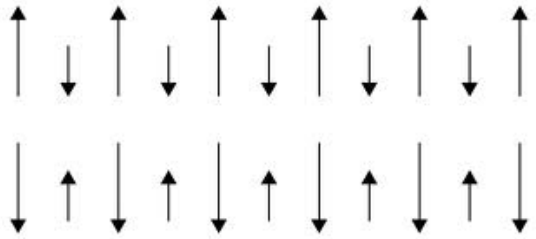

Figure 2.7: Magnetic structure in a ferrimagnet [90].

magnetic Curie temperature. We can follow the procedure used to describe antiferromagnets in order to determine the magnetization and susceptibility of ferrimagnets [30]. In the presence of an applied field (B_o), the total magnetic field acting on magnetic moments at each sublattice is the same as in equations (2.4.14) and (2.4.15). However, in ferrimagnets the sublattices are not identical. This means that $\vec{M}_A \neq \vec{M}_B$, $\lambda_{AA} \neq \lambda_{BB}$ with essentially negative interaction associated with λ_{AB}. The magnetization of each sublattice is explained by using the Brillouin function. The net magnetization collapses to zero at a critical temperature T_C which is also referred to as the Curie temperature. The magnetic moments of each sublattice [85] is given by

$$M_i(J,T) = M_A(0)B(J,x_i) \tag{2.5.2}$$

where

$$x_i = \frac{\mu^i_{eff} B^i_{int}}{k_B T}. \tag{2.5.3}$$

μ^i_{eff} is the effective magnetic moment. The total magnetization in each sublattice is the same as in equations (2.4.16) and (2.4.17). The spontaneous magnetizations will appear when $T < T_C$. The expression for the Curie temperature of ferrimagnets can be shown to be [85]

$$T_C = \frac{1}{2}\left((\lambda_{AA}C_A + \lambda_{BB}C_B) \pm \sqrt{(\lambda_{AA}C_A - \lambda_{BB}C_B)^2 + 4C_A C_B \lambda^2_{AB}}\right). \tag{2.5.4}$$

By combining the two sublattice theory with the mean-field theory, the susceptibility of the ferrimagnets above T_C follows an expression of the form [85]

$$\frac{1}{\chi} = \frac{T - \theta_p}{C_A + C_B} - \frac{C'}{T - \theta'} \tag{2.5.5}$$

where the constants C', θ', C_A, C_B are the microscopic parameters of the material. Hence, above the transition temperature, the variation of the inverse susceptibility with temperature for ferrimagnets is expected to follow a hyperbolic behaviour [81, 85, 88, 91].

2.6 Superparamagnetism

Superparamagnetism is a unique feature of magnetic nanosized particles. Ferromagnetic materials of a few nanometers radius of about $R \gtrsim 10$ nm become unstable when the energy barrier to magnetic reversal is comparable to $k_B T$ due to thermal excitation. Therefore, the material behaves like a paramagnetic macro-spin [85]. This behaviour is explained on the basis of the Stoner-Wohlfarth model of single-domain nanoparticles [85]. The theory assumes an ensemble consisting of widely spaced, isolated, non-interacting single-domain particles with a coherent rotation of the magnetization of each particle [85]. Superparamagnetic properties are influenced by the magnetocrystalline anisotropy which is caused by the spin-orbit $(L-S)$ coupling in a crystal. The magnetocrystalline anisotropy energy (E_A) for single-domain particle of uniaxial anisotropy is approximately given by [92]

$$E_A = KV \sin^2\theta \tag{2.6.1}$$

where K is the effective uniaxial anisotropy energy per unit volume, V is the volume of the nanoparticle and θ is the angle between the directions of the moment and the easy axis. The magnetic properties of the nanosize particles depend on the energy barriers, measuring time (τ_o) and relaxation time (τ) [93]. The inverse spin-flip frequency is known as relaxation time which can be obtained by using Néel-Brown relaxation law [85, 93]

$$\tau = \tau_o \exp\left(\frac{E_A}{k_B T_B}\right) \tag{2.6.2}$$

where τ_o^{-1} is the ferromagnetic resonance frequency in the demagnetizing field and T_B is the blocking temperature for the nanoparticle [94, 95].

Experimentally, superparamagnets do not show hysteresis in the variation of their isothermal magnetization as a function of applied magnetic field [65]. The superparamagnetic state vanishes with the reduction in temperature. The magnetization curve shows a rapid transition when decreasing the temperature of the sample. A transition temperature T_B called the blocking temperature can be defined which increases with increasing particle size [65]. In the superparamagnet region $T_B < T < T_C$, the magnetization response of the particles under the influence of an applied field H is given by [92, 93, 96, 97]

$$\frac{M(T)}{M_S(0)} = \coth\left(\frac{\mu H}{k_B T}\right) - \frac{k_B T}{\mu H} = L\left(\frac{\mu H}{k_B T}\right) \tag{2.6.3}$$

where L is the Langevin's function and μ is the moment of the superparamagnetic particle. Due to the collective excitations, the magnetizations of the nanoparticles can be expressed as

$$M(T) \approx M_S(0)\left(1 - \frac{k_B T}{2KV}\right). \tag{2.6.4}$$

2.7 Magnetic inter-particle interactions

In this section, we briefly describe the most important interactions which are responsible for magnetic properties. Magnetic moments in solids can interact through magnetic dipole-dipole, exchange and spin wave interactions. The exchange interaction is a pure quantum mechanical effect, which is attributed to the Coulomb interaction and Pauli exclusion principle [81]. The exchange interaction is the largest

magnetic interaction in solids which is responsible for the existence of parallel (ferromagnetic) and antiparallel (antiferromagnetic and ferrimagnetic) spin alignments. The exchange interaction can be mediated by different mechanisms depending on the material being studied.

2.7.1 Dipole-dipole interaction

The direct interaction energy (E_d) between two magnetic dipoles $\vec{\mu_i}$ and $\vec{\mu_j}$ depends on their distance of separation ($\vec{r}$) and their relative orientations [81, 98]. This energy is given by

$$E_d = \frac{\mu_o}{4\pi r^3}\left(\vec{\mu_i}\cdot\vec{\mu_j} - \frac{3}{r^2}(\vec{\mu_i}\cdot\vec{r})(\vec{\mu_j}\cdot\vec{r})\right). \tag{2.7.1}$$

We can estimate the strength of the magnetic dipole interaction by assuming two identical magnetic moments ($\mu_i = \mu_j = 1\ \mu_B$) separated by about 2 Å [81]. We also assume that $\vec{\mu_i} \uparrow\uparrow \vec{\mu_j}$ and $\vec{\mu} \uparrow\uparrow \vec{r}$. From equation (2.7.1) we get

$$|E_d| \simeq \frac{\mu_o \mu_B^2}{2\pi r^3}. \tag{2.7.2}$$

This gives a magnetic interaction energy $|E_d| \simeq 2\times10^{-24}$ J. A thermal energy $\sim k_B T$ would be required to destroy this parallel alignment. Assuming $k_B T_C \simeq |E_d|$, we find $T_C \sim 0.1$ K. For most ferromagnetic materials T_C is at least 10^2 K [81, 98]. Clearly the magnetic dipole interaction cannot be responsible for magnetic order in materials.

2.7.2 Direct exchange interactions

In materials where the magnetic atoms are relatively close to each other, the interaction between magnetic moments occurs through partially overlapping localised atomic orbitals between atoms. The magnetic moments couple together through direct exchange interactions. This is associated with the Heisenberg model for magnetism. The interaction is based on Coulomb interaction and Pauli exclusion principle which does not allow any two electrons to be in the same quantum state. For simplicity we will assume a system consisting of two atoms A and B each with

independent electrons at position vectors $\vec{r_1}$ and $\vec{r_2}$ [99]. We are interested in the interaction of the two electron spins. Since the electrons are fermions, their total wave function ($\Psi = \psi\chi$) has to be antisymmetric in order to satisfy the Pauli exclusion principle. Two possible situations arise for the total wave function. The first situation represents a symmetric spatial part ψ combined with an antisymmetric spin part χ, which leads to a singlet state with zero total spin ($S_{total} = 0$). The second situation represents an antisymmetric spatial part ψ combined with symmetric spin parts χ which leads to triplet states with $S_{total} = 1$ [81, 98]. The corresponding total wave function for the singlet state (Ψ_S) and triplet (Ψ_T) states can be expressed as follows:

$$\Psi_S(\vec{r_1}, \vec{r_2}) = [\psi_A(1)\psi_B(2) + \psi_A(2)\psi_B(1)][\alpha(1)\beta(2) - \alpha(2)\beta(1)] \tag{2.7.3}$$

and

$$\Psi_T(\vec{r_1}, \vec{r_2}) = [\psi_A(1)\psi_B(2) - \psi_A(2)\psi_B(1)] \begin{cases} \alpha(1)\alpha(2) \\ \alpha(1)\beta(2) + \alpha(2)\beta(1) \\ \beta(1)\beta(2) \end{cases} \tag{2.7.4}$$

$\alpha(i)$ donates the spin-up state of the i^{th} electron with $m_S = -1/2$. $\beta(j)$ donates the spin-down state of the j^{th} electron with $m_S = +1/2$. The energies of the two possible situations can be calculated from the Hamiltonian $\hat{H}(\vec{r_1}, \vec{r_2})$ for the two electrons as follows

$$E_S = \int \Psi_S^*(\vec{r_1}, \vec{r_2})\hat{H}(\vec{r_1}, \vec{r_2})\Psi_S(\vec{r_1}, \vec{r_2})dr_1^3 dr_2^3 \tag{2.7.5}$$

and

$$E_T = \int \Psi_T^*(\vec{r_1}, \vec{r_2})\hat{H}(\vec{r_1}, \vec{r_2})\Psi_T(\vec{r_1}, \vec{r_2})dr_1^3 dr_2^3. \tag{2.7.6}$$

The energy splitting between the singlet and triplet states can be defined as $2J_{12}$. The exchange integral J_{12} can be deduced from equations (2.7.5) and (2.7.6) to be [85, 98]

$$J_{12} = \frac{E_S - E_T}{2} = \int \psi_A^*(\vec{r'})\psi_B^*(\vec{r})\hat{H}(\vec{r'}, \vec{r})\psi_A(\vec{r'})\psi_B(\vec{r})dr'^3 dr^3. \tag{2.7.7}$$

If the exchange integral $J_{12} > 0$, the singlet state will have higher energy ($E_S > E_T$). In this case the preferred state will be the triplet state. This means that the spins

between the two electrons will be parallel to each other in ferromagnetic alignment. On the other hand if $J_{12} < 0$, the singlet state will have lower energy ($E_S < E_T$). The singlet will be the preferred state which is associated with antiparallel spin arrangement (antiferromagnetic coupling). These results can be expressed in terms of a Heisenberg Hamiltonian of the form

$$H_E = -2J_{12}\hat{\vec{S}}_1 \cdot \hat{\vec{S}}_2. \tag{2.7.8}$$

Note that for a bound state of spins $H_E < 0$ always. If $J_{12} > 0$, parallel spins occur while for $J_{12} < 0$, the spins arrangement will be antiparallel as before. In a lattice, the general Heisenberg Hamiltonian can be generalised to a sum over all pairs of atoms on lattice sites i and j [82] giving

$$H_E = -2\sum_{i>j} J_{ij}\hat{\vec{S}}_1 \cdot \hat{\vec{S}}_2. \tag{2.7.9}$$

By using the Heisenberg model we can also justify the mean field theory. We proceed by replacing spins by their thermal averages. Hence

$$\langle H_E \rangle = -2\sum_{i>j} J_{ij}\langle\hat{\vec{S}}_i\rangle \cdot \langle\hat{\vec{S}}_j\rangle. \tag{2.7.10}$$

$\langle\hat{\vec{S}}_i\rangle$ can be replaced by the magnetization $\vec{M}_i$ for n atoms per unit volume where

$$\vec{M} = ng\mu_B\langle\vec{S}_i\rangle. \tag{2.7.11}$$

Thus

$$\langle H_E \rangle = -\sum_{i>j}\left(\frac{2J_{ij}\vec{M}_i}{n^2g^2\mu_B^2}\right) \cdot \vec{M}_j. \tag{2.7.12}$$

For a homogeneously magnetised material $\vec{M}_i = \vec{M}_j = \vec{M}$. $\sum J_{ij}$ can be defined in terms of a single exchange constant J_o associated with Z nearest neighbour interactions where

$$\sum J_{ij} = ZJ_o n. \tag{2.7.13}$$

Hence

$$\langle H_E \rangle = -\frac{2ZJ_o}{ng^2\mu_B^2}\vec{M} \cdot \vec{M} = -\vec{B}_{int} \cdot \vec{M}. \tag{2.7.14}$$

This gives

$$B_{int} = \frac{2ZJ_o}{ng^2\mu_B^2}M = \lambda M. \tag{2.7.15}$$

Hence from equation (2.7.10) and for $J = S$ [85]

$$T_C = \frac{2ZJ_oS(S+1)}{3k_B}. \tag{2.7.16}$$

2.7.3 Indirect exchange interactions

This is responsible for interaction of magnetic moments that are relatively far from each other. This takes place via intermediary atoms or conduction electrons. If the intermediary is a non-magnetic ion, the interaction is called superexchange. This is the basic mechanism for the interaction of magnetic moments in magnetic insulators. In addition, superexchange tends be a common mode of interaction in antiferromagnetic materials. Superexchange can also be described by a Heisenberg Hamiltonian, where the sign of the exchange integral is obtained by the metal-oxygen-metal bond angle and the $d-$electron configurations in transition metals [100].

The RKKY (Ruderman-Kittel-Kasuya-Yosida) interaction occurs in metals with localized magnetic moments through the polarization of the conduction electrons. In this interaction, $J_{ij}(r)$ leads to long-range oscillatory coupling between core spins [85, 81]. The coupling is characterized by the variation of the effective exchange integral $J_{eff}(x)$ with distance x which is given by

$$J_{eff}(x) = \frac{9\pi J_{sf}^2 \nu^2}{64E_F} \frac{\sin x - x\cos x}{x^4}. \tag{2.7.17}$$

E_F is the Fermi energy, J_{sf} is the exchange integral for $s-f$ coupling and ν is the number of electrons per atom into the conduction band. The sign of J_{eff} oscillates between positive and negative values with distance between ions. This leads to ferromagnetic or antiferromagnetic coupling as shown in Figure 2.8.

In the rare earth metals, S alone is no longer a good quantum number. The interactions between spins must take into account spin-orbit coupling. This introduces a factor $G = (g-1)^2 J(J+1)$ into the exchange coupling where the effective coupling is

$$J_{RKKY} = GJ_{eff}. \tag{2.7.18}$$

G is called the de Gennes factor. The effect of the factor is important in rare earth metals and compounds [85].

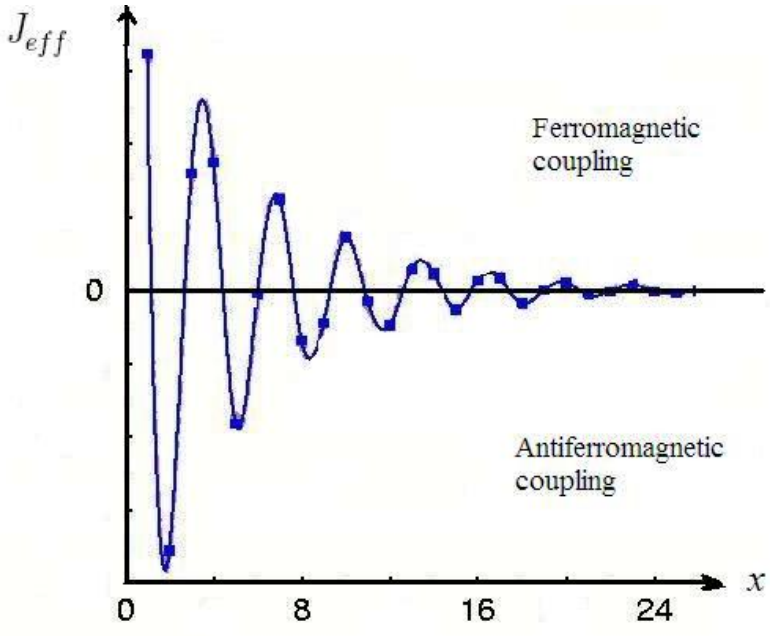

Figure 2.8: Graph of J_{eff} versus x.

2.8 Spin waves

We consider a system of N nearest neighbour spins of magnitude S on a line or a ring. For a simple ferromagnetic, the interaction between spins at sites j based on the Heisenberg interaction is given by [86, 101]

$$U = -2J_o \sum_{j=1}^{N} \vec{S}_j \cdot \vec{S}_{j+1}. \tag{2.8.1}$$

At $T = 0$ K, there will be a perfect alignment of spins $\uparrow\uparrow\uparrow\uparrow\uparrow$ .... $\uparrow\uparrow\uparrow^{j}\uparrow^{j+1}$. The total exchange energy in the ground state of the ferromagnetic will be $U_o = -2J_oNS^2$. For $T > 0$ K, the first excited state spin alignment can be approximated by the reversal of a single spin say $\uparrow\uparrow\uparrow\uparrow\downarrow\uparrow\uparrow\uparrow\uparrow$. Unfortunately this spin reversal is found to involve too much energy. In practice, we find that all atoms share the spin reversal. This gives rise to wavelike fluctuations in the spin orientations on the whole lattice known as spin waves [98].

We can now consider the interaction of the j^{th} spin with its nearest neighbours ... $\nwarrow^{j-1}\nearrow^{j}\nwarrow^{j+1}$ .... The interaction energy is clearly

$$U_j = -\vec{S}_j \cdot 2J_o(\vec{S}_{j-1} + \vec{S}_{j+1}). \tag{2.8.2}$$

We can easily show that

$$U_j = -\vec{\mu}_j \cdot \vec{B}_j \tag{2.8.3}$$

where μ_j is the magnetic moment at site j and $\vec{B}_j$ is the effective magnetic field [101, 102]. Equation (2.8.3) implies that a torque ($\vec{\tau}_j \equiv -\vec{\mu}_j \times \vec{B}_j$) acts on the j^{th} spin. The effect of a magnetic field on a magnetic moment is to induce a torque on it. Increasing temperature results in spin reorientations. Finite torques act on magnetic moments whenever spin orientations begin to change [98]. Hence, the reduction in the magnetization with increasing temperature occurs through the excitation of spin waves.

Spin waves are also quantized similar to photons or phonons. Quantized spin fluctuations are called magnons. Each mode of spin wave has energy $E_k = (n_k + 1/2)\hbar\omega$. The excitation of magnons causes a fall in magnetization with increasing temperature [85]. The temperature dependence of the magnetizations at low temperature ($T \ll T_C$) due to spin wave excitations can be shown to be

$$M(T) = M_S(0)(1 - AT^{3/2} - CT^{5/2} - ...) \tag{2.8.4}$$

where A and C are the crystal structure parameters [103]. From equation (2.8.4) we can deduce the Bloch $T^{3/2}$ law which is expressed as

$$M(T) = M_S(0)(1 - AT^{3/2}). \tag{2.8.5}$$

A modified Bloch's law has the form

$$\frac{M_S(T)}{M_S(0)} = \left[1 - \left(\frac{T}{T_o}\right)^{\beta}\right]. \tag{2.8.6}$$

$1/T_0$ is the Bloch's constant which depends on the structure of the material and β is the Bloch's exponent which depends on the nature, size and surface treatment of the sample. Values of β of at least 1.5 have been observed in bulk materials. In nanoparticle materials we fine $\beta \simeq 2$ [93, 104, 105]. Near T_C the reduced magnetization follows a different law of the form

$$\frac{M_S(T)}{M_S(0)} \propto (T - T_C)^{\beta}. \tag{2.8.7}$$

where $\beta \simeq 0.34$ [81, 85].

2.9 Magnetic domain structure

A piece of iron at room temperature exhibits apparent no magnetization even though its Curie temperature is about 1043 K [98]. The reason for this is because of the formation of the domain structure. The individual domains have spontaneous magnetizations with magnetic moments that are oriented parallel to each other. In the demagnetized state, the magnetization vectors in different domains point randomly in different directions give rise to zero average net magnetization, $\vec{M} = 0$ below the Curie temperature [81, 93]. The domains are separated by domain walls (Bloch's wall) or domain boundaries in which the direction of the magnetization changes by either 90^o or 180^o [81]. Experiments show that the application of small external fields of about $\approx 10^{-6}$ T [85] can easily magnetize some materials such as iron while for other materials like cobalt this more difficult to do. An external field is needed to align the magnetization of various domains in the same parallel direction.

The state in which all magnetic moments point in one direction has higher energy than the demagnetized state. Domains form in order to minimise the magnetostatic energy both inside and outside of the material [106]. We can illustrate this by considering a spontaneously magnetised single-domain in applied field $\vec{B}_o$. The discontinuity at the surfaces of the normal component of magnetization creates free poles. This leads to a demagnetizing field $D\vec{M}$ which is given by

$$D\vec{M} \sim \frac{b}{l}\vec{M}. \tag{2.9.1}$$

Here D is the demagnetizing factor which depends on the shape of the sample of breadth b and length l. The internal field responsible for producing magnetization is given by

$$\vec{B}_{oi} = \vec{B}_o - D\vec{M}. \tag{2.9.2}$$

The magnetic energy is therefore

$$U_m = -\frac{1}{2}\vec{B}_{oi} \cdot \vec{M} - \vec{B}_o \cdot \vec{M}. \tag{2.9.3}$$

In the absence of applied fields, the magnetic energy tends to self-energy ($U_m \rightarrow U_S$) which is called the magnetostatic self-energy given by

$$U_S = \frac{1}{2}DM_S^2. \tag{2.9.4}$$

This is the energy that is minimised in the formation of the domains. For domains of closure there are no surface poles and therefore the magnetic energy tends to zero. Domains that form have macroscopic size that depend on the size and shape of the crystal, internal strains and applied magnetic fields. There is homogeneous magnetization in each domain. The transition from one domain to another across a domain wall involves spin reversal, which is associated with an increase in exchange energy between spins. Figure 2.9 shows a typical domain wall. The abrupt change of the spin direction increases the exchange energy by $4J_oS^2$ per atom per boundary [98]. Allowing for a gradual transition of spin directions in N increments from one

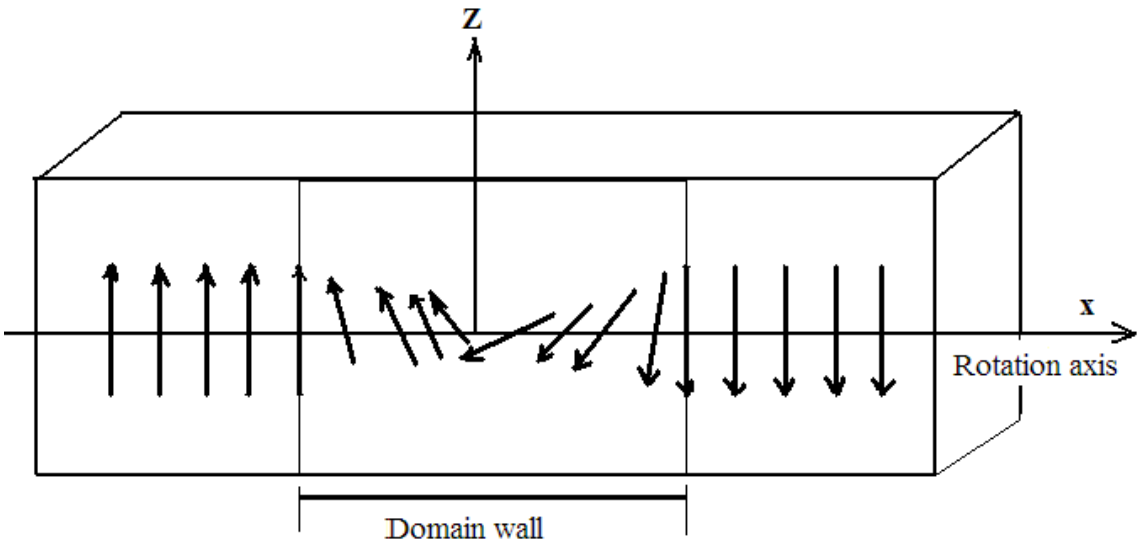

Figure 2.9: Schematic diagram of a domain wall of a ferromagnet.

domain to another increases the exchange energy by $J_oS^2\pi/N$. This is much less than $4J_oS^2$. The wall itself exhibits $1/a^2$ spin rotation axes per unit area. The total wall exchange energy density of the domain boundary per unit area is therefore given by

$$E_{ex}^{Bloch} = \frac{\pi^2 JS^2}{Na^2} \tag{2.9.5}$$

where a is the lattice parameter. Crystal properties are usually not isotropic in their behaviour. This means that properties tend to depend on crystal directions. This is typical of magnetization curves of various materials under the influence of an applied magnetic field. There are "easy" and "difficult" directions of magnetization

due to spin-orbital interaction. Rotating spins from their preferred orientations requires additional energy known as magnetocrystalline anisotropy energy. The energy is usually expressed for uniaxial nanoparticle magnetic materials in terms of an empirical anisotropy coefficient K. The anisotropy energy can then be expressed by

$$E_C^{hexagonal} = K_1 V \sin^2\theta + K_2 V \sin^4\theta \tag{2.9.6}$$

where θ is the angle of magnetizations $\vec{M}$ with respect to the c axis for hexagonal structure and V is the volume of the sample. The anisotropy energy for iron with cubic structure is given as a series expansion of the direction cosines (α_i) of the saturation magnetization relative to the crystal structure [100] in the form

$$E_C^{cubic} = K_1 V(\alpha_1^2\alpha_2^2 + \alpha_2^2\alpha_3^2 + \alpha_3^2\alpha_1^2) + K_2 V(\alpha_1^2\alpha_2^2\alpha_3^2) + ... \tag{2.9.7}$$

The parameters K_1 and K_2 are the first and second anisotropy constants respectively. The interplay between K_1 and K_2 determines the directions of hard and easy axes [81]. The anisotropy energy in all the materials decreases with increasing measuring temperature. The anisotropy vanished near $T = T_C$ because the spins are then randomly oriented in the paramagnetic state [100].

The properties of a domain wall are obtained by the competition between the exchange energy and the magnetic anisotropy energy. The domain-wall energy increases with both the exchange energy and the anisotropy energy because both favour a collinear moment orientation. The domain wall width increases with the exchange energy but decreases with increasing magnetic anisotropy energy [107]. The displacement of a domain wall of a bulk magnetic material will be affected by several other factors such as crystal defects, chemical impurities and lattice strains.

When the particle diameter of a bulk material decreases towards to some critical particle size (D_C) of a few nanometers, the formation of domain walls becomes harder to achieve. Therefore, the sample prefers a single-domain rather than a multi-domain structure [108].

2.10 Magnetization processes

The hysteresis loop is the response of a magnetic material to a cyclic applied magnetic field which is related to the existence of domains [109]. This is essential to all magnetic materials used for magnetic data recording, electric transformers and permanent magnets [107]. The hysteresis loop depends on the magnetic history of the sample and the speed at which the external field is swept. The magnetization of a sample due to an applied field occurs by two processes namely by domain wall moments and by rotation of the magnetization within a domain. The moments rotate into the direction of the external magnetic field. Figure 2.10 shows a typical hysteresis loop and the domain structures of bulk ferromagnets at $T < T_C$ [93]. Ferromagnetic materials exhibit long-range ordering phenomenon at atomic level which causes atomic magnetic moments to line up parallel with each other in a domain. Within a domain, the magnetization is finite, but for entire sample, the material will

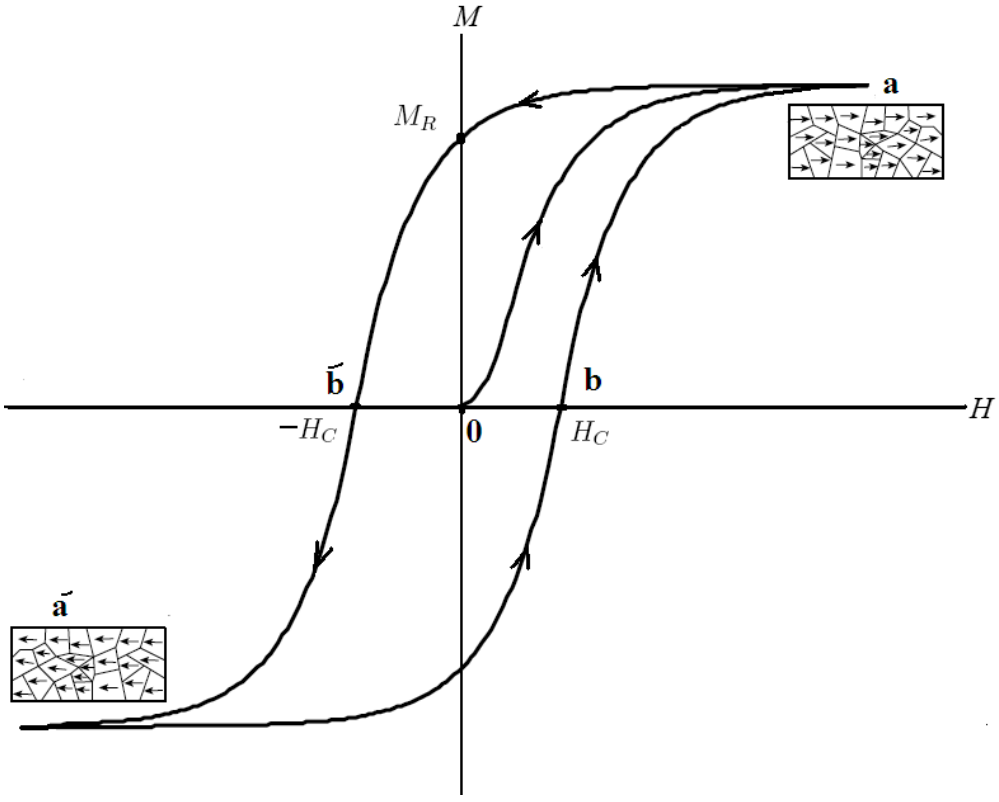

Figure 2.10: Hysteresis loop of a ferromagnet.

usually be in a demagnetized state because of the many domains that are randomly oriented with respect to each another. As seen in Figure 2.10 at points a and $a^{'}$, all of the magnetic domains are aligned in the direction of the magnetic applied field and the material reaches the point of the saturation of the magnetization. The saturation field is the applied magnetic field at which the domain structure is removed. Points b and $b^{'}$ show that some magnetic domains are still aligned even though the applied field is zero, which is attributed to the remanence magnetism in a material. At these points, a ferromagnetic material is not fully demagnetized which attributed to partial reorientation in domains. The magnetic remanence (M_R) is referred to the magnetization that remains when the applied field is decreased to zero.

Information about magnetic parameters such as coercive field, saturation magnetization, maximum magnetization and remanent magnetization can be obtained from a hysteresis loop. The value of the saturation magnetization (M_S) can be deduced from magnetization data using of the empirical law of approach to saturation magnetization given by [93, 110, 111]

$$M(H) = M_S(0)\left(1 - \frac{a}{H} - \frac{b}{H^2} - ....\right) + \chi H \tag{2.10.1}$$

where a and b are the fit parameters. χ is the high-field susceptibility attributed to the field-induced band splitting. The coercive field (coercivity, H_C) is the field that must be applied in the direction opposite to the saturation field in order to reduce the magnetization to zero after the sample was driven to saturation [107]. The coercive field strongly depends on the particle diameter. In the nanoparticle systems an increase in grain size leads to increased coercive field up to a critical grain size (D_C) where the particle evolves from single-domain to multi-domain structure [108]. The Kneller's law for the variation of coercive field with temperature is given by

$$H_C(T) = H_C(0)\left[1 - \left(\frac{T}{T_B}\right)^{1/2}\right] \tag{2.10.2}$$

where $H_C(0)$ is the coercive field at $T = 0$ K.

Chapter 3

Mössbauer spectroscopy

Rudolf L. Mössbauer discovered in 1958 the recoil-free emission and resonant absorption of γ-rays [112, 113]. The resulting Mössbauer spectroscopy technique has been used in different fields such as Life Sciences, Physics, Chemistry, Biology and Metallurgy to provide useful information of bonding, structure, dynamic and magnetic properties of materials [112, 114]. The Mössbauer effect has been detected in several isotopes such as ^{57}Fe, ^{61}Ni, ^{119}Sn, ^{151}Eu, ^{161}Dy, ^{186}Os and ^{191}Ir [112, 115]. The technique requires a source of γ-rays, an absorber and the means of modulating the energy of the emitted γ-rays [85]. ^{57}Fe Mössbauer is a popular tool that is used to observe and investigate the magnetic hyperfine parameters because there are many materials for practical use that contain iron. The natural abundance ^{57}Fe isotope in such materials is 2.12 % [85]. ^{57}Co isotope in Rh matrix is usually the preferred source of γ-rays. It has a half-life of 270 days and decays to ^{57}Fe in the excited state. The 14.41 keV excited state is critical for Mössbauer spectroscopy and γ-rays from this state can resonantly be absorbed by ^{57}Fe nuclei in another material.

3.1 Mössbauer effect

The Mössbauer effect is associated with the emission and absorption of γ-rays by identical nuclei in the source and absorber respectively without loss of energy. This is attributed to the recoil of a nucleus and without thermal broadening [115]. This is

possible for nuclei of atoms that are bound in a solid by Doppler shifting the energy of the γ-rays to take care of the recoil of the nuclei during emission or absorption of radiation. Due to energy and momentum conservation, the energy of recoil (E_R) of a nucleus of mass M after the emission or absorption of a γ-ray can be shown to be

$$E_R = \frac{E_\gamma^2}{2Mc^2} \tag{3.1.1}$$

where c is the speed of light. For a bound atom in a solid, the recoil momentum is shared by to the entire solid. Hence, M in equation (3.1.1) can be replaced by an effective mass which is much larger. This leads to a much reduced values of E_R. Doppler shifting the energy of the source by

$$\delta E = E_\gamma \frac{v}{c} \tag{3.1.2}$$

is more easily achieved by moving the source with velocities $v \sim 1$ cm/s [115].

3.2 Recoilless emissions

The fraction of the recoilless emission (f) from a Mössbauer source is based on the vibrational properties of a crystal lattice. The Mössbauer effect depends on the γ-rays emitted or absorbed in zero-phonon processes which are associated with transitions between the excited states and ground states of nuclei [85]. The general expression for recoilless fraction of decays for emitted γ-rays without lattice excitation in zero-phonon processes is given by

$$f = exp\left(-\frac{E_\gamma^2 \langle x^2 \rangle}{(\hbar c)^2}\right) \tag{3.2.1}$$

where $\langle x^2 \rangle$ is the mean-square thermal displacement amplitude of the emitting nucleus in the direction of wave vector $\vec{k}$ of the γ-ray. Equation (3.2.1) is similar to the Debye-Waller coefficient, which governs the intensity of elastic scattering for X-rays and neutrons in solids [85]. A realistic model of f depends on the Debye model of a solid. In the model, atoms vibrate up to a maximum cut-off frequency known as the Debye frequency (ω_D). The Debye approximation [116] for equation (3.2.1) gives

$$f = exp\left\{-\frac{3E_R}{2k_B\theta_D}\left[1 + 4\left(\frac{T}{\theta_D}\right)^2 \int_0^{\frac{\theta_D}{T}} \frac{x dx}{e^x - 1}\right]\right\} \tag{3.2.2}$$

where $x = \hbar\omega/(k_B T)$ and $\theta_D = \hbar\omega_D/k_B$ is the Debye temperature. Equation (3.2.2) shows that the recoilless fraction (f) increases as the temperature decreases in agreement with the observation by Mössbauer with ^{191}Ir nuclei [117]. The equation also indicates that the Mössbauer recoilless fraction is large when θ_D is large and the recoil energy (E_R) is small at low temperature. The Mössbauer effect is also limited to relatively low energy γ-radiation emissions. Equation (3.2.2) indicates clearly that the effect is extremely difficult to observe in gas or liquid phases due to large values of $\langle x^2 \rangle$ [116].

Experimentally, the variation of the absorption cross-sections (σ_{Exp}) with energy for a thin absorber is defined as

$$\sigma_{Exp}(E_\gamma) = \sigma_o \left[1 + 4 \left(\frac{E_\gamma - E_o}{\Gamma_s + \Gamma_a} \right)^2 \right]^{-1} \tag{3.2.3}$$

where Γ_s and Γ_a are the full-width of resonant absorption at half-maximum of the source and absorber respectively. E_o is the nuclear transition energy and σ_o is the total cross-section for resonance absorption of a γ-ray by a resonant isotope which is given by

$$\sigma_o = \frac{\lambda^2}{2\pi} \frac{(1 + 2I_{ex})}{(1 + 2I_g)} \frac{1}{1 + \alpha}. \tag{3.2.4}$$

I_{ex} and I_g are the nuclear spins for excited state and ground state respectively and α is the integral conversion coefficient of the γ-ray transition with wavelength λ [115]. The absorption cross-section for ^{57}Fe is about 2.2×10^{-8} cm^2, which is at least 200 times greater than photoelectric absorption [113].

Nuclear energy levels in solids can be modified by their surroundings. These energy levels can be investigated using Mössbauer spectroscopy by measuring the variation of the resonant absorption of the nuclei with energy (or velocity) of the source. This allows small energy changes caused by the hyperfine interactions between nuclei and surrounding electrons to be determined [112, 115]. Figure 3.1 shows the Mössbauer spectrum recorded for the transmitted γ-ray counts through a thin absorber as a function of velocity of the source [116]. Figure 3.2 shows the decay process for the ^{57}Co radioactive source which is used for Mössbauer spectroscopy. ^{57}Co decays by electron capture to the excited energy state of ^{57}Fe with $I_{ex} = 5/2$. This is a metastable state which can decay directly to the ground state ($I_g = 1/2$) with

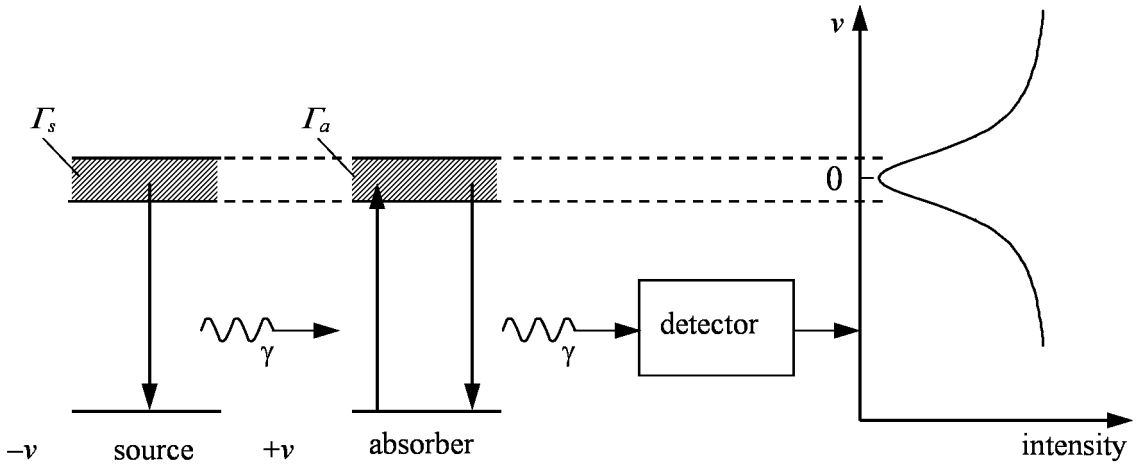

Figure 3.1: Measuring a Mössbauer spectrum [116].

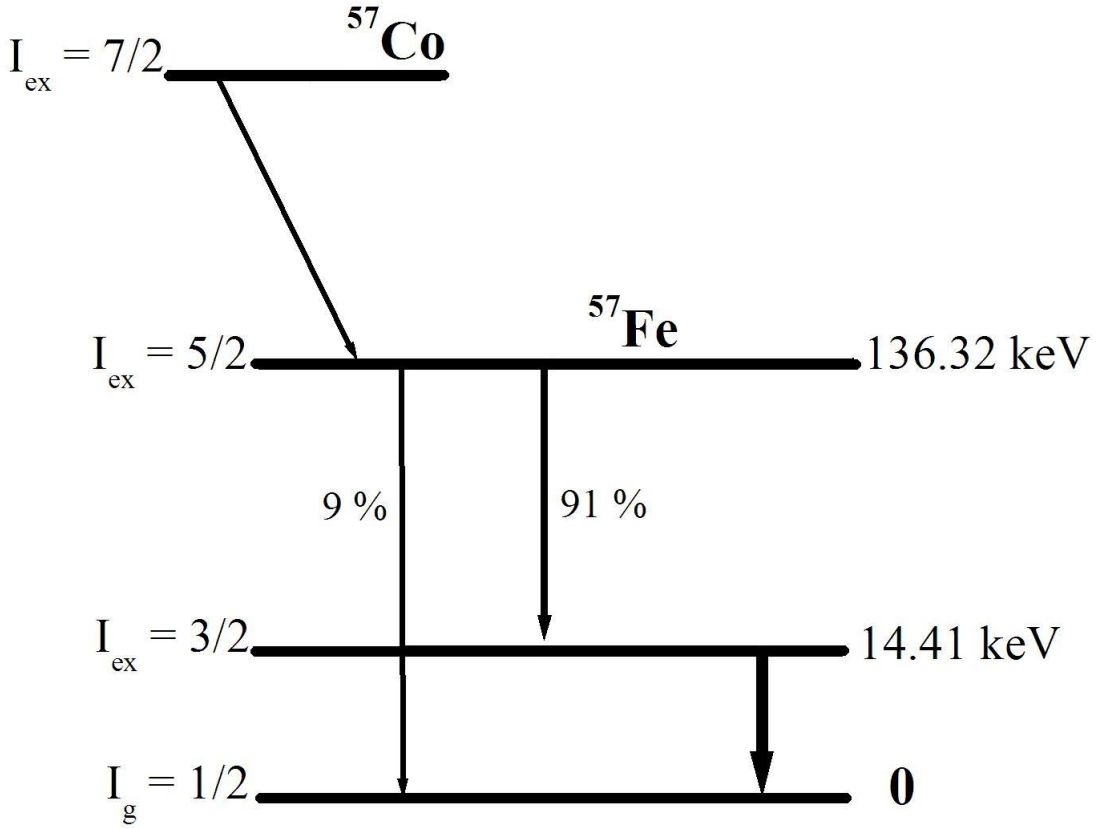

Figure 3.2: Schematic diagram of the nuclear decay for ^{57}Co showing emission of a Mössbauer γ-ray corresponding to $E_R = 14.41$ keV.

9 % probability or to excited state ($I_{ex} = 3/2$) with 91 % probability. Mössbauer spectroscopy is associated with the transition from the state with $I_{ex} = 3/2$ to the state with $I_g = 1/2$ with energy difference of 14.41 keV.

3.3 Hyperfine interactions

In Mössbauer spectroscopy nuclei are used as probes of the local environment. Electrostatic and magnetic interactions of a nucleus with its surroundings causes a small shift and splitting of the nuclear energy levels. The interactions of the nuclei with their surroundings are known as hyperfine interactions. These include isomer shift (δ), magnetic quadrupole interaction (Δ) and magnetic hyperfine interaction (H). These interactions are illustrated in Figure 3.3.

3.3.1 Isomer Shift

The isomer shift of absorption lines in a Mössbauer spectrum are due to the changes in the electron density at the nucleus of an atom in a solid. The shift occurs because of the difference in the $s-$electron density at nuclear sites between the source and absorber. As a result, the centroid of the Mössbauer spectrum is shifted from zero velocity as shown in Figure 3.3. The non-relativistic approximation of the isomer shift with Doppler velocity is given by

$$\delta = \frac{2\pi}{5} Ze^2 \left(|\psi_S(0)|^2 - |\psi_a(0)|^2\right) (R_{ex}^2 - R_g^2) \tag{3.3.1}$$

where Z is the atomic number, e is the electronic charge, $|\psi_a(0)|^2$ and $|\psi_s(0)|^2$ are the $s-$electron densities at nuclear sites of the absorber and source respectively. R_{ex} and R_g are the nuclear radii in the excited state and ground state of emitting and absorbing nuclei. Usually we assume that the change in nuclear radius ($\Delta R = R_{ex} - R_g$) to be constant. Therefore, for a fixed Mössbauer source the isomer shift in equation (3.3.1) can be expressed as

$$\delta = K_o - K|\psi_a(0)|^2 \tag{3.3.2}$$

where K_o and K are the relevant constants. Equation (3.3.2) indicates that the isomer shift varies as a function of $s-$electron density ($|\psi_a(0)|^2$) at absorber nuclei

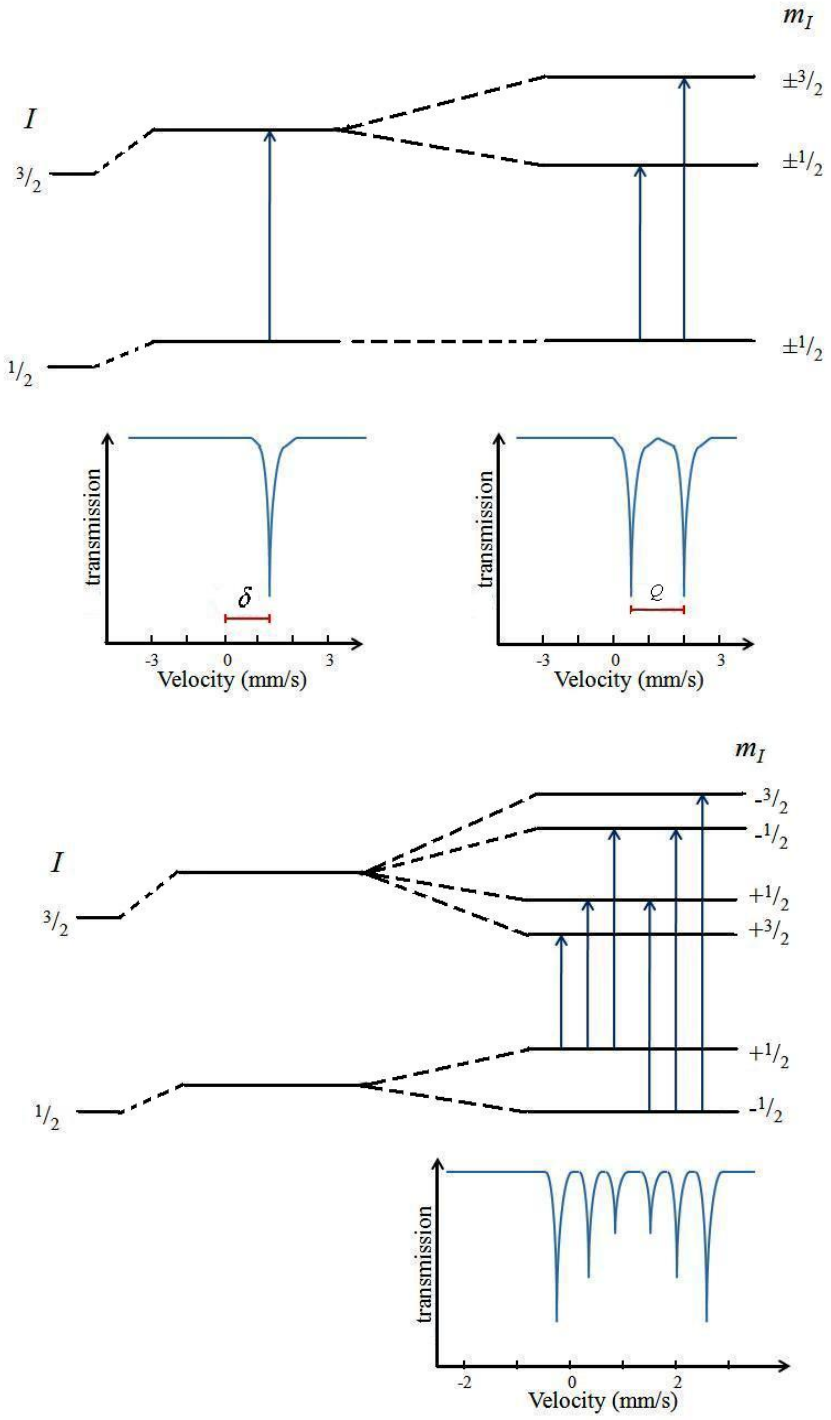

Figure 3.3: Effects of isomer shift, electric quadrupole splitting and magnetic hyperfine splitting on the nuclear energy levels of a free atom [118].

which can be affected by $s-$, $p-$, $d-$, and $f-$electrons as well as by covalency and formation of bonds [115]. For example, Fe^{2+} and Fe^{3+} ions have different values of δ, while they have similar $s-$electrons. This difference in δ is attributed to the additional $d-$electron in Fe^{2+} ion that decreases the net attractive Coulomb potential for the $3s-$electrons. This leads to a decrease in the charge density at the nucleus. The difference in isomer shift between Fe^{2+} and Fe^{3+} ions was found to be 0.9 mm/s, which is larger than the natural line width (LW) of the Fe^{2+} ion and therefore can be observed by Mössbauer experiments [116]. The isomer shift is quoted by velocity units (in mm/s) rather than in energy units. 1 mm/s is equivalent to 4.8×10^{-8} keV for ^{57}Fe isotope [115]. Values of isomer shifts of absorbers are usually quoted with respect to a standard reference absorber such as $\alpha-$iron.

3.3.2 Quadrupole splitting

The quadrupole splitting (Δ) is a result of the interaction of the nuclear quadrupole moment with the gradient of the electric field $\vec{\bigtriangledown}E$ due to other charges in the crystal [113]. A nuclear quadrupole moment shows the deviation of the nucleus from spherical symmetry. Nuclei with $I > 1/2$ have non-spherical symmetry charge distribution, therefore can exhibit quadrupole splitting [115]. The quadrupole splitting also reflects the local structure in the vicinity and the symmetry of the bonding environment of a Mössbauer atom [112].

The electric field gradient is specified by two independent parameters namely field gradient tensor $V_{zz} = (\partial^2 V/\partial Z^2)$ along $z-$axis and an asymmetry parameter $\eta = (V_{xx} - V_{yy})/V_{zz}$ with $0 \leq \eta \leq 1$ [113]. The Hamiltonian of the interaction between the nuclear electric quadrupole moment (Q) and the gradient of the electric field is given by

$$H_Q = \vec{Q} \cdot \vec{\bigtriangledown}E. \tag{3.3.3}$$

The eigenvalues of the above Hamiltonian is found to be

$$E_Q = \frac{eQV_{zz}}{4I(2I-1)}(3m_I^2 - I(I+1))\left(1 + \frac{\eta^2}{3}\right)^{\frac{1}{2}}. \tag{3.3.4}$$

$m_I = I, I-1, ..., -I$ is the magnetic quantum number [117]. In the case of ^{57}Fe

with spins 3/2 and 1/2, equation (3.3.4) can be reduced to

$$E_Q = \pm\frac{eQV_{zz}^2}{4}\left(1+\frac{\eta^2}{3}\right)^{\frac{1}{2}}. \tag{3.3.5}$$

This gives a doublet corresponding to the transitions $\pm 3/2 \rightarrow \pm 1/2$ and $\pm 1/2 \rightarrow \pm 1/2$ [117]. For a non-zero field gradient, the excited energy level with $I = 3/2$ splits into two energy sub-levels corresponding to $m_I = \pm 3/2$ and $m_I = \pm 1/2$ as shown in Figure 3.3. This means that the Mössbauer spectrum appears as two peaks separated by quadrupole splitting, $\bigtriangledown = eV_{zz}Q/2$ [91].

3.3.3 Magnetic hyperfine interaction

The magnetic hyperfine structure arises from the interaction of the nuclear magnetic dipole moment ($\vec{\mu}$) with the magnetic field ($\vec{H}$) at the site of the nucleus. The Hamiltonian for the magnetic dipole interaction is specified by [115]

$$H_d = -\vec{\mu}\cdot\vec{H} = -g_n\mu_n\vec{I}\cdot\vec{H} \tag{3.3.6}$$

where g_n is the nuclear g-factor, μ_n is the nuclear magneton and I is the nuclear spin. The energy levels of the system can be shown to be [114]

$$E_m = -\frac{\mu H m_I}{I} = g_n\mu_n H m_I. \tag{3.3.7}$$

The magnetic field splits the nuclear levels with spins I into $2I+1$ equally spaced non-degenerate sub-levels (see Figure 3.3). The splitting between adjacent level is $g_n\mu_n H$ [115]. In Mössbauer spectroscopy preferential absorption of γ-rays occur between the sublevels of the excited nuclear state and sublevels of the ground state [113] consistent with the selection rules $\Delta m = 0, \pm 1$. This leads to six absorption lines called Zeeman lines with a centroid that is close to the velocity $v \gtrsim 0$ channel in the spectrum as shown in Figure 3.3.

The scalar product $\vec{I}\cdot\vec{H}$ contained in equation (3.3.6) represents the observation at a time-scale of the order of 10^{-8}s [115]. The hyperfine field (H) is generated by the polarising effects of unpaired electron spins (I). The spin direction flips after a period of time by one or more mechanisms associated with electronic spin relaxation [115]. In paramagnetic materials, the spin relaxation is rapid. This results in the magnetic

field having a zero time average value. Hence, no magnetic field can be recorded. However, in the ferromagnetic, antiferromagnetic and ferrimagnetic materials, the relaxation rates are effectively slower and the splitting of energy levels can be seen. There are also intermediate possibilities of observation where the electronic spins are relaxing on a time-scale that is similar to that of nuclear transitions. This results in complicated spectra. Examples of such materials are superparamagnets which can embrace both unusual fast and slow relaxations [115].

Chapter 4

Experimental techniques

In this chapter we review the synthesis, structural characterization and the techniques for magnetic and electrical measurements relevant to the present study. Glycol-thermal and high-energy ball milling methods were used to produce the materials studied in the current work. The structures of the compounds studied were investigated by using X-ray diffraction (XRD), transmission electron microscopy (TEM) and high-resolution transmission electron microscopy (HRTEM). The magnetic properties were obtained using ^{57}Fe Mössbauer spectroscopy, vibrating sample magnetometer (VSM) and superconducting quantum interference device (SQUID) magnetometers. A four probe proportional-integral-derivative (PID) type controller was used to perform the resistivity measurements.

4.1 Synthesis and structural characterization

4.1.1 Glycol-thermal

The glycol-thermal process is one of the common techniques of synthesizing compounds from aqueous solutions of metal salts. The starting materials in this method are high-purity metal chlorides or nitrates and a precipitating reagent such as ammonia, sodium hydroxide or potassium hydroxide. The stirring, reaction temperature, pressure and washing stage play important roles in obtaining homogeneous and single-phase crystallization of the compounds. Figure 4.1 shows a Watlow series

Figure 4.1: Watlow series stirred pressure reactor with a PARR 4843 controller.

stirred pressure reactor with a PARR 4843 controller which was used to prepare the compounds. The 4843 Controller is a full digital temperature control system offering PID control loops for both heating and cooling along with Ramp and Soak temperature profile programming [119]. Table 4.1 shows the settings for operating the reactor. A typical operating schedule of the reactor is shown in Figure 4.2. Formation of single phase structure is much easier to achieve by glycol-thermal process than by solid state reaction [120]. The synthesis of the compounds occurs at relatively low temperature compared to at least a 1000 ^{o}C in solid state reaction.

All the raw starting materials used with their purity are shown in Table 4.2. The materials were supplied by Sigma-Aldrich company. Suitable stoichiometric amounts of metal chlorides were mixed in deionised water by a magnetic stirrer for about 20 minutes. Ammonia hydroxide solution was added drop-wise to the chloride mixture

Table 4.1: The general and special set-up configurations of the PARR 4843 controller for the pressure reactor [119].

(i) General fixed settings				
$Level_1$	$Level_2$	$Level_3$	$Level_A$	$Level_C$
tune: off	SP1.P: 97	SP1.d: ssd	An.hi: 997	Addr: 0
bAnd: 9.9	hAnd: off	SP2.d: rLK	An.Lo: 0	bAud: 9600
int.t: 4.8	PL.1: 100	Burn: uP.SC	hi.in: 50.0	dAtA: 18nl
aEr.t: 100	PL.2: 100	rEU.d: lr.2d	lo.10.0	abuC: off
aAC: 1.5	SP2.A: Cool	rEU.L: in.2n	dECP: 0000	
CYC.t: 20	SP2.b: none	SPAn: 0.0	SP3.A: none	
oFSt: 0	diSP: 1o	2Ero: 0.0	SP3.b: none	
SP.LK: off	hi.SC: 800	ChEK: off	SET.3: 0	
SEt.2: 0	LO.SC: 0	rEAd: UAro, 0.0	hK5.3: 2.2	
Bnd.2: 2.0	inPt: tCL	tECh: CtA, 0.0	brn.3: UP.SC	
CYC.2: on.off	unit: psi	UEr: 954.0	rEU.3: 3d	
		rSEt: none		
(ii) Special variable settings				
ProG 1	SEG_1	$SEGl_2$	SEG_3	SEG_4
Run: (on or off)	Type: Spr	Type: Soak or	Type: Spr	Type: Soak
FAiL: rSET, ConT	Sprr: 200	Step or Loop or	SPrr: 200 degree	Sin: 10 min
or hold	t.SP: 150	CALL or E.op	t.SP: 25 dgree	E.oP: none
St.U: PU	hb.U: off	Edit: dEL	hb.U: off	
or SP	and E.oP: none	or inS	E.oP: none	
SPru: hour		Sint: 360 (6hrs)		
or 60 s		E.op: none		

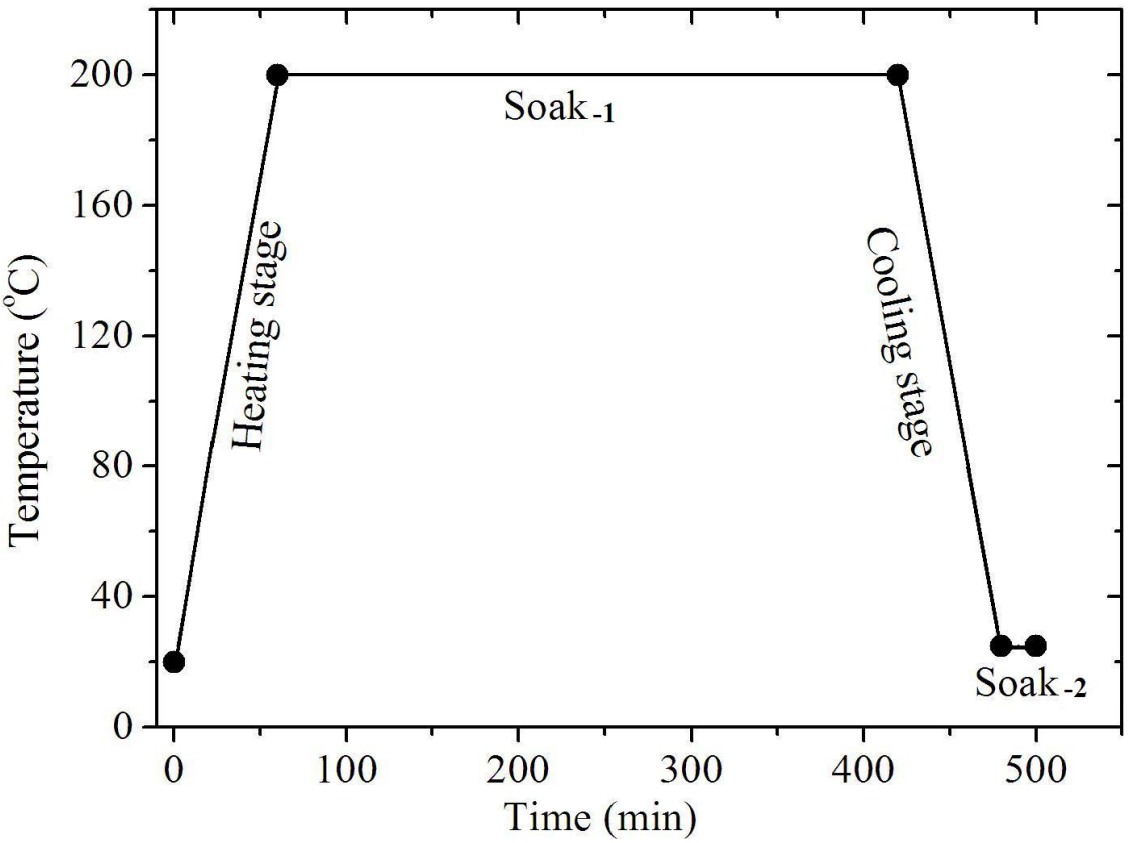

Figure 4.2: Operating schedule for the PARR 4843 controller.

Table 4.2: The starting compounds of metal chlorides, nitrates and oxides.

Compound	Chemical symbol	Purity (%)
Iron chloride	$FeCl_3.6H_2O$	99
Manganese chloride	$MnCl_2$	99
Cobalt chloride	$CoCl_2$	99.999
Magnesium chloride	$MgCl_2.6H_2O$	99
Strontium chloride	$SrCl_2.2H_2O$	99
Cerium chloride	$CeCl_3.7H_2O$	99.9
Neodymium chloride	$NdCl_3.6H_2O$	99.9
Samarium chloride	$SmCl_3.6H_2O$	99.99
Europium chloride	$EuCl_3.6H_2O$	99.9
Gadolinium chloride	$GdCl_3.6H_2O$	99.999
Terbium chloride	$TbCl_3.6H_2O$	99.9
Dysprosium chloride	$DyCl_3.6H_2O$	99.9
Holmium chloride	$HoCl_3.6H_2O$	99.9
Ytterbium chloride	$YbCl_3.6H_2O$	99.9
Lutetium chloride	$LuCl_3.6H_2O$	99.9
Iron nitrate	$Fe(NO_3)_3.9H_2O$	98
Manganese nitrate	$Mn(NO_3)_2.4H_2O$	99
Magnesium nitrate	$Mg(NO_3)_2.6H_2O$	99.999
Iron oxide	Fe_2O_3	99.998
Manganese oxide	MnO	99.99
Cobalt oxide	Co_3O_4	99.995

under rapid stirring until a pH $\approx$ 9 was a achieved to ensure complete precipitation. When nitrates were used as starting materials, KOH or NaOH solution was used for the formation of the precipitates. The precipitate was then washed several of times by deionised water over a Whatman glass microfibre filter (GF/F) until all the chloride ions were removed as confirmed by using a standard solution of $AgNO_3$. The wet precursor was dispersed in 250 ml of ethylene glycol by rapid stirring and thereafter transferred into a glass lining in a stainless steel pressure vessel with a capacity of 500 ml. The pressure vessel was heated to 200 ^{0}C and the pressure was gradually allowed to increase to about 140 Psi. These conditions were held for 6 hours following the schedule in Figure 4.2. After cooling to room temperature, the sample was filtered and washed by deionised water and finally by ethanol. This was followed by drying under a 250 W infra-red lamp in air for at least 12 hours. The dried sample was removed from the filter paper and homogenised by an agate mortar and pestle.

4.1.2 High-energy ball milling

High-energy ball milling is one of the effective methods for mixing, synthesizing and particle size reduction of materials [121]. The milling time and the rotation speed of the vials are important factors in the process [122]. We have used a Retsch planetary ball mill type PM 400 MA to synthesize some of our samples. Figure 4.3 shows a picture of the planetary ball mill used. This facility has four grinding stations and can be operated to a maximum speed of 300 rev/min [121]. The recommended speed is 200 rev/min for long grinding periods. The grinding environment consists of 250 ml hardened steel vials with an appropriate number of balls that depends on the samples size. Suitable covers of the vials available allow for grinding in air or inert gas atmosphere.

$Mn_xCo_{1-x}Fe_2O_4$ compounds with x = 0, 0.5 and 1.0 were produced by high-energy ball milling. The purity of the starting metal oxides are also shown in Table 4.2. The required weights of the oxides used were mixed in the jars together with hardened steel balls and then milled in air atmosphere for at least 60 hours. We used a ball mass to sample mass ratio of 20:1. Small amounts of sample was

Figure 4.3: Schematic of a Retsch planetary ball mill PM 400 MA [121].

removed from the vials after 1, 3, 5, 10, 20, 40 and 60 hours of milling for structure and magnetic characterizations studies. The $Mn_{0.5}Co_{0.5}Fe_2O_4$ compound was also synthesized from a mixture of single phases $MnFe_2O_4$ and $CoFe_2O_4$ ferrites. The reaction procedure in this case is defined by

$$0.5\ MnFe_2O_4 + 0.5\ CoFe_2O_4 \longrightarrow Mn_{0.5}Co_{0.5}Fe_2O_4.$$

This preparation procedure from single-phase ferrites is similar to the work on $Mn_{0.5}Zn_{0.5}Fe_2O_4$ ferrite [27].

4.1.3 X-ray diffraction

X-rays have wavelengths which are comparable to inter-atomic spacing ($\sim$ 1 Å), hence are ideally suited to probe materials by diffraction. The powder X-ray diffraction (XRD) is a powerful technique that can be used to determine the structure of a material. The technique can also be used to examine the formation of single phase and purity of the synthesized compounds [123]. XRD is based on the use of monochromatic beam of X-rays with wavelengths λ in the range: $0.01 - 10$ nm to probe a material. The scattered radiation from a sample produces a diffraction pattern with intensity peaks at positions that satisfy Bragg's law [86, 123]

$$n\lambda = 2d \sin\theta. \tag{4.1.1}$$

n is an integer which expresses the order of the diffraction, d is the inter-planar spacing of the diffracting crystal planes with Miller indices (hkl) and θ is the angle between the plane and the incident beam. Figure 4.4 shows a monochromatic beam of X-rays being reflected from a particular set of parallel planes (hkl). The inter-planar spacing, d, of the cubic spinel structure is related to the lattice parameter,

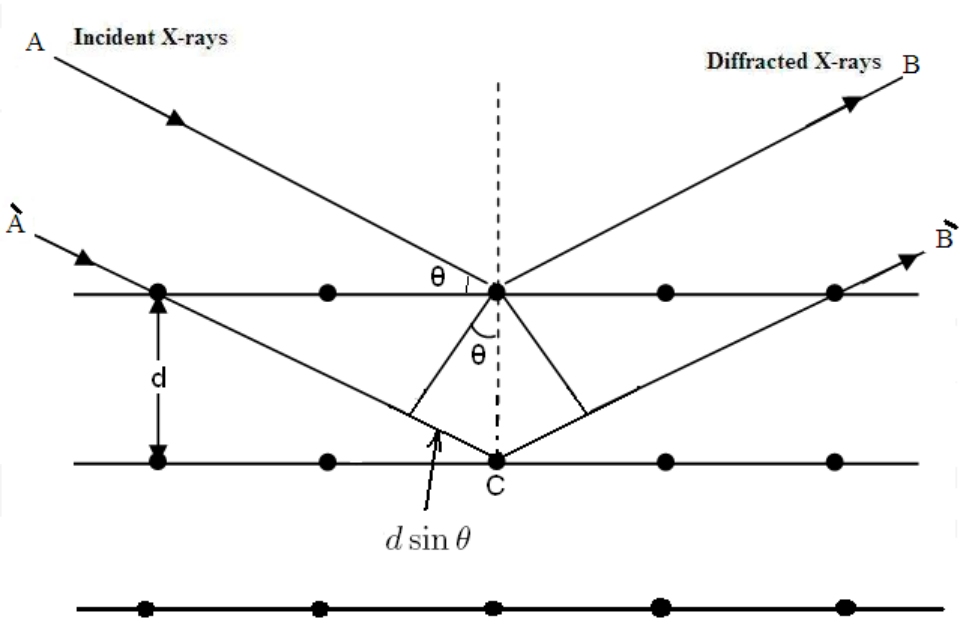

Figure 4.4: Geometry of reflection of X-rays from two adjacent atomic planes.

a, by the relationship [86]

$$d = \frac{a}{\sqrt{h^2 + k^2 + l^2}}. \tag{4.1.2}$$

The width of an XRD peak can be related to the average grain size D by the Debye-Scherrer formula [123, 124] which is given by

$$D = \frac{K\lambda}{W_{hkl}\cos\theta}. \tag{4.1.3}$$

W_{hkl} is the line broadening of the diffraction peak at its full-width at half-maximum (FWHM), K is the crystal shape factor near unity, λ is the wavelength of the monochromatic X-ray beam and θ is the Bragg's angle (see Figure 4.4). From the X-ray measurements we can deduce the so-called X-ray density (ρ_{XRD}) of a sample which reflects the packing of atoms in a unit cell. The X-ray density of a sample can be estimated from the values of the lattice parameter (a) using the formula [123]

$$\rho_{XRD} = \frac{8M}{N_A a^3} \tag{4.1.4}$$

where 8 is the number of atoms per unit cell of the cubic spinel lattice, M is the molecular weight of the compound and N_A is the Avogadro's number. The X-ray diffraction patterns are also affected by compressive and tensile stresses in a material. Compressive stresses cause the space surrounding a unit cell to become smaller. The shift in the diffraction peaks will be an indication of the microstrain created by the distribution of compressive and tensile forces. The microstrain (ε) developed during synthesis and annealing processes is given by [125]

$$\varepsilon = \frac{W_{hkl}}{4\tan\theta}. \tag{4.1.5}$$

Porosity refers to the volume of the open space between the grains to the total volume. The percentage porosity $P(\%)$ of a sample can be computed from bulk density (ρ_{Bulk}) and X-ray density (ρ_{XRD}) [18, 21] using the formula

$$P(\%) = \left(1 - \frac{\rho_{Bulk}}{\rho_{XRD}}\right) \times 100. \tag{4.1.6}$$

The percentage porosity of the compounds reduces significantly after annealing at higher temperature. The reduction in porosity with increasing annealing temperature can be explained based on larger grains created during sintering. Low values

of percentage porosity indicate a higher degree of homogeneity in the synthesized samples [6].

Our XRD measurements were performed on a Philips X-ray diffractometer type PW1710. The diffractometer uses a monochromatic beam of CoK_{α} radiation with an average wavelength 1.7903 Å. The sample size for XRD measurements was usually at least 0.3 g. The measurements were obtained in the range of 2θ from 20^o to 80^o in steps of 0.01^o.

4.1.4 Transmission electron microscopy

Transmission electron microscopy (TEM) is capable of revealing the structured information of materials with atomic-scale resolution. TEM appears in several types of equipment such as high-resolution electron microscopy (HRTEM), scanning transmission electron microscopy (STEM) and atomic electron microscopy (AEM). A TEM facility consists of four main components namely an electron optical column, vacuum system, electronics and control software. Figure 4.5 shows a typical picture of a TEM facility. TEM has been extensively used to examine the structure and the crystalline defects such as cracks, dislocations in the compounds such as metals, alloys, ceramics, glasses, polymers, semiconductors and mixtures of these materials [127]. When extended to HRTEM, information on individual atomic planes or columns of the atoms can be obtained [128]. We have used a type Jeol_JEM 1010 TEM and a type Jeol_JEM-2100 HRTEM to study the microstructure and to estimate the grain sizes of some of our samples [126].

In TEM, images of the samples can be obtained on suitably prepared thin specimens by appropriate lenses which gather information from very small regions of the sample [85, 128]. The images are formed from the interaction of electrons with the sample. The specimen must be thin enough to transmit electrons and to allow enough intensity of electrons to fall on a fluorescent screen. The maximum resolution of a TEM is limited by the wavelength of the probing source and the aperture of the system [129].

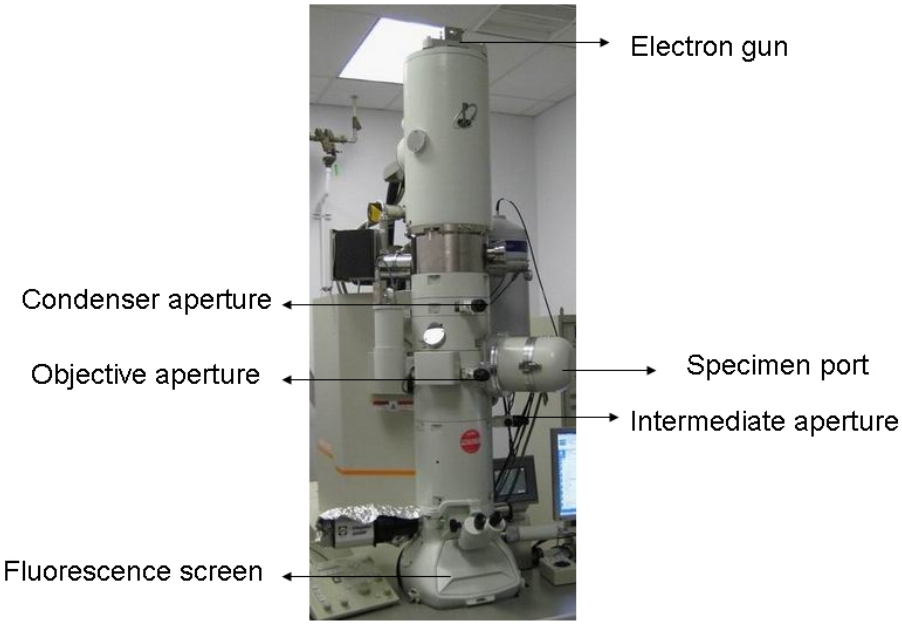

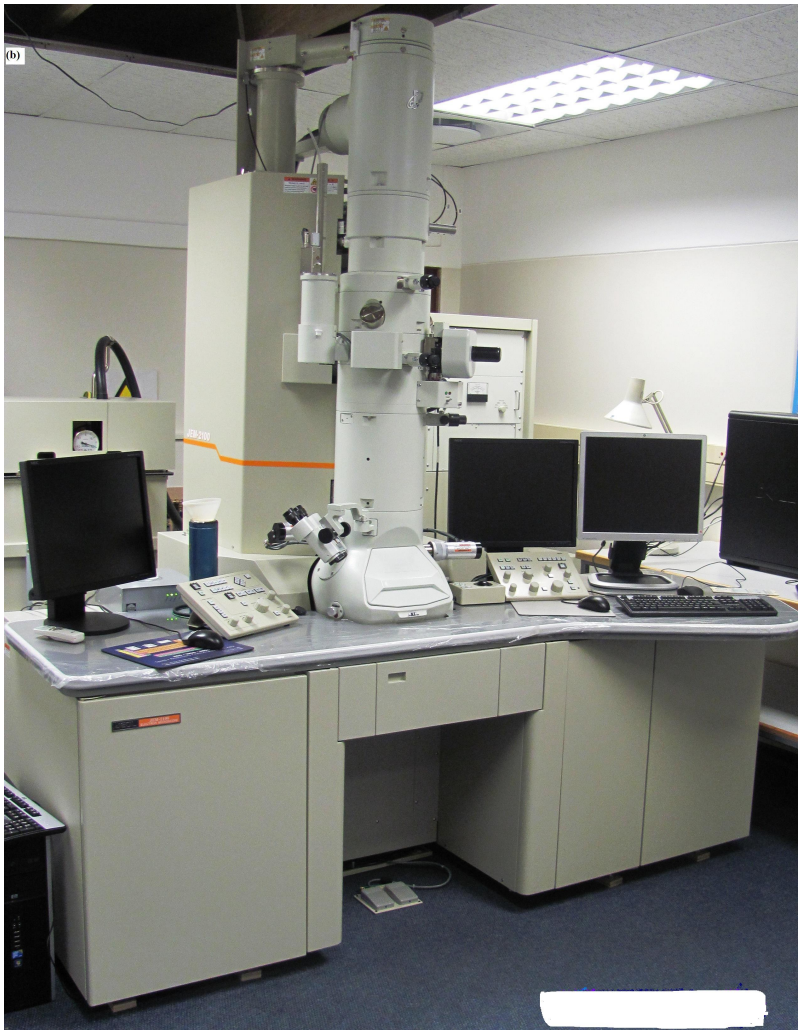

Figure 4.5: A picture of HRTEM [129].

4.2 Magnetic characterization

4.2.1 Mössbauer measurements

^{57}Fe Mössbauer spectrometer is a popular technique for observation and investigation of the magnetic hyperfine parameters of a material. It can be used to determine the distribution of the metal cations in tetrahedral and octahedral sites in spinel ferrites. Figure 4.6 shows a basic set-up of a Mössbauer spectrometer used in transmission geometry which consists of several components. ^{57}Fe Mössbauer spectra were obtained by using a conventional spectrometer with a 25 mCi ^{57}Co source sealed in Rh matrix which was vibrated at constant acceleration. The Mössbauer spectrum grows with time as the transmitted intensity is accumulated as a function of velocity of the source. The data for individual velocities are accumulated simultaneously by several repetitions of the velocity sweeps [91]. The measurements were recorded in

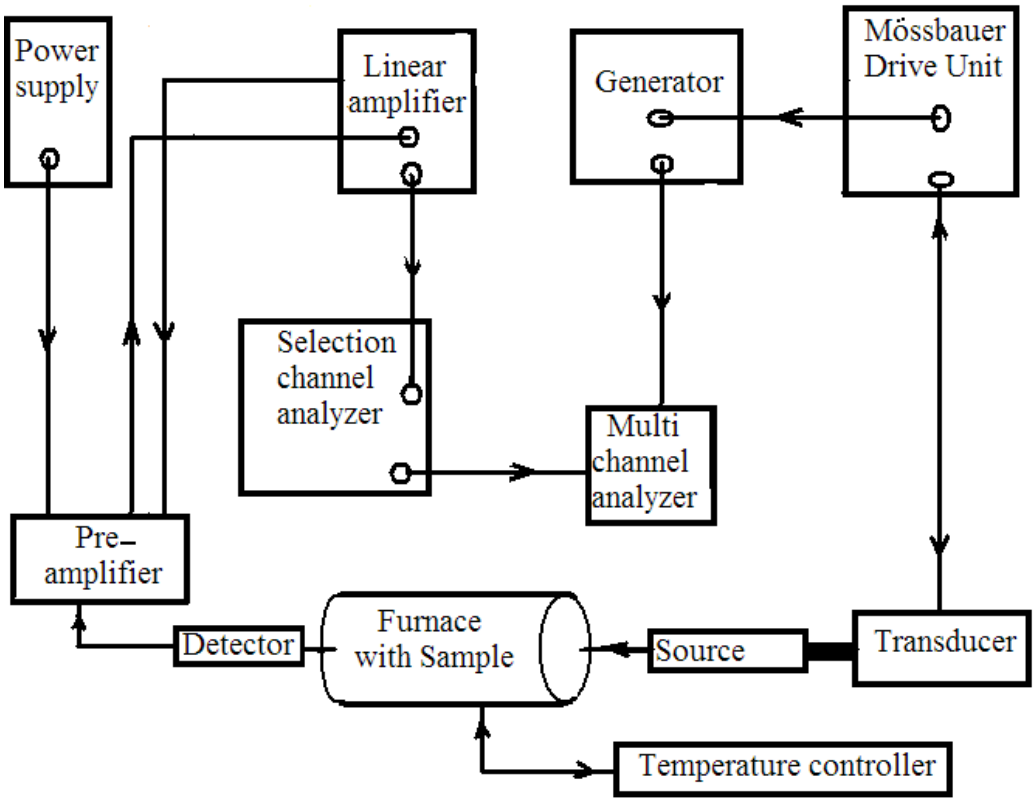

Figure 4.6: Experimental set-up of a Mössbauer spectrometer.

the temperature range of $27 \leq T \leq 200$ ^{o}C in zero applied magnetic fields. The measurements were performed on as-prepared, as-milled and thermal annealed samples. The experimental data were fitted by using Recoil Mössbauer analysis software program to deduced the Mössbauer parameters and the populations of iron atoms at different sites. A standard (99.5 %) iron foil with thickness of about 0.025 mm was used to calibrate the Mössbauer spectra.

4.2.2 Vibrating sample magnetometer

A vibrating sample magnetometer (VSM) is a widely used instrument for the characterization of the magnetic behaviour of materials. The VSM set-up in our lab shown in Figure 4.7 is a LakeShore model 735 instrument which consists of an EM4-HVA electromagnet, 642 electromagnet bipolar power supply, 450 Gaussmeter, 340 temperature controller, Neslab ThermoFlex 2500 chiller and a 735 VSM controller. The measurement components are connected to a National Instruments IEEE-488 interface card by PCI-GPIB cables. Windows interface software is used to operate the instrument.

Figure 4.7: Experimental set-up for magnetic measurements of the VSM system.

The principle of VSM measurement is based on Faraday's law of electromagnetic induction which relies on the detection of an induced voltage in a set of pick-up coils [130]. This induced voltage is proportional to the magnetic moment of a sample and hence its magnetization [131]. A VSM works by detecting the voltage induced by a varying field associated with a vibrating sample. The sample is positioned at the geometric centre of the pick-up coils. This procedure is known as saddling [131, 132]. The VSM was calibrated by using a standard high-purity (99.995 %) spherical nickel sample of known saturation magnetization ($M_m = 54.7$ emu/g) [132].

4.2.3 Superconducting quantum interference device

A superconducting quantum interference device (SQUID) magnetometer is the most sensitive detector of magnetic flux of a material [133]. It used to detect and measure the magnetic moment of a sample. It is highly sensitive because the device can respond to a fraction of the flux quantum [134]. A SQUID combines the physical phenomenon of flux quantization and Josephson tunnelling [133]. A dc SQUID consists of a superconducting loop interrupted by a pair of parallel Josephson junctions. The Josephson effect involves the coherent tunnelling of Cooper pairs through a thin barrier separating two superconductors [133].

Figure 4.8 shows a typical picture of a SQUID Magnetic Property Measurement System (MPMS). In some systems the measurement can be performed over a wide temperature range and in applied magnetic fields of up to several Tesla. A dc SQUID of type MPMS-xL was used in the present work to characterize the magnetization as a function of magnetic field and temperature.

4.3 Electrical measurements

The four-point probe is one of common techniques for measuring the electrical resistivity of materials. The four-point probe arrangement consists of four sharp metal tips which are collinear and equally spaced (S apart). The probes are pressed into contact with the flat surface of a sample to be studied. The electrical current (I) from a constant current source is delivered to the sample through the two outer

Figure 4.8: A picture of a SQUID magnetometer [135].

probes. The two inner probes monitor the voltage drop across the sample [136]. Figure 4.9 shows a schematic diagram of the four-point probe. The technique can be used in a wide range of materials such as metals, alloys, semiconductors and ferrites over a wide temperature range [137, 138].

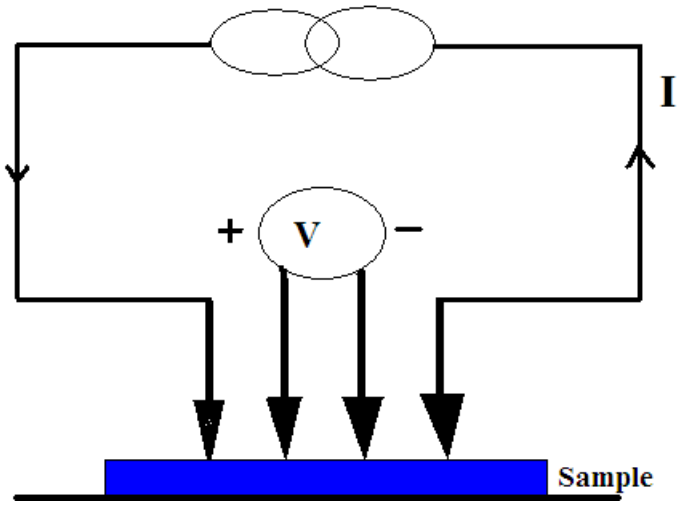

Figure 4.9: Schematic diagram of four-point probe experiment.

The calculation for the resistivity of a sample depends on the relative size of the thickness of a sample (t) and the distance between the probes (S) [139]. If the thickness of a sample is much larger than the spacing between probes ($t \gg S$), the resistivity (ρ) is calculated by the formula

$$\rho = 2\pi S \left(\frac{V}{I}\right) \tag{4.3.1}$$

where V is the measured voltage across the two inner probes and I is the current through the sample. For a very thin sheet of material where $t \ll S$ the resistivity is calculated by the formula

$$\rho = \frac{\pi}{\ln 2} t \left(\frac{V}{I}\right). \tag{4.3.2}$$

Our electrical measurements system consists of a Proportional-Integral-Derivative (PID) controlled oven, low current source for high resistivity measurements and a digital microvoltmeter [140].

Chapter 5

Structure, magnetic and electrical properties of $Mn_xCo_{1-x}Fe_2O_4$ nanoferrites

5.1 Introduction

In this chapter, we investigate the structural, magnetic and electrical properties of $Mn_xCo_{1-x}Fe_2O_4$ compounds synthesized via glycol-thermal route. In these compounds, the magnetization is expected to depend on the distribution of the magnetic Fe^{3+}, Mn^{2+} and Co^{2+} ions amongst the tetrahedral (A) and octahedral (B) sites. The octahedrally coordinated high spin Co^{2+} ions exhibit a strong spin-orbital coupling which introduce a large magneto-crystalline anisotropy [141]. Mn- doped $CoFe_2O_4$ ferrites show large magneto-mechanical effects and high sensitivity to mechanical stress. This makes these materials suitable for application as stress sensors [19]. The properties also depend significantly on the resulting particle sizes after synthesis and sintering. Smaller particle sizes are obtained for higher Mn content and larger sizes with increased sintering temperature [19, 20]. We are therefore interested in correlating the effects of Mn substitution on the structural, magnetic and electrical properties of Co ferrites produced by different methods and synthesis routes. The variation of the resistivity with temperature in mixed ferrites is usually discussed on the basis of the Arrhenius formula which has a T^{-1} dependence

[18, 142]. In the present case, we also study the $T^{-1/2}$ dependence associated with electrical conduction between grains [79, 143].

5.2 Experimental details

$Mn_xCo_{1-x}Fe_2O_4$ compounds with x ranging from 0.0 to 0.6 were synthesized by the glycol-thermal method from high-purity metal chlorides [18, 19, 20, 21]. Additional samples at $x = 0$, 0.5 and 1 were synthesized by high-energy ball milling [17] from high-purity metal oxides. The sample with $x = 0.5$ is denoted as Sample A. Another sample of $Mn_{0.5}Co_{0.5}Fe_2O_4$ (Sample B) was also produced by milling a mixture of two single phase $MnFe_2O_4$ and $CoFe_2O_4$ ferrites. The $Mn_{0.5}Co_{0.5}Fe_2O_4$ sample produced directly by the glycol-thermal process will be referred to as sample C. Details for the glycol-thermal and the high-energy ball milling techniques employed here have been discussed in chapter 4.

Single-phase formation and structure analysis of the samples was based on XRD data obtained at room temperature. The XRD spectra of the samples were obtained using CoK_α radiation with wavelength λ=1.7903 Å on a Phillips diffractometer type PW1710. The average particle diameters of the powders were also obtained by TEM measurements on a type Jeol_JEM-1010 instrument in order to confirm estimates of particle sizes from XRD measurements.

The ^{57}Fe Mössbauer spectra were recorded at about 300 K in zero field using a conventional constant acceleration Mössbauer spectrometer with a ^{57}Co source sealed in rhodium matrix. A standard natural iron foil was used to calibrate the spectra in terms of the transmitted intensity against velocity of the source. The measurements were performed on the as-prepared samples and on samples annealed at 700 ^{o}C. The Mössbauer spectra for the as-prepared samples were obtained at different absorption temperatures (323, 373, 423 and 473 K) in a Mössbauer furnace. We also recorded Mössbauer spectra at room temperature for the as-milled and annealed Sample A and B.

The magnetization measurements were performed using two different systems. A Quantum Design MPMS SQUID magnetometer was used to measure magneti-

zations in applied fields of up 50 kOe in the temperature range of $2 - 380$ K. The magnetizations as a function of applied magnetic field of up to 14 kOe were also obtained at room temperature on a LakeShore 735 VSM.

The D. C. resistivity measurements were carried out in air by the four-point probe method from about 300 to 400 K in a Proportional-Integral-Derivative (PID) controlled micro-oven. The electrical measurements were performed on either or both faces of pelletized samples annealed from 600 – 1100 ^{o}C under argon atmosphere. Each sample was annealed for 6 hours at each annealing temperature T_A. The pellets were initially compacted in an evacuated 13 mm diameter ICL die at a pressure of 1.5×10^8 N m^{-2} for 2 minutes. In the present four probe set-up the spacing between the probes $S = 0.2$ cm. The pelletized samples studied had thicknesses in the range $0.06 - 0.09$ cm. Hence, the relevant equation used to calculate resistivities was equation (4.3.2).

5.3 Results and discussion

5.3.1 X-ray diffraction and transmission electron microscopy measurements

The XRD patterns of the as-prepared samples of $Mn_xCo_{1-x}Fe_2O_4$ with $0 \leq x \leq 0.6$ are shown in Figure 5.1. All the major peaks characterize the basic single-phase cubic spinel structure. The main intensity peaks in Figure 5.1 correspond to reflections from (111), (220), (311), (400), (422), (511) and (440) planes which characterize the spinel structure. The X-ray diffraction peaks have broad widths that is evidence for crystallite size distribution [28]. The broad nature of the peaks is indicative of small grain or particle sizes. Figure 5.2 shows the variations of the XRD patterns of milled $Mn_{0.5}Co_{0.5}Fe_2O_4$ (Samples A and B) after annealing at different temperatures. Some impurity peaks are observed to emerge at $2\theta \approx 38^o$ and 52^o which are more significant for Sample A, and least for Sample C ($Mn_{0.5}Co_{0.5}Fe_2O_4$ produced by glycol-thermal method in Figure 5.1). The impurity peaks have been attributed to an intermediate haematite α-Fe_2O_3 phase [44]. No significant changes

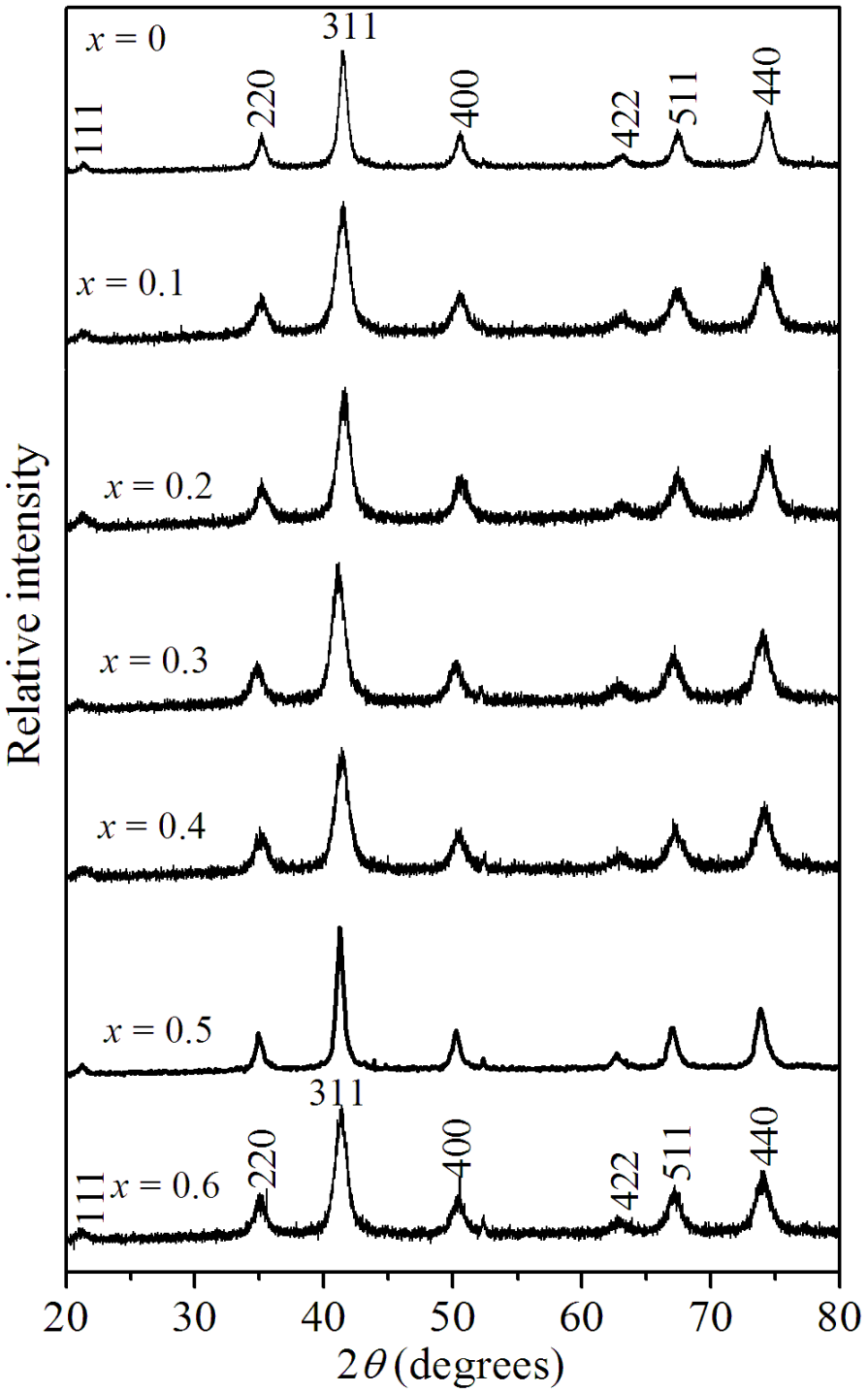

Figure 5.1: XRD patterns for the as-prepared samples of $Mn_xCo_{1-x}Fe_2O_4$.

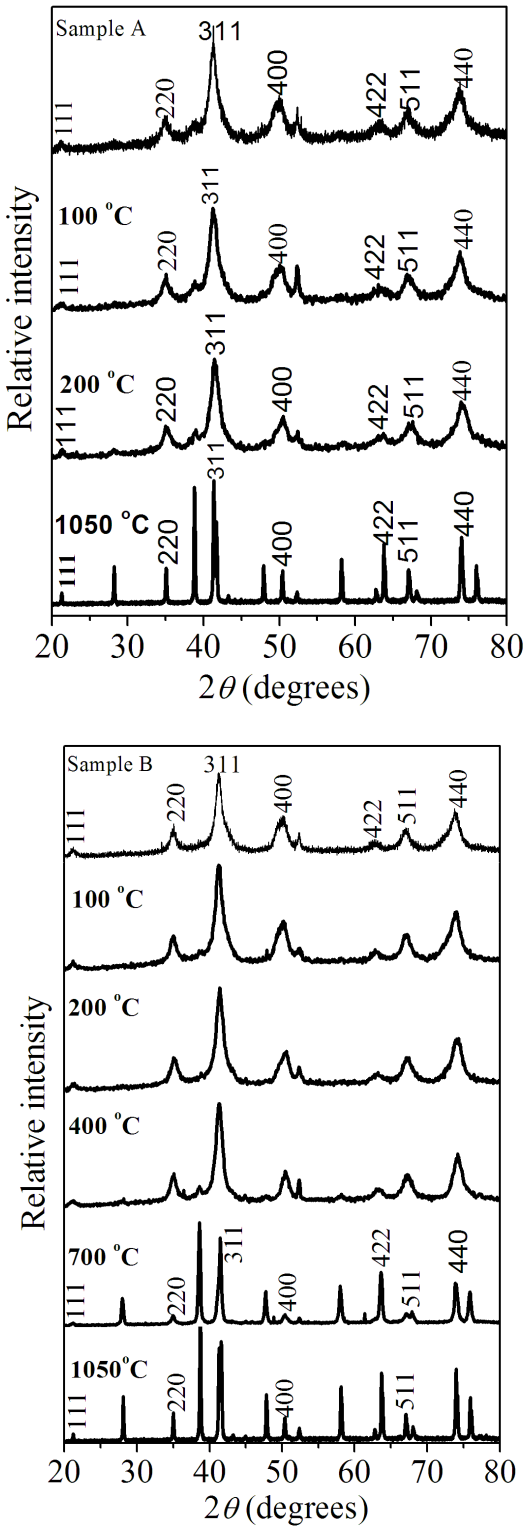

Figure 5.2: XRD patterns for the as-milled and the annealed Samples A and B.

to the XRD patterns are observed until after an annealing temperature of about 400 ^{o}C. Above this temperature, significant changes to the patterns are observed as more impurity peaks grow. The impurity peaks are attributed to oxidation, which may occur in Mn-Co ferrites. This leads to the formation metal oxides. The reaction processes during annealing temperature appear to depend on the oxygen partial pressure in the furnace and the processing temperature. At low annealing temperature in air, the Mn-Co ferrites tend to oxidize, because the oxygen partial pressure of the environment is higher than the pressure of the decomposition reaction in ferrites [2].

The average grain sizes were calculated using the Debye-Scherrer equation (4.1.3) [57]. Direct measurement of the grain size and powder morphology for the as-prepared samples and for samples annealed at 500 and 700 ^{o}C were also performed by transmission electron microscope (TEM). The TEM pictures are shown in Figures 5.3 – 5.7. The shapes of the particles appear to be nearly spherical with a significant spread in the particle sizes for all the compounds studied. Hence, the mean square estimation of the diameters has been used to calculate the average grain size D_{TEM} from at least 25 particles on each micrograph. The average particle diameters as calculated from XRD data (D_{XRD}) and observed by TEM measurements (D_{TEM}) are shown in Table 5.1. The calculated D_{XRD} and measured D_{TEM} values of the grain sizes are in good agreement. The particle sizes for $x = 0.1$ – 0.4 and $x = 0.6$ samples are almost the same at about 8 nm. We also observe that at compositions $x = 0$ and $x = 0.5$ corresponding $CoFe_2O_4$ and $Mn_{0.5}Co_{0.5}Fe_2O_4$, the grain sizes are nearly the same and lower at the others compositions. We suspect the higher stability of the compounds at $x = 0$ and $x = 0.5$ where the complete symmetry in the proportion of atoms on tetrahedral sites would tend to favour larger nanoparticles. The lattice parameters, a for the as-prepared samples deduced from X-ray patterns are also shown in Table 5.1. For $x = 0.1 - 0.6$, there are no significant changes in the lattice parameters, densities and porosities with composition, x. This may be due to similar ionic radii of Mn (0.089 nm) and Co (0.084 nm). Grain sizes and bulk densities increase with annealing temperature while porosities show a decrease as expected.

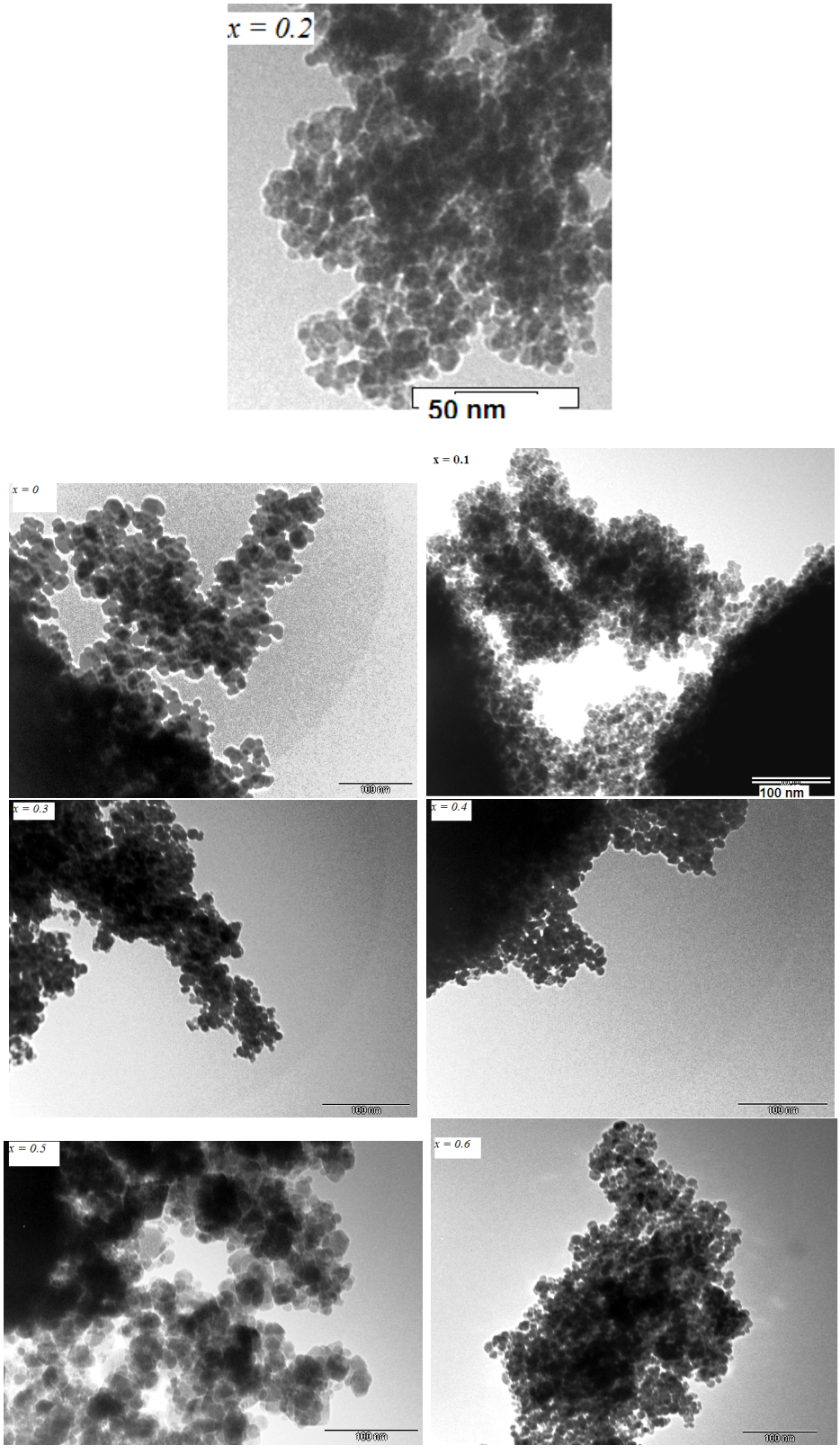

Figure 5.3: TEM micrographs for the as-prepared $Mn_xCo_{1-x}Fe_2O_4$ samples.

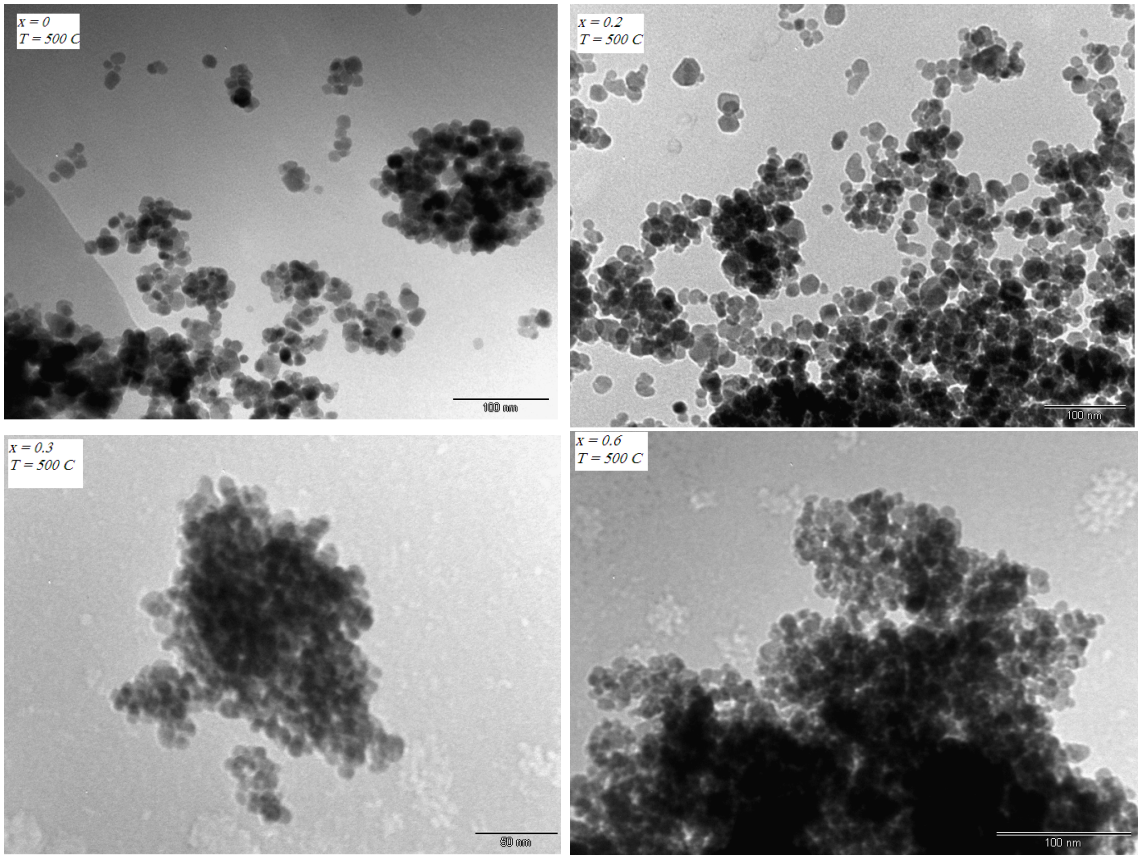

Figure 5.4: TEM micrographs for $Mn_xCo_{1-x}Fe_2O_4$ samples annealed at 500 ^oC. The length of the ruler corresponds to 100 nm.

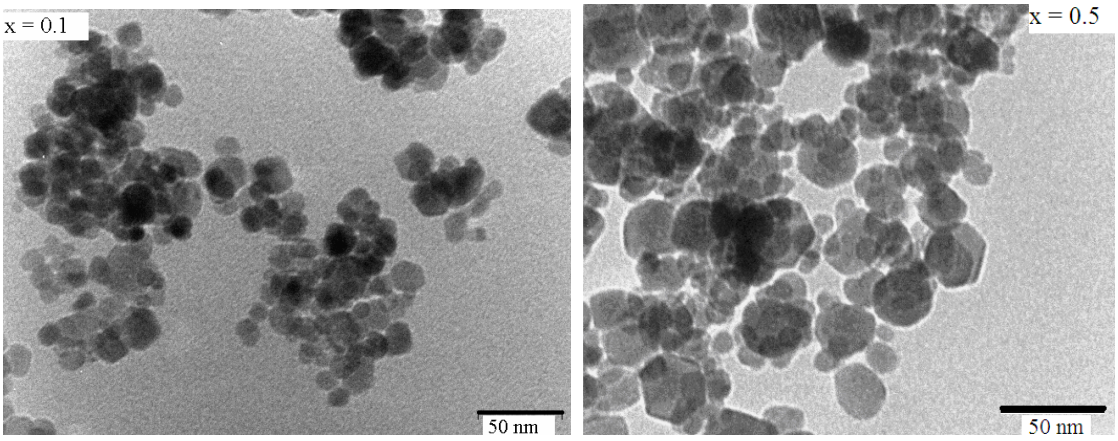

Figure 5.5: TEM micrographs for $Mn_xCo_{1-x}Fe_2O_4$ samples annealed at 500 ^oC. The length of the ruler corresponds to 50 nm.

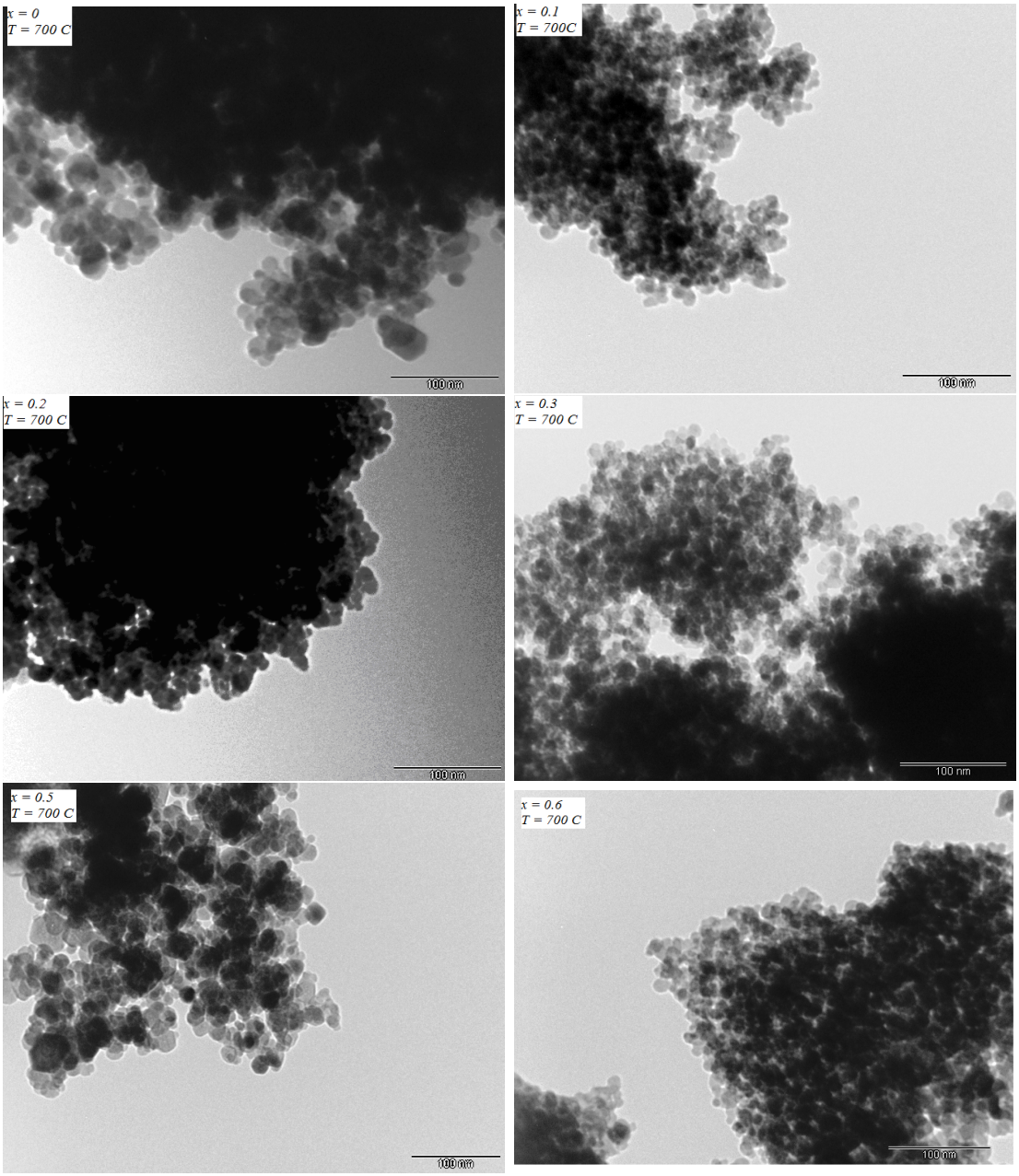

Figure 5.6: TEM micrographs for $Mn_xCo_{1-x}Fe_2O_4$ samples annealed at 700 ^oC. The length of the ruler corresponds to 100 nm.

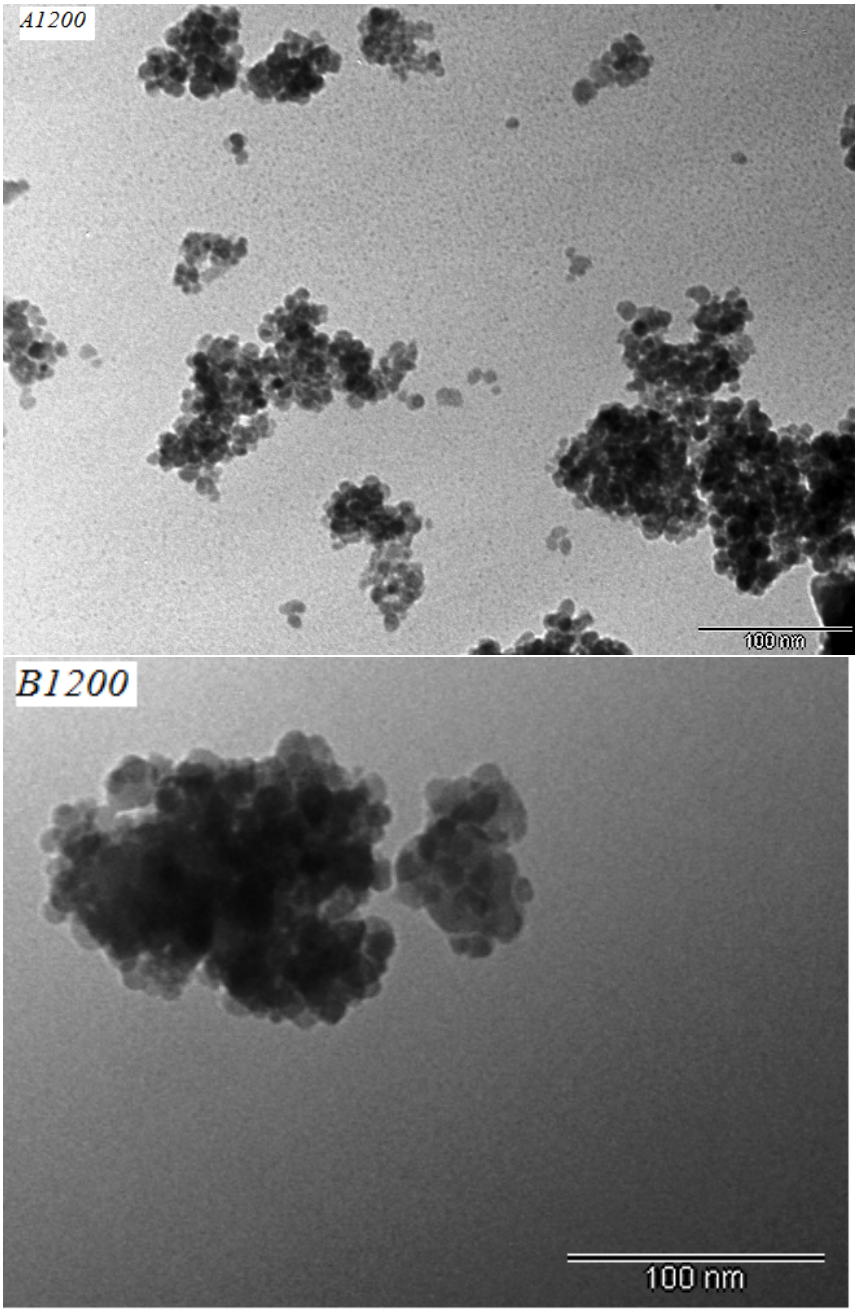

Figure 5.7: TEM micro-structures for Samples A and B annealed at 200 ^{o}C. The length of the ruler corresponds to 100 nm.

Table 5.1: Grain sizes (D), lattice parameters (a), bulk densities (ρ_{Bulk}), X-ray densities (ρ_{XRD}) and percentage porosities (P) for the as-prepared samples and samples annealed at different temperatures for $Mn_xCo_{1-x}Fe_2O_4$ prepared by glycol-thermal method. The sample corresponding to $x = 0.5$ is referred to as Sample C.

	D (nm)	D_{TEM} (nm)			a (nm)	ρ_{Bulk} (cm/g^3)		ρ (cm/g^3)	P (%)	
x	D_{XRD}	raw	500	700		600	1050	ρ_{XRD}	600	1050
	± 0.05	± 1.7	± 2	± 2	$\pm 10^{-4}$	± 0.03	± 0.04	± 0.04	± 0.3	± 0.1
0	12.09	12.4	12	14	0.8376	2.67	4.70	5.30	49.7	11.3
0.1	7.19	7.3	8	10	0.8348	2.79	4.73	5.40	47.9	11.6
0.2	7.72	7.8	16	20	0.8340	2.64	4.69	5.41	50.8	12.5
0.3	7.35	7.3	10	12	0.8423	2.68	4.27	5.42	48.4	17.8
0.4	7.35	7.7	–	–	0.8395	2.75	4.65	5.44	52.7	11.2
0.5	13.41	13.4	16	17	0.8425	2.60	4.30	5.47	49.6	16.8
0.6	8.06	8.2	9	12	0.8406	2.59	4.26	5.66	50.2	18.1

The X-ray densities (ρ_{XRD}) were calculated using equation (4.1.4) [6]. The values of ρ_{XRD} are also shown in Table 5.1. The XRD densities reflect the packing of the atoms in a unit cell. These values for our samples are comparable to those of similar compounds [37]. The values of ρ_{XRD} for Sample A and Sample B are 5.18±0.02 g/cm^3 and 5.23±0.02 g/cm^3 respectively. The bulk densities (ρ_{Bulk}) of the samples deduced from the geometry of samples after annealing at 600 ^{o}C and 1050 ^{o}C are also given in Table 5.1.

The percentage porosities (P) of the samples were deduced from bulk and X-ray densities using the equation (4.1.6). As shown in Table 5.1, the porosity of the compounds reduced significantly after annealing at higher temperature. The reduction in porosity with increased annealing temperature can be explained based on large grains created during sintering. Low values of the porosity indicate a higher degree of homogeneity in the synthesized samples [6].

The microstrain (ε) for the as-milled samples and for the annealed Samples A and B were estimated using the equation (4.1.5). The grain sizes, lattice parameters and microstrains deduced from XRD data are given in Table 5.2. After milling for 60 hours the grain sizes for Samples A and B were found to be 7.23±0.03 nm and 7.58±0.03 nm respectively. The grain sizes for both samples increased with the increasing annealing temperature. No significant changes in the lattice parameters are observed. Sample A, produced from metal oxides initially has a higher strain. No significant difference in the micro-strain is observed for samples annealed at 100 ^{o}C and higher temperatures as shown in Figure 5.8. The micro-strains decreased with increasing annealing temperature. This is attributed to the relief of the microstrains due to crystallite growth [144, 145].

Table 5.2: Grain sizes (D), lattice parameters (a) and microstrains (ε) for the as-milled and annealed Samples A and B.

Sample	T_A (^{o}C)	D (nm) ± 0.02	a (nm) ± 0.0003	ε ± 0.00002
A	27	7.23	0.8414	0.00170
A	100	7.84	0.8415	0.00146
A	200	8.02	0.8379	0.00141
B	27	7.58	0.8412	0.00150
B	100	7.81	0.8417	0.00146
B	200	8.16	0.8398	0.00140
B	400	9.82	0.8415	0.00116
B	500	10.31	-	-

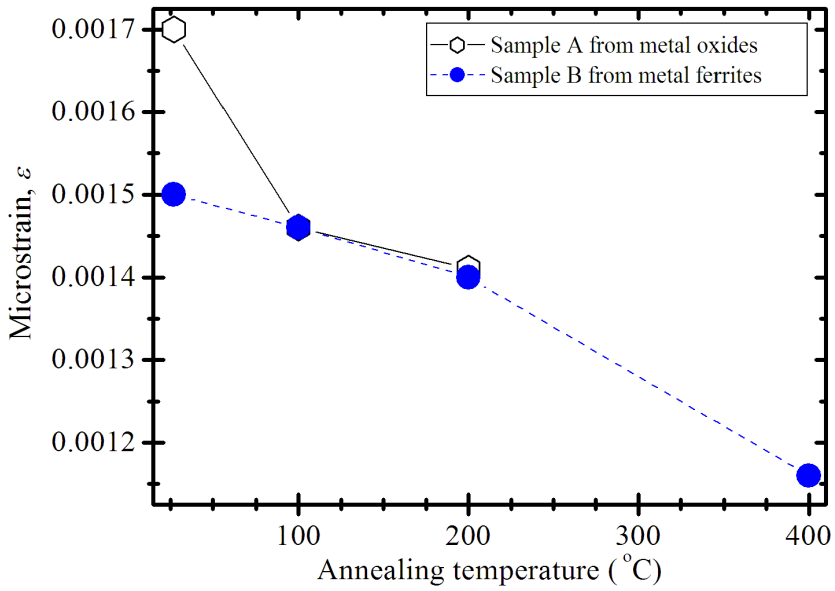

Figure 5.8: Microstrains for the as-milled samples and annealed samples of Samples A and B.

5.3.2 Mössbauer measurements

^{57}Fe Mössbauer spectra for the as-prepared $Mn_xCo_{1-x}Fe_2O_4$ were recorded at different absorber temperatures (300, 323, 373, 423 and 473 K) are shown in Figures 5.9 – 5.11. In Figure 5.12 we show the room temperature Mössbauer spectra recorded for samples annealed at 700 ^{o}C. Figures 5.13 and 5.14 show the typical Mössbauer spectra for the as-milled samples and samples annealed at 200 and 400 ^{o}C for Samples A and B. All the spectra appear closely related. The spectra for all samples recorded at room temperature show Zeeman sextets, which indicate ferrimagnetic behaviour of the compounds. Magnetic relaxations are observed in the as-milled samples of Samples A and B. The spectra have been fitted by two sextets corresponding to the oxidation state of Fe^{3+} ions at tetrahedral (A) and octahedral (B) sites of the spinel structure [146, 147]. The solid lines are the result of fittings to the experimental data and correspond to individual components (sextets or doublets). At least one doublet was required in the fits which we associate with Fe ions in the paramagnetic states. The paramagnetic doublets may also arise from the fine superparamagnetic grains of ferrites [147]. Two doublets were used to fit Mössbauer data for samples in paramagnetic states. An additional sextet was also required to get better fits to the data for the as-milled samples and samples annealed at 200 and 400 ^{o}C for A and B which we attribute to small Fe clusters induced by milling [17, 148]. Sextets and doublets were assigned to tetrahedral or octahedral sites based on the fitted results of isomer shifts and hyperfine fields. Isomer shifts and hyperfine fields on tetrahedral sites are expected to be lower due to higher symmetry as opposed to octahedral sites [147, 149, 150]. The tetrahedral sublattice is also associated with a higher degree of covalent bonding [151, 152]. The Mössbauer parameters, namely isomer shifts (δ), hyperfine fields (H), line widths (LW) and site population fractions (f) of Fe^{3+} ions on A and B sites for studies samples are presented in Tables 5.3 – 5.6.

We have observed no significant systematic changes in the values of isomer shifts and line widths with composition, measuring temperature or annealing temperature for the all the samples studied. Insignificant change in isomer shifts indicates that the $s-$electron density is not much affected by substitution of Co by Mn atoms or by thermal relaxation of the lattice. The values of the line widths and the hyperfine

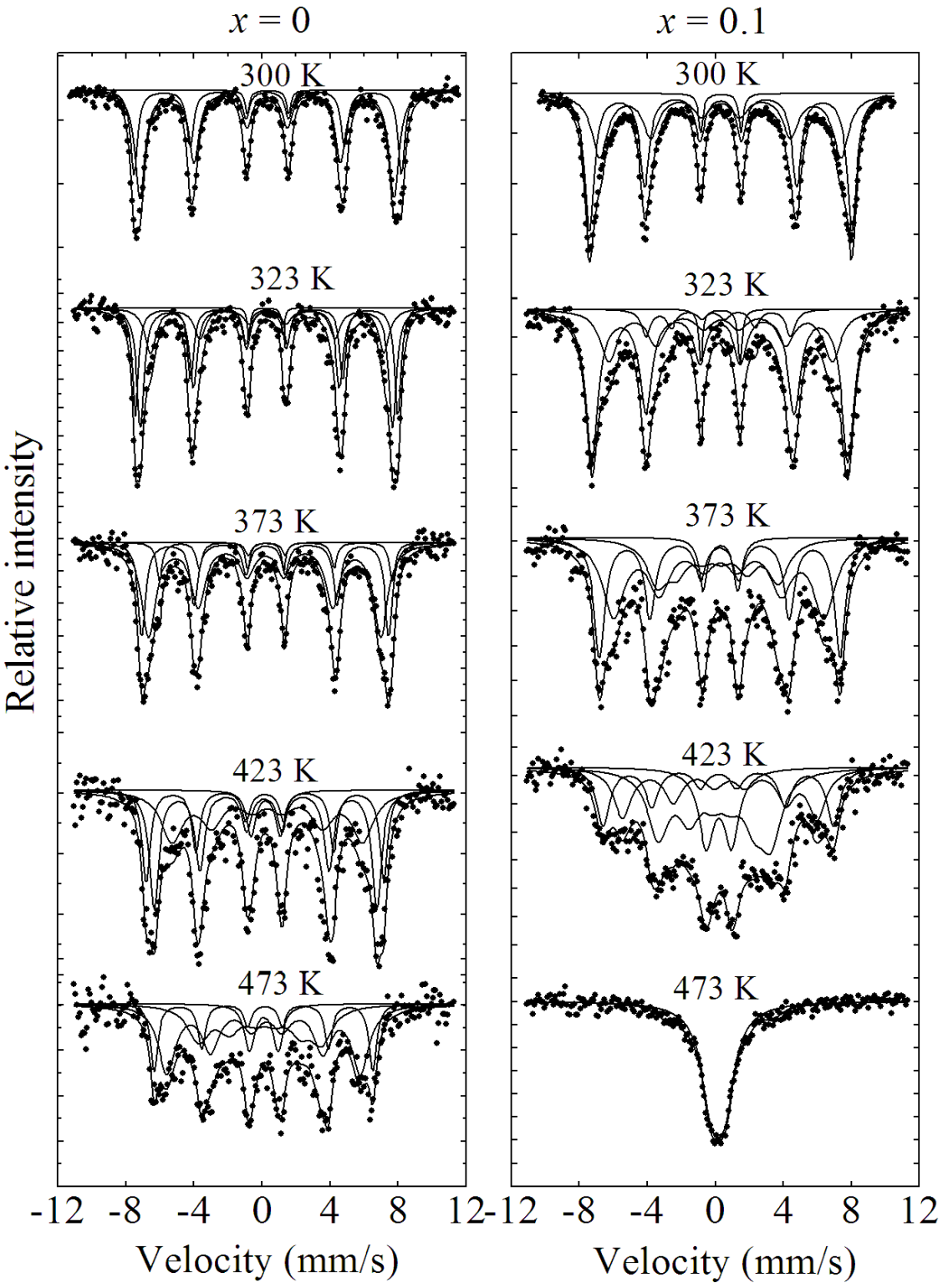

Figure 5.9: Mössbauer spectra for the as-prepared $Mn_xCo_{1-x}Fe_2O_4$ samples ($x = 0$ and 0.1) recorded at different temperatures.

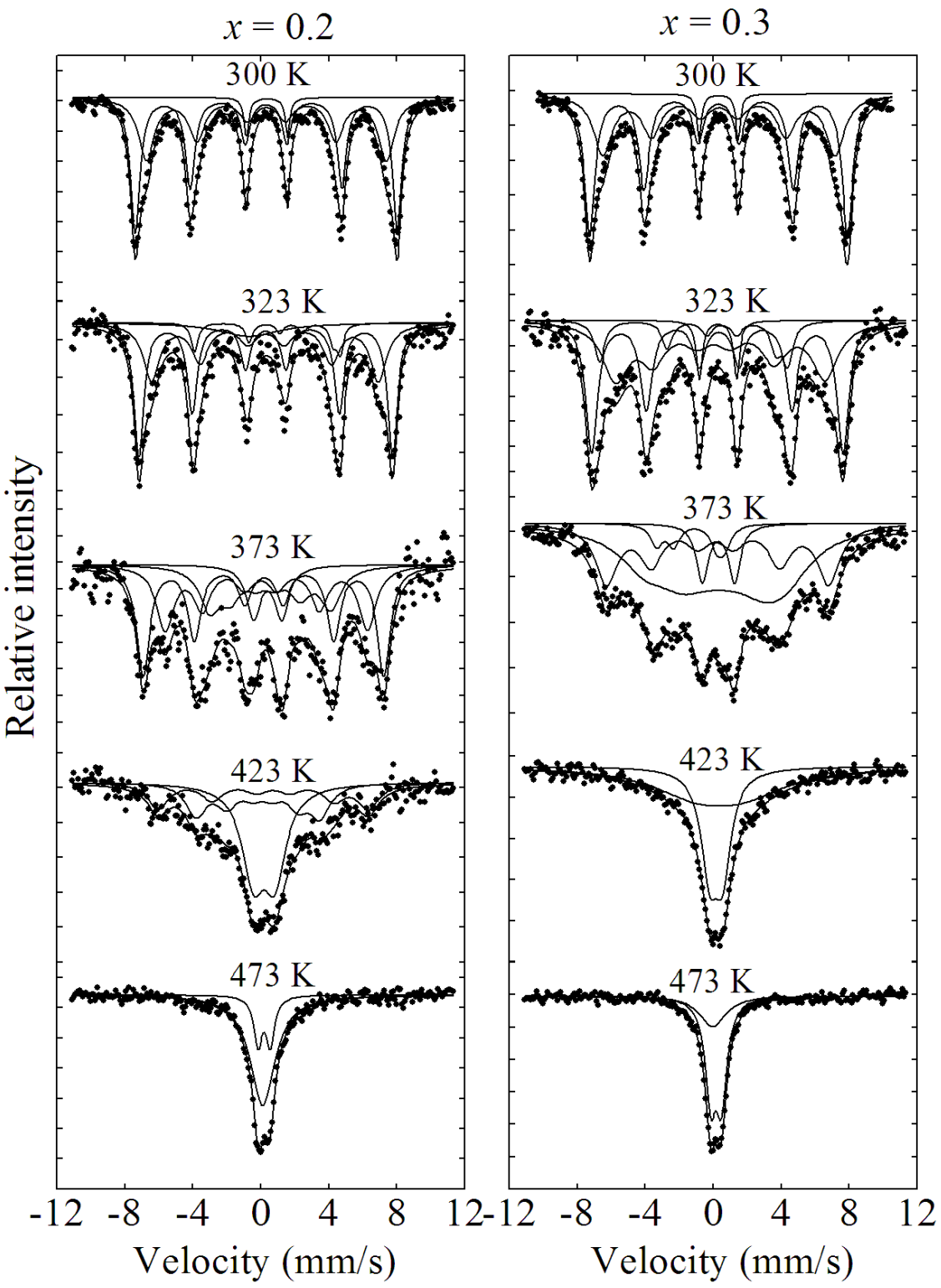

Figure 5.10: Mössbauer spectra for the as-prepared $Mn_xCo_{1-x}Fe_2O_4$ samples (x = 0.2 and 0.3) recorded at different temperatures.

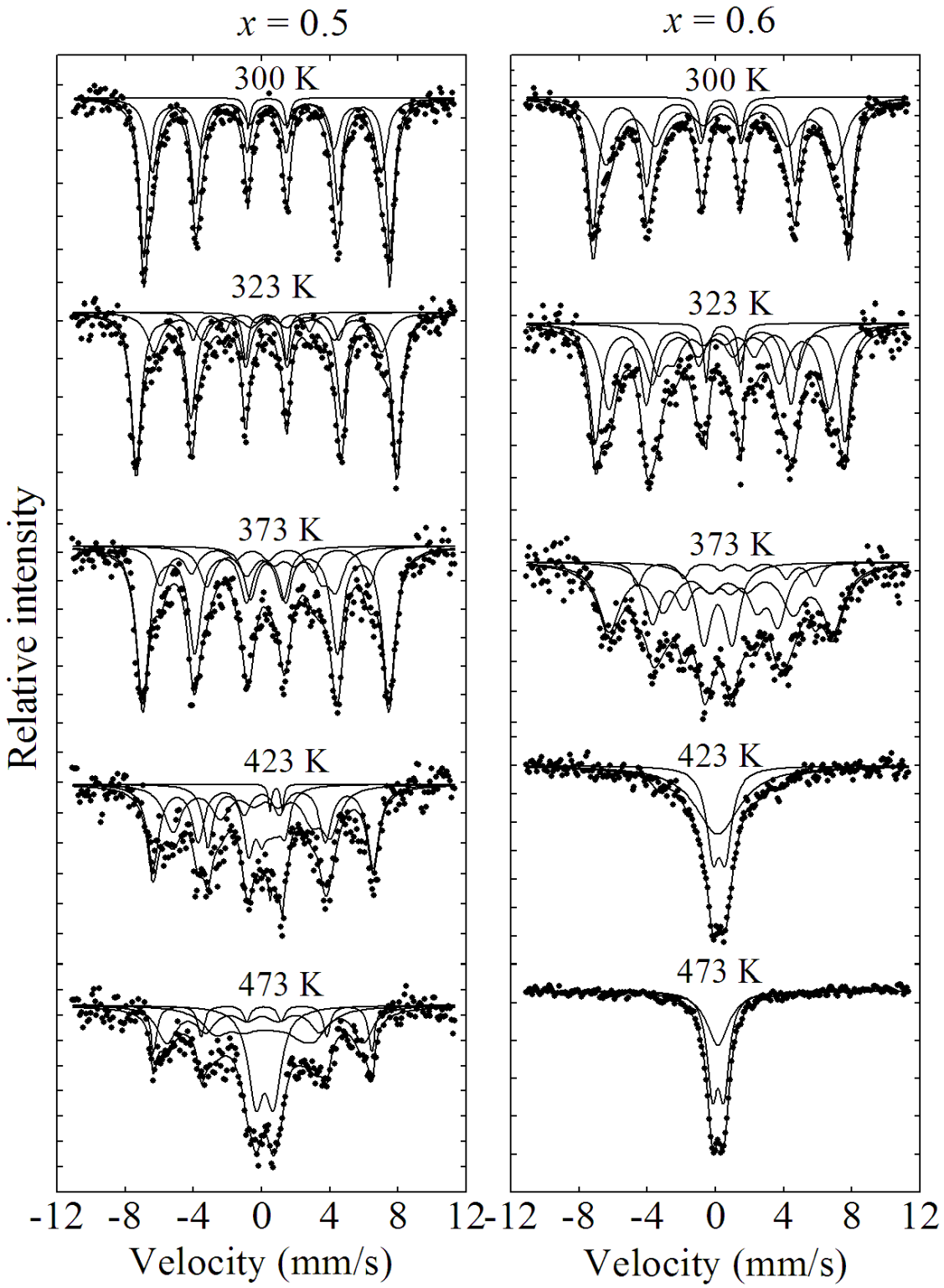

Figure 5.11: Mössbauer spectra for the as-prepared $Mn_xCo_{1-x}Fe_2O_4$ samples (x = 0.5 and 0.6) recorded at different temperatures.

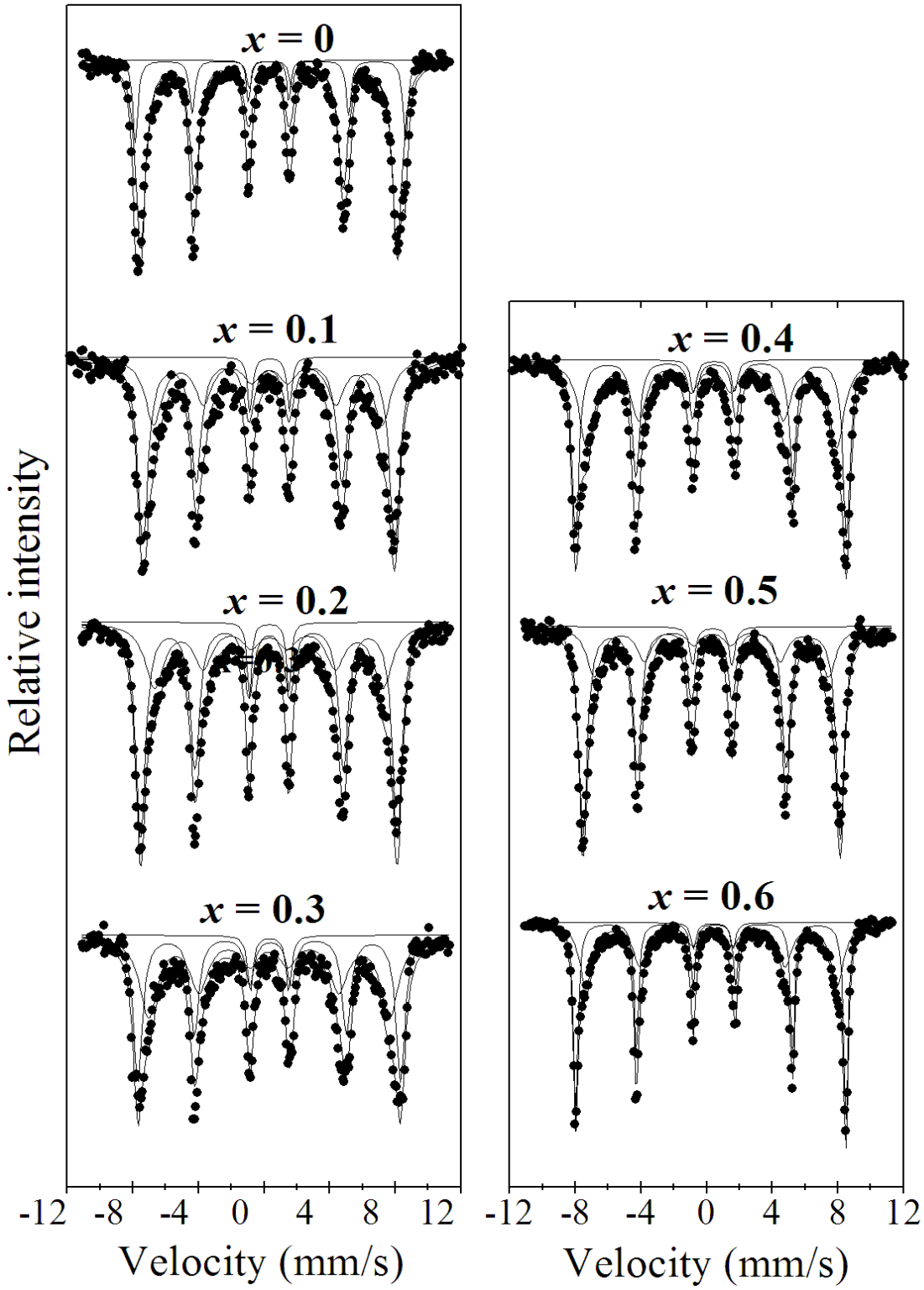

Figure 5.12: Room temperature Mössbauer spectra for $Mn_xCo_{1-x}Fe_2O4$ samples annealed at 700 ^oC.

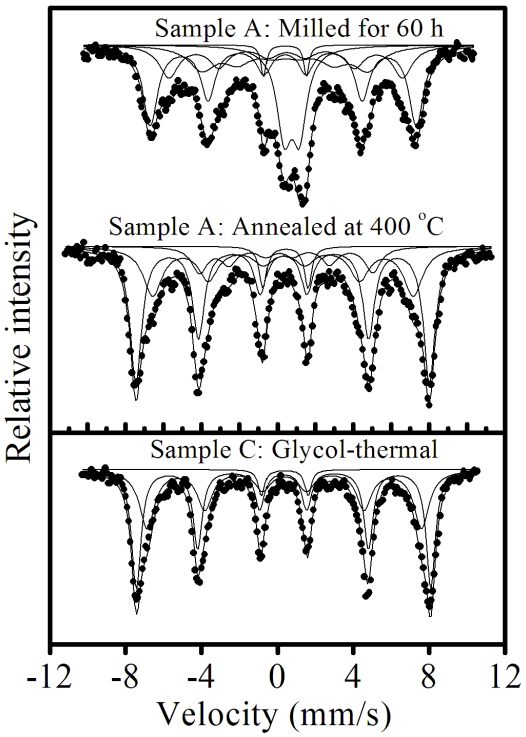

Figure 5.13: Mössbauer spectra for as-milled, annealed samples of sample A and as-prepared sample C.

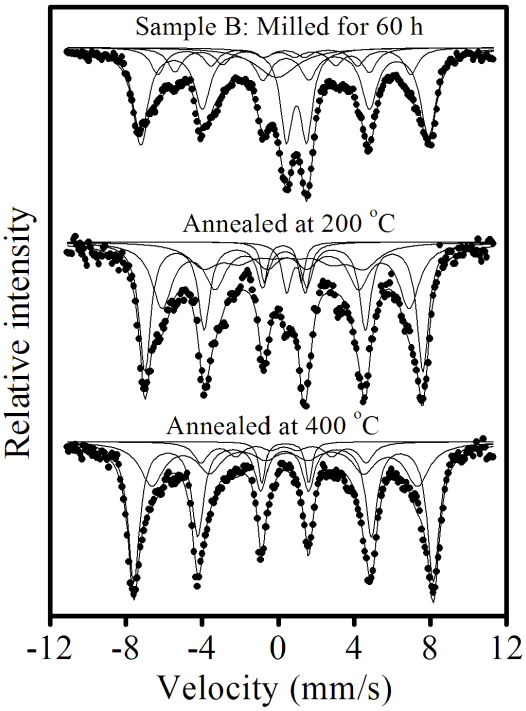

Figure 5.14: Mössbauer spectra for as-milled and annealed samples of Sample B.

Table 5.3: Isomer shifts (δ), hyperfine fields (H), line widths (LW) and Fe^{3+} fraction (f) on A and B sites for the as-prepared samples of $Mn_xCo_{1-x}Fe_2O_4$ with $0 \leq x \leq 0.2$ recorded at T = 300, 323, 373, 423, and 473 K.

Sample	T	δ (mm/s)		H (kOe)			LW (mm/s)		f (%)	
x	(K)	δ_A	δ_B	H_A	H_B	H_{3rd}	LW_A	LW_B	f_A	f_B
		$\pm$0.08	$\pm$0.03	$\pm$7	$\pm$3	$\pm$7	$\pm$0.02	$\pm$0.02		
0	300	0.30	0.33	462	487	–	0.35	0.24	63.2	33.2
0	323	0.27	0.27	460	479	426	0.26	0.21	42.6	31.8
0	373	0.17	0.20	423	450	425	0.50	0.26	56.9	30.7
0	423	0.30	0.35	348	406	433	0.80	0.33	34.1	35.8
0	473	0.02	0.18	224	353	399	0.75	0.60	28.6	44.3
0.1	300	0.30	0.31	440	479	–	0.55	0.33	41.4	55.0
0.1	323	0.32	0.27	407	467	264	0.61	0.44	27.8	60.9
0.1	373	0.24	0.25	384	439	221	0.80	0.40	40.8	32.5
0.1	423	0.16	0.18	206	420	354	0.74	0.45	38.6	20.9
0.1	473	0.13	0.28	–	–	–	0.55	2.16	50.0	50.0
0.2	300	0.32	0.31	438	478	–	0.55	0.33	41.8	54.1
0.2	323	0.26	0.28	414	463	266	0.57	0.34	35.8	49.4
0.2	373	0.16	0.17	369	439	221	0.61	0.50	29.3	39.5
0.2	423	-0.04	0.43	226	384	–	0.70	0.74	29.5	24.6
0.2	473	0.10	0.19	–	–	–	0.89	0.29	77.8	22.2

Table 5.4: Isomer shifts (δ), hyperfine fields (H), line widths (LW) and Fe^{3+} fraction (f) on A and B sites for the as-prepared samples of $Mn_xCo_{1-x}Fe_2O_4$ with $0.3 \leq x \leq 0.6$ recorded at T = 300, 323, 373, 423, and 473 K.

Sample	T	δ (mm/s)		H (kOe)			LW (mm/s)		f (%)	
x	(K)	δ_A	δ_B	H_A	H_B	H_{3rd}	LW_A	LW_B	f_A	f_B
		$\pm$0.01	$\pm$0.04	$\pm$10	$\pm$11	$\pm$5	$\pm$0.03	$\pm$0.08		
0.3	300	0.34	0.31	424	471	–	0.65	0.37	41.1	55.0
0.3	323	0.21	0.28	382	459	343	0.91	0.41	40.5	42.9
0.3	373	0.40	0.19	258	405	30	1.90	0.78	54.8	31.1
0.3	423	0.17	0.36	–	–	–	0.59	3.10	43.3	56.7
0.3	473	-0.04	0.17	–	–	–	0.92	0.38	27.5	72.5
0.5	300	0.32	0.37	416	494	–	0.41	0.29	38.2	58.6
0.5	323	0.37	0.28	415	474	265	0.51	0.34	23.3	62.1
0.5	373	-0.19	0.24	380	448	234	0.44	0.42	14.7	57.6
0.5	423	-0.17	0.04	287	401	74	0.63	0.42	33.1	40.3
0.5	473	0.39	0.12	181	358	396	0.96	0.68	28.3	29.8
0.6	300	0.33	0.31	418	467	–	0.70	0.36	47.0	48.3
0.6	323	0.11	0.23	401	454	253	0.56	0.40	37.9	39.0
0.6	373	0.14	0.53	230	407	323	0.60	0.66	29.4	45.8
0.6	423	0.12	0.21	–	–	224	1.60	0.44	55.3	36.6
0.6	473	0.13	0.15	–	–	–	0.79	0.37	38.6	61.4

Table 5.5: Isomer shifts (δ), hyperfine fields (H), line widths (LW) and Fe^{3+} fraction (f) on A and B sites for $Mn_xCo_{1-x}Fe_2O_4$ samples annealed at 700 ^{o}C measured at $T = 300$ K.

Sample	δ (mm/s)		H (kOe)		LW (mm/s)		f (%)	
x	δ_A	δ_B	H_A	H_B	LW_A	LW_B	f_A	f_B
	± 0.04	± 0.01	± 5	± 1	± 0.08	± 0.03		
0	0.29	0.39	485	511	0.36	0.18	79.3	17.3
0.1	0.29	0.29	432	476	0.62	0.39	35.2	60.6
0.2	0.30	0.30	432	485	0.69	0.35	34.9	60.5
0.3	0.30	0.35	455	496	0.67	0.33	49.1	45.4
0.4	0.29	0.37	472	512	0.55	0.25	49.5	46.8
0.5	0.32	0.31	443	486	0.55	0.30	28.4	67.2
0.6	0.33	0.37	474	510	0.48	0.16	47.4	48.7

Table 5.6: Isomer shifts (δ), hyperfine fields (H), line widths (LW) and Fe^{3+} fraction (f) on A and B sites for raw samples and annealed samples of Samples A, B and C measured at $T = 300$ K.

Sample	T	δ (mm/s)		H (kOe)			LW (mm/s)		f (%)	
	(^{o}C)	δ_A	δ_B	H_A	H_B	H_{3rd}	LW_A	LW_B	f_A	f_B
		± 0.02	± 0.04	± 3	± 4	± 6	± 0.02	± 0.02		
A	27	0.36	0.47	434	382	271	0.46	0.60	38	20
A	400	0.30	0.32	426	480	283	0.38	0.60	30	52
B	27	0.33	0.37	412	469	317	0.44	0.50	13	47
B	200	0.33	0.43	403	453	261	0.36	0.65	34	39
B	400	0.31	0.40	433	488	269	0.38	0.73	32	54
C	200	0.32	0.37	416	494	–	0.41	0.29	38.2	58.6

fields for samples recorded at room temperature are comparable to those reported for similar compounds [150]. However, in the present case we have observed an enhancement of the hyperfine fields at both tetrahedral and octahedral sites for the $x = 0.5$ sample. The magnetic hyperfine fields are observed to decreased gradually with increasing measuring temperatures for all the as-prepared samples as shown in Figure 5.15. The transition temperature (T_C) for the as-prepared $Mn_xCo_{1-x}Fe_2O_4$ samples can be deduced from Mössbauer spectra recorded at different temperatures (Figures 5.9 – 5.11). We expect $T_C > 473$ K for samples with $x = 0$ and 0.5. For samples with $x = 0.1$, 0.2 and 0.6, $423 < T_C < 473$ K. While for $x = 0.3$, then $373 < T_C < 423$ K. Broad central doublets are observed in the as-milled samples, which disappear drastically with increased sintering temperature. The reductions of doublets with increasing annealing temperature appear to be related to the formation of the single-phase. The spectra for samples annealed at 400 ^{o}C are comparable with those of similar compounds prepared by sol-gel method [50]. There is no evidence of a broad doublet in the spectra for Sample C. This also compared well with an insignificant haematite phase as indicated by XRD results for Sample C in Figure 5.1. The values of isomer shifts, hyperfine fields and line widths are similar to those previously reported [35, 153]. As can be see in Figures 5.13 and 5.14, Samples A and B for $Mn_{0.5}Co_{0.5}Fe_2O_4$ have been found to have similar ^{57}Fe Mössbauer spectra before and after annealing at 1050 ^{o}C. The spectrum for each sample changes significantly due to the annealing effect. This is attributed to changes of both grain sizes and impurity phases with thermal annealing [17].

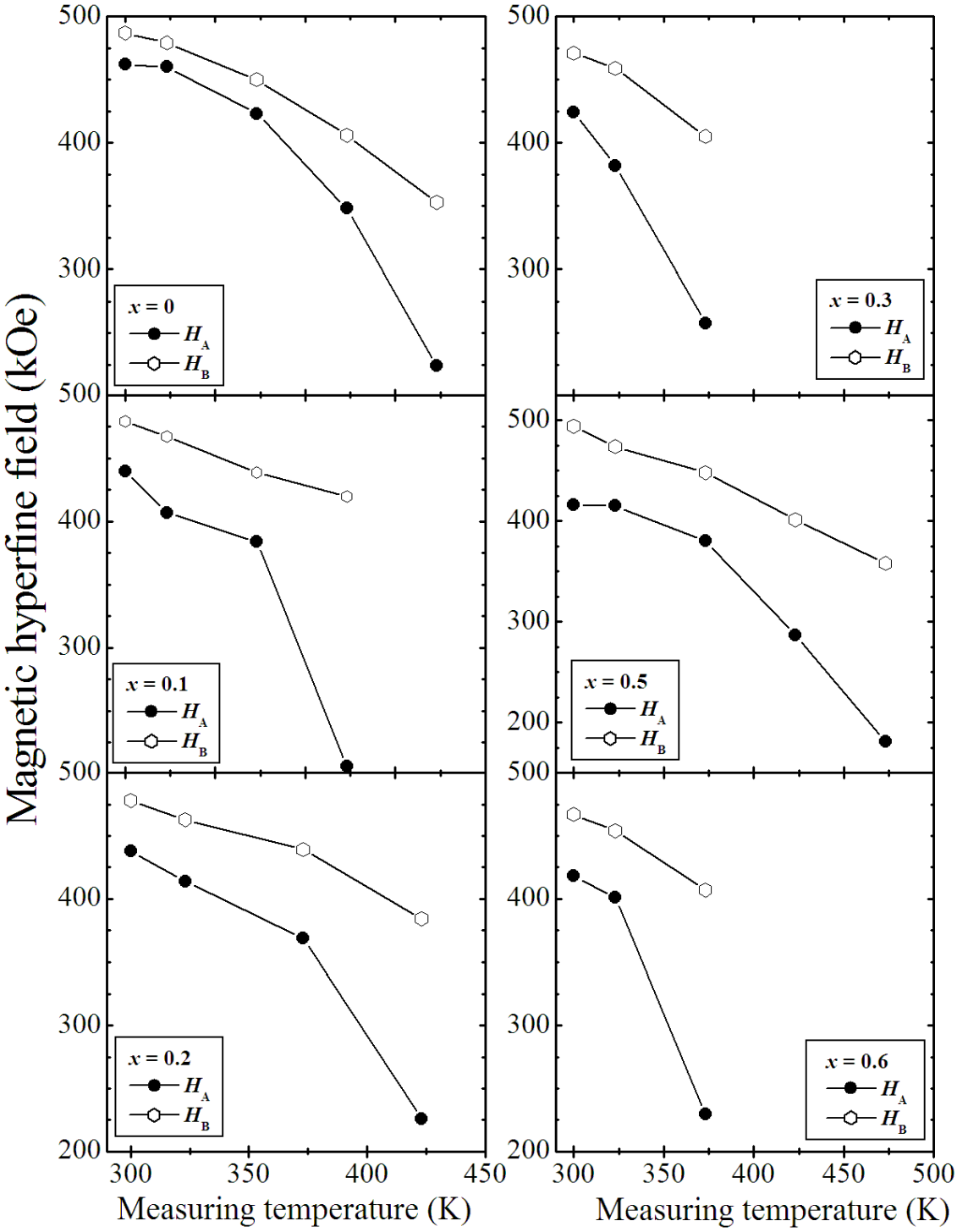

Figure 5.15: Magnetic hyperfine fields for the as-prepared $Mn_xCo_{1-x}Fe_2O_4$ samples measured at different temperatures.

5.3.3 Magnetization measurements

Figures 5.16 – 5.18 show the room temperature hysteresis loops for the as-prepared and annealed (500 ^{o}C and 700 ^{o}C) $Mn_xCo_{1-x}Fe_2O_4$ samples. The measurements were obtained using a VSM in an external applied magnetic field of up to 14 kOe. In Figures 5.19 and 5.20 we show the hysteresis loops for the as-milled samples and samples annealed at 100, 200, 300, 400 and 500 ^{o}C for Samples A and B. In Figures 5.21 – 5.24 we show the best fit curves to the initial magnetization data. The calculated values of various parameters deduced from the hysteresis loops are given in Tables 5.7 and 5.8. Magnetization properties such as coercive field (H_C), saturation magnetization (M_S) and remanent magnetization (M_R) are affected differently by Mn content and annealing temperature. The behaviour of coercive fields as a function of annealing temperature are shown in Figure 5.25. The coercive fields are significantly reduced by Mn substitution. The changes in saturation magnetization are not as dramatic. In Figures 5.26 and 5.27 we have plotted the coercive fields, saturation magnetizations, maximum magnetizations and remanent magnetizations as a function of annealing temperature for Samples A and B. The magnetization does not appear to saturate even at the maximum applied field. The slow approach to saturation can be explained on the basis of the disordered spin configuration at the surface of the magnetic nanoferrites [104]. The coercive field is a measure the magnetization reversal processes under the action of an applied field. It depends on the domain structure, particle sizes and crystalline anisotropy. $CoFe_2O_4$ is known to have high H_C due to the strong anisotropy associated with the Co atoms [53]. The substitution by Mn atoms with lower anisotropy leads to a reduction in H_C. The coercive field of $CoFe_2O_4$ nanoparticles have been studied as a function of particle size. The results show a maximum coercive field at about 25 nm [71, 97]. In the present case, all the samples studied have grain sizes below 25 nm. The present results of coercive field correlate very well with changes in particle sizes. The field responses of the three samples A, B and C are sensitive to the method of preparation and route.

The ratio M_R/M_S is referred to as the squareness of a hysteresis loop [154] where M_R is the remanent magnetization. The ratio increases with increasing annealing

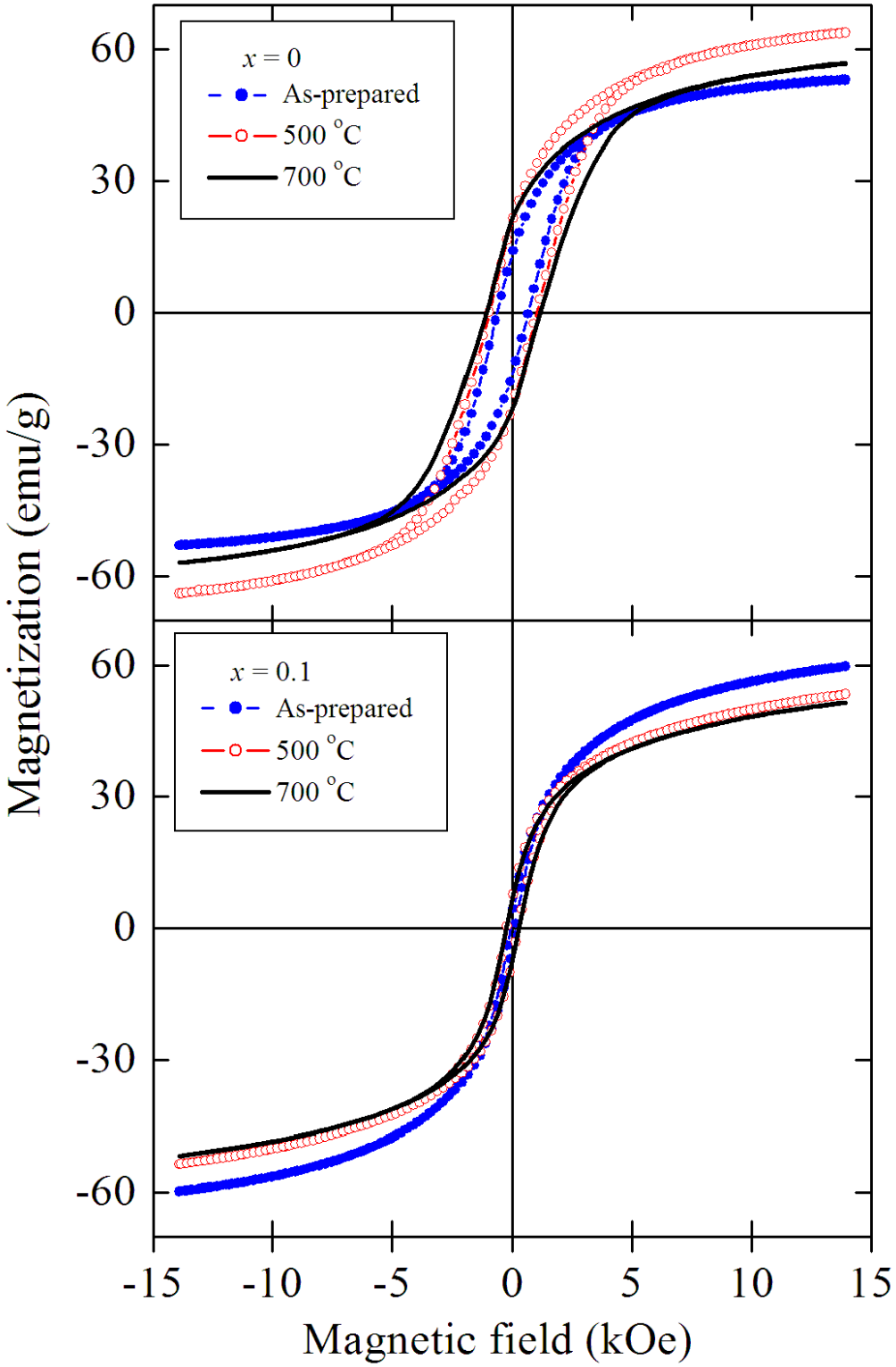

Figure 5.16: Room temperature hysteresis loops for the as-prepared and annealed samples of $Mn_xCo_{1-x}Fe_2O_4$ ($x = 0$ and 0.1).

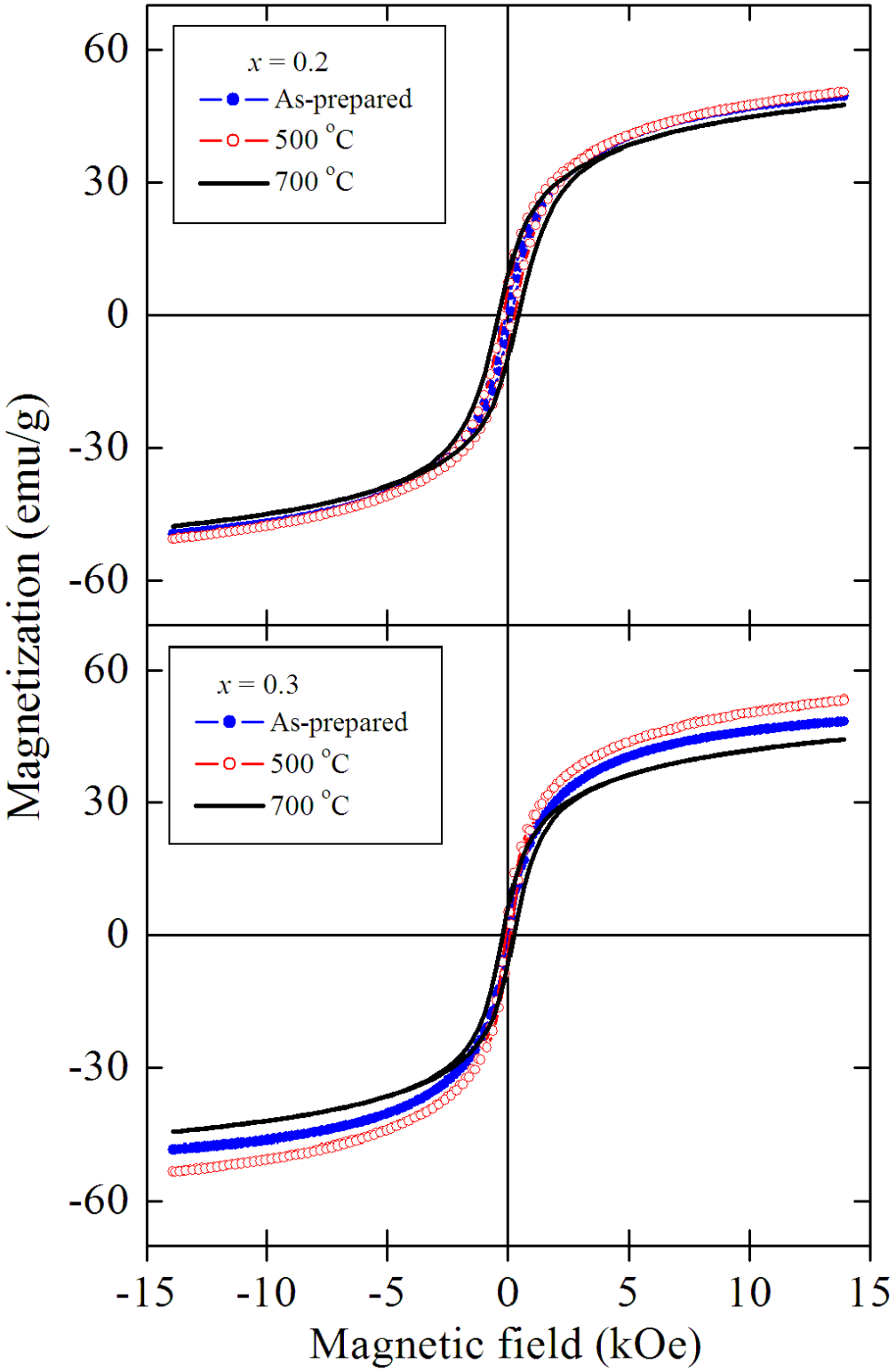

Figure 5.17: Room temperature hysteresis loops for the as-prepared and annealed samples of $Mn_xCo_{1-x}Fe_2O_4$ ($x = 0.2$ and 0.3).

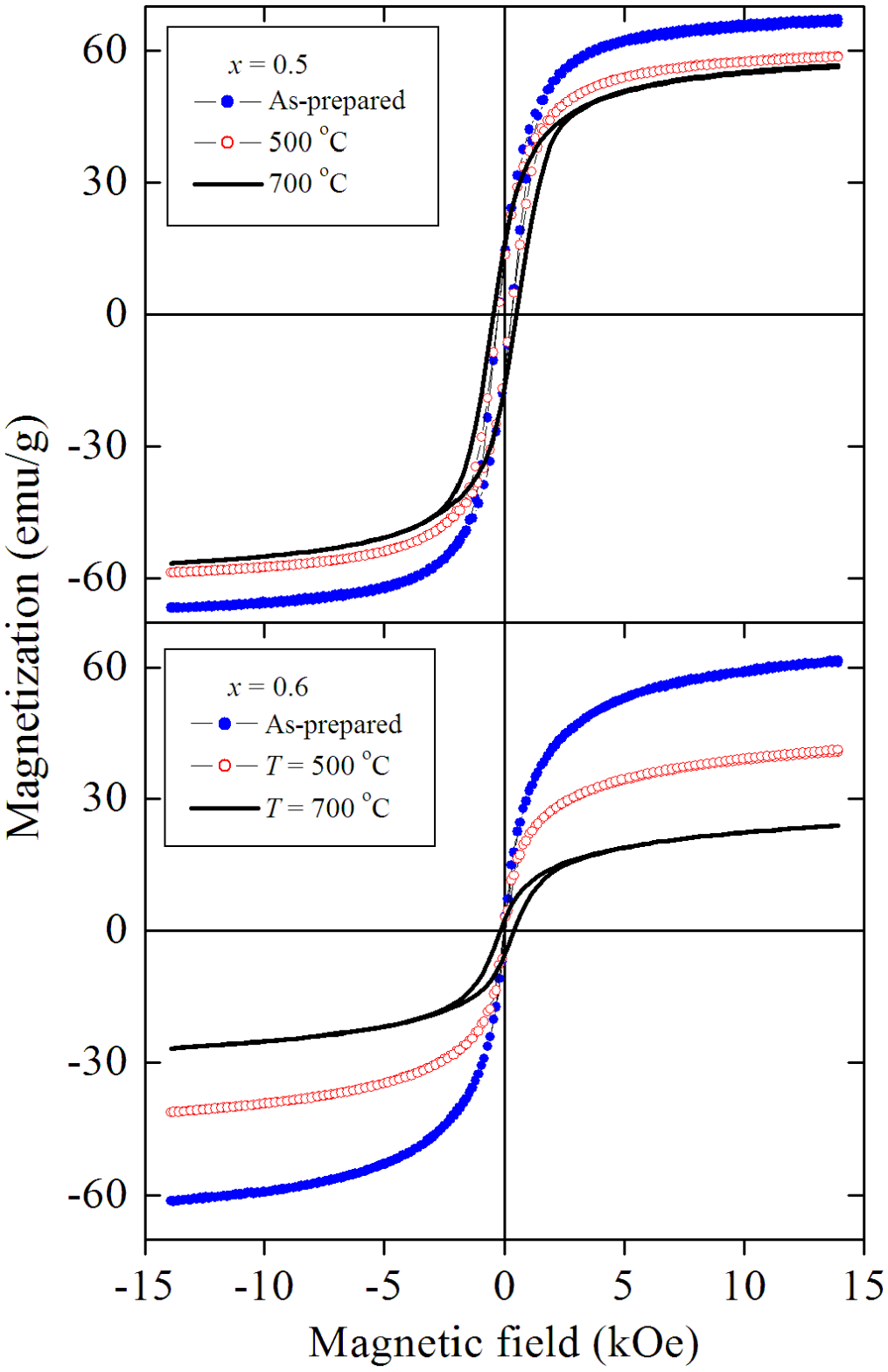

Figure 5.18: Room temperature hysteresis loops for the as-prepared and annealed samples of $Mn_xCo_{1-x}Fe_2O_4$ ($x = 0.5$ and 0.6).

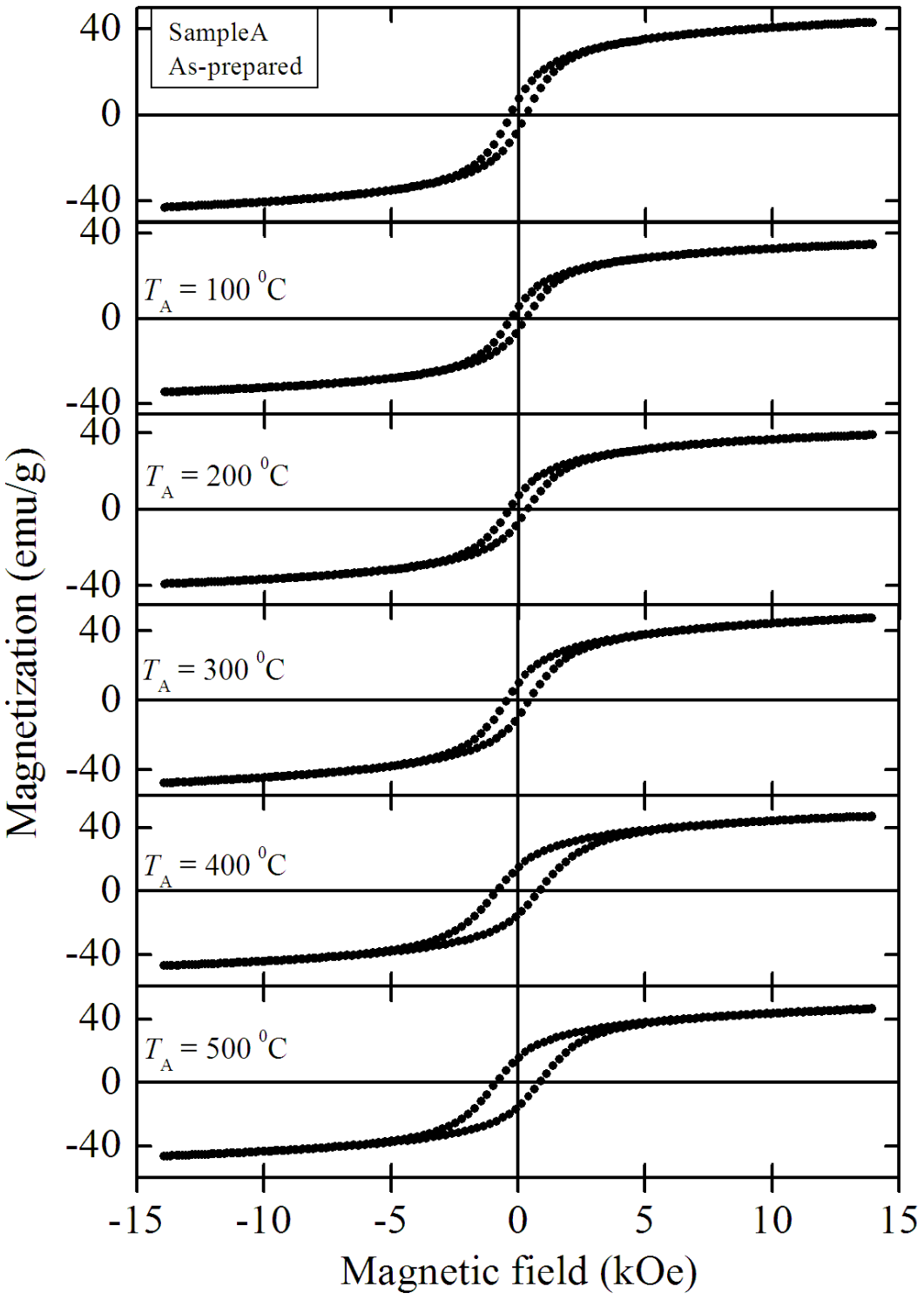

Figure 5.19: Room temperature hysteresis loops for Sample A annealed at different temperatures.

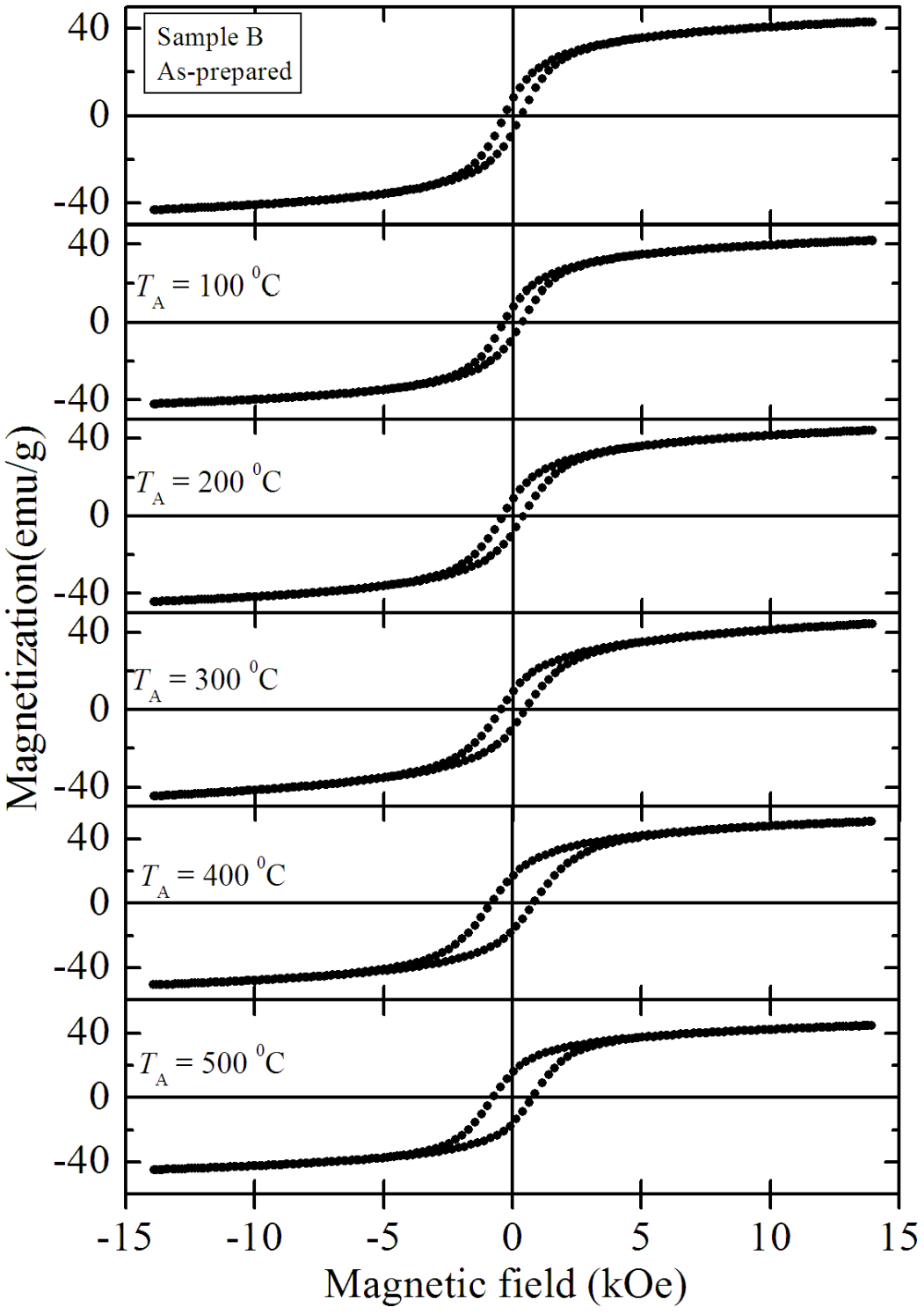

Figure 5.20: Room temperature hysteresis loops for Sample B annealed at different temperatures.

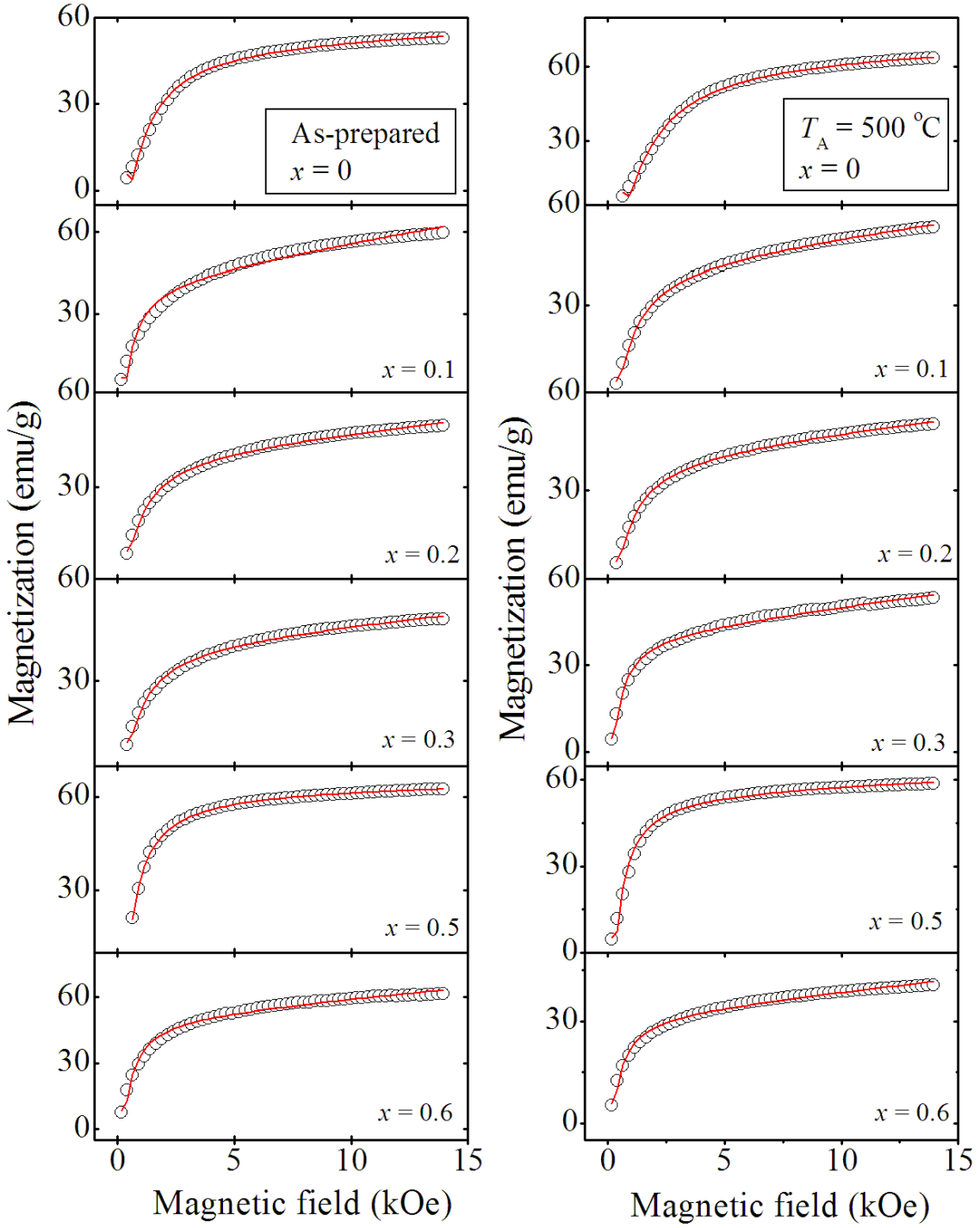

Figure 5.21: Initial magnetizations as a function of magnetic field for the as-prepared and samples annealed at 500 ^{o}C of $Mn_xCo_{1-x}Fe_2O_4$ measured at 300 K. The solid lines are the best fit to the data based on equation (2.10.1).

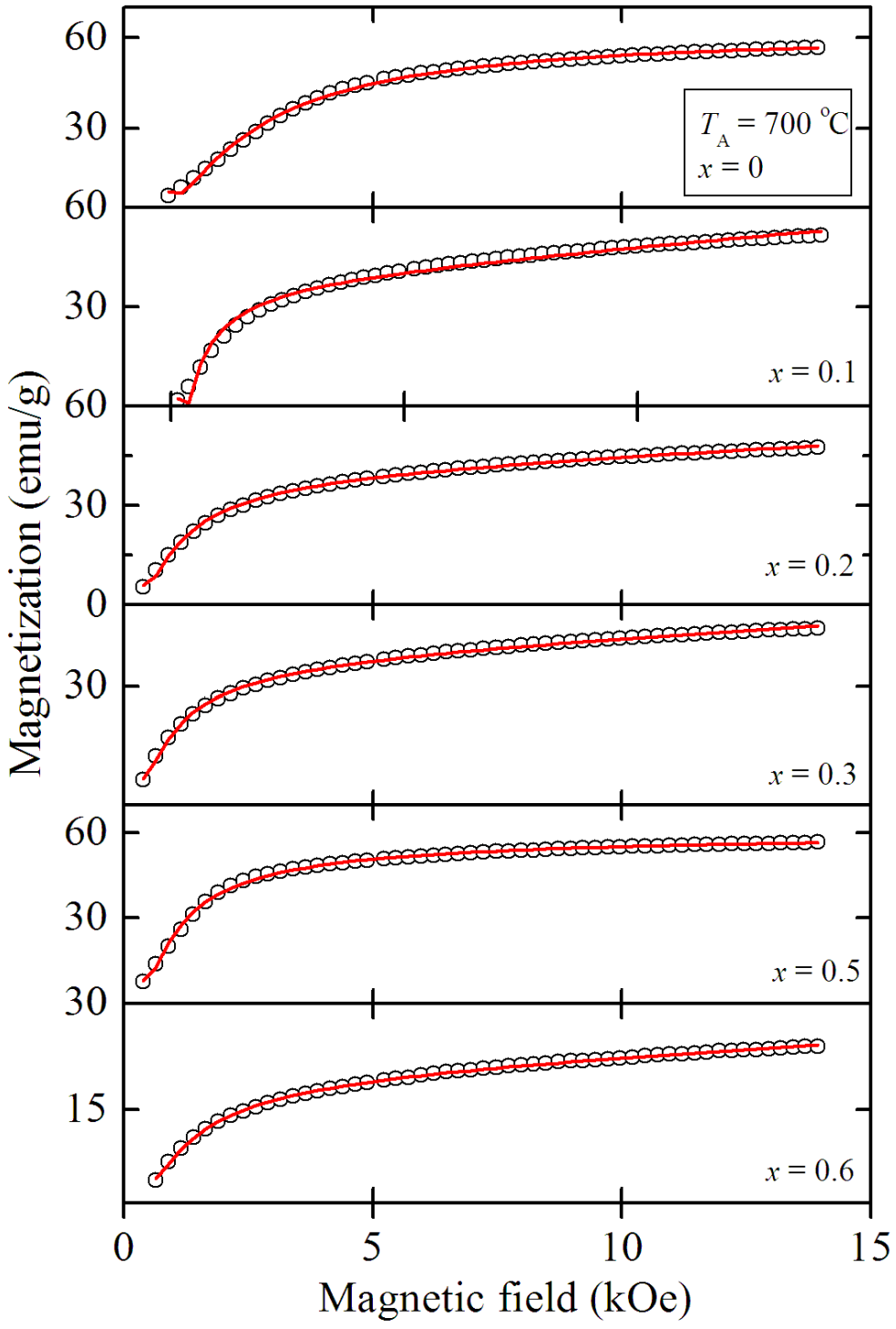

Figure 5.22: Initial magnetizations as a function of magnetic field for $Mn_xCo_{1-x}Fe_2O_4$ samples annealed at 700 °C measured at room temperature. The solid lines are the best fit to the data based on equation (2.10.1).

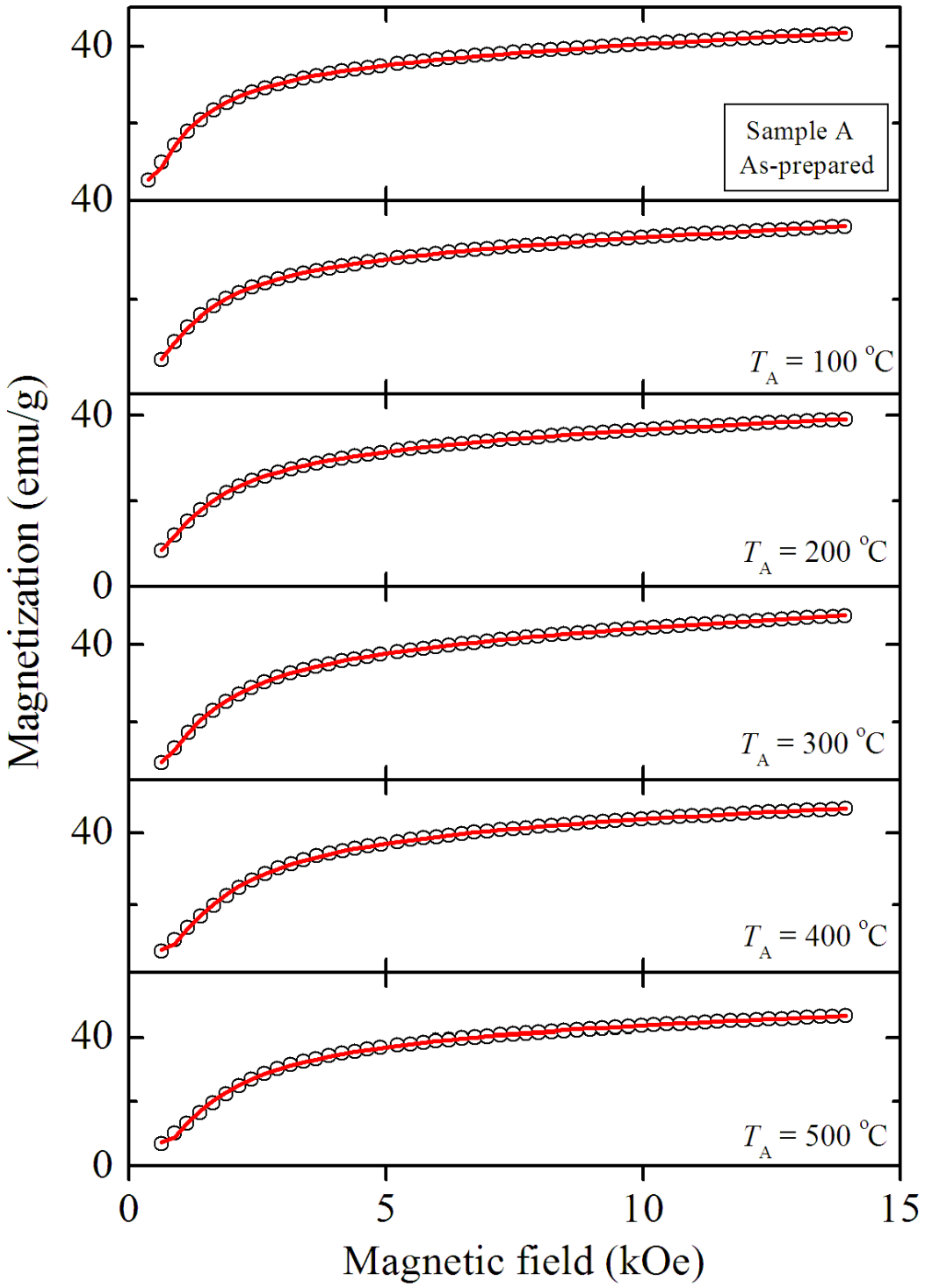

Figure 5.23: Initial magnetizations as a function of magnetic field for Samples A annealed at different temperatures measured at 300 K. The solid lines are the best fit to the data based on equation (2.10.1).

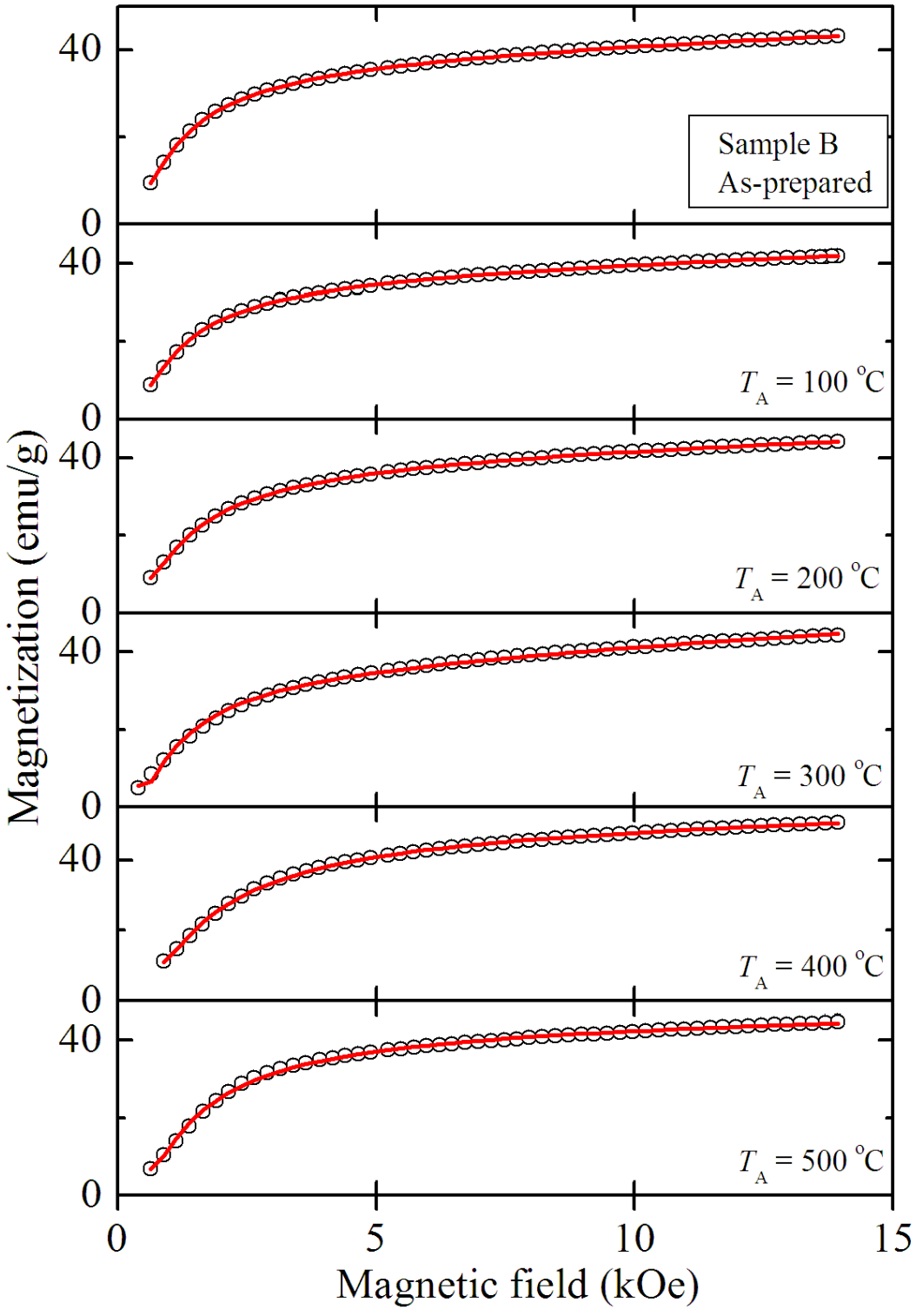

Figure 5.24: Initial magnetizations as a function of magnetic field for Sample B annealed at different temperatures measured at 300 K. The solid lines are the best fit to the data based on equation (2.10.1).

Table 5.7: Coercive fields (H_C), saturation magnetizations (M_S), maximum magnetizations (M_m), remanent magnetizations (M_R), magnetic moment per molecule (μ) and ratio M_R/M_S for the as-prepared samples and samples annealed at 500 and 700 ^{o}C of $Mn_xCo_{1-x}Fe_2O_4$ measured at room temperature.

Sample x	T (^{o}C)	H_C (Oe) ±6	M_S (emu/g) ±0.1	M_m (emu/g) ±0.1	M_R (emu/g) ±0.1	μ (μ_B) ±0.01	M_R/M_S
0.0	200	631	53.8	53.0	13.6	2.23	0.253
0.1	200	92	42.7	59.7	3.4	2.50	0.080
0.2	200	102	41.8	49.5	3.4	2.07	0.081
0.3	200	24	41.8	48.4	1.5	2.02	0.036
0.5	200	257	63.4	67.0	13.4	2.91	0.211
0.6	200	13	51.6	69.9	1.6	2.56	0.031
		±5	±0.1	±0.1	±0.4	±0.01	
0.0	500	980	68.3	63.8	20.9	2.68	0.306
0.1	500	231	43.3	53.4	7.0	2.24	0.162
0.2	500	218	41.7	50.5	6.8	2.11	0.164
0.3	500	78	41.4	53.1	3.8	2.22	0.092
0.5	500	276	57.1	58.7	12.3	2.44	0.215
0.6	500	38	32.3	41.0	1.8	1.70	0.056
		±12	±0.1	±1	±0.3	±0.01	
0.0	700	1123	67.4	57	21.6	2.39	0.320
0.1	700	247	38.4	52	7.0	2.16	0.182
0.2	700	382	41.0	48	9.5	1.99	0.220
0.3	700	212	23.7	44	6.4	1.85	0.270
0.5	700	469	59.0	56	16.5	2.35	0.280
0.6	700	56	20.5	25	4.0	1.06	0.195

Table 5.8: Coercive fields (H_C), saturation magnetizations (M_S), maximum magnetizations (M_m), remanent magnetizations (M_R) and parameters a, b and χ were obtained from empirical law of approach to saturation for Samples A and B annealed at different temperatures and measured at room temperature.

Sample	T ^{o}C	H_C (Oe) ±2	M_S (emu/g) ±0.2	M_m (emu/g) ±0.1	M_R (emu/g) ±0.1	a Oe^{-1} ±0.007	b Oe^{-2} ±0.004	χ ±0.01
A	as-milled	307	37.6	43.1	6.8	0.744	-0.158	0.56
	100	293	29.8	34.7	5.3	0.737	-0.157	0.48
	200	355	33.8	39.9	6.8	0.785	-0.175	0.53
	300	446	42.5	47.6	9.7	0.960	-0.294	0.57
	400	919	44.7	46.9	14.9	1.173	-0.404	0.41
	500	955	44.6	46.4	15.4	1.155	-0.394	0.39
B	as-milled	321	40.0	43.2	7.4	0.805	-0.201	0.42
	100	354	38.4	42.0	7.6	0.811	-0.201	0.42
	200	403	41.0	44.2	8.7	0.917	-0.265	0.42
	300	485	37.3	44.5	9.4	0.863	-0.208	0.71
	400	930	51.0	50.6	16.8	1.229	-0.469	0.27
	500	950	45.2	44.7	16.0	1.060	-0.323	0.18

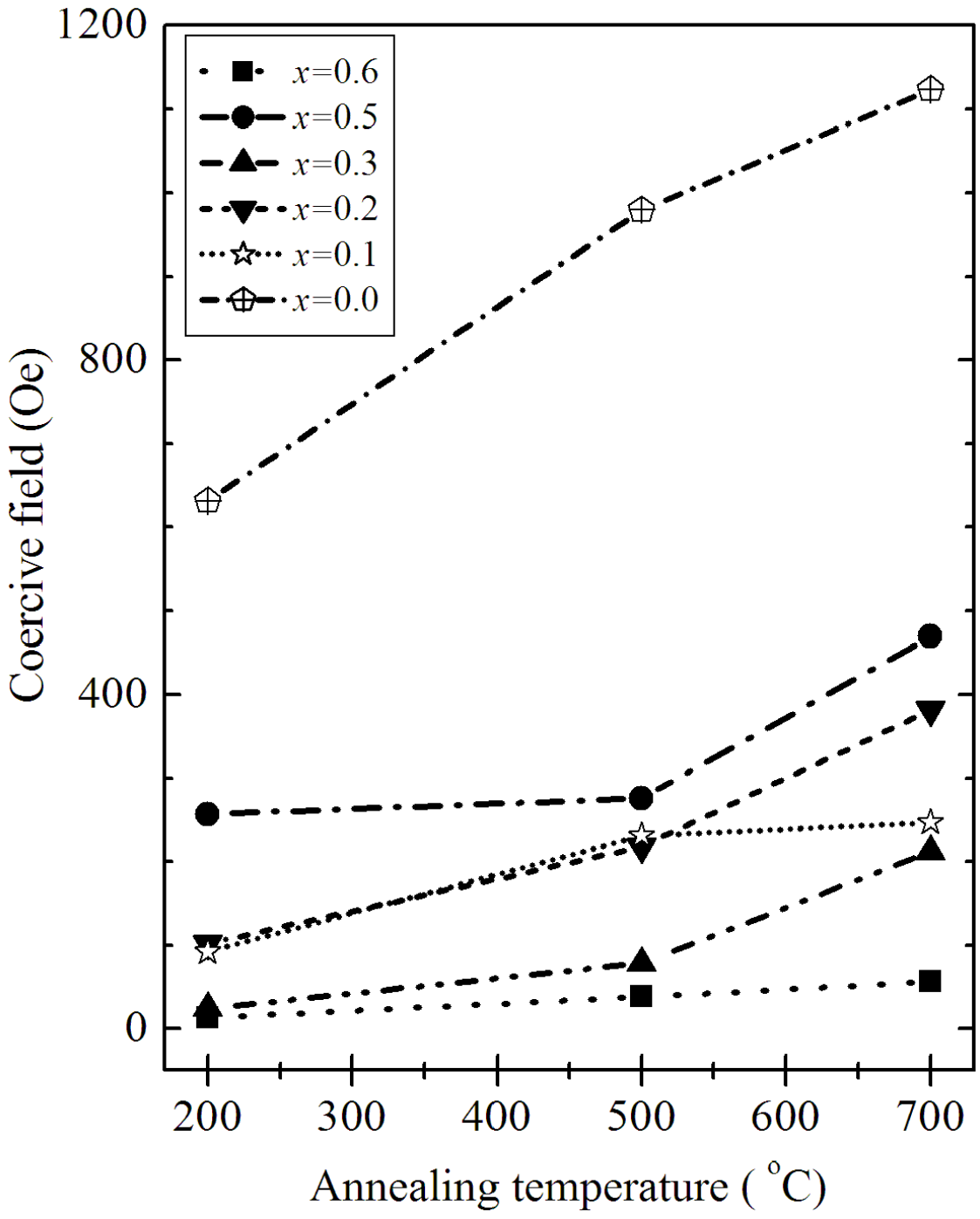

Figure 5.25: Coercive fields for annealed samples of $Mn_xCo_{1-x}Fe_2O_4$ measured at room temperature.

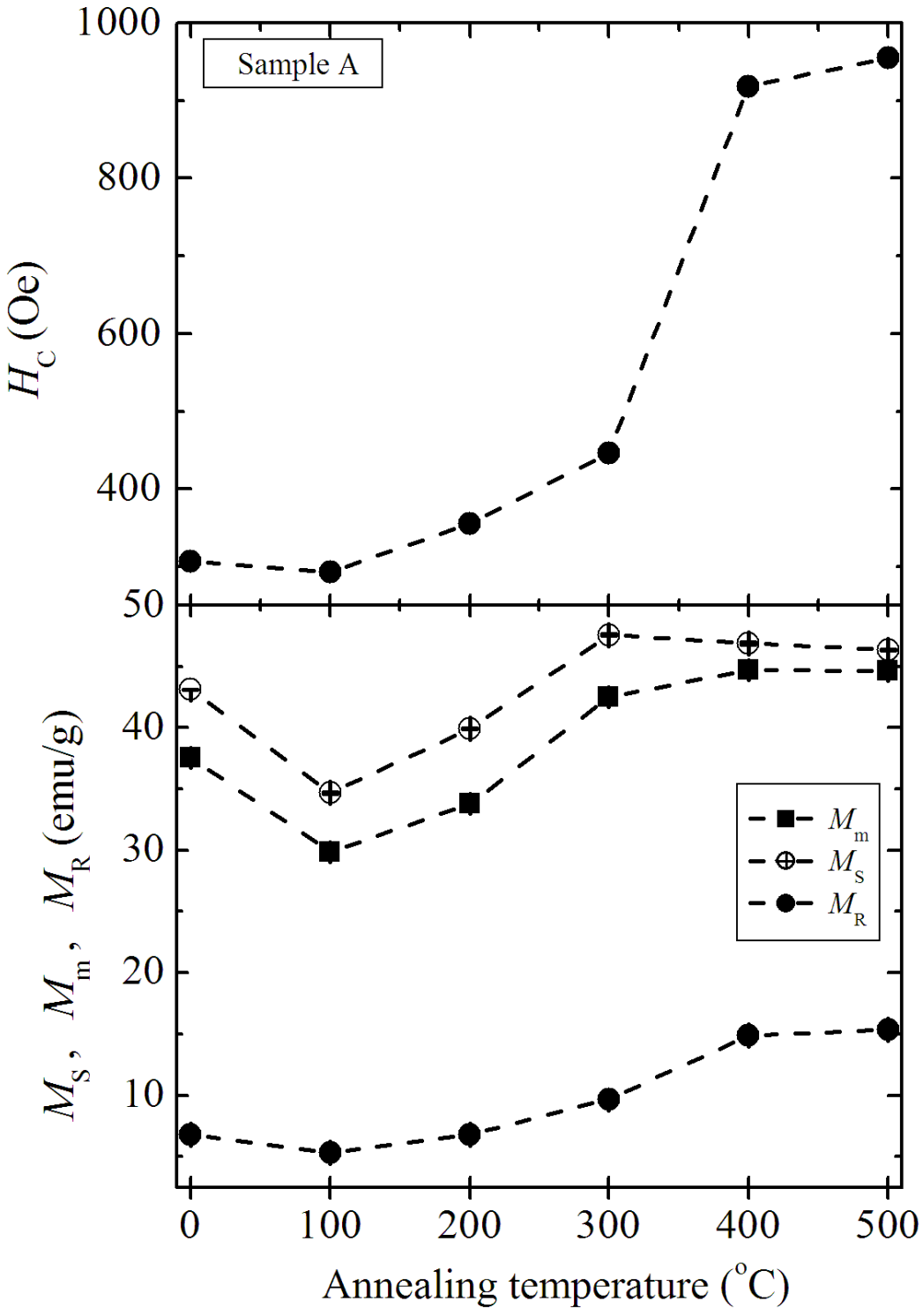

Figure 5.26: Coercive fields, saturation magnetizations and remanent magnetizations for annealed Sample A measured at room temperature.

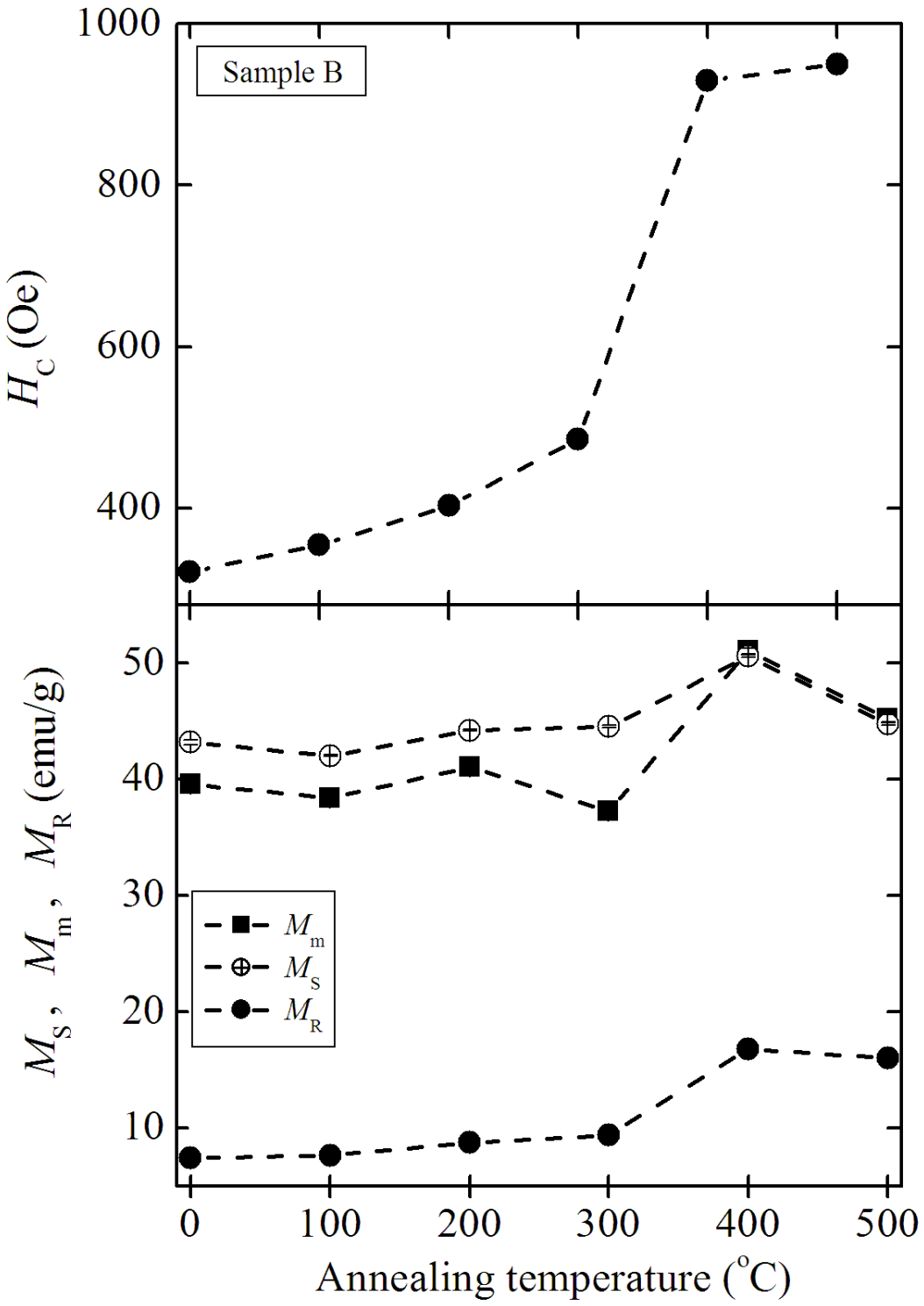

Figure 5.27: Coercive fields, saturation magnetizations and remanent magnetizations for annealed Sample B measured at room temperature.

temperature for $Mn_xCo_{1-x}Fe_2O_4$ samples as shown in Table 5.7 which we attribute to the increase of the average particle diameters [97]. Mn appears to strongly influence spin alignment in domains at higher annealing temperature [6]. Changes in M_S and M_R can be explained on the basis on Néel's theory and distribution of cations at A and B sites [97]. Thermal annealing changes the distribution of metal ions between A and B sites. The spins at A and B sites are assumed to be antiparallel to each other. Within A and B sites we have parallel spins. The net magnetization comes as a result of the uncompensated magnetic moments mediated by A–B superexchange interactions. The Fe^{3+} ions in spinel ferrite strongly prefer the B sites [72]. Relatively higher values of magnetizations are obtained for $x = 0.5$ composition. This is similar to the earlier observation by Shobana et al [73]. In Table 5.7 we also show calculated values of magnetic moments per molecule based on the equation

$$\mu = \frac{M_o M_S}{5585} \tag{5.3.1}$$

where M_o is the molecular mass in grams [96, 155]. Similar values of μ have been reported for Mn- Mg ferrites [57] under the influence of spin disorder due to the effects of sample surfaces. These surface effects govern the magnetic properties of the fine particles. Reduced saturation magnetization for nanoparticles is attributed to the canting of spins on the surface which weakens the exchange coupling [155]. Evidence of spin-spin canting can also be deduced from the Mössbauer data.

Field cooling (FC) and zero field cooling (ZFC) magnetizations as a function of temperature for both samples $x = 0.1$ and $x = 0.5$ are shown in Figures 5.28 and 5.29 respectively. The lower curve for each sample in both Figures correspond to ZFC and the upper curve to FC. In ZFC, a sample is cooled in zero field from room temperature to the lowest temperature at about 2 K where a measuring field is applied. The sample is cooled and magnetization recorded in the same measuring field in FC. The magnetization measurements were performed with increasing temperature from 2 K to about 380 K in external magnetic fields of 0.05 kOe, 0.20 kOe and 10.0 kOe. The magnetization for the FC curves decrease continuously with increasing temperature.

ZFC and FC magnetizations coincide at a spin freezing temperature which de-

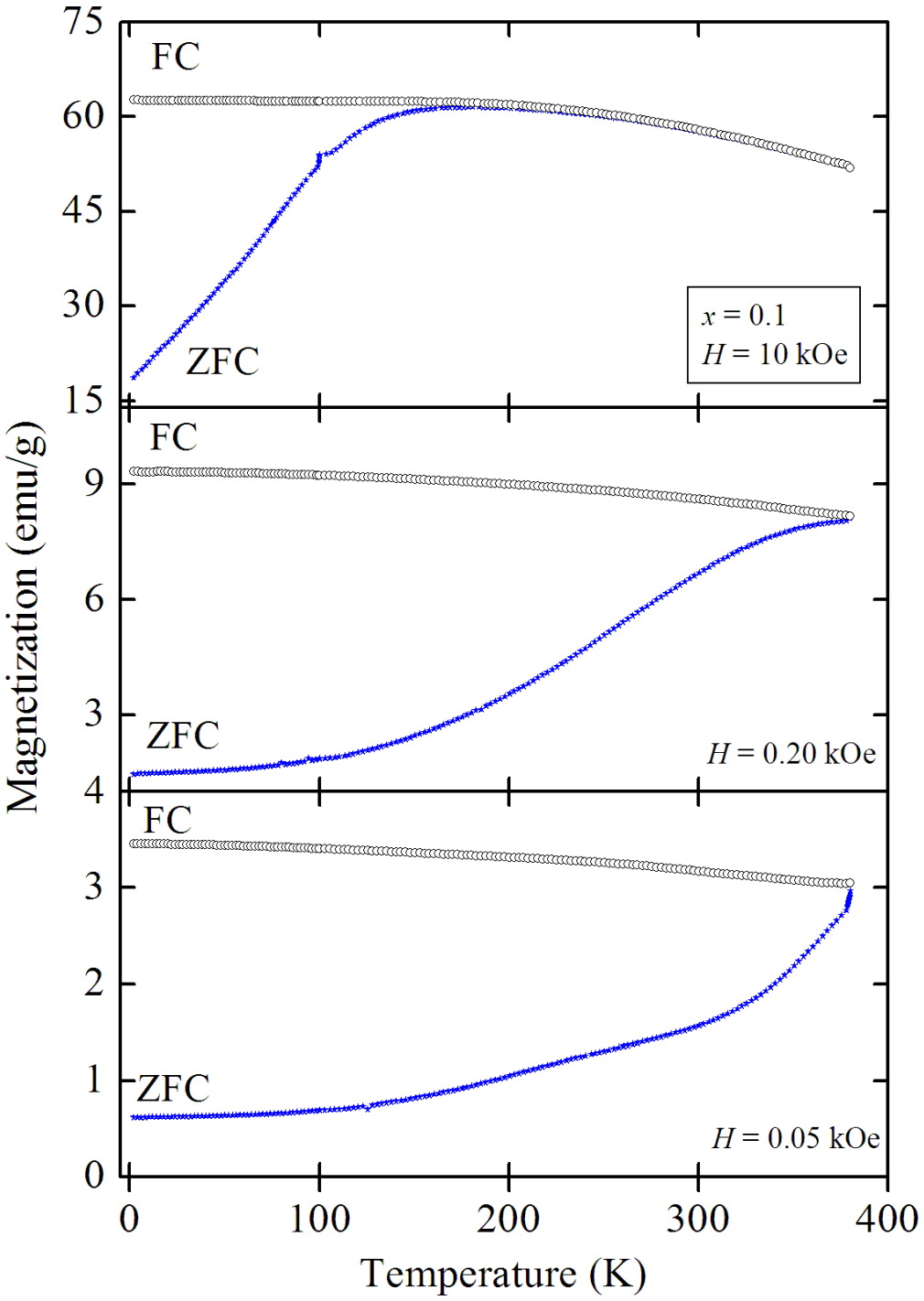

Figure 5.28: Temperature dependence of ZFC and FC magnetizations for the as-prepared sample of $Mn_{0.1}Co_{0.9}Fe_2O_4$ measured in different static applied magnetic fields.

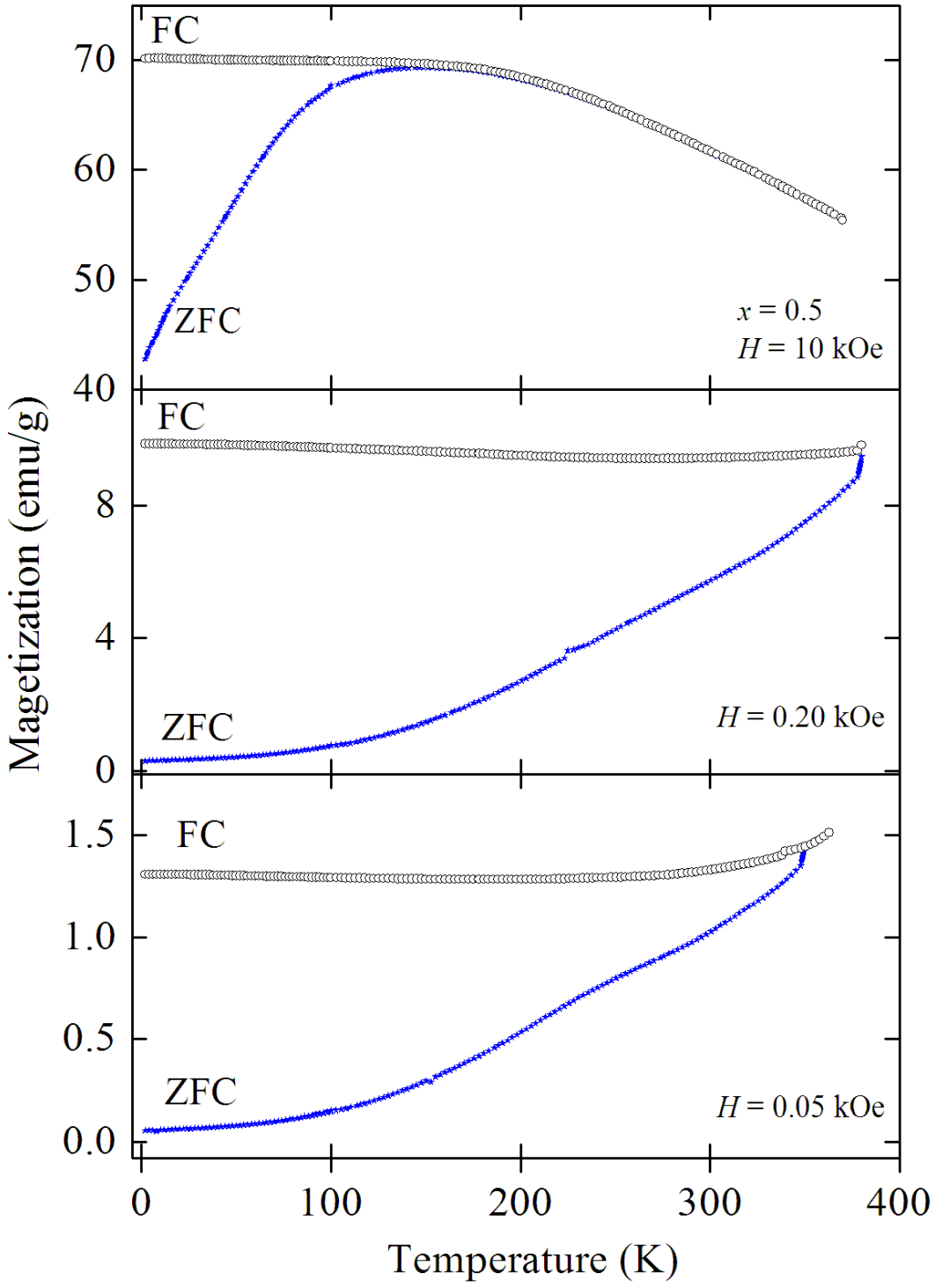

Figure 5.29: Temperature dependence of ZFC and FC magnetizations for the as-prepared sample of $Mn_{0.5}Co_{0.5}Fe_2O_4$ measured in different static applied magnetic fields.

pends on the applied field. ZFC magnetization curves increase gradually with increasing temperature and reach maximum values at blocking temperatures of about 150 K and 200 K for $x = 0.5$ and 0.1 respectively. The width of the peak in the ZFC curve is associated with particle size distribution [156]. A particle with a particular size has a certain blocking temperature. Wide peaks are observed in our samples which indicate a wide distribution of particle sizes as confirmed by TEM measurements. The slow decrease in magnetization with further increase in temperature is associated with disordering of particle spins. One of the characteristic features of the plots in Figures 5.28 and 5.29 are reduced magnetizations at low temperature for ZFC samples. Similar behaviour of FC and ZFC magnetization has been considered to be spin-glass like behaviour [157].

In Figures 5.30 and 5.31 we present the hysteresis loops for the as-prepared $Mn_{0.1}Co_{0.9}Fe_2O_4$ and $Mn_{0.5}Co_{0.5}Fe_2O_4$ samples measured at 4, 50, 100, 200 and 300 K in applied magnetic fields of up to 50 kOe using a SQUID magnetometer. The coercive fields, saturation magnetizations and remanent magnetizations were deduced from the hysteresis loops. The results are tabulated in Table 5.9. A low coercive field at 300 K suggests superparamagnetic-like behaviour of the nanoparticles. The hysteresis loops below at 100 K are distorted. This has been attributed to the freezing of disordered spin states [104]. The saturation magnetizations have been taken at the highest measured field. In Figure 5.32 we show the variations of coercive field, saturation magnetization and remanent magnetization as a function of measuring temperature. The samples become magnetically harder at lower temperature due to the freezing of spins, which makes magnetization reversal harder to achieve. Hence, there is increased coercive field at lower temperature. As expected, the saturation magnetization and remanent magnetization decrease with increasing temperature. The squareness of the hysteresis loops (M_R/M_S) (Table 5.9) for both samples $x = 0.1$ and $x = 0.5$ decrease with increasing temperature. Figures 5.33 and 5.34 show the fits to the coercive field data for the as-prepared $Mn_{0.1}Co_{0.9}Fe_2O_4$ and $Mn_{0.5}Co_{0.5}Fe_2O_4$ nanoferrites. The temperature dependence of the coercive fields follows the Kneller's law (equation (2.10.2)) [97]. The coercive field data is fitted over the entire temperature range with $\alpha = 1/2$. The temperature depen-

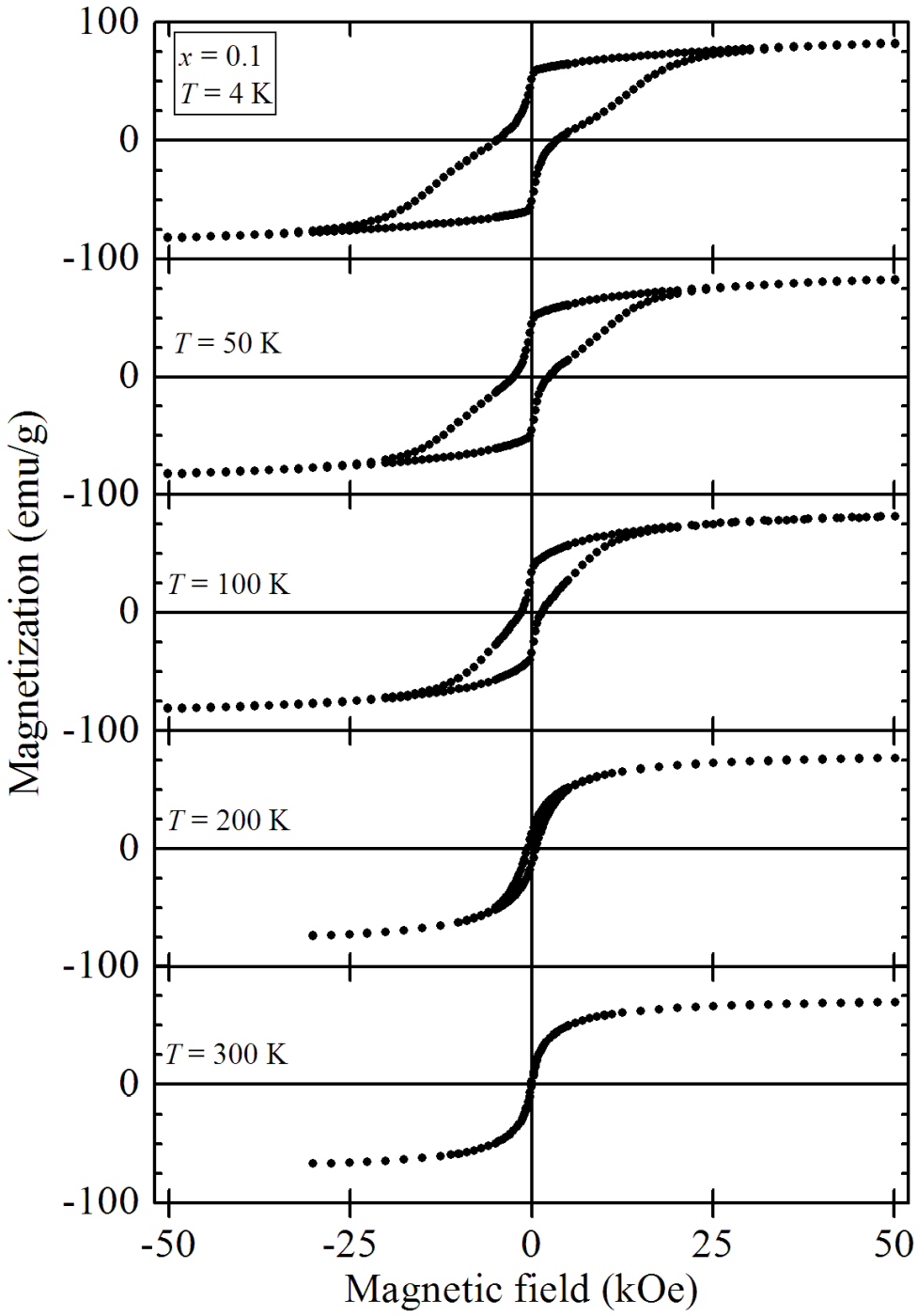

Figure 5.30: Hysteresis loops for the as-prepared sample of $Mn_{0.1}Co_{0.9}Fe_2O_4$ recorded at different isothermal temperatures.

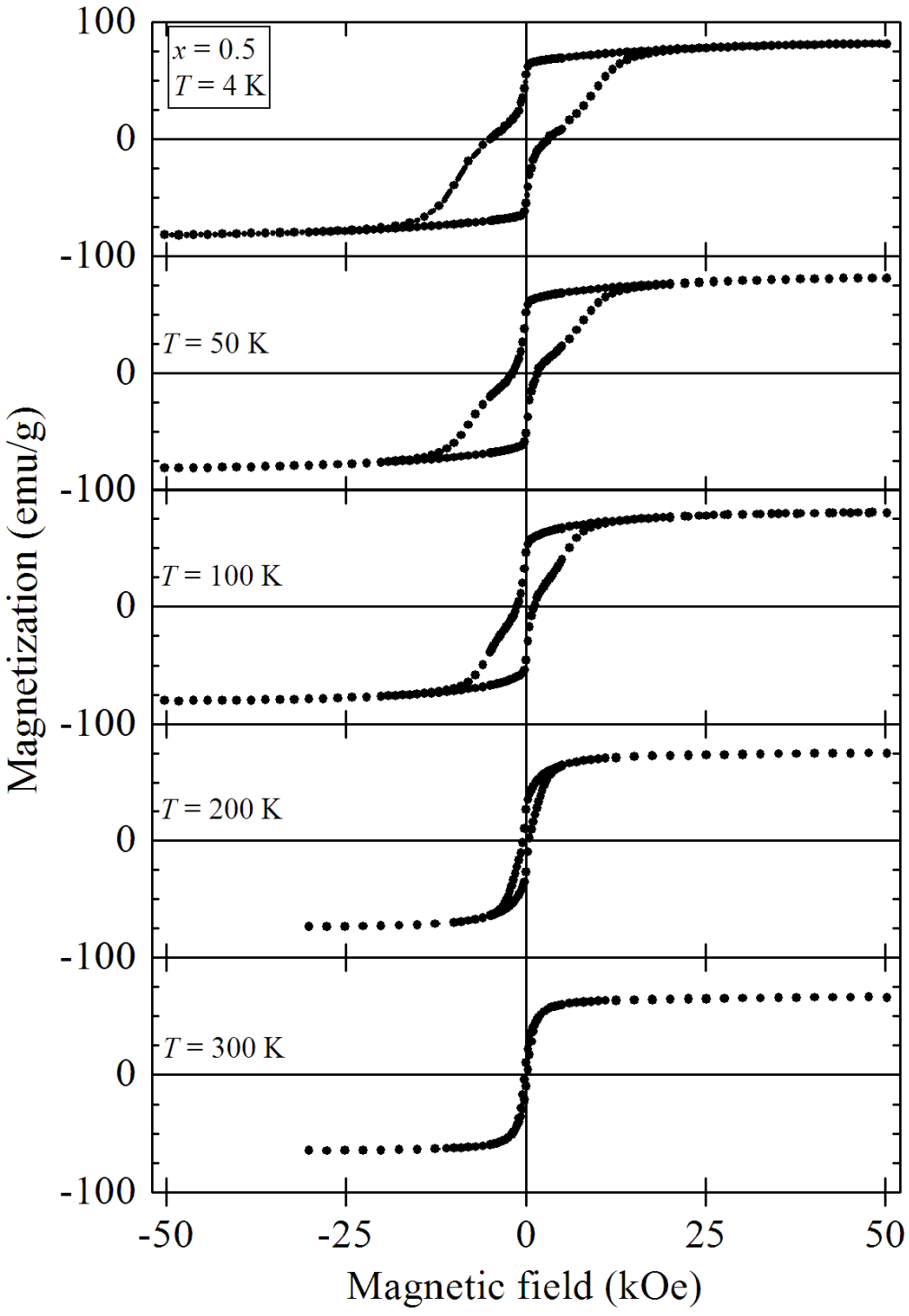

Figure 5.31: Hysteresis loops for the as-prepared sample of $Mn_{0.5}Co_{0.5}Fe_2O_4$ recorded at different isothermal temperatures.

Table 5.9: Coercive fields (H_C), saturation magnetizations (M_S), remanent magnetizations (M_R), magnetic moment per molecule (μ) and ratio M_R/M_S for the as-prepared $Mn_xCo_{1-x}Fe_2O_4$ samples measured at different isothermal temperatures.

Sample x	T (K)	H_C (Oe) ± 1	M_S (emu/g) ± 0.1	M_R (emu/g) ± 0.3	M_R/M_S	μ (μ_B) ± 0.04
0.1	4	1997	82.2	51.6	0.63	3.45
”	50	1541	82.1	44.3	0.54	3.44
”	100	1029	81.7	34.0	0.42	3.43
”	200	565	77.1	12.7	0.16	3.23
”	300	58	69.4	2.2	0.03	2.91
0.5	4	1449	81.7	54.8	0.72	3.39
”	50	1115	81.5	51.5	0.63	3.38
”	100	962	80.4	45.8	0.57	3.35
”	200	474	74.9	26.7	0.36	3.12
”	300	174	66.1	10.2	0.15	2.75

dence of magnetizations are shown in Figure 5.35. The saturation magnetizations vary according to the modified Bloch's law (equation (2.8.6)) where $\beta > 1.5$. This is associated with single-domain nanoparticles [158, 159] due to the confinement effects of the spin-wave spectra for magnetic clusters. The Bloch's equation appears to fit the saturation magnetization data over the entire temperature range with values of β equal to 2.3±0.2 and 2.1±0.1 for $Mn_{0.1}Co_{0.9}Fe_2O_4$ and $Mn_{0.5}Co_{0.5}Fe_2O_4$ respectively.

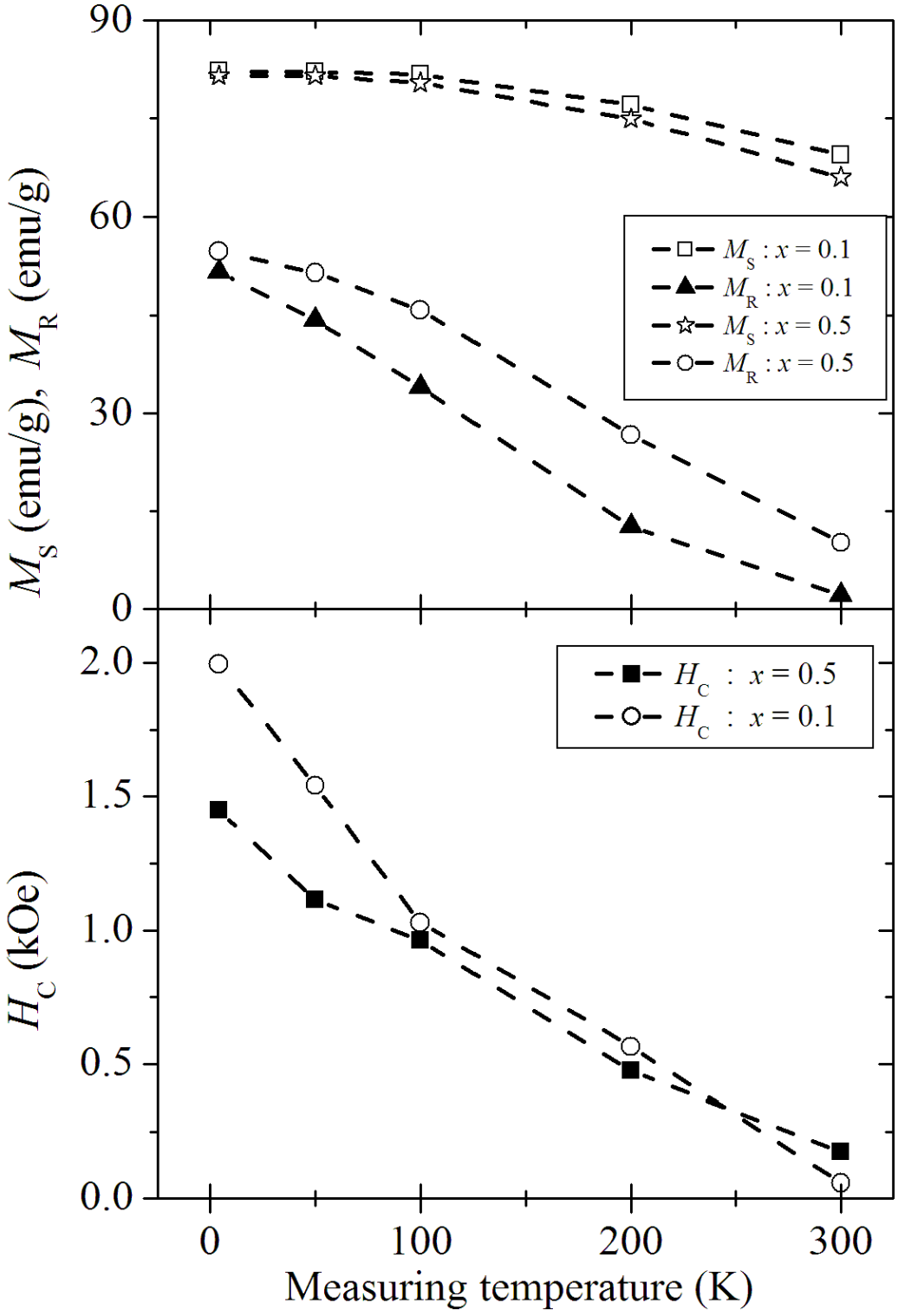

Figure 5.32: Variation of coercive fields, saturation magnetizations, maximum magnetizations and remanent magnetizations with measuring temperature for $Mn_xCo_{1-x}Fe_2O_4$ samples.

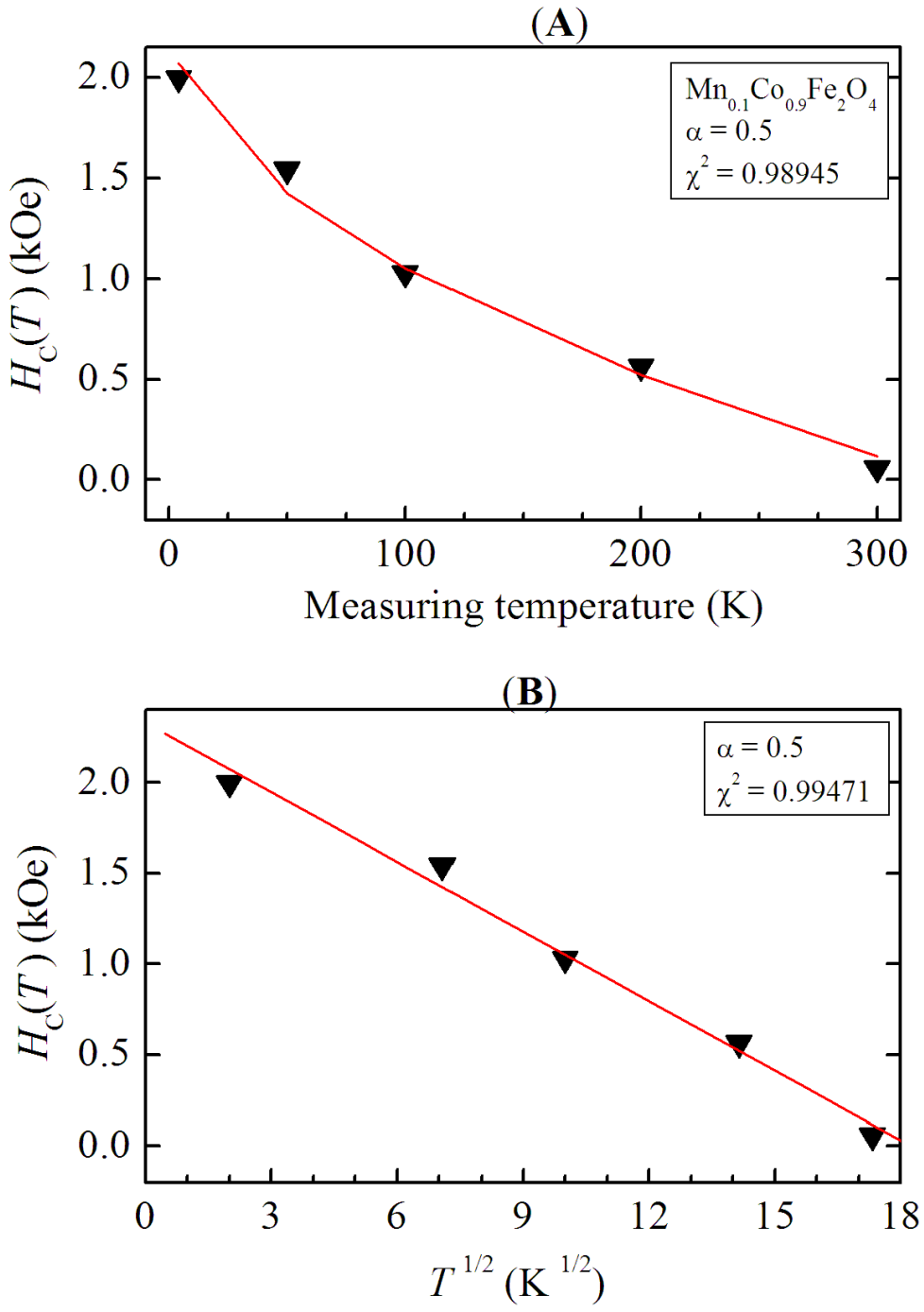

Figure 5.33: Coercive fields for the as-prepared $Mn_{0.1}Co_{0.9}Fe_2O_4$ sample measured at different temperatures. The solid lines are best fits to the data based on the Kneller's law.

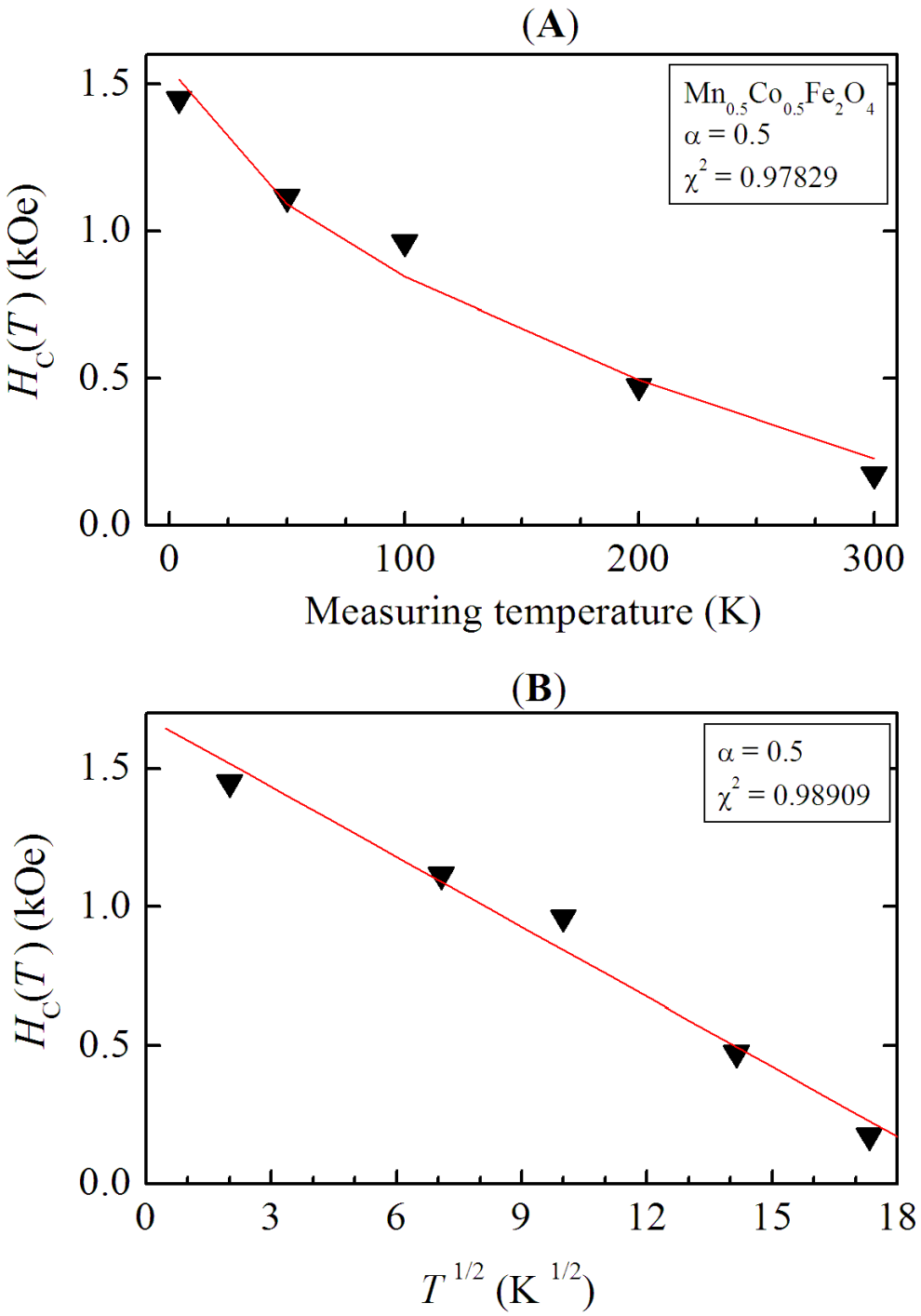

Figure 5.34: Coercive fields for the as-prepared $Mn_{0.5}Co_{0.5}Fe_2O_4$ sample measured at different temperatures. The solid lines are best fits to the data based on the Kneller's law.

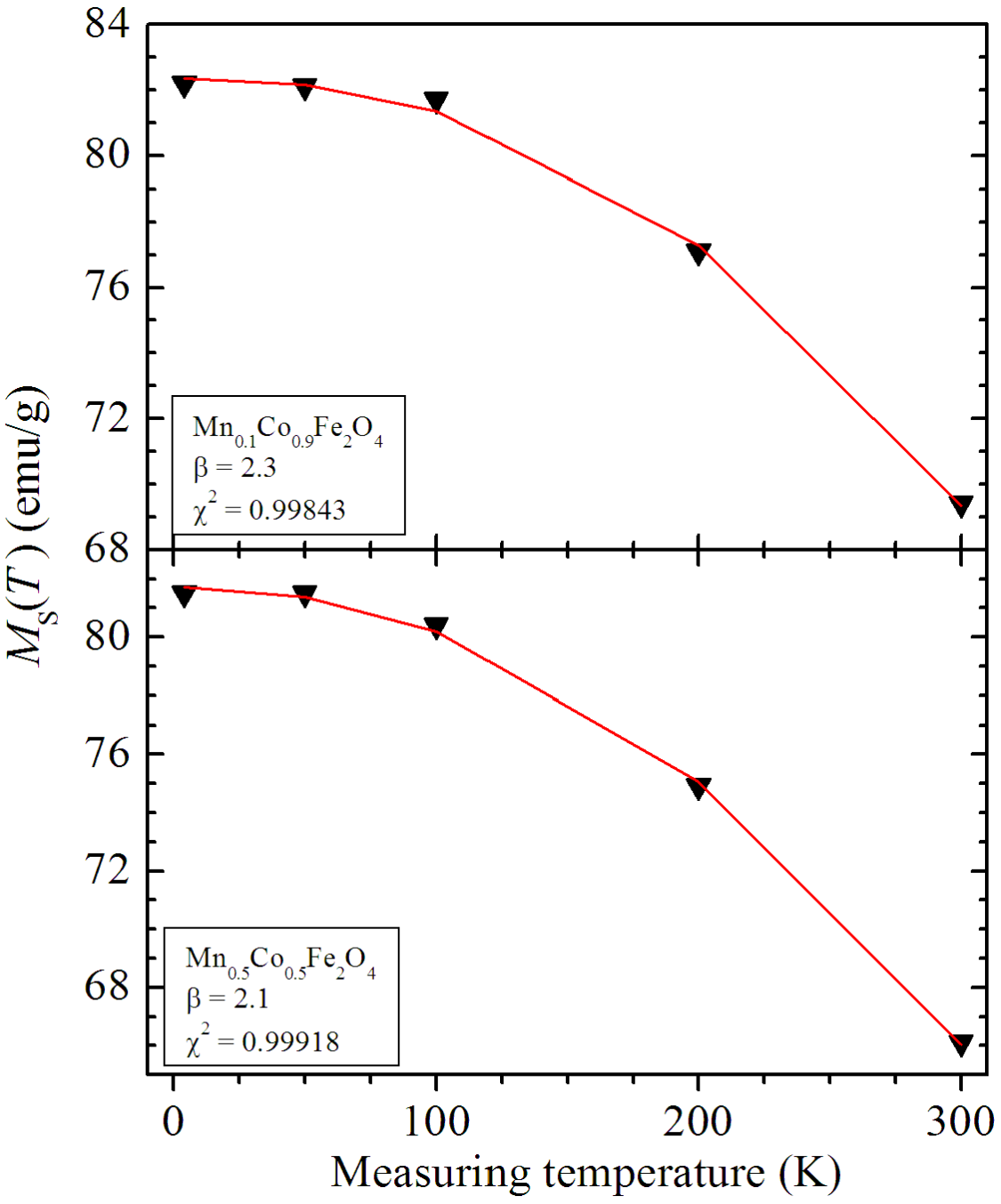

Figure 5.35: Saturation magnetizations for the as-prepared $Mn_xCo_{1-x}Fe_2O_4$ samples measured at different temperatures. The solid lines are best fits to the data based on the modified Bloch's law.

5.4 Electrical resistivity

5.4.1 Introduction

Ferrite materials have high resistance because the metal ions are isolated by oxygen ions from each other. They have been known to exhibit semiconductor behaviour based on a hopping mechanism which obeys the Arrhenius equation [142] where the resistivity at a finite temperature T varies as

$$\rho(T) = \rho_o \exp\left(\frac{E_{a1}}{k_B T}\right). \tag{5.4.1}$$

E_{a1} is the activation energy which is the minimum energy needed for an electron to jump from one ion to a neighbouring ion and ρ_o is a constant. The activation energy depends on the magnetic state of a material. In the ordered state in a ferromagnet, the activation energy is lower compared to the value for a paramagnet due to the effect of magnetic spin-disorder. In the paramagnetic state, the sintering temperature decreases the concentration of the current carriers and this changes the conduction mechanism [142].

One way in which the ferrite electrical resistivity can be explained is through the Verwey-de Boer mechanism [84, 160]. In this mechanism, the electrons are exchanged between the ions of different valence states amongst the same element in a compound. Increasing the measuring temperature may also lead to a random distribution of the ions over equivalent crystallographic lattice sites A or B. The B site sublattices are known to be responsible for electrical resistivity in ferrites [161]. Therefore, partial reduction of Fe^{3+} to Fe^{2+}, Mn^{3+} to Mn^{2+} or Co^{3+} to Co^{2+} can be expected to occur in $Mn_xCo_{1-x}Fe_2O_4$. The variation of the resistivity with composition in ferrites can therefore be explained as an electron exchange transfer between the same elements [84, 162]. The resistivity also depends on the sintering conditions and the number of ions which form during the preparation of such samples [160]. Fe^{2+}, Co^{3+} and Mn^{3+} are formed during the sintering process based on the Verwey-de Boer mechanism [161].

The electrical resistivity can also be explained on the basis of the tunnelling effect of charge carriers. In this process, the conductivity in granular materials

occurs because of the transport of the electrical charge by tunnelling between grains. The charge carriers are generated from the transfer of electrons from neutral to neighbouring charged grains. The possible polaronic conduction can therefore be written as: $Fe^{2+} \longleftrightarrow Fe^{3+}+e^{-}$, $Mn^{2+} \longleftrightarrow Mn^{3+}+e^{-}$ and $Co^{2+} \longleftrightarrow Co^{3+} + e^{-}$. The electrical transport properties of the metal-insulator granular samples are usually discussed under two different physical conditions [79, 143] namely at "high-field and low-temperature" and at "low-field and high-temperature". In this study, we only considered the conductivity at "low-field and high-temperature". The variation of the tunnelling resistivity with temperature in granular metals strongly depends on the electrostatic charge energy which is needed to generate the positive and negative charged grains. In this system, the charge carriers can be thermally activated at high temperature. Sheng et al [79] have suggested that the temperature dependence of resistivity due to the tunnelling between neighbouring grains can be expressed by [79, 80, 143, 163]

$$\rho(T) = \rho_o \exp\left[2\left(\frac{E_{a2}}{k_B T}\right)^{1/2}\right] \tag{5.4.2}$$

where E_{a2} is the tunnelling activation energy between grains. The temperature variation of resistivity of our samples will therefore be tested against equations (5.4.1) and (5.4.2).

5.4.2 Results and discussion

The variation of resistivity according to equation (5.4.1) is similar to that of semiconductor materials. This is associated with the hopping movements of electrons or holes between divalent and trivalent metal cations. In the present case for $Mn_xCo_{1-x}Fe_2O_4$ oxides, the hopping is suspected to be between Fe^{2+} and Fe^{3+} (or Mn^{2+} and Mn^{3+} or Co^{2+} and Co^{3+}) ions through intervening oxygen anions. The plots of $\ln\rho$ versus T^{-1} for $Mn_xCo_{1-x}Fe_2O_4$ are given in Figures 5.36. Good linear fits are obtained to the fitted data. Plots of $\ln\rho$ versus $T^{-1/2}$ are shown in Figure 5.37 which have slightly better correlation coefficients to the plots in Figure 5.36. The activation energies E_{a1} and E_{a2} deduced from linear fits to the data in Figure 5.36 and Figure 5.37 are given in Table 5.10. Two distinct sets of plots at

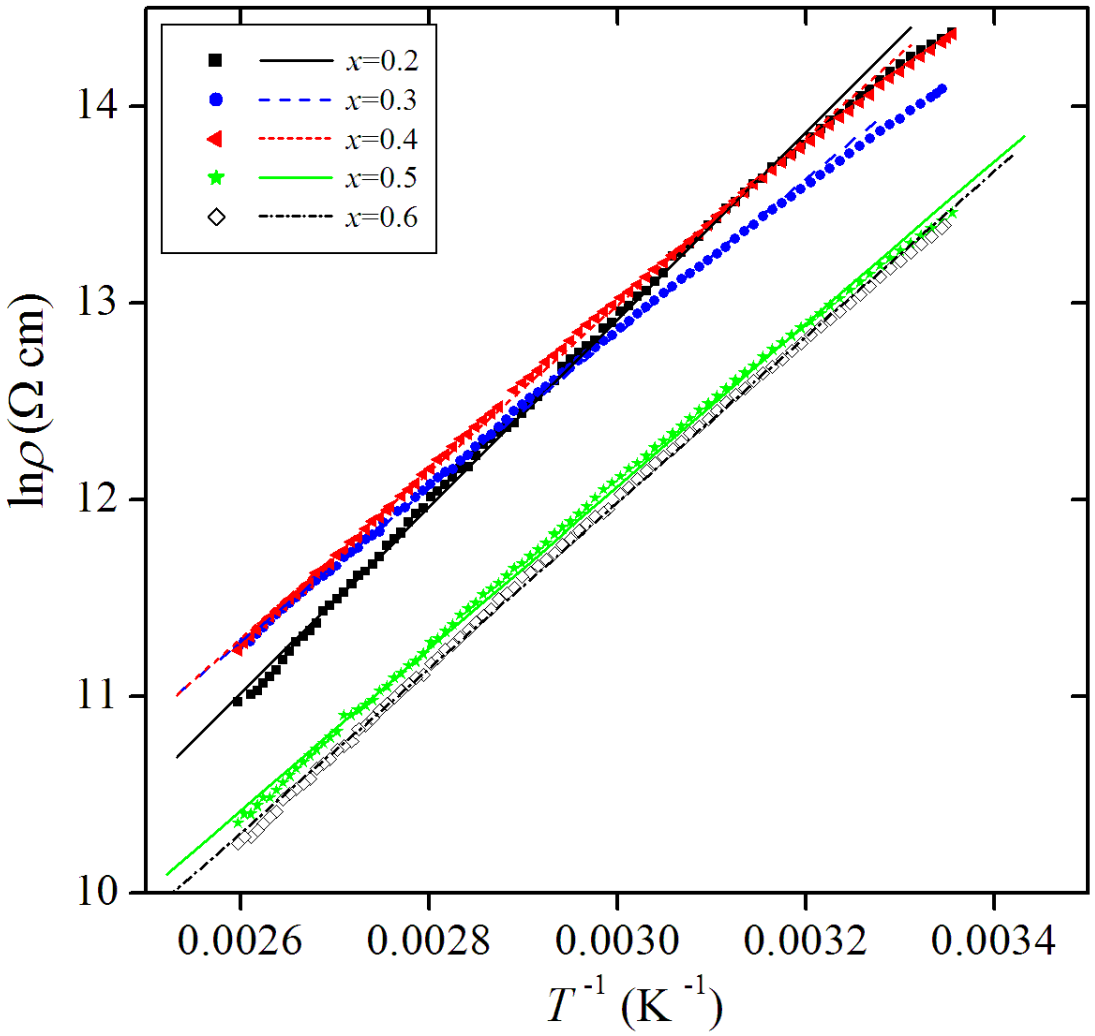

Figure 5.36: $\ln \rho$ versus T^{-1} for $Mn_xCo_{1-x}Fe_2O_4$ samples synthesized by glycol-thermal reaction. The lines are best linear fits to the data. Pellets were annealed at 1050 ^{o}C.

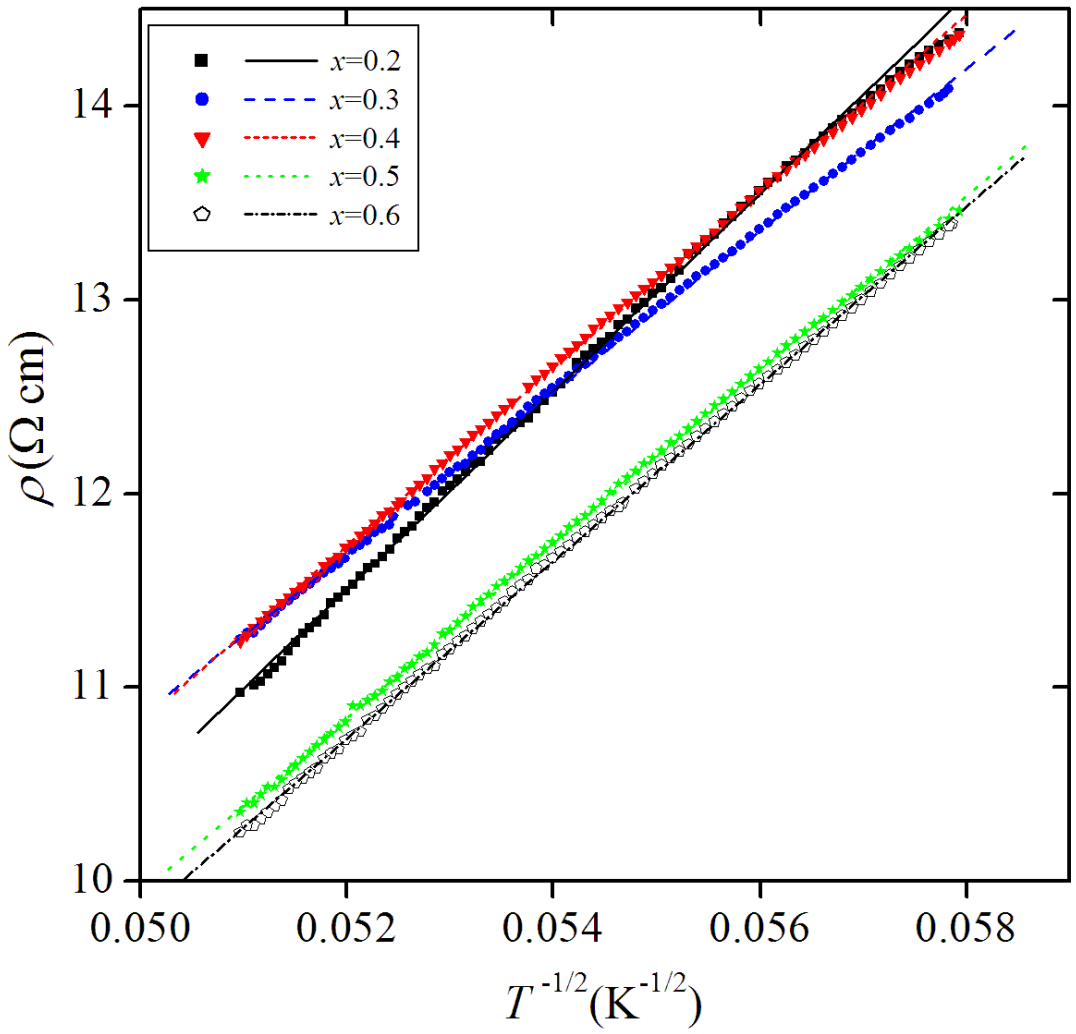

Figure 5.37: $\ln \rho$ versus $T^{-1/2}$ for $Mn_xCo_{1-x}Fe_2O_4$ samples synthesized by glycol-thermal reaction. The lines are best linear fits to the data. Pellets were annealed at 1050 ^{o}C.

Table 5.10: Activation energies for $Mn_xCo_{1-x}Fe_2O_4$ deduced from the best fits of equations (5.4.1) and (5.4.2).

Sample	E_{a1} (eV)	E_{a2} (eV)
x	± 0.001	± 0.02
0.2	0.398	5.47
0.3	0.330	3.75
0.4	0.358	4.42
0.5	0.355	4.33
0.6	0.366	4.50

higher ($x = 0.2, 0.3, 0.4$) and lower ($x = 0.5, 0.6$) values of resistivities can be identified in Figures 5.36 and 5.37. We suspect this to be more an artefact of the surfaces of the pellets probed than a composition dependence. For this set of measurements we did not distinguish which surfaces of the pellet were being probed.

We have therefore performed systematic measurements of the resistivity on a single pellet where we take into account the surface that is being probed. The two surfaces of a pellet slightly differ in appearance. On surface is on the shiny side (face 1) and the other is on the dull side (face 2). Different characteristics of the two surfaces suggest slight non-uniformity in the compaction of the pellets. This suggests a concentration gradient across the thickness of the pellet. Figures 5.38 – 5.44 show the variations of electrical resistivity as a function of T^{-1} and $T^{-1/2}$ for a pellet of a $Mn_{0.5}Co_{0.5}Fe_2O_4$ sample which was annealed for 6 hours at 600, 700, 800, 900, 1000, 1050 and 1100 ^{o}C. The values of E_{a1} and E_{a2} deduced from the slopes in Figures 5.38 –5.44 are given in Table 5.11 respectively. The measurements were recorded on the same pellet following each annealing procedure. The resistivity measurements appear to distinguish the characteristics of the two surfaces. Higher resistivities were obtained when the dull surface (face 2) was probed. Therefore any systematic measurements on different pellets must take into account the surfaces of the pellets. In Figure 5.45 we show the activation energies E_{a1} and E_{a2} plotted as a function

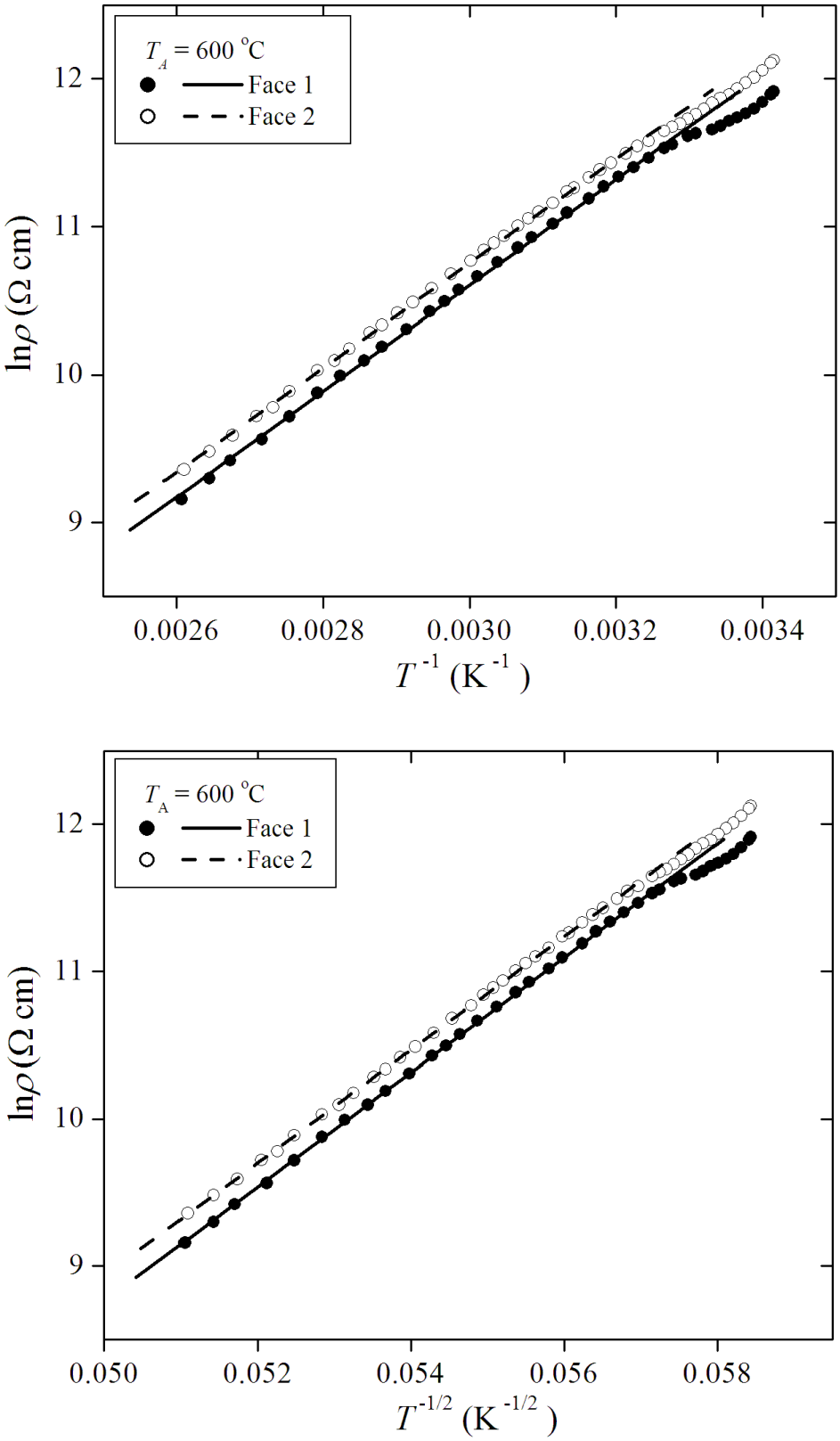

Figure 5.38: $\ln \rho$ versus T^{-1} and $T^{-1/2}$ for a milled $Mn_{0.5}Co_{0.5}Fe_2O_4$ sample. The lines are best linear fits to the data. The pellet was annealed at 600 ^{o}C.

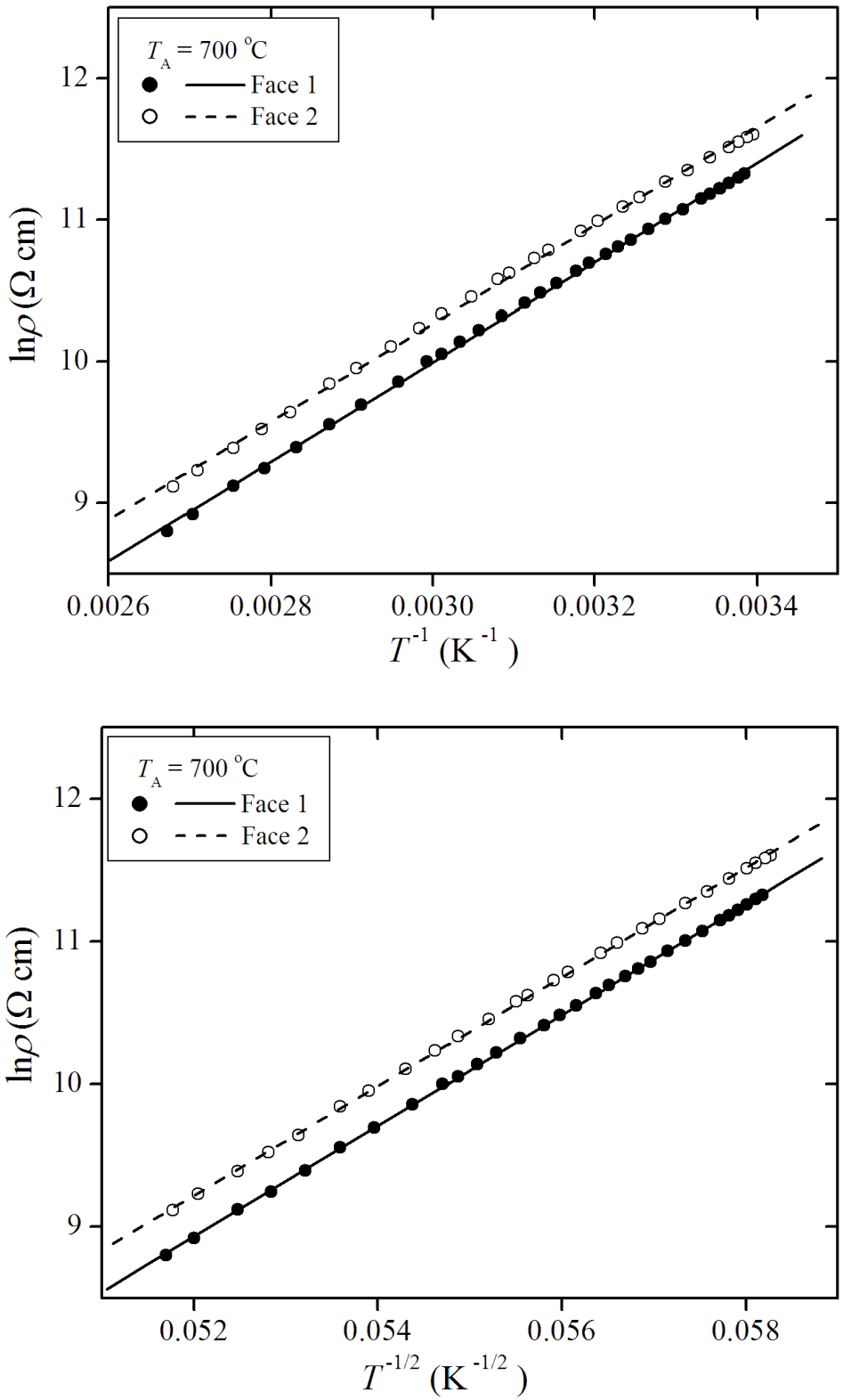

Figure 5.39: $\ln \rho$ versus T^{-1} and $T^{-1/2}$ for a milled $Mn_{0.5}Co_{0.5}Fe_2O_4$ sample. The lines are best linear fits to the data. The pellet was annealed at 700 ^{o}C.

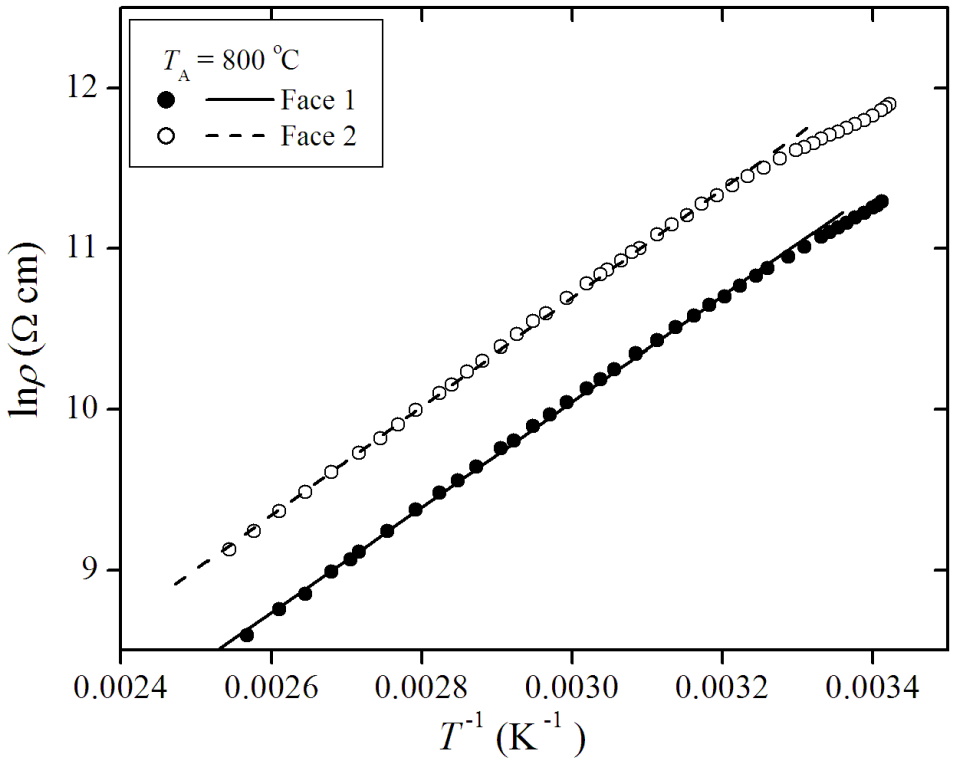

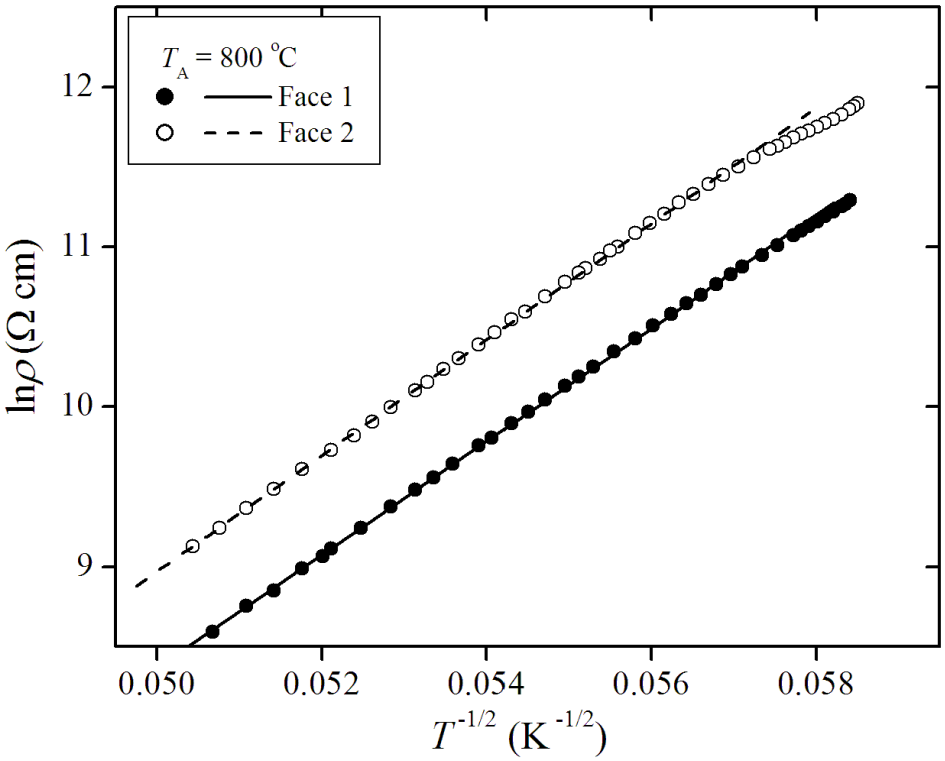

Figure 5.40: $\ln \rho$ versus T^{-1} and $T^{-1/2}$ for a milled $Mn_{0.5}Co_{0.5}Fe_2O_4$ sample. The lines are best flinear fits to the data. The pellet was annealed at 800 ^{o}C.

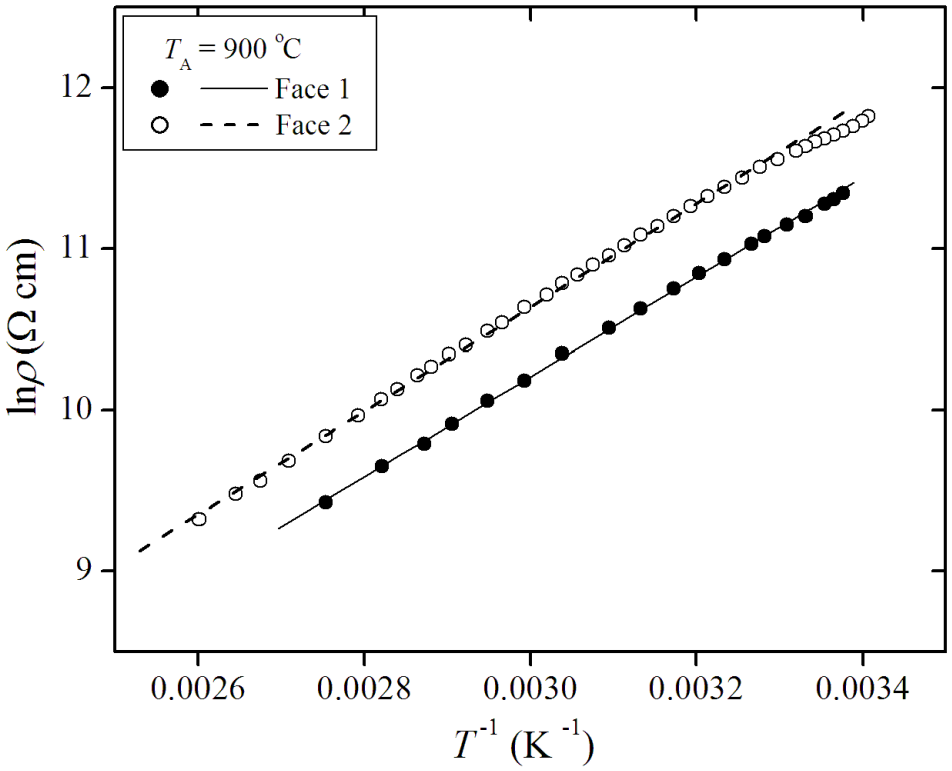

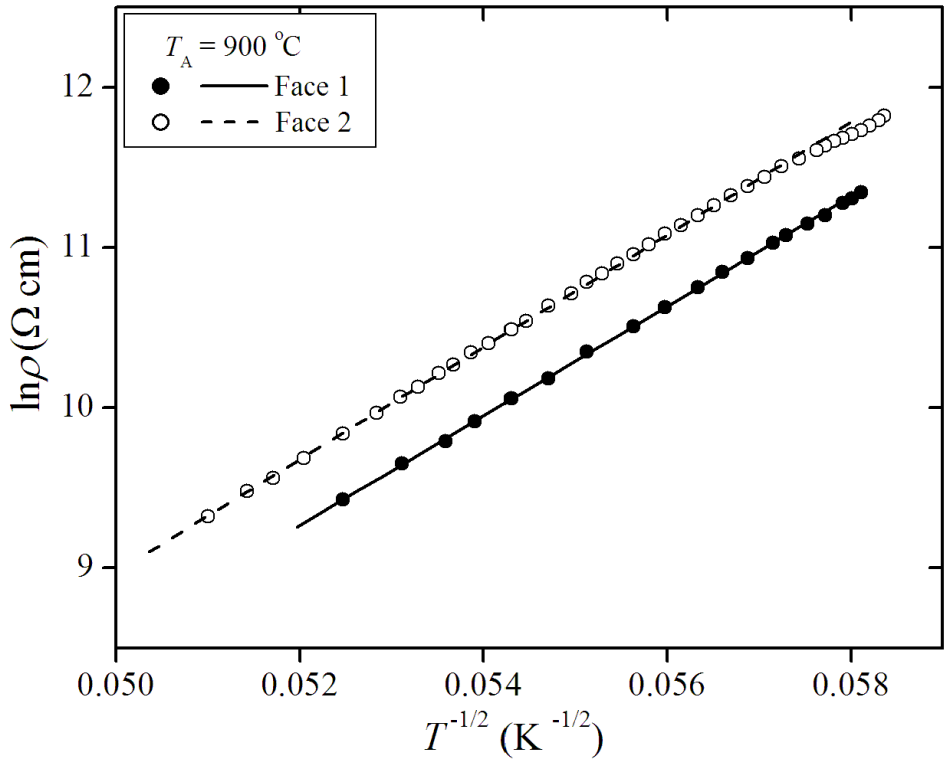

Figure 5.41: $\ln \rho$ versus T^{-1} and $T^{-1/2}$ for a milled $Mn_{0.5}Co_{0.5}Fe_2O_4$ sample. The lines are best linear fits to the data.The pellet was annealed at 900 ^{o}C.

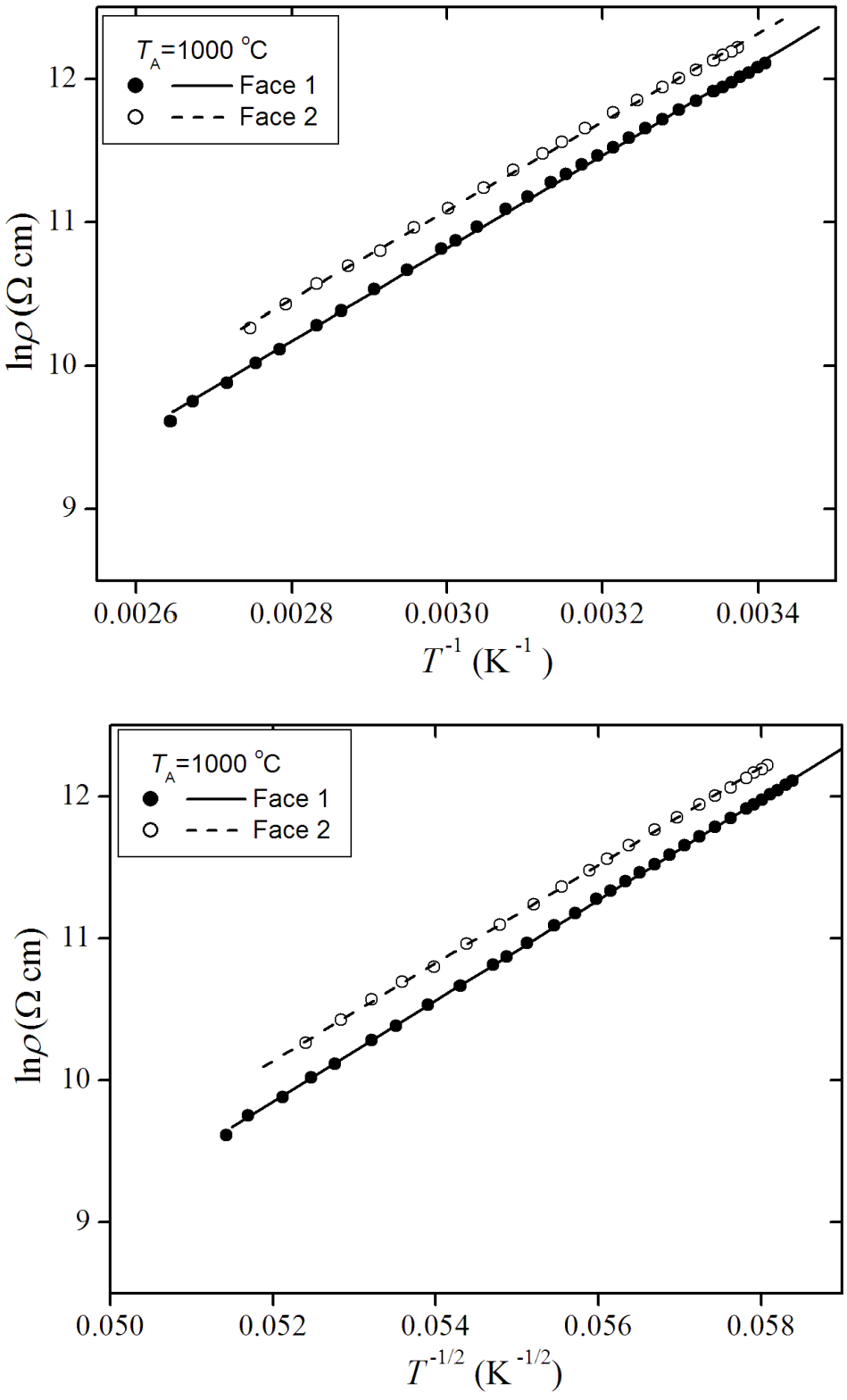

Figure 5.42: $\ln \rho$ versus T^{-1} and $T^{-1/2}$ for a milled $Mn_{0.5}Co_{0.5}Fe_2O_4$ sample. The lines are best linear fits to the data. The pellet was annealed at 1000 ^{o}C.

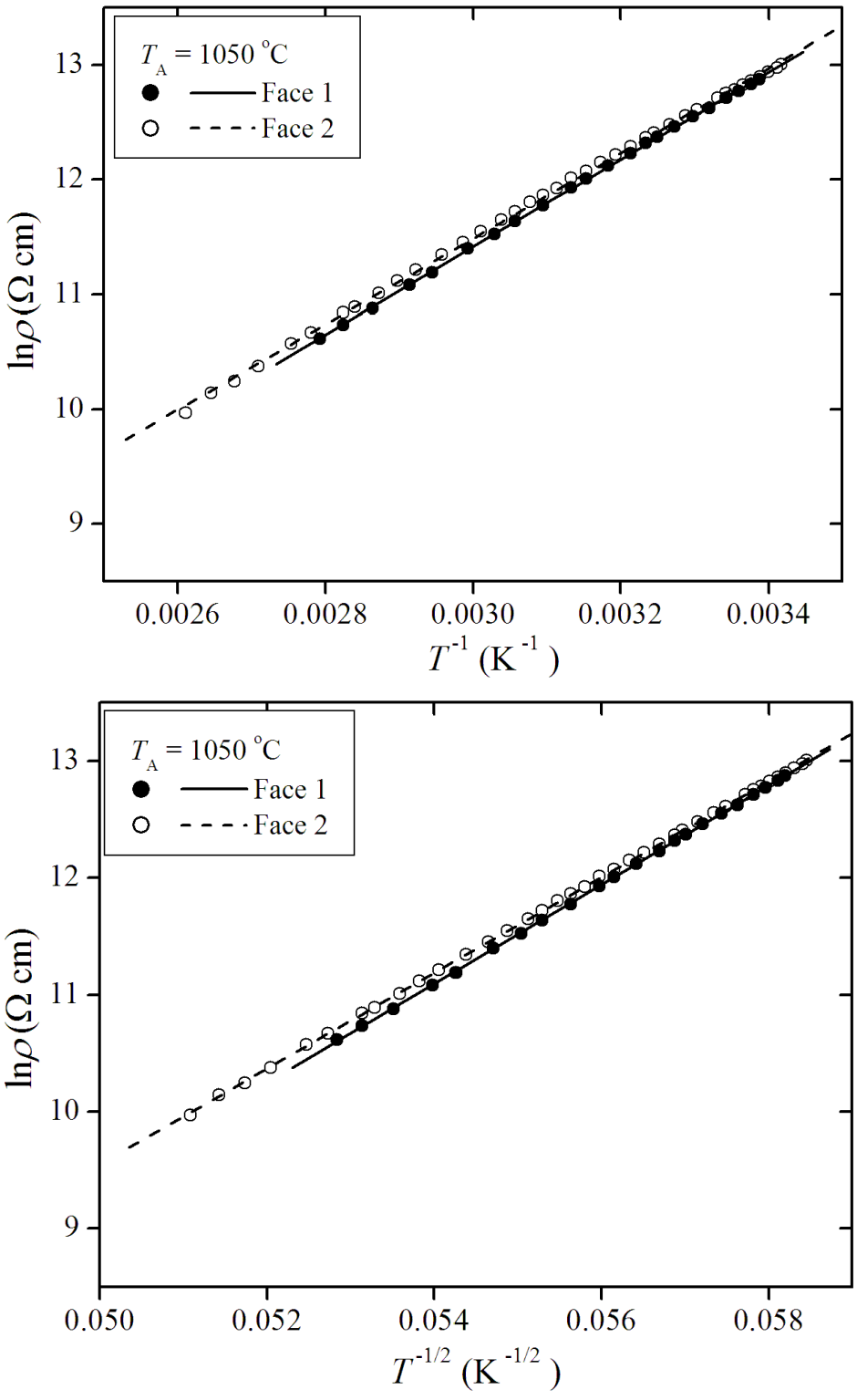

Figure 5.43: $\ln \rho$ versus T^{-1} and $T^{-1/2}$ for a milled $Mn_{0.5}Co_{0.5}Fe_2O_4$ sample. The lines are best linear fits to the data.The pellet was annealed at 1050 ^{o}C.

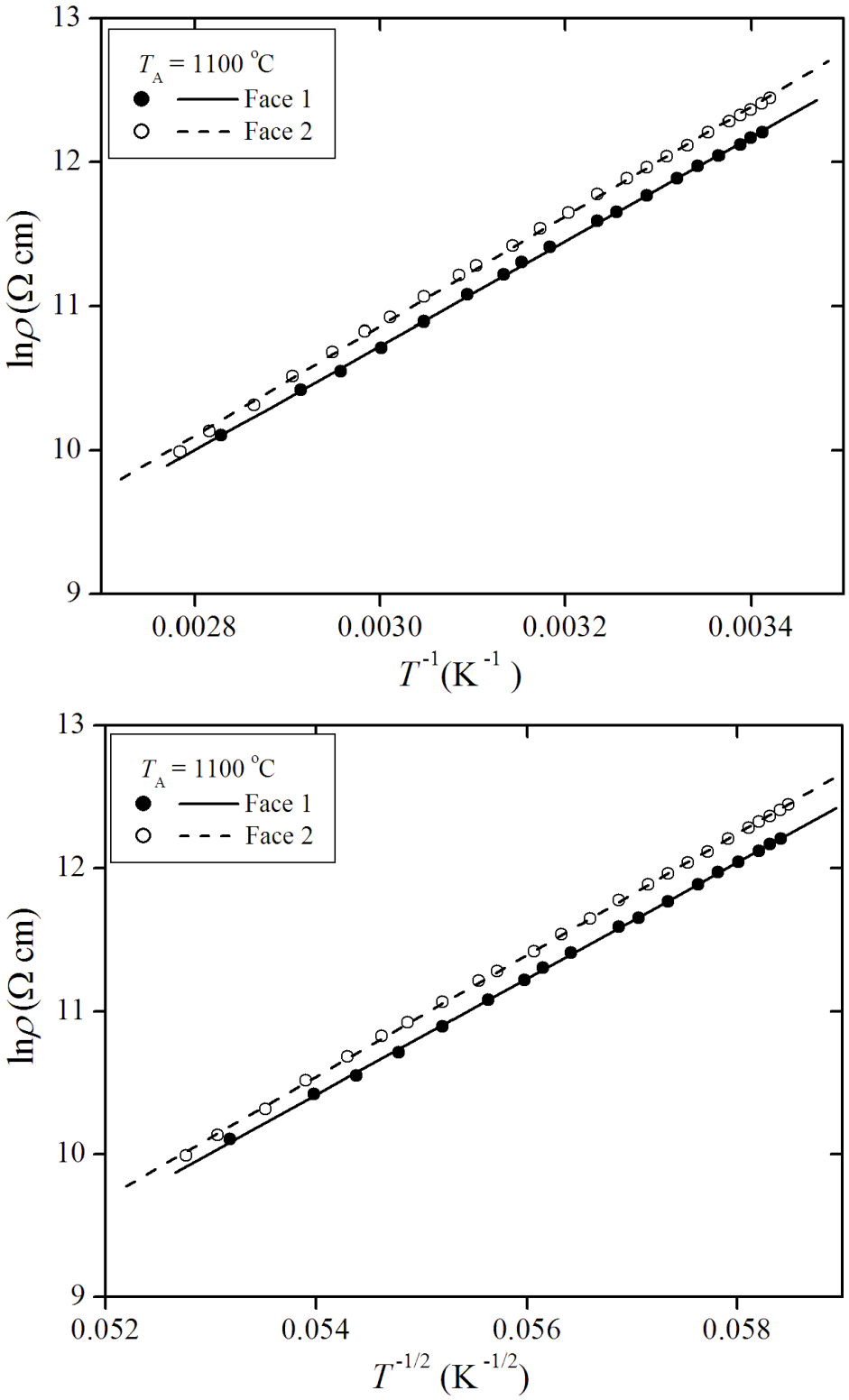

Figure 5.44: $\ln \rho$ versus T^{-1} and $T^{-1/2}$ for a milled $Mn_{0.5}Co_{0.5}Fe_2O_4$ sample. The lines are best linear fits to the data. The pellet was annealed at 1100 ^{o}C.

Table 5.11: Activation energies for $Mn_{0.5}Co_{0.5}Fe_2O_4$ annealed at different temperatures deduced from the best fits of equations (5.4.1) and (5.4.2).

T_A	Face 1		Face 2	
^{o}C	E_{a1} (eV) ± 0.0001	E_{a2} (eV) ± 0.02	E_{a1} (eV) ± 0.0001	E_{a2} (eV) ± 0.03
600	0.3076	3.25	0.3050	3.17
700	0.3030	3.25	0.2984	3.16
800	0.2779	2.74	0.2800	2.76
900	0.2637	2.49	0.2763	2.65
1000	0.2775	2.72	0.2664	2.54
1050	0.3200	3.61	0.3282	3.88
1100	0.3122	3.56	0.3281	3.90

of annealing temperature T_A. Similar trends are observed which indicate similar intrinsic behaviour in the measurements on either faces of the pellets. Minimum values of activation energies are obtained for annealing temperatures around 900 - 1000 ^{o}C. We suspect that for this range of T_A values the sample may be transforming from single-domain to multi-domain structure.

The activation energies based on equation (5.4.1) are consistent with some previous measurements [4, 6, 78]. The resistivity based on tunnelling between grains gives much larger activation energies and better fits to the data than that based on semiconductor behaviour. We suspect that higher activation energies would be required in order to promote conduction by hole or electron movements between charged and neutral grains.

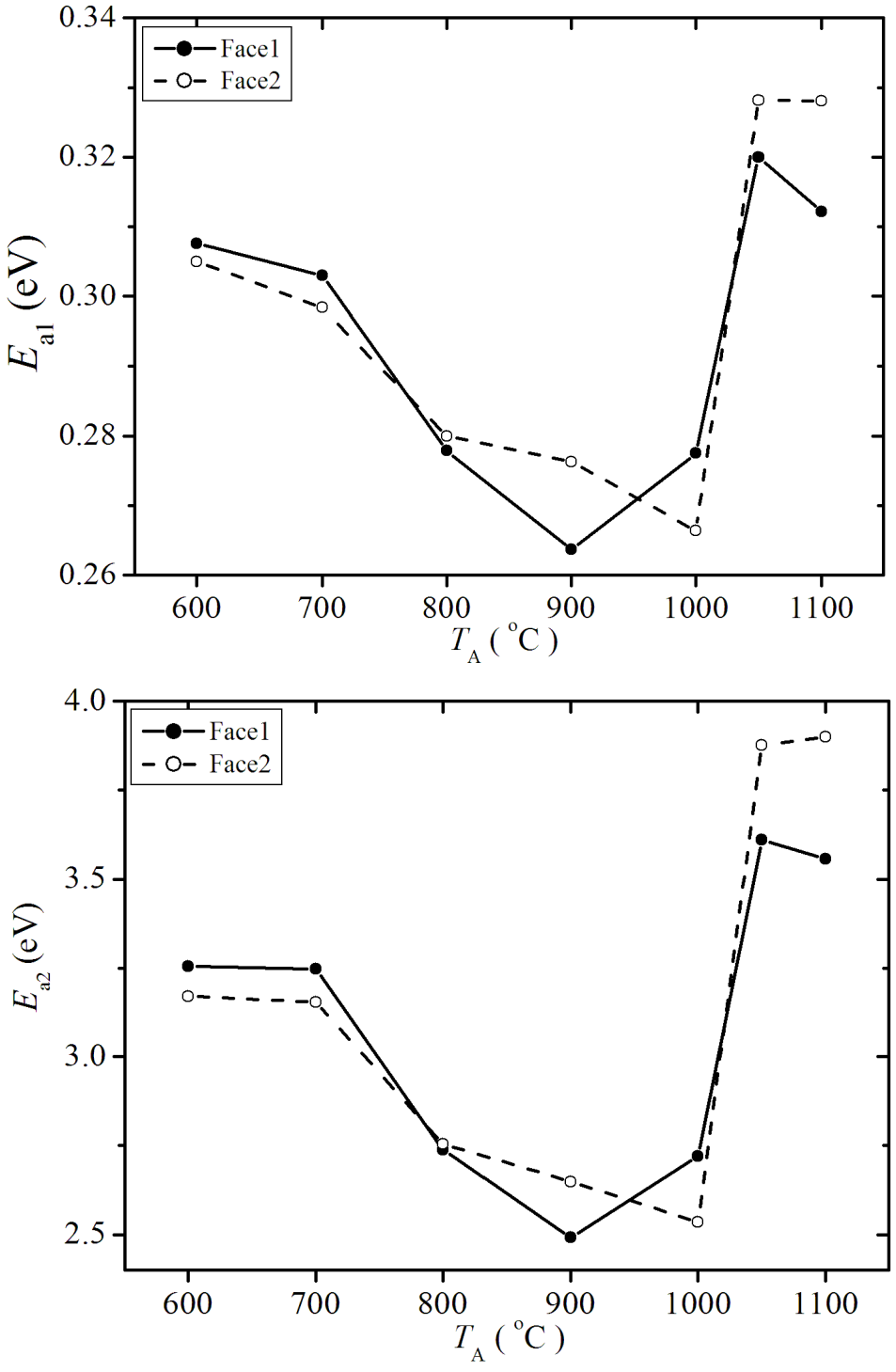

Figure 5.45: Variations of activation energy with annealing temperature for $Mn_{0.5}Co_{0.5}Fe_2O_4$.

5.5 Conclusions

We have successfully made $Mn_xCo_{1-x}Fe_2O_4$ nanoparticle compounds using glycol-thermal method and high-energy ball milling. We have obtained higher particle sizes for the samples with $x = 0$ and 0.5 due to higher stability when there is higher symmetry in the proportion of atoms on tetrahedral sites. The samples prepared by the glycol-thermal method appear to be of higher quality than milled samples. Better quality samples are also obtained from $MnFe_2O_4$ and $CoFe_2O_4$ as starting materials than from metal oxides. For the sample with $x = 0.5$, the XRD density is higher and the hyperfine fields are enhanced on both A and B sites by thermal annealing. Slight reduction in hyperfine fields due to thermal annealing are observed in the $Mn_{0.1}Co_{0.9}Fe_2O_4$ sample.

Coercive fields were observed to increase with increasing annealing temperature and grain sizes which we associate with transformation from single-domain to multi-domain structure [148]. The coercive fields of Mn- substituted $CoFe_2O_4$ are greatly reduced compared to the un-substituted compound, due to reduced anisotropy and particle size. Spin–glass–like behaviour has been observed at low temperature in the two Mn substituted samples. From the FC and ZFC measurements the state of magnetization appears to be higher in the $Mn_{0.5}Co_{0.5}Fe_2O_4$ sample. The spin freezing at low temperature also appears to be stronger. Our results also show evidence for superparamagnetic behaviour of the samples investigated. The temperature-dependent of saturation magnetizations and coercive fields follow the modified Bloch's law and Kneller's law respectively associated with uniaxial symmetry of the nanoparticles.

The temperature dependence of resistivity of $Mn_xCo_{1-x}Fe_2O_4$ nanoferrites compacts seem more favourable to the tunnelling effect of charge carriers between grains. The resistivity and activation energy of a sample has been found to depend on the annealing temperature and the surface of the pellet that being probed.

Chapter 6

Structure and magnetic properties of (Mg, Sr)$_{0.2}$Mn$_{0.1}$Co$_{0.7}$Fe$_2$O$_4$ nanoferrites

6.1 Introduction

In this part of the thesis, we discuss the structural and magnetic properties of (Mg, Sr)$_{0.2}$Mn$_{0.1}$Co$_{0.7}$Fe$_2$O$_4$ nanoferrites. The magnetic interactions in ferrite compounds containing divalent cations and transition elements can be achieved by cation-cation interactions due to direct overlap of the cation $d-$electron wave functions [29]. Change in the divalent element composition can lead to significant differences in properties [96]. Reduction in the scale of the bulk materials to less than 100 nm produces materials that exhibit unusual properties such as superparamagnetic relaxation phenomena and spin-canted structures due to surface effects. These features are not observed in related bulk materials [164].

In the previous chapter we investigated the properties of Mn$_x$Co$_{1-x}$Fe$_2$O$_4$ compounds. We are now interested in the effect of the substitutions by Mg and Sr in this system and more specially on Mn$_{0.3}$Co$_{0.7}$Fe$_2$O$_4$. Therefore, we have synthesized (Mg, Sr)$_{0.2}$Mn$_{0.1}$Co$_{0.7}$Fe$_2$O$_4$ nanoferrites in order to compare any differences in the properties due to Mg and Sr substitutions. Mg and Sr are group two elements which have similar electronic configuration but differ significantly in atomic or covalent

radii. Sr has a covalent radius of 195±10 pm while Mg has 141±7 pm [165]. It is therefore interesting to investigate how this affects the micro-structure, distribution of cations on tetrahedral (A) and octahedral (B) sites, hyperfine parameters and magnetizations for the as-prepared and annealed samples.

6.2 Experimental details

Nanocrystalline $Mg_{0.2}Mn_{0.1}Co_{0.7}Fe_2O_4$ and $Sr_{0.2}Mn_{0.1}Co_{0.7}Fe_2O_4$ powders ferrites were synthesized from high-purity metal chlorides by the glycol-thermal method following a procedure reported elsewhere in our previous works [21, 22] and also discussed in chapter 4. The characterizations of the structure of the compounds were performed at room temperature by XRD and TEM. XRD measurements were made on a Phillips diffractometer type PW 1710 using CoK_α radiation with wavelength of 1.7903 Å. TEM measurements were carried on a type Jeol_JEM-1010 instrument. Mössbauer spectra were recorded at room temperature using a conventional spectrometer with a ^{57}Co Mössbauer source sealed in rhodium matrix which was vibrated at a constant acceleration. A SQUID magnetometer was used to determine the magnetization measurements from 4 to 300 K in magnetic fields of up to 50 kOe. The basic magnetization measurements included hysteresis loops, zero field-cooling (ZFC) and field cooling (FC) magnetizations measurements. In ZFC, the samples were first cooled down from 400 K to 4 K without an applied field. This was followed by magnetization measurements in an external applied field from 4 to 400 K. ZFC and FC measurements were obtained at different static magnetic fields of 0.05, 0.20 and 10.0 kOe. The variation of room temperature hysteresis loops with annealing temperature for samples annealed at 300, 400, 500, 600, 700 and 800 ^oC under argon atmosphere for $Mg_{0.2}Mn_{0.1}Co_{0.7}Fe_2O_4$ and $Sr_{0.2}Mn_{0.1}Co_{0.7}Fe_2O_4$ were also investigated by using a LakeShore model 735 vibrating sample magnetometer (VSM). In this case, the hysteresis loops were obtained in external applied magnetic fields of up to 14 kOe only.

6.3 Results and discussion

6.3.1 X-ray diffraction and transmission electron microscopy measurements

The X-ray patterns of the as-prepared $Mg_{0.2}Mn_{0.1}Co_{0.7}Fe_2O_4$ and $Sr_{0.2}Mn_{0.1}Co_{0.7}Fe_2O_4$ samples are shown in Figure 6.1. The diffraction peaks were successfully indexed to the cubic spinel structure. The spectra clearly indicate formation of the pure single-phase spinel structure with space group of $Fd\bar{3}m$. The broadening of the peaks indicates the synthesis of nanosized ferrite particles. The average particle diameters (D) were estimated from the most intense (311) peak of the XRD profile using the Debye-Scherrer equation (4.1.3) [6, 17]. The lattice parameters (a) were calculated from Bragg's law and equation (4.1.2) [86]. The results of the calculated particle sizes and lattice parameters are given in Table 6.1.

Grain sizes and microstructures for the as-prepared (Mg, Sr)$_{0.2}Mn_{0.1}Co_{0.7}Fe_2O_4$ powders were also investigated by using TEM. Typical TEM micrograph images of the powders are shown in Figure 6.2. The grain sizes of the as-prepared nanoparticles estimated from the TEM are in good agreement with those from XRD. Figure 6.2 shows grains that are nearly uniform in size and spherical in shape. In order to estimate the bulk densities (ρ_{Bulk}), the as-prepared samples were pressed into cylindrical pellets at a pressure of about 1.5×10^8 N/m^2. ρ_{Bulk} is calculated from the knowledge of the mass and the physical dimensions of the pellet. X-ray densities (ρ_{XRD}) for the as-prepared samples were calculated using the equation (4.1.4). The percentage porosity (P) of the as-prepared sample (synthesized at 200 ^{o}C) and samples annealed at 400 ^{o}C and 700 ^{o}C were estimated using the equation (4.1.6). Bulk densities, XRD densities and percentage porosities are given in Table 6.2. The porosity of the compounds reduce significantly after annealing at higher temperature.

The reduction in porosity with increasing annealing temperature is explained based on larger grains created during the sintering process at higher temperature. Low values of porosity indicate a higher degree of homogeneity in the synthesized samples [73]. The decrease in porosity is consistent with increase in bulk density and annealing temperature [105]. No significant difference is observed in the porosities

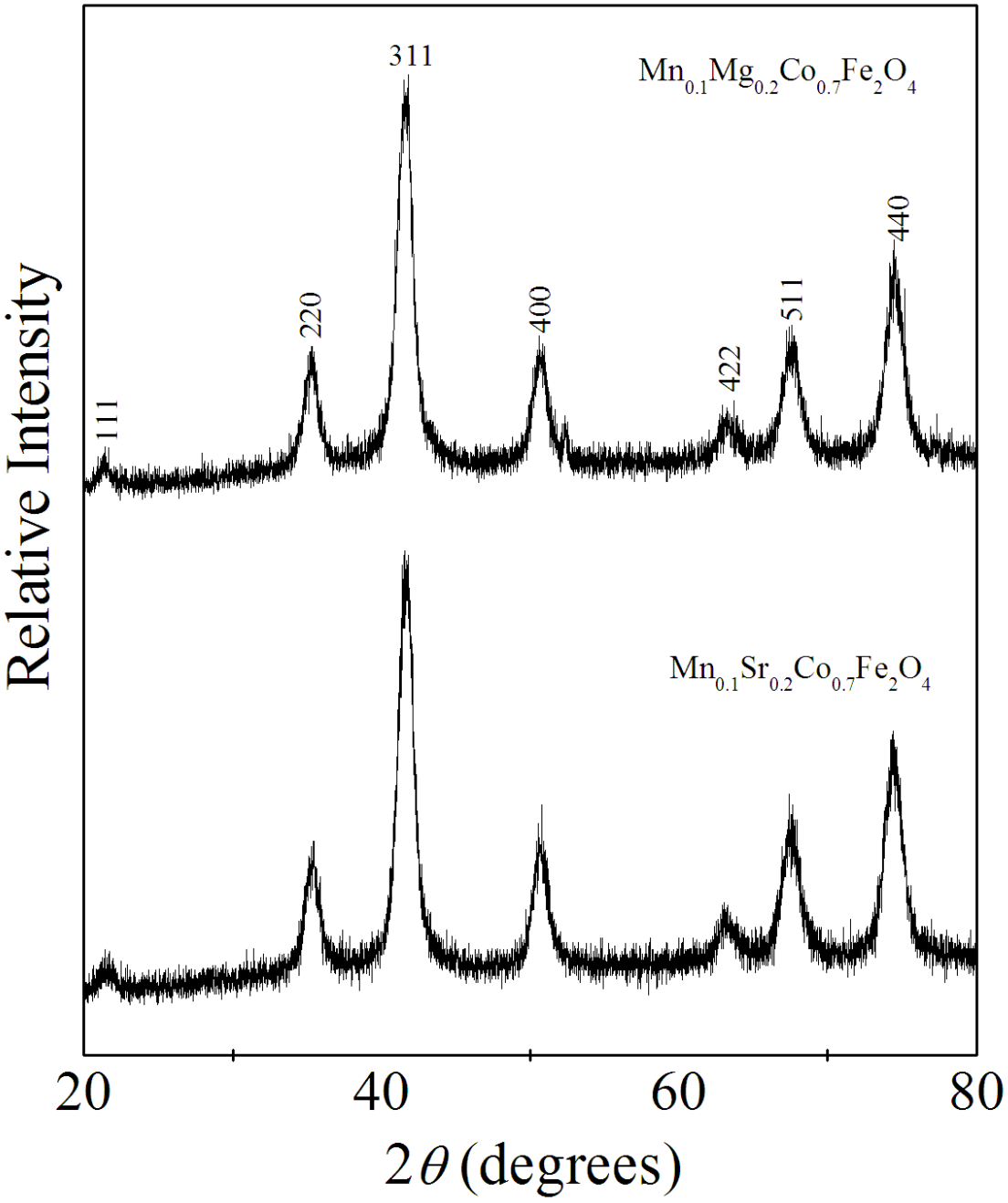

Figure 6.1: XRD patterns for the as-prepared samples of (Mg, $Sr)_{0.2}Mn_{0.1}Co_{0.7}Fe_2O_4$.

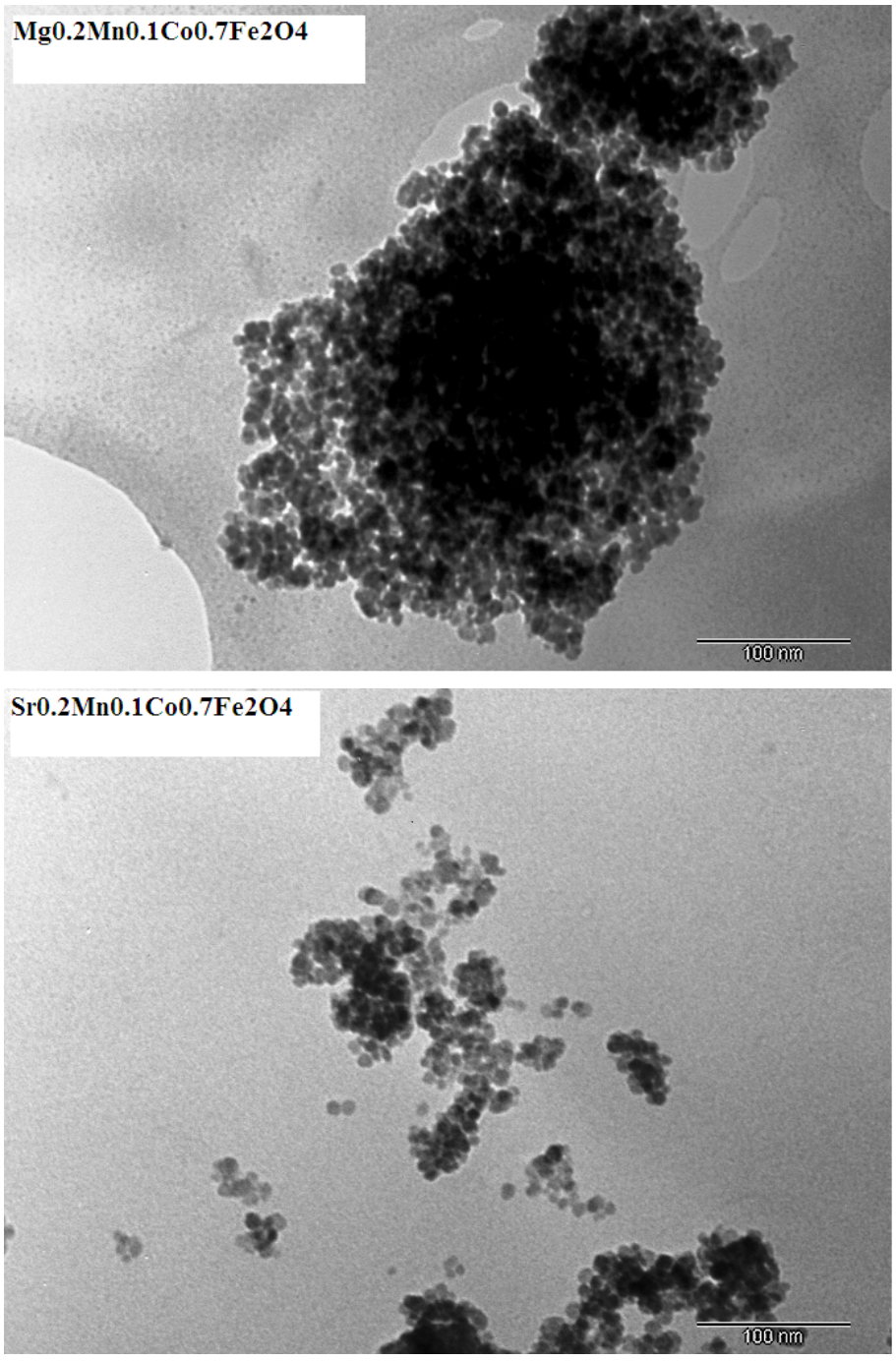

Figure 6.2: TEM micrographs for the as-prepared samples of (Mg, Sr)$_{0.2}$Mn$_{0.1}$Co$_{0.7}$Fe$_2$O$_4$. The length of the ruler corresponds to 100 nm.

Table 6.1: Grain sizes (D) and lattice parameters (a) for the as-prepared samples.

	D (nm)		a (nm)
Sample	D_{XRD} ±0.01	D_{TEM} ±0.4	±0.0001
$Mn_{0.3}Co_{0.7}Fe_2O_4$	7.35	7.3	0.8423
$Mg_{0.2}Mn_{0.1}Co_{0.7}Fe_2O_4$	8.22	8.3	0.8365
$Sr_{0.2}Mn_{0.1}Co_{0.7}Fe_2O_4$	8.06	8.5	0.8359

Table 6.2: X-ray densities (ρ_{XRD}), bulk densities (ρ_{Bulk}) and percentage porosities (P) of the as-prepared samples and samples annealed at 400 and 700 ^{o}C.

	ρ (g/cm^3)	ρ_{Bulk} (g/cm^3)			P (%)		
Sample	ρ_{XRD} ±0.04	ρ ±0.03	ρ_{400} ±0.03	ρ_{700} ±0.04	P ±0.3	P_{400} ±0.3	P_{700} ±0.2
$Mg_{0.2}Mn_{0.1}Co_{0.7}Fe_2O_4$	5.16	2.76	2.80	3.42	46.5	45.7	33.7
$Sr_{0.2}Mn_{0.1}Co_{0.7}Fe_2O_4$	5.44	2.62	2.72	3.67	51.8	50.1	32.6

for the samples annealed at 700 ^{o}C.

6.3.2 Mössbauer measurements

^{57}Fe Mössbauer absorption spectra of the mixed spinel of $Mg_{0.2}Mn_{0.1}Co_{0.7}Fe_2O_4$ and $Sr_{0.2}Mn_{0.1}Co_{0.7}Fe_2O_4$ nanoferrites are presented in Figure 6.3. The spectra were recorded at room temperature on the as-prepared and annealed samples. At least two sextets and one doublet are required to fit the experimental data. The two sextets are associated with the populations of the Fe^{3+} ion at tetrahedral (A) and octahedral (B) sites. An additional sextet for the as-prepared sample of $Mg_{0.2}Mn_{0.1}Co_{0.7}Fe_2O_4$ was required in order get a better fit to the experimental data may be attributed to an intermediate haematite $\alpha-Fe_2O_3$ phase [17] with Fe atoms in high-spin state [167]. The doublets were included in the fits to account for the phenomenon of superparamagnetism associated with single-domain nanoparticles. The spectra for annealed samples exhibit superposition of two Zeeman sextets. The sextet corresponding to a higher hyperfine field is attributed to Fe^{3+} ions on B sites. The other sextet corresponding to a lower hyperfine field is attributed to Fe^{3+} ions on A sites [147]. This difference in hyperfine fields is associated with higher degree of the covalent bonding on the A site sub-lattice where there is a greater degree of spin delocation [166]. Table 6.3 consists of the Mössbauer parameters namely isomer shifts, hyperfine fields, line widths and fraction population of Fe^{3+} ions on A site and B site. The two sextets used to fit Mössbauer spectra of $Mg_{0.2}Mn_{0.1}Co_{0.7}Fe_2O_4$ and $Sr_{0.2}Mn_{0.1}Co_{0.7}Fe_2O_4$ samples indicate ferrimagnetic behaviour of the compounds [62, 168].

Compared to be parent compound $Mn_{0.3}Co_{0.7}Fe_2O_4$ (Tables 5.1 and 5.4) the Mg and Sr substitutions have an effect on the properties. Overall there appears to be some enhancements of the hyperfine fields induced by the substitutions and thermal annealing which we associate with changes in the grain sizes. Our results show similar hyperfine parameters in both Mg and Sr substituted compounds annealed at the same temperature. The difference in the sizes of Mg and Sr appears not to have a significant effect on the hyperfine fields. The isomer shifts for both the as-prepared and annealed compounds on A sites and B sites did not also vary significantly. Hence,

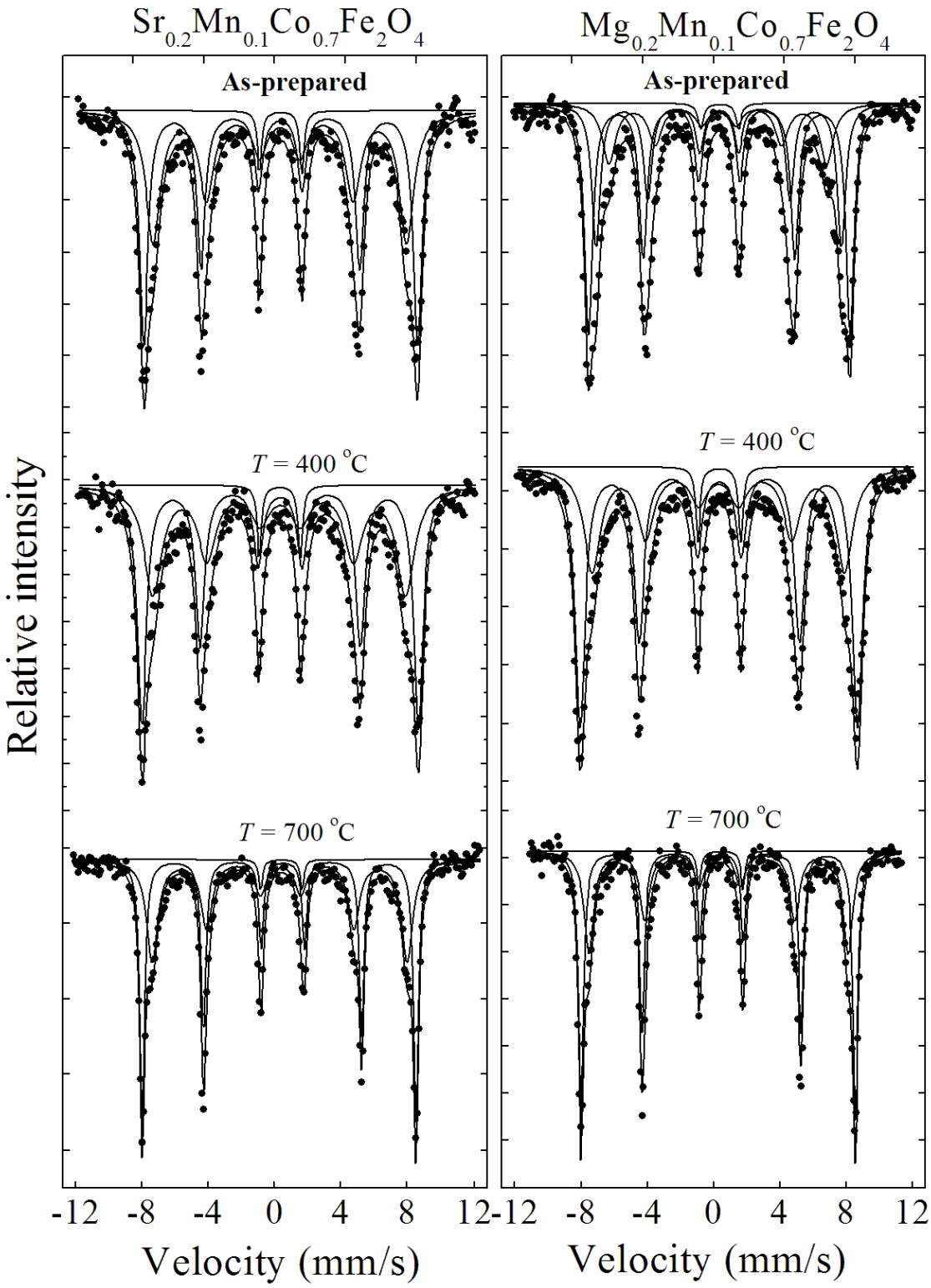

Figure 6.3: Mössbauer spectra for the as-prepared and annealed samples of (Mg, Sr)$_{0.2}$Mn$_{0.1}$Co$_{0.7}$Fe$_2$O$_4$.

Table 6.3: Isomer shifts (δ), hyperfine fields (H), line widths (LW) and Fe^{3+} fraction (f) on A and B sites for the as-prepared and annealed samples of $Mg_{0.2}Mn_{0.1}Co_{0.7}Fe_2O_4$ (Mg) and $Sr_{0.2}Mn_{0.1}Co_{0.7}Fe_2O_4$ (Sr).

	δ (mm/s)		H (kOe)			LW (mm/s)		f (%)			
Sample	δ_A ±0.04	δ_B ±0.03	H_A ±5	H_B ±1	H_{3rd} ±7	LW_A ±0.05	LW_B ±0.04	f_A	f_B	f_{3rd}	$f_{doublet}$
Mg	0.29	0.31	431	459	382	0.29	0.28	30.8	47.6	19.8	1.8
Mg-400	0.28	0.30	443	487	–	0.56	0.34	38.2	58.1	-	3.7
Mg-700	0.33	0.37	485	514	–	0.35	0.18	41.1	55.9	-	3.0
Sr	0.29	0.32	445	481	–	0.49	0.29	46.2	50.4	-	3.4
Sr-400	0.29	0.31	444	485	–	0.60	0.32	44.0	52.3	-	7.7
Sr-700	0.32	0.38	477	512	–	0.41	0.18	45.9	51.9	-	2.2

the $s-$electron charge distribution of Fe^{3+} nuclei at tetrahedral and octahedral sites were not much influenced by the substitutions and annealing temperatures.

6.3.3 Magnetization measurements

The magnetic properties for the as-prepared and annealed (T_A = 300, 400, 500, 600, 700 and 800 ^{o}C) samples were measured in a maximum applied field of 14 kOe at 300 K. Figures 6.4 and 6.5 show the variation of magnetizations as a function of applied magnetic field. The samples exhibit hysteresis which increases with increasing T_A. Figures 6.6 and 6.7 show the initial magnetization curves as a function of magnetic field. The saturation magnetizations were obtained from best fit curve to the experimental data based on the empirical relation for approach to saturation given in equation (2.10.1). The magnetic properties deduced from hysteresis loops such as coercive field H_C, maximum magnetization M_m, saturation magnetization M_S, remanent magnetization M_R and high-field susceptibility χ are shown in Tables 6.4 and 6.5. Figures 6.8 and 6.9 show the variation of coercive field, maximum magnetization, saturation magnetization, remanent magnetization as a

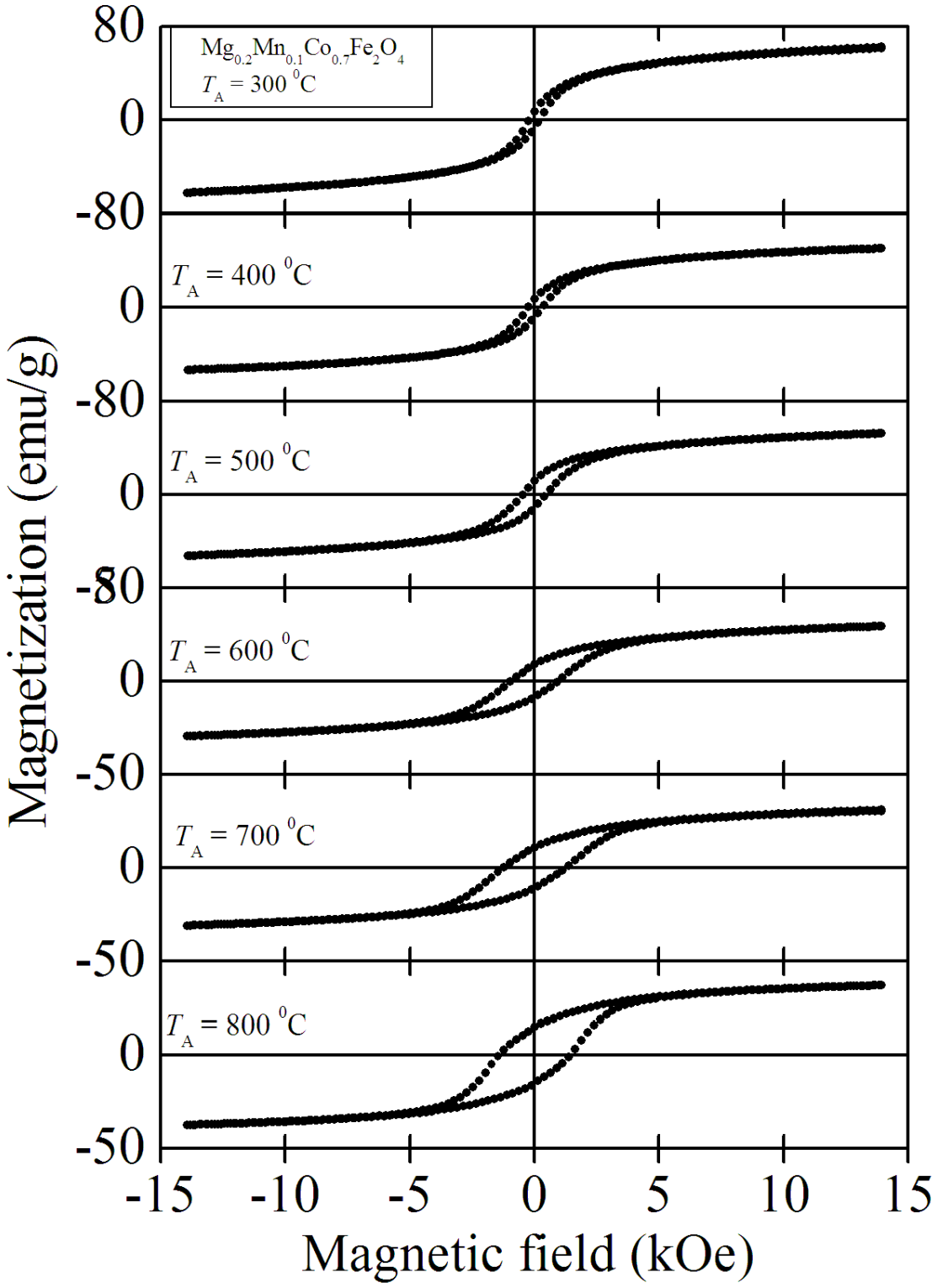

Figure 6.4: Hysteresis loops for annealed samples of $Mg_{0.2}Mn_{0.1}Co_{0.7}Fe_2O_4$ measured at 300 K.

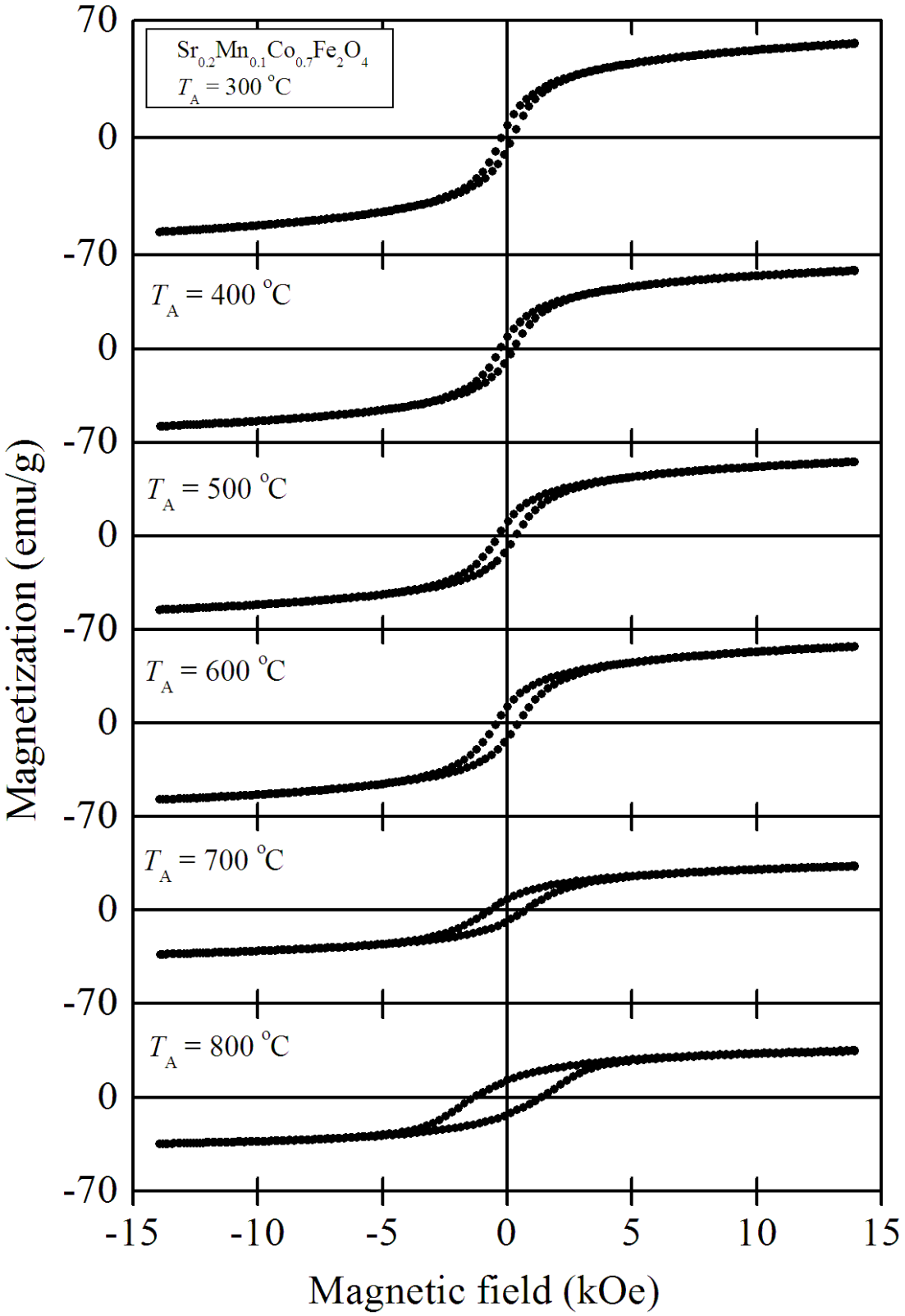

Figure 6.5: Hysteresis loops for annealed samples of $Sr_{0.2}Mn_{0.1}Co_{0.7}Fe_2O_4$ measured at 300 K.

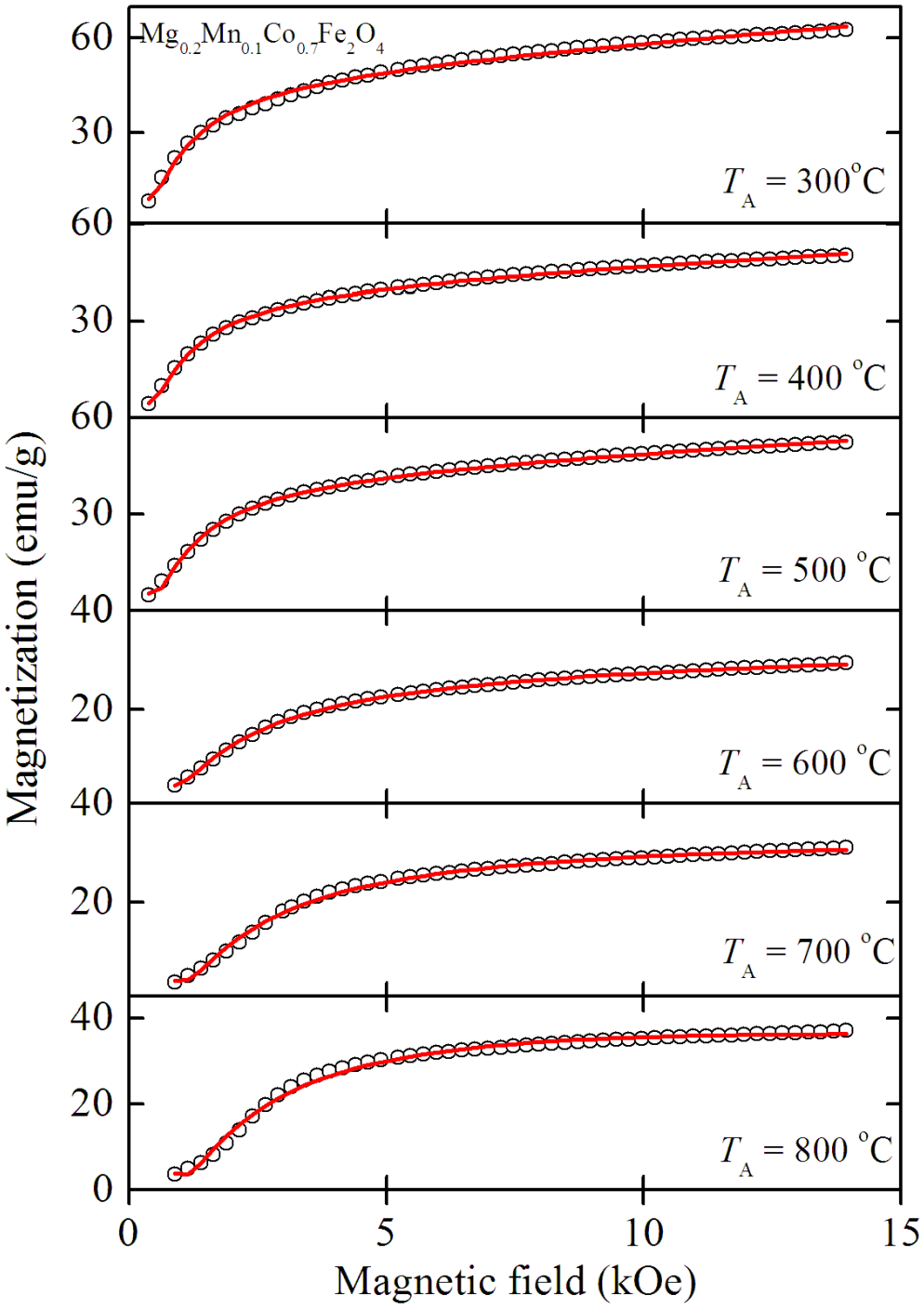

Figure 6.6: Initial magnetizations as a function of magnetic field for annealed samples of $Mg_{0.2}Mn_{0.1}Co_{0.7}Fe_2O_4$ measured at 300 K. The solid lines are the best fit curves to the data based on equation (2.10.1).

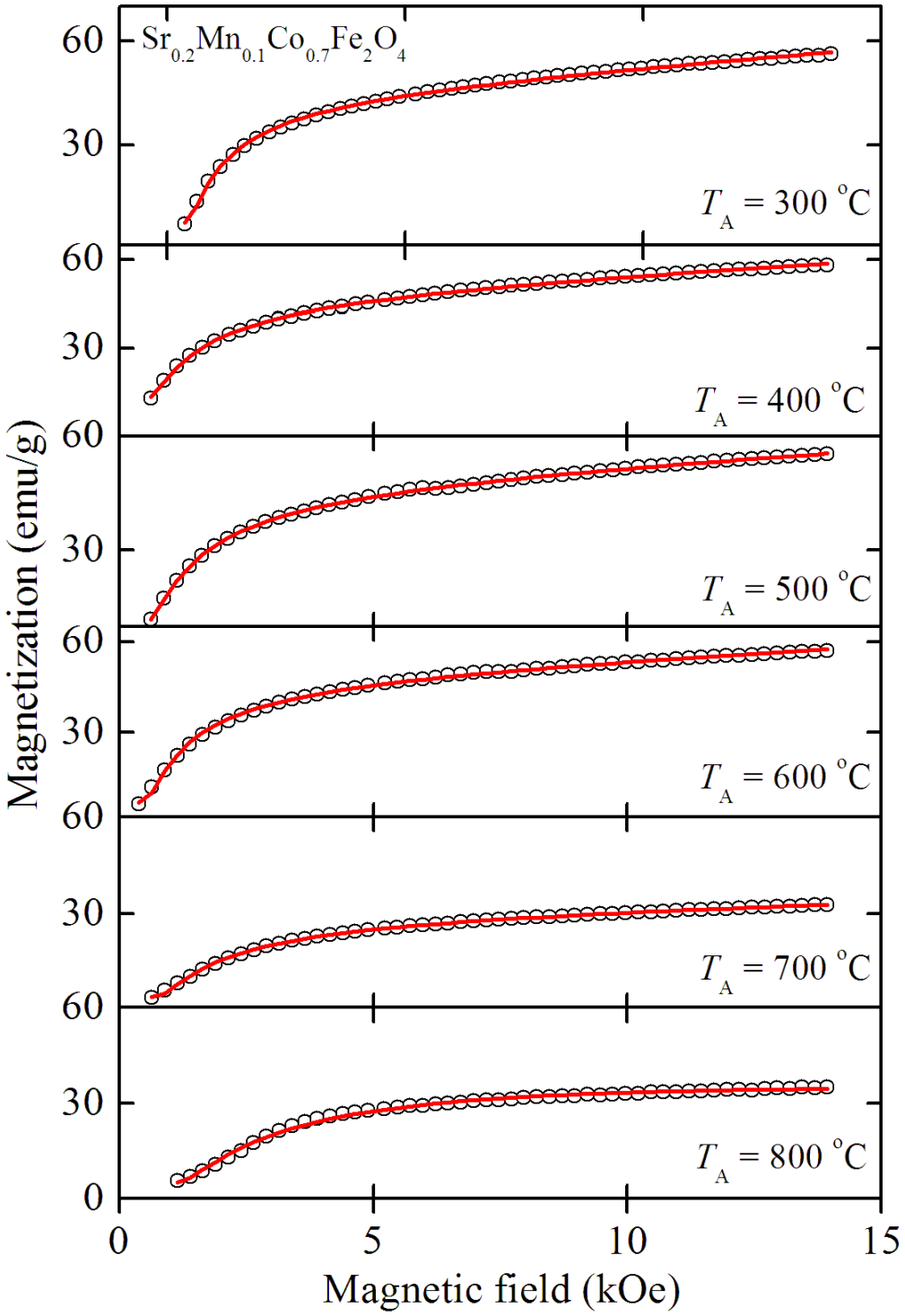

Figure 6.7: Initial magnetizations as a function of magnetic field for annealed samples of $Sr_{0.2}Mn_{0.1}Co_{0.7}Fe_2O_4$ measured at 300 K. The solid lines are the best fit curves to the data based on equation (2.10.1).

Table 6.4: Coercive fields (H_C), saturation magnetizations (M_S), maximum magnetizations (M_m), remanent magnetizations (M_R) and parameters obtained using the best fit curves to the data based on equation (2.10.1) for annealed $Mg_{0.2}Mn_{0.1}Co_{0.7}Fe_2O_4$ samples measured at 300 K.

T (^{o}C)	H_C (Oe) ±2	M_S (emu/g) ±0.4	M_m (emu/g) ±0.4	M_R (emu/g) ±0.4	a (Oe^{-1}) ±0.06	b (Oe^{-2}) ±0.05	χ ±0.07
300	181	49.9	62.5	6.7	0.71	-0.15	1.17
400	207	41.9	51.7	7.4	0.77	-0.16	0.80
500	463	44.4	52.5	11.5	0.85	-0.20	0.79
600	1028	29.5	30.1	8.8	1.50	-0.67	0.16
700	1463	31.0	36.0	11.0	1.78	-0.89	-0.06
800	1725	37.2	48.5	15.0	1.87	-0.94	-0.42

Table 6.5: Coercive fields (H_C), saturation magnetizations (M_S), maximum magnetizations (M_m) remanent magnetizations (M_R) and parameters obtained using the best fit curves to the data based on equation (2.10.1) for annealed $Sr_{0.2}Mn_{0.1}Co_{0.7}Fe_2O_4$ samples measured at 300 K.

T (^{o}C)	H_C (Oe) ±2	M_S (emu/g) ±0.6	M_m (emu/g) ±0.4	M_R (emu/g) ±0.4	a (Oe^{-1}) ±0.01	b (Oe^{-2}) ±0.009	χ ±0.06
300	196	40.9	56.3	7.1	0.68	-0.137	1.42
400	248	42.7	58.0	7.8	0.80	-0.210	0.91
500	331	41.5	55.3	9.8	0.82	-0.219	0.75
600	424	48.9	57.2	11.8	0.79	-0.174	0.81
700	721	27.3	33.0	8.3	1.22	-0.429	0.39
800	1460	31.8	34.9	13.1	1.86	-0.959	-0.27

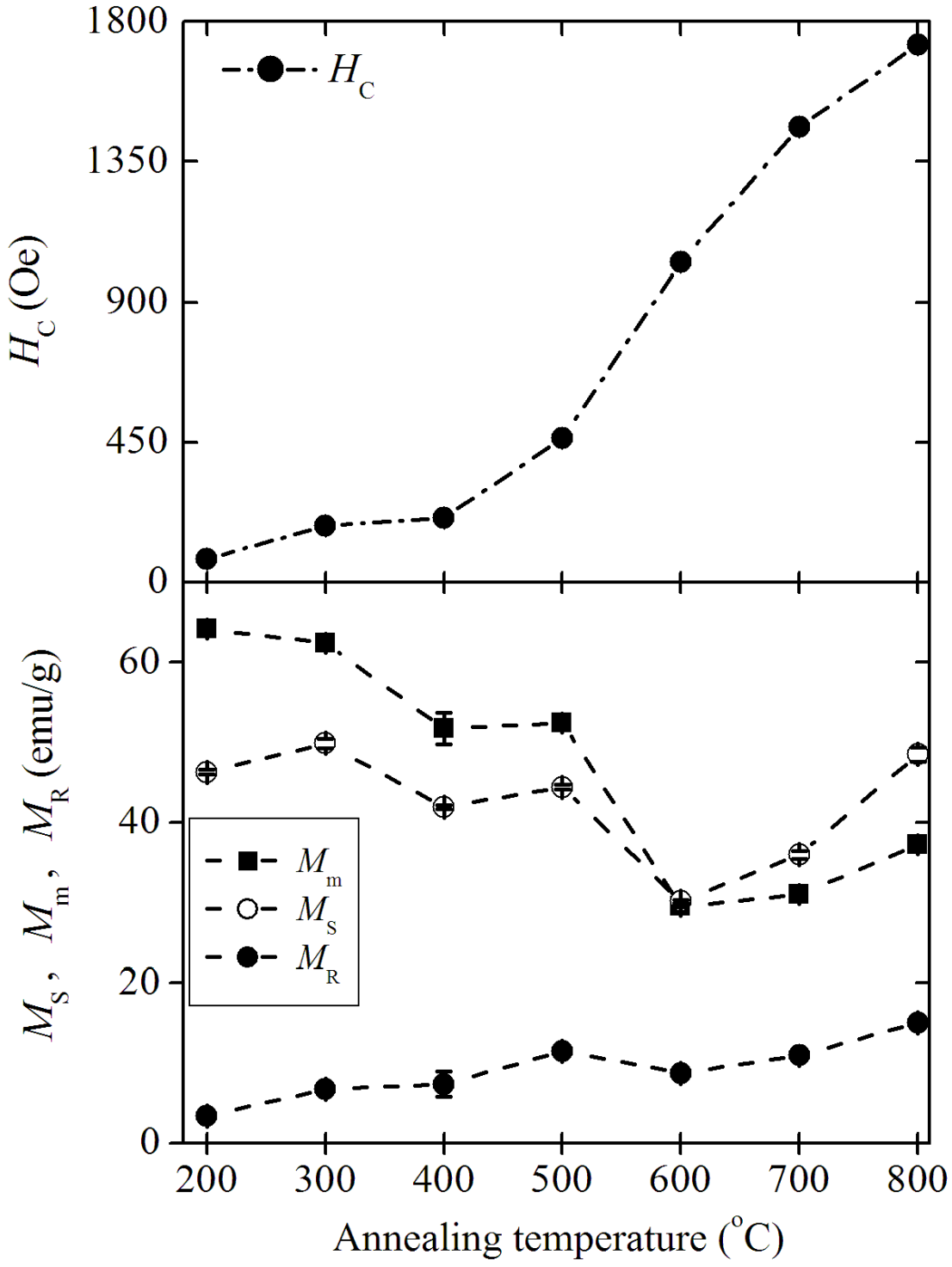

Figure 6.8: Coercive fields, saturation magnetizations and remanent magnetizations of $Mg_{0.2}Mn_{0.1}Co_{0.7}Fe_2O_4$ plotted as a function of annealing temperature.

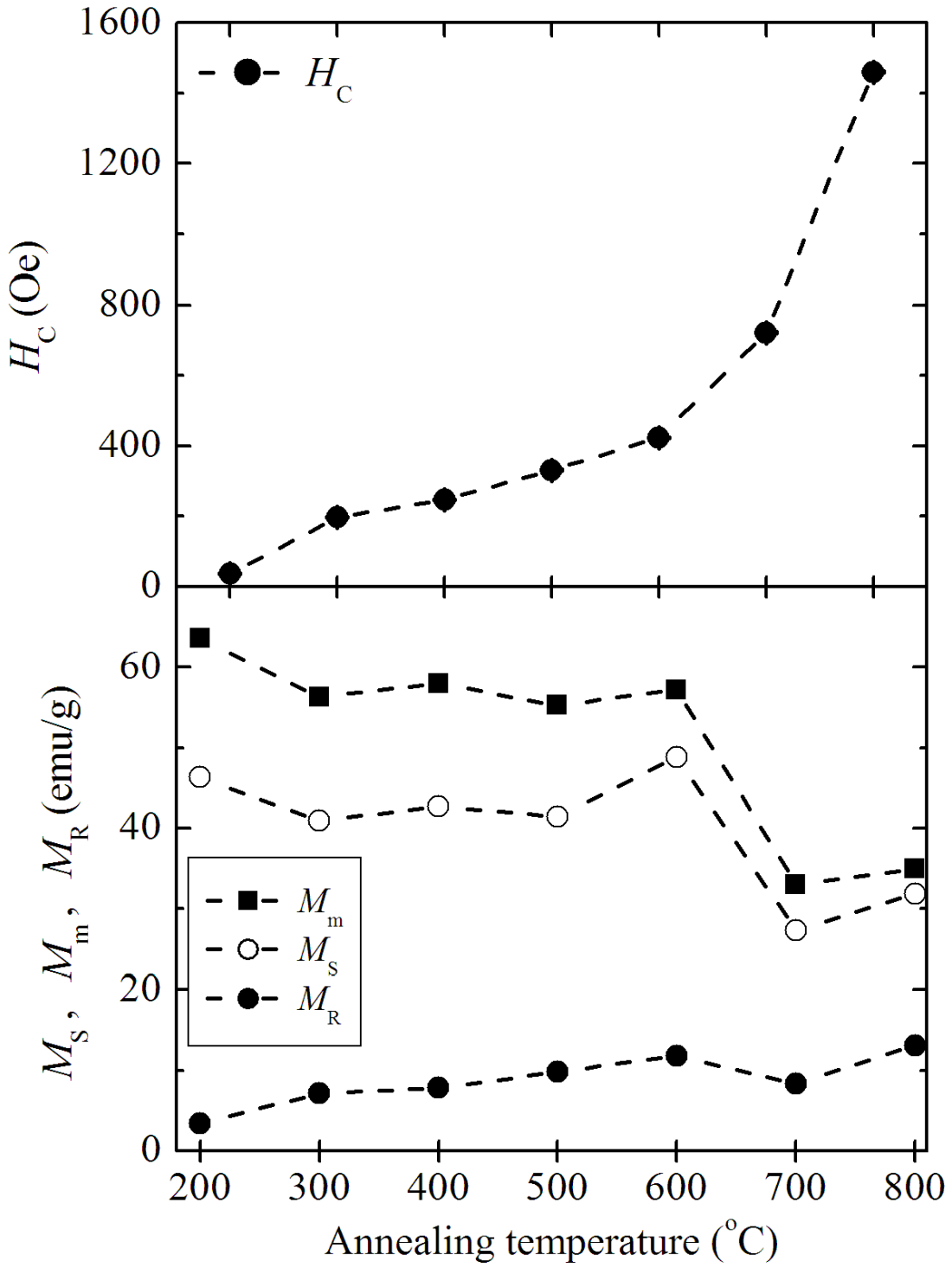

Figure 6.9: Coercive fields, saturation magnetizations and remanent magnetizations of $Sr_{0.2}Mn_{0.1}Co_{0.7}Fe_2O_4$ plotted as a function of annealing temperature.

function of annealing temperature. Similar trends in magnetic properties of Mg- and Sr-substituted compounds are observed. The as-prepared oxides synthesized at 200 ^{o}C have the smallest H_C which increases gradually at higher annealing temperature T_A. The increase in coercive field with annealing temperature is attributed to increasing grain sizes as the samples transform from single-domain to multi domain structure. For $T_A \geq 500$ ^{o}C Mg-substituted samples have higher coercive fields than Sr-substituted samples. The changes of the M_S, M_R and H_C in the Mg- and Sr-substituted samples may be related to the modifications of the grain sizes and the distortion of the magnetocrystallite anisotropy caused by thermal annealing [169]. The distortion on the surface of the ultra-fine particles due to the interaction of the transition metal ions with the oxygen atoms in spinel structure may also contribute to the reduction of the saturation magnetization [169]. The magnitudes of the fit parameters $|a|$ and $|b|$ (in Tables 6.4 and 6.5) increase with increase in T_A while χ decreases. The lowest values of magnetizations at $T_A = 600$ ^{o}C and 700 ^{o}C are observed for Mg- and Sr-substituted samples respectively.

Typical temperature variation of the magnetizations obtained on a SQUID magnetometer under zero field cooling (ZFC) and field cooling (ZF) for $Mg_{0.2}Mn_{0.1}Co_{0.7}Fe_2O_4$ and $Sr_{0.2}Mn_{0.1}Co_{0.7}Fe_2O_4$ oxides in external static magnetic fields of 0.05, 0.20 and 10.0 kOe are shown in Figures 6.10 and 6.11. As before in ZFC, the samples were cooled in zero field from room temperature to the lowest temperature after which a field is applied and the magnetizations measured with increasing temperature. Under FC the samples were cooled in the same applied field and the magnetization measured as a function of temperature. The ZFC magnetizations are lower and coincide with FC magnetizations at a higher temperature that depends on the applied field. Broad peaks of ZFC magnetizations depend on particle size distribution and blocking temperature [170, 171]. The blocking temperature decreases with increasing applied field. Similar behaviour has been observed in a $ZnFe_2O_4$ oxide [159].

Figures 6.12 and 6.13 show hysteresis loops obtained at 4, 50, 100, 200 and 300 K in applied magnetic fields of up to 50 kOe. The samples become magnetically harder at lower temperature, which we associate with spin freezing. The loops ap-

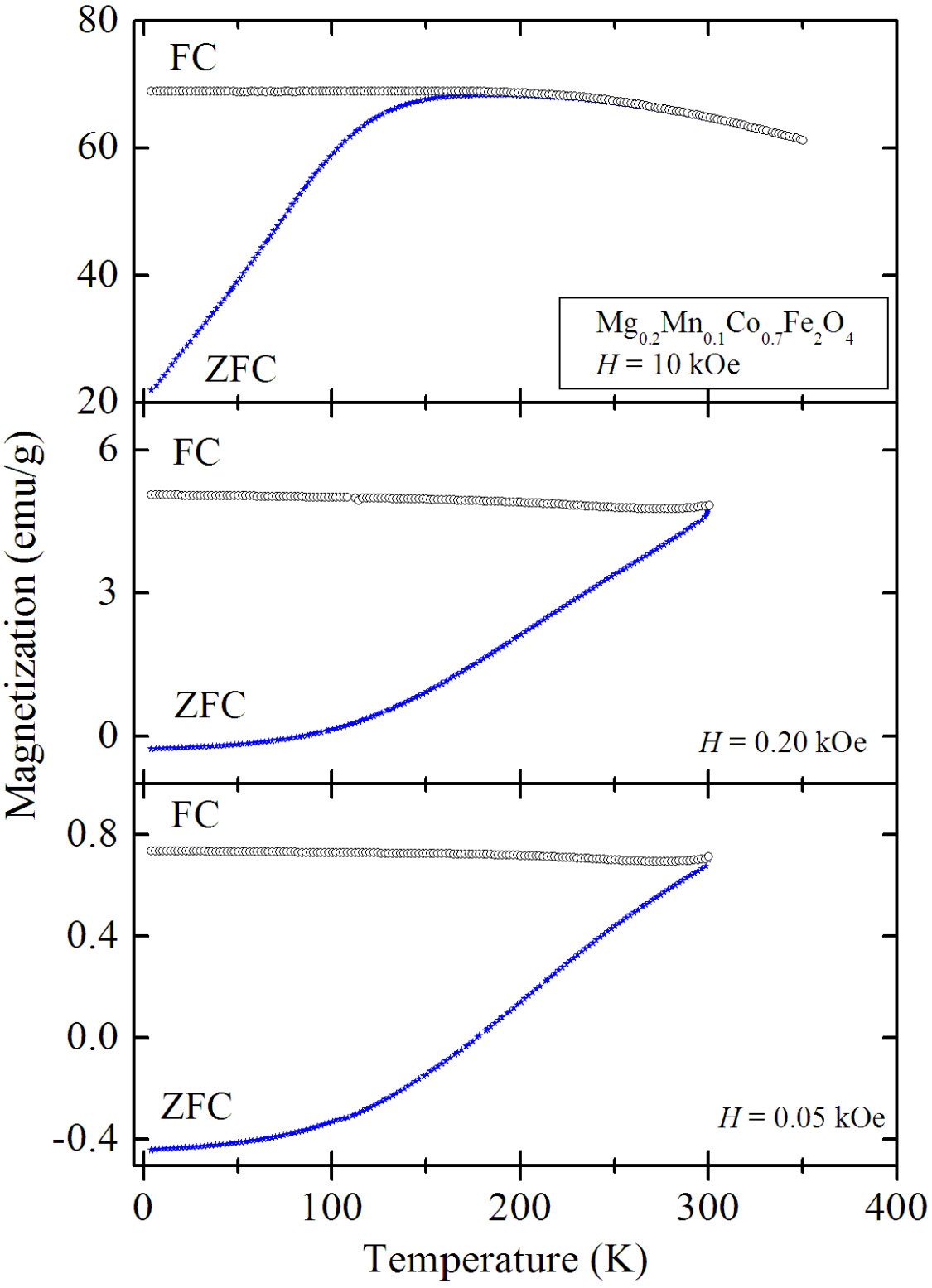

Figure 6.10: Temperature dependence of ZFC and FC magnetizations of $Mg_{0.2}Mn_{0.1}Co_{0.7}Fe_2O_4$ measured in different external static magnetic fields.

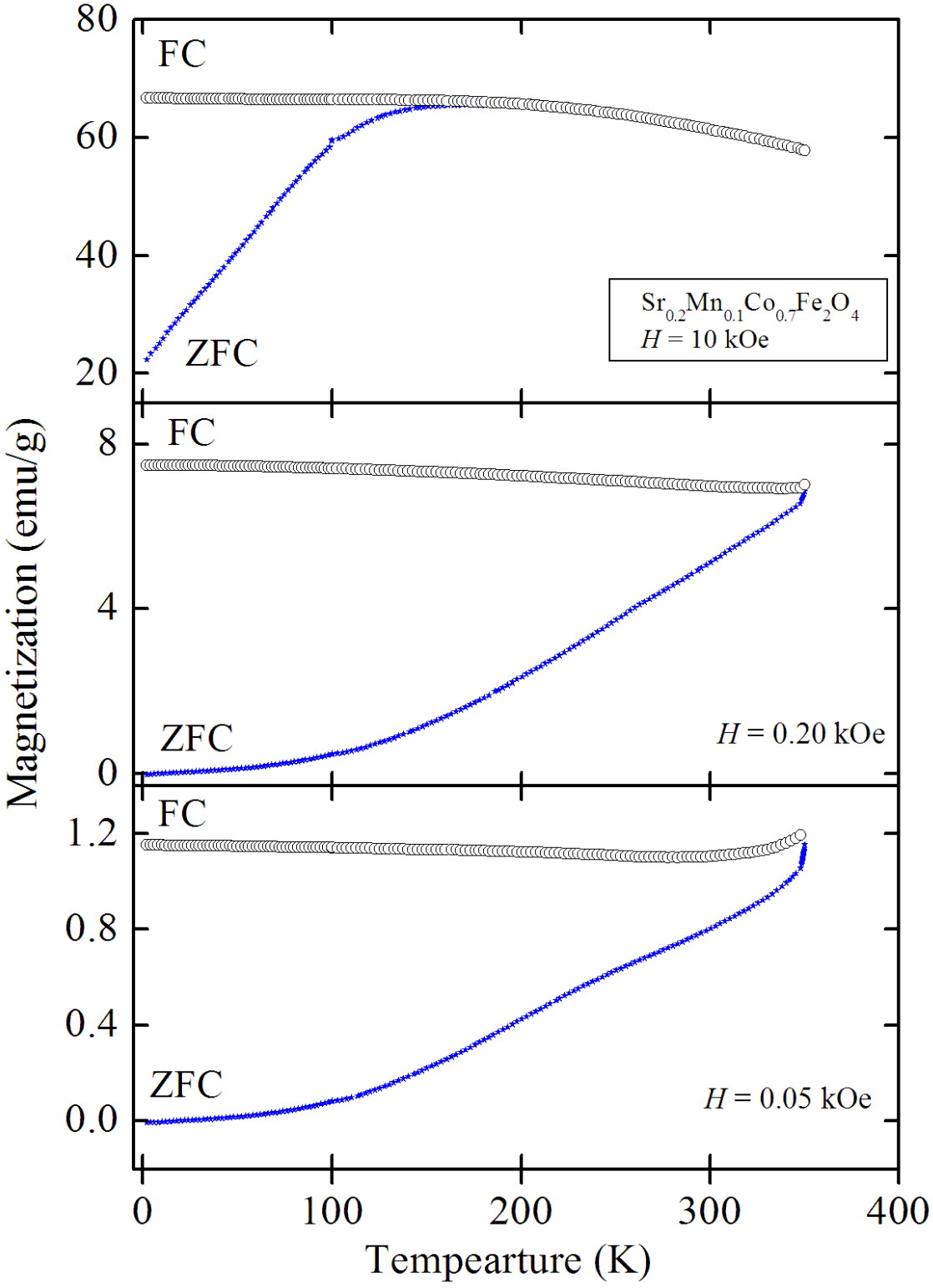

Figure 6.11: Temperature dependence of ZFC and FC magnetizations of $Sr_{0.2}Mn_{0.1}Co_{0.7}Fe_2O_4$ measured in different external static magnetic fields.

pear distorted more especially in the $Sr_{0.2}Mn_{0.1}Co_{0.7}Fe_2O_4$ sample. This behaviour is similar to $ZnFe_2O_4$ sample [104]. The distortion of the hysteresis loops at low temperature may be attributed to the freezing of the disordered spin states [172]. The distortion may also be attributed to the existence of two types magnetic phases at the same temperature [173]. We also observe bigger distortion in the hysteresis loops for the Sr-substituted sample at $T \leq 100$ K. We suspect a higher effect of spins disorder and lower spin freezing for the larger Sr than for the smaller Mg atom when the surface to volume ratio increase. Thus, the fraction of the atoms that lie near or on the surface make the rotation of the spins easier in the Sr-substituted compound. As can be seen from the hysteresis loops in Figures 6.12 and 6.13, the magnetizations do not completely saturate even in external fields of 50 kOe. The surface-spin structure of the nanoparticles will also contribute to the non-saturating magnetization [104]. The coercive fields (H_C), saturation magnetizations (M_S) and remanent magnetizations (M_R) estimated from hysteresis loops are given in Table 6.6. In the present case, the change in coercive field for $Mg_{0.2}Mn_{0.1}Co_{0.7}Fe_2O_4$ is much larger than for $Sr_{0.2}Mn_{0.1}Co_{0.7}Fe_2O_4$ when the temperature of the samples change from 300 K to 4 K. The low temperature measurements appear to provide more revealing differences between Mg and Sr based samples.

The temperature dependence of the coercive fields in particulate media has been observed to follow the Kneller's law (equation (2.10.2)) [97]. The observed temperature dependences of coercive fields for our samples are consistent with $\alpha = 1/2$ as confirmed by linear plots of $H_C(T)$ against $T^{1/2}$ shown in Figures 6.14 and 6.15. The variation of saturation magnetizations with measuring temperature were observed to vary according to the modified Bloch's law (2.8.6) where β is at least 1.5 [158, 159]. We attribute this to the confinement effects of the spin-wave spectrum for magnetic clusters. Bloch's law appears to fit the saturation magnetization data over the entire temperature range with values of β equal to 2.39 ± 0.07 and 2.3 ± 0.1 for $Mg_{0.2}Mn_{0.1}Co_{0.7}Fe_2O_4$ and $Sr_{0.2}Mn_{0.1}Co_{0.7}Fe_2O_4$ respectively. Figure 6.16 shows the temperature dependence of saturation magnetization of $(Mg, Sr)_{0.2}Mn_{0.1}Co_{0.7}Fe_2O_4$ ferrites. These results are similar to the behaviour of nanoparticles with uniaxial symmetry in $CoFe_2O_4$ ferrites [97].

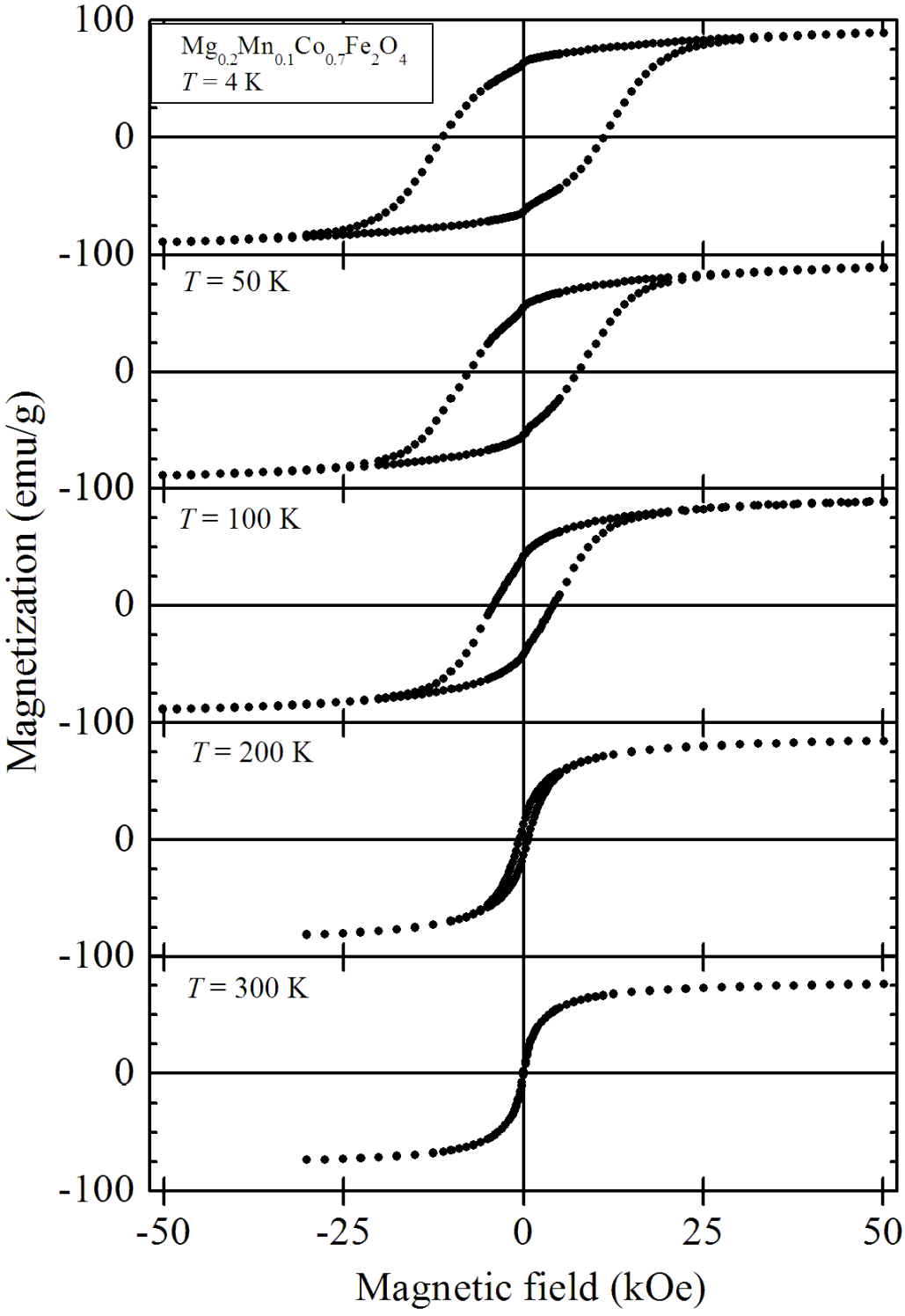

Figure 6.12: Hysteresis loops of $Mg_{0.2}Mn_{0.1}Co_{0.7}Fe_2O_4$ measured at different temperatures.

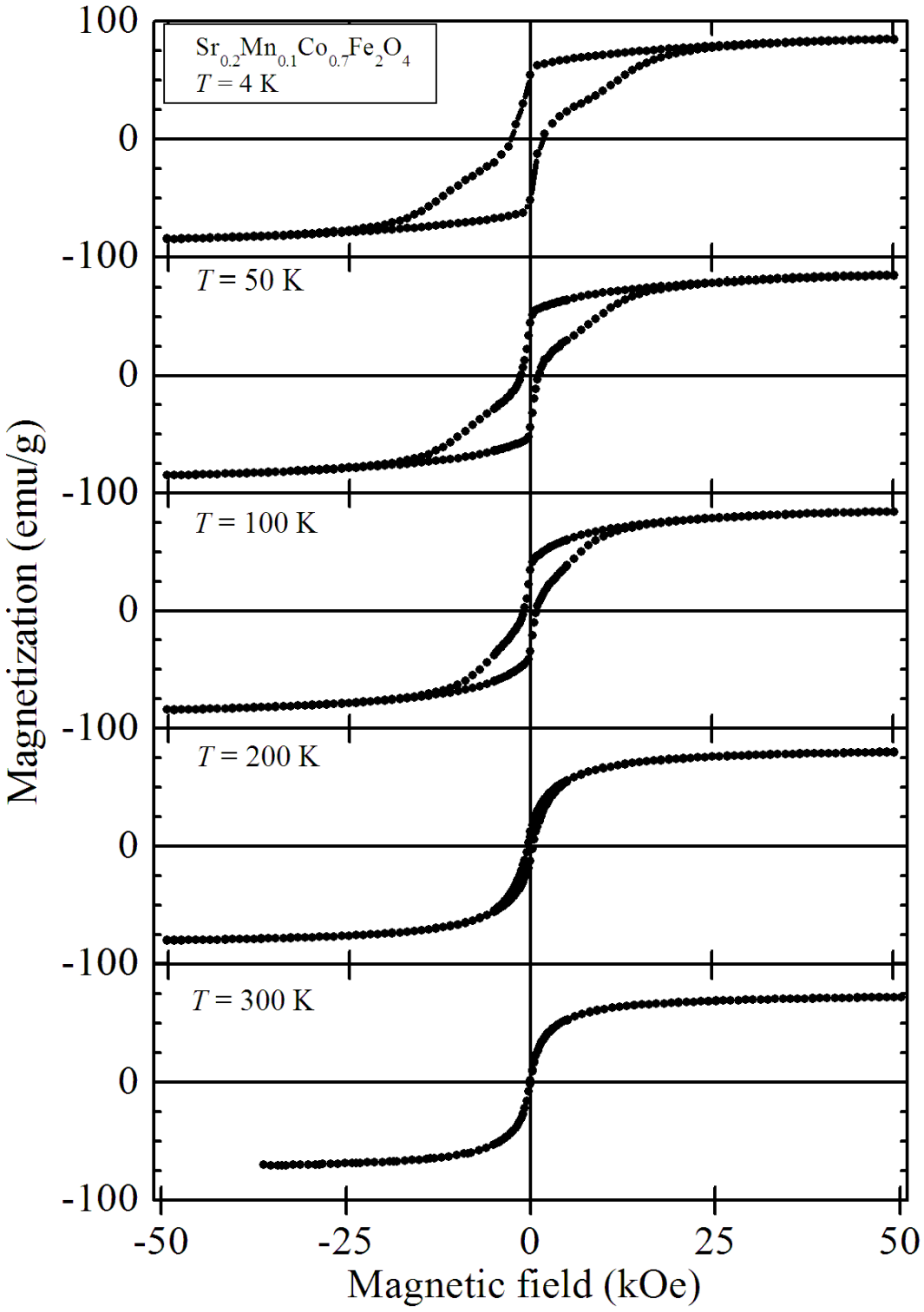

Figure 6.13: Hysteresis loops of $Sr_{0.2}Mn_{0.1}Co_{0.7}Fe_2O_4$ measured at different temperatures.

Table 6.6: Coercive fields (H_C), saturation magnetizations (M_S), remanent magnetizations (M_R), ratio M_R/M_S and magnetic moment per molecule (μ) for the as-prepared samples as a function of measuring temperature.

Sample	T (K)	H_C (Oe) ± 1	M_S (emu/g) ± 0.4	M_R (emu/g) ± 0.4	M_R/M_S	μ (μ_B)
$Mg_{0.2}Mn_{0.1}Co_{0.7}Fe_2O_4$	4	10698	89.2	62.9	0.71	3.63
”	50	6557	89.0	54.7	0.61	3.62
”	100	3790	88.4	42.4	0.48	3.60
”	200	573	84.1	13.2	0.16	3.42
”	300	46	75.9	2.0	0.03	3.19
$Sr_{0.2}Mn_{0.1}Co_{0.7}Fe_2O_4$	4	3024	84.8	52.9	0.62	3.64
”	50	1089	84.8	44.3	0.52	3.65
”	100	778	84.1	34.7	0.41	3.62
”	200	350	79.9	12.7	0.16	3.43
”	300	45	72.3	1.7	0.02	3.11

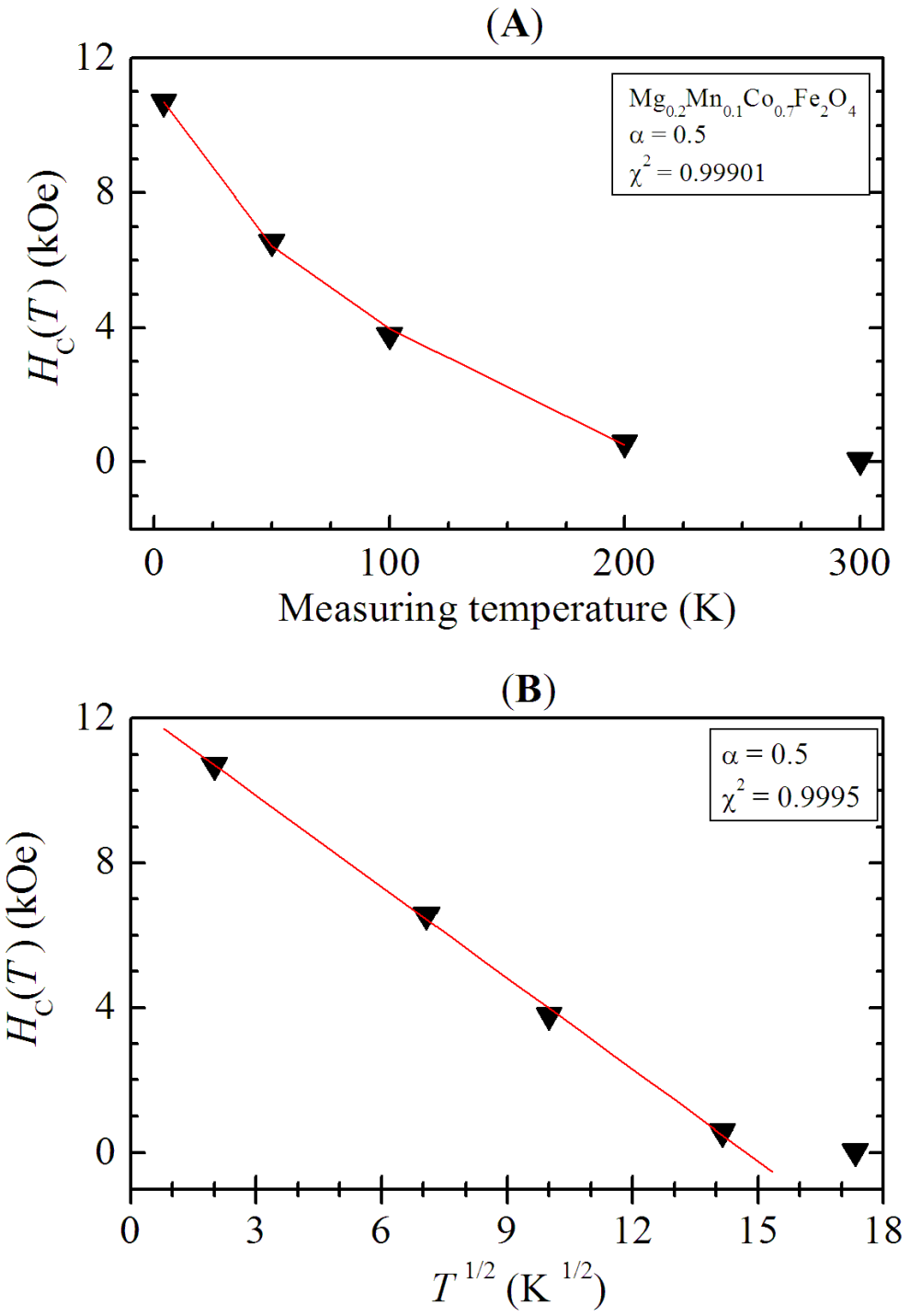

Figure 6.14: Variation of coercive fields with measuring temperature of the as-prepared $Mg_{0.2}Mn_{0.1}Co_{0.7}Fe_2O_4$ sample. The solid lines are based on Kneller's law.

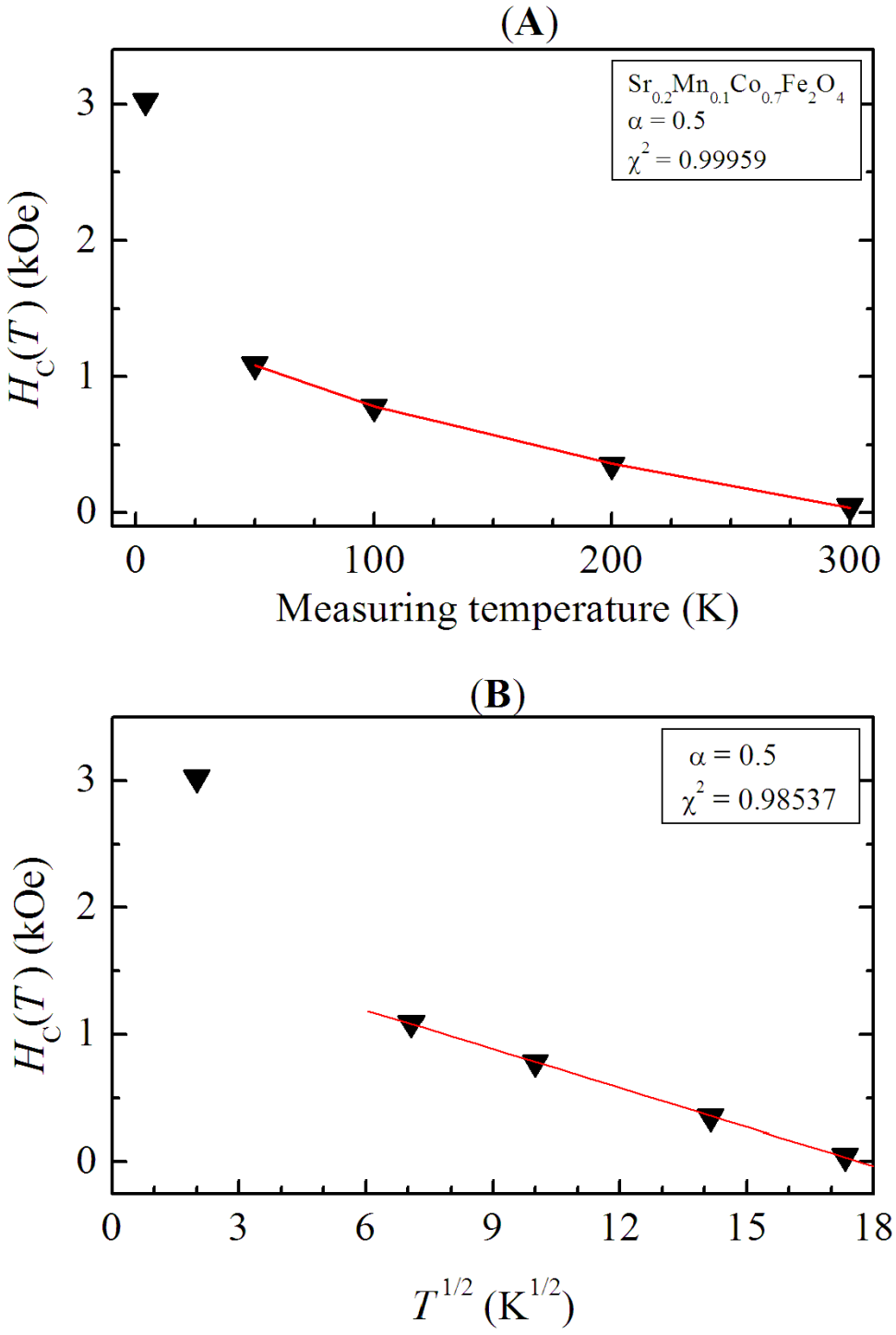

Figure 6.15: Variation of coercive fields with measuring temperature of the as-prepared $Sr_{0.2}Mn_{0.1}Co_{0.7}Fe_2O_4$ sample. The solid lines are based on Kneller's law.

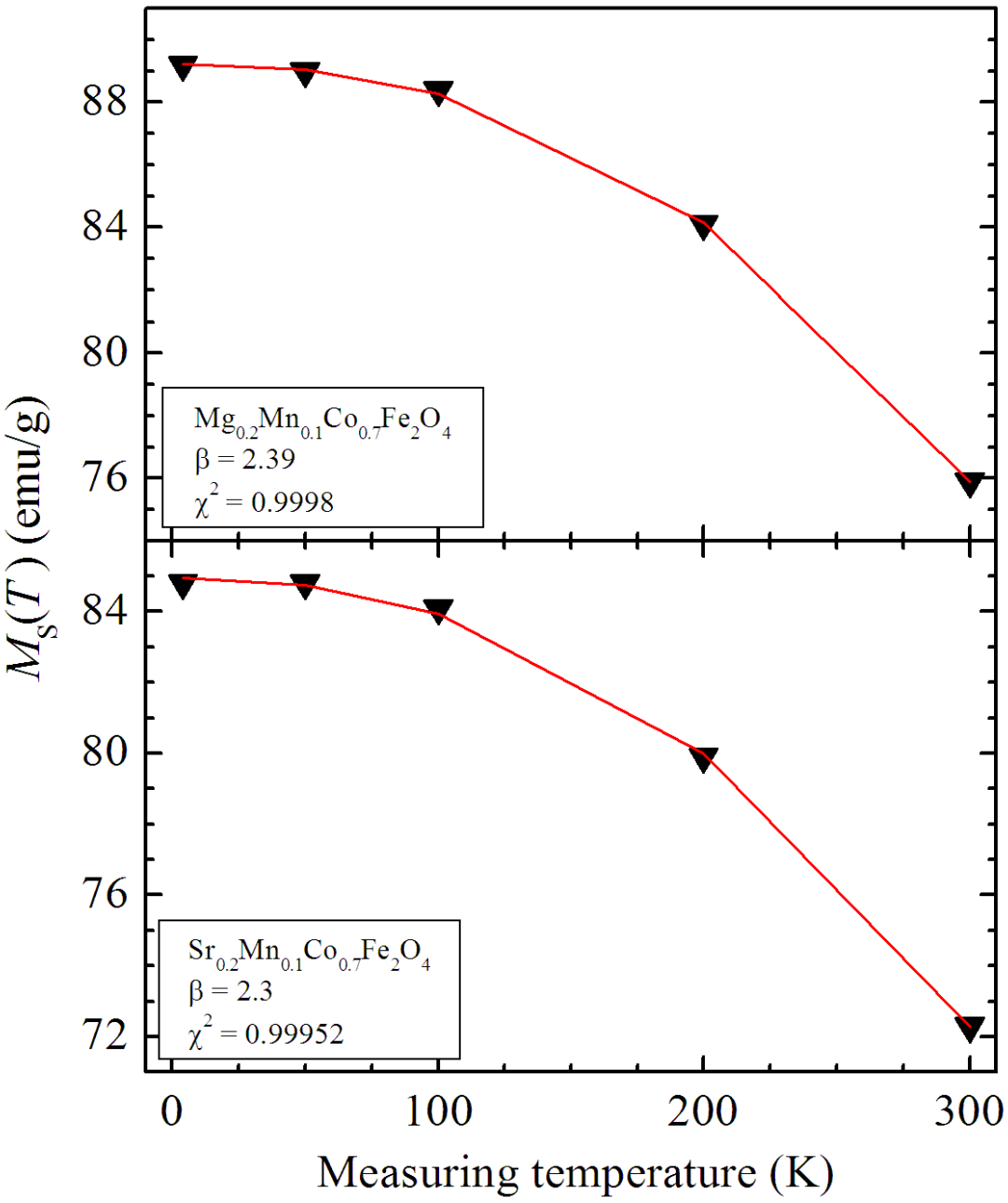

Figure 6.16: Variation of saturation magnetizations with measuring temperature of the as-prepared (Mg, Sr)$_{0.2}$Mn$_{0.1}$Co$_{0.7}$Fe$_2$O$_4$ samples. The solid lines are fits due to Bloch's law (2.8.6).

6.4 Conclusions

Nanoparticles of $Mg_{0.2}Mn_{0.1}Co_{0.7}Fe_2O_4$ and $Sr_{0.2}Mn_{0.1}Co_{0.7}Fe_2O_4$ ferrites with single-phase cubic spinel were synthesized directly by the glycol-thermal method. There were no significant difference in the particle sizes of the two materials as determined by XRD and TEM analysis. Mg and Sr are incorporated into the structure without significantly changing the coordination between ions in the spinel structure. The porosities of the Mg- and Sr-substituted compounds were found to decrease with increasing annealing temperature consistent with increases in bulk densities. This is related to the larger grains created during the annealing process at higher temperature. Some enhancement of the hyperfine fields for both Sr- and Mg- substituted samples induced by the substitutions and thermal annealing are observed which we associate with changes in the grain sizes. The $s-$electron charge densities of Fe^{3+} ions at A and B sites were not influenced significantly by the substitutions of Mg and Sr or by sintering temperatures. The coercive field results show the evolution from single-domain to multi-domain structure with increased thermal annealing temperature. Evidence of spin freezing was confirmed by ZFC and FC magnetizations measurements. Spin freezing at low temperature appears to be associated with increased magnetic hardness. Furthermore, our results show evidence of temperature-dependent of coercive field which reveal a clear distinction between Mg and Sr based samples. In both cases the coercive fields follow Kneller's law of the form $H_C(T) = H_C(0)[1 - (T/T_B)^{\alpha}]$ usually associated with uniaxial symmetry of the nanoparticles. The temperature dependence of the saturation magnetizations were observed to vary with temperature according to the modified Bloch's law of the form $M_S(T) = M_S(0)[1 - (T/T_0)^{\beta}]$ with an average β value of 2.34. These results are consistent with the nanoparticle nature of the studied compounds.

Chapter 7

Structure and magnetic properties of $Mg_xMn_{1-x}Fe_2O_4$ nanoferrites

7.1 Introduction

In this chapter we present the structure and magnetic properties of $Mg_xMn_{1-x}Fe_2O_4$ nanosized compounds with $0 \leq x \leq 1.0$. The samples were synthesized at low reaction temperature of about 200 ^oC by using the glycol-thermal method. We have managed to produce samples with particle sizes in the range between 7 and 16.3 nm. The structures and magnetic properties of the synthesized samples were investigated on the as-prepared samples and on samples annealed at different temperatures. The evolutions of the properties as a function of composition have been investigated by XRD, TEM, Mössbauer spectroscopy, VSM and SQUID measurements.

7.2 Experimental details

High-purity metal nitrates were used as starting materials to make 0.1 molar (M) solutions for the glycol-thermal process. The synthesis procedures is similar to what we have presented before [23]. 5 M solution of excess KOH was slowly added to the mixture of nitrate solutions under rapid stirring until full precipitation was achieved [23]. The precipitate was washed several times by deionised water and finally by 200 ml of ethanol. The clean precipitate was dispersed in 300 ml of ethylene glycol

under rapid stirring. The mixture was reacted in a stainless steel pressure vessel. The mixture was heated to 200 ^{o}C for 6 hours and at a gauge pressure over the sample of 100 psi. The cooled products were filtered and washed by deionized water and finally by ethanol. The recovered compounds were dried under a 250 W infrared lamp for at least 12 hours, homogenized and divided into several specimens, which were subsequently sintered at different temperatures for structure and magnetic studies.

The XRD patterns for the $Mg_xMn_{1-x}Fe_2O_4$ compounds were obtained at room temperature using a monochromatic beam of CoK_α radiation (λ = 1.7903 Å). TEM measurements were obtained by TEM type Jeol_JEM-1010 instrument on the $Mg_{0.5}Mn_{0.5}Fe_2O_4$ sample. The Mössbauer spectra were recorded at about 300 K using a conventional constant acceleration Mössbauer spectrometer with a ^{57}Co source sealed in Rh matrix. A standard high-purity alpha-iron foil of was used to calibrate the Mössbauer spectra. The spectra were recorded in zero external applied magnetic fields. Basic room temperature magnetization measurements of hysteresis curves for the as-prepared and samples annealed at 700 ^{o}C of $Mg_xMn_{1-x}Fe_2O_4$ were performed on LakeShore model 735 VSM. The SQUID magnetometer was used to study the temperature dependence of magnetizations from 4 K to 380 K in magnetic fields of up to 50 kOe. These measurements included hysteresis loops, zero field cooling (ZFC) and field cooling (FC) magnetizations.

7.3 Results and discussion

7.3.1 X-ray diffraction and transmission electron microscopy measurements

Figure 7.1 shows the room temperature XRD patterns for the as-prepared samples $Mg_xMn_{1-x}Fe_2O_4$ ferrites with $0 \leq x \leq 1.0$. All the major peaks have been indexed with respect to the basic spinel structure. No impurity phases are detected in the all the samples and no additional sintering at high temperature was required to achieve single-phase formation. The sample corresponding to x = 0.0 ($MnFe_2O_4$)

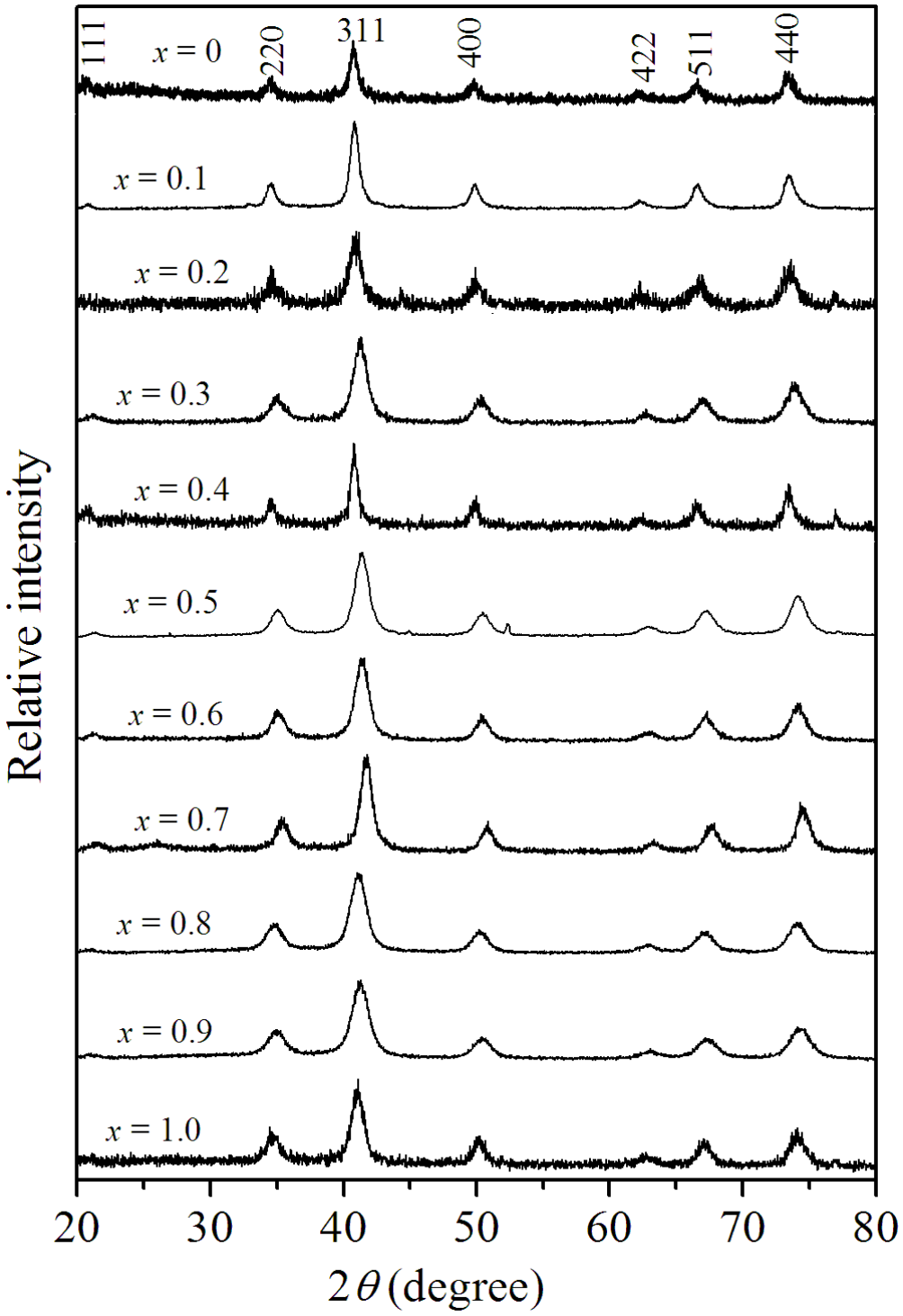

Figure 7.1: XRD patterns for the as-prepared samples of $Mg_xMn_{1-x}Fe_2O_4$.

was annealed in air at 500 ^{o}C, 1000 ^{o}C and 1100 ^{o}C in order to study the thermal stability of the spinel structure. Figure 7.2 shows the resulting XRD patterns. $MnFe_2O_4$ ferrite phase is unstable when the sample is annealed in air above 500 ^{o}C. The impurity phases have been identified to be due to the formation of Fe_2O_3 and Mn_2O_3 in oxygen rich environments [2]. In Table 7.1 we show various parameters of $Mg_xMn_{1-x}Fe_2O_4$ samples which have been deduced from XRD measurements and physical dimensions of the pelletized samples. The average grain sizes, G were estimated from broadening of the (311) XRD peak by using the Debye-Scherrer formula (equation (4.1.3)) [6]. The average particle sizes of the as-prepared samples range from 7.0±0.2 nm to 16.3±0.2 nm. The lattice parameters, a were calculated from XRD data using Bragg's law and the equation (4.1.2) [86]. We have also obtained from XRD data estimates of microstrains, ε in our samples by using equation (4.1.5). The X-ray densities, ρ_{XRD} for the as-prepared samples of $Mg_xMn_{1-x}Fe_2O_4$ were calculated by using the formula (4.1.4) [123]. The bulk densities, ρ_{Bulk} were determined on pelletized samples annealed at 700 ^{o}C. ρ_{Bulk} is obtained from the direct measurement of the physical dimensions of a pellet and its mass. The percentage porosities, $P(\%)$ of the samples were deduced from ρ_{Bulk} and ρ_{XRD} using the equation (4.1.6). Figure 7.3 shows the behaviour of lattice parameters and grain sizes as a function Mg-concentration, x. Some systematic changes are obtained but not entirely over the full concentration range. In Table 7.2 we illustrated the values of the XRD densities, bulk densities and percentage porosities for the as-prepared sample and annealed sample at 400 ^{o}C and 700 ^{o}C for the $Mg_{0.5}Mn_{0.5}Fe_2O_4$ sample. We observe that the bulk density is increased by increasing the annealing temperature, which is consistent with decreasing porosity [6].

Figure 7.4 shows the TEM micrograph for the as-prepared $Mg_{0.5}Mn_{0.5}Fe_2O_4$ nanoferrite. The micrographs can be used to calculated particle sizes and to provide directly information of particle size distribution and shape. The results show nearly spherical particles of approximately 8 nm.

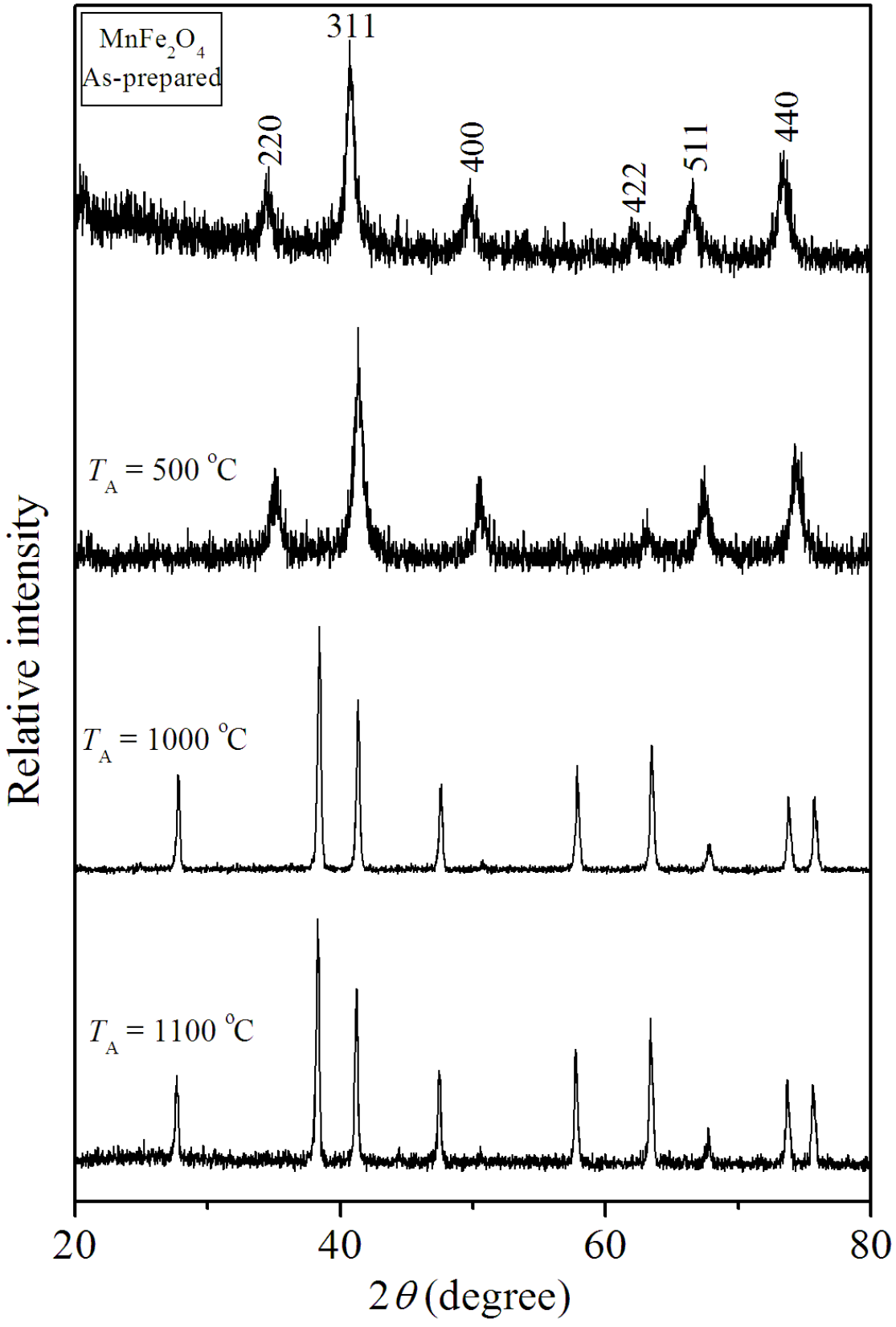

Figure 7.2: Effect of annealing temperature on the XRD patterns of $MnFe_2O_4$.

Table 7.1: Grain sizes (G), lattice parameters (a), X-ray densities (ρ_{XRD}), bulk densities (ρ_B), percentage porosities (P) and microstrains (ε) for the as-prepared samples of $Mg_xMn_{1-x}Fe_2O_4$ nanoferrites.

Sample x	G (nm) ±0.2	a (nm) ±0.0002	ρ_{XRD} (g/cm^3) ±0.02	ρ_{Bulk} (g/cm^3) ±0.06	P (%) ±2	ε ±0.00002
0	14.8	0.8527	-	-	-	0.00087
0.1	13.7	0.8508	4.91	3.13	36	0.00093
0.2	11.9	0.8500	4.85	2.78	42	0.00179
0.3	8.4	0.8424	4.93	4.57	7	0.00152
0.4	16.3	0.8515	4.70	3.55	24	0.00079
0.5	8.8	0.8404	4.82	2.79	42	0.00142
0.6	8.3	0.8400	4.75	2.48	47	0.00138
0.7	10.0	0.8337	4.79	2.61	45	0.00118
0.8	8.8	0.8452	4.53	2.63	58	0.00161
0.9	7.0	0.8424	4.51	2.03	54	0.00175
1.0	9.2	0.8466	-	-	-	0.00129

Table 7.2: XRD density (ρ_{XRD}), bulk densities (ρ_B) and percentage porosities (P) for the as-prepared sample and sample annealed at 400 ^{o}C and 700 ^{o}C for $Mg_{0.5}Mn_{0.5}Fe_2O_4$.

ρ (g/cm^3)				P (%)		
ρ_{XRD}	ρ_B	ρ_{B400}	ρ_{B700}	P	P_{400}	P_{700}
4.82	2.36	2.44	2.79	50.93	49.38	42.17

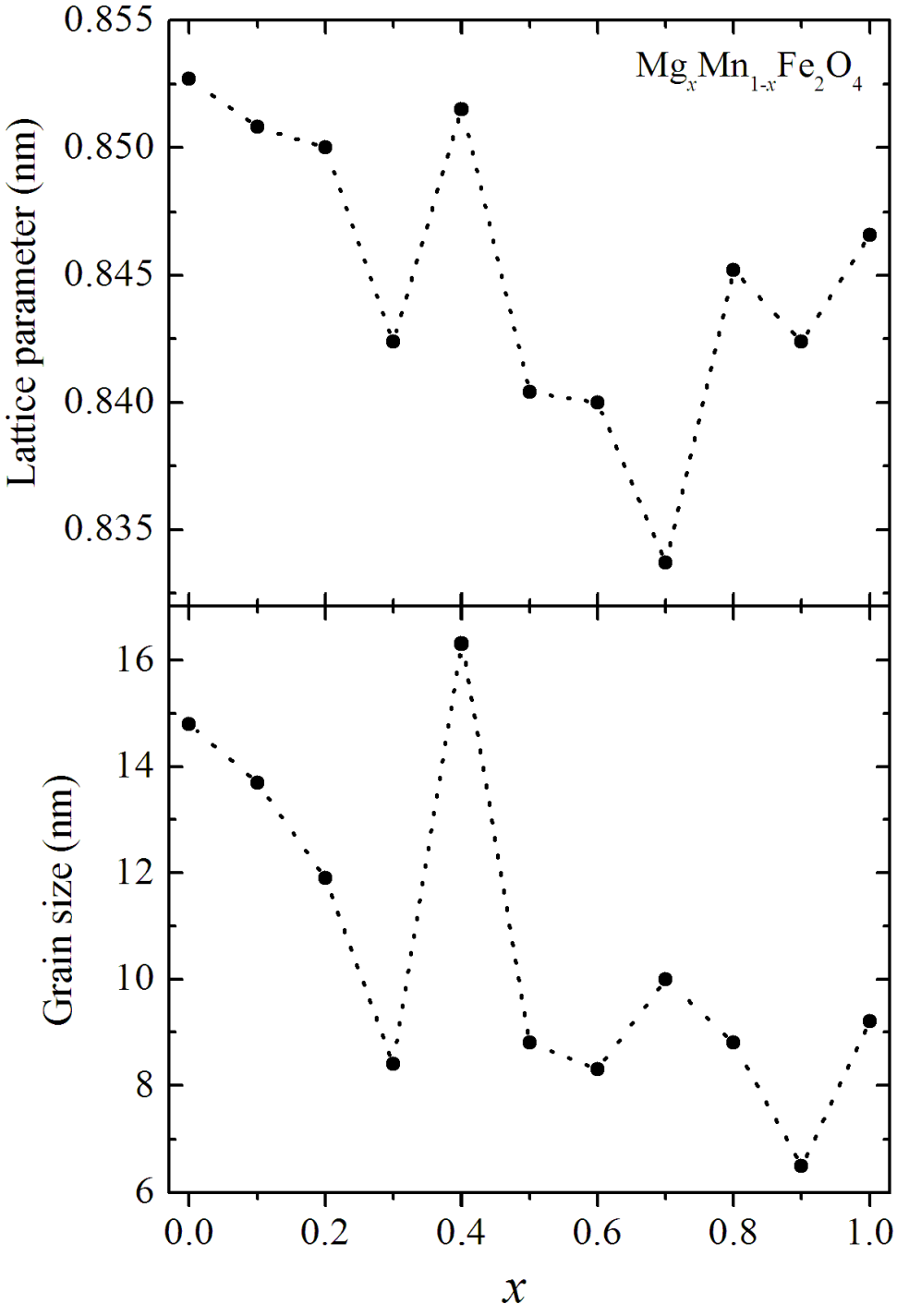

Figure 7.3: Grain sizes and lattice parameters for the as-prepared samples of $Mg_xMn_{1-x}Fe_2O_4$.

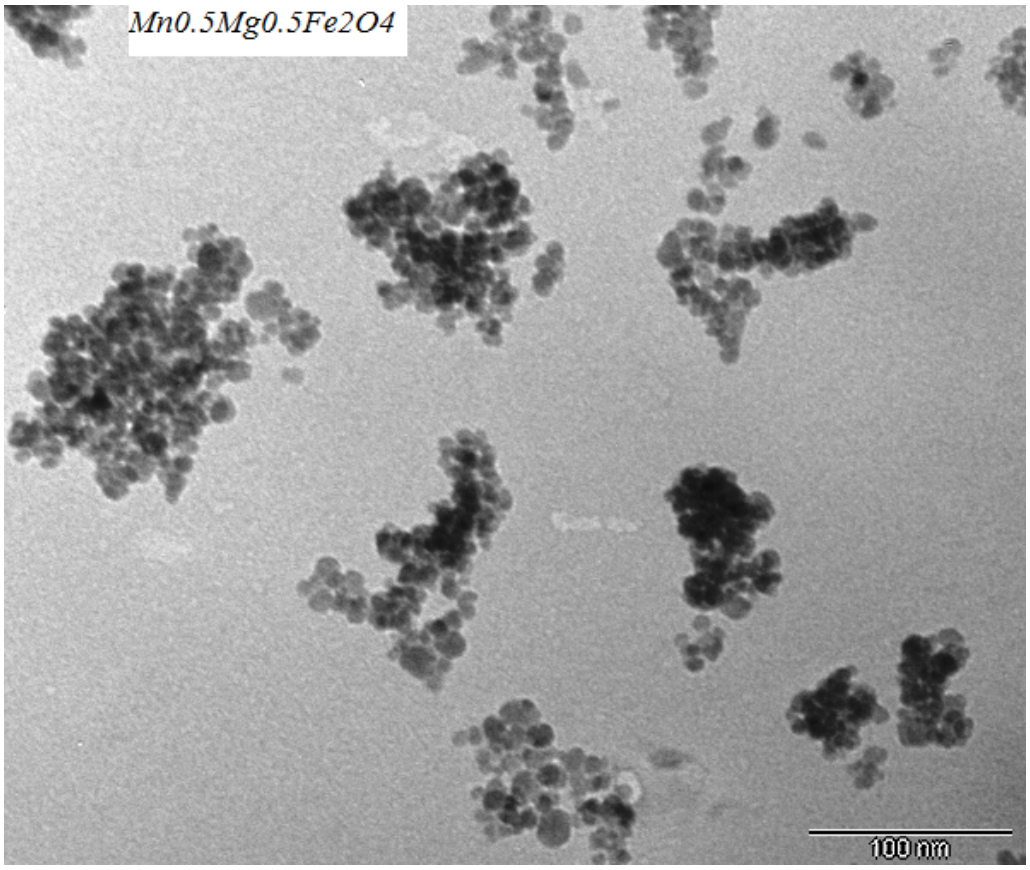

Figure 7.4: TEM image for the as-prepared sample of $Mg_{0.5}Mn_{0.5}Fe_2O_4$.

7.3.2 Mössbauer measurements

The ^{57}Fe Mössbauer absorption spectra for the as-prepared and annealed Mg_xMn_{1-x}-Fe_2O_4 samples are shown in Figures 7.5 and 7.6 respectively. The spectra were recorded at about 300 K. The spectra for samples with particles smaller than 9 nm appear relaxed. Two sextets and one doublet were used to fit the data in the ordered magnetic state. The spectra for samples with larger grains ($G > 10$ nm) required an extra sextet. Each sextet corresponds to Fe^{3+} ions in ordered spin states distributed on tetrahedral (A) or octahedral (B) sites. The third sextet with low hyperfine field may be associated with Fe^{3+} ions in grain boundaries [174]. A doublet is associated with particles in paramagnetic state. Sextets and doublets were assigned to A or B sites based on the fitted results of isomer shifts and hyperfine fields which are supposed to be lower at A site because of higher cubic symmetry and covalent nature of the tetrahedral bonds [17, 35, 149, 175]. Tables 7.3 and 7.4 show the

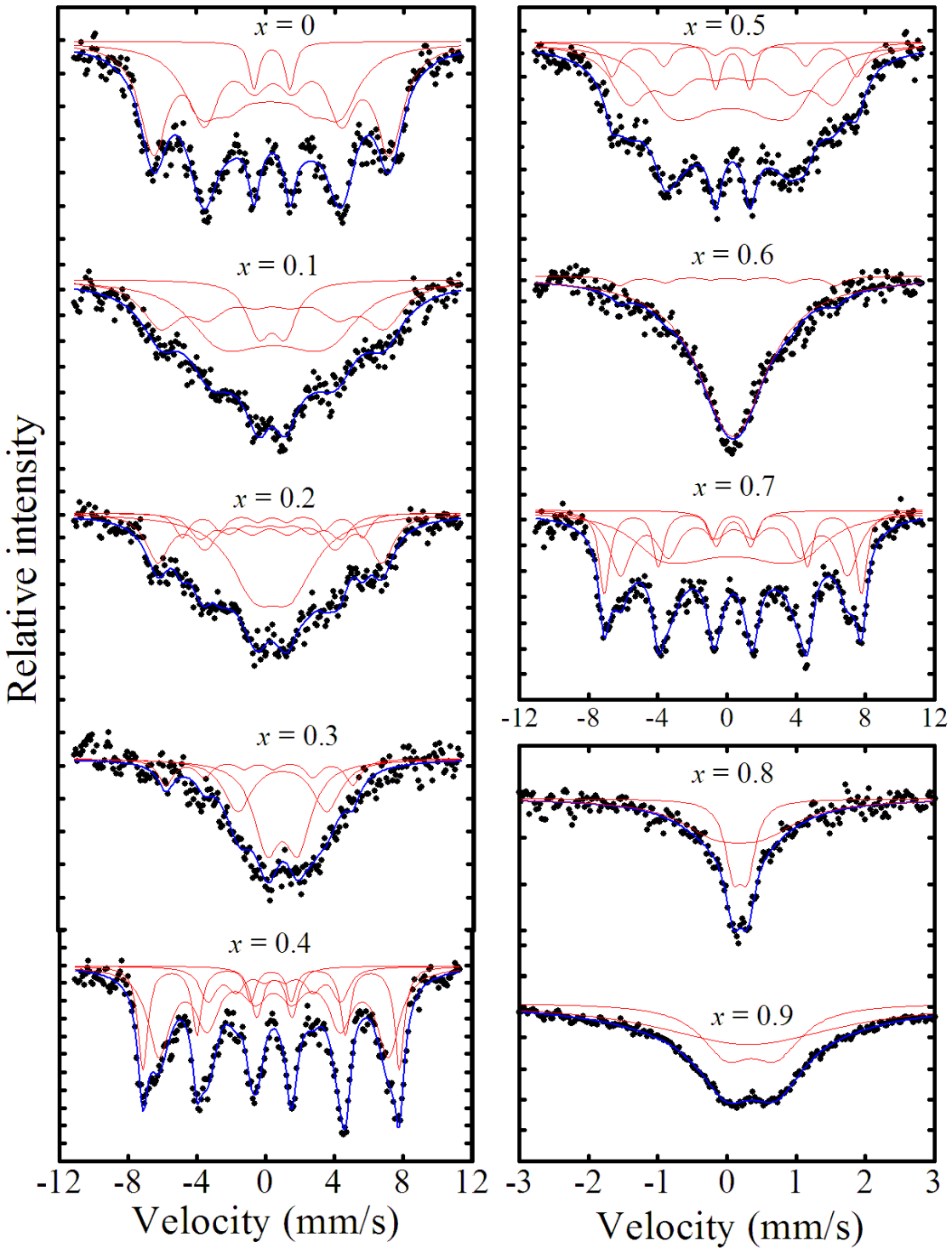

Figure 7.5: Mössbauer spectra for the as-prepared samples of $Mg_xMn_{1-x}Fe_2O_4$ measured at $T = 300$ K.

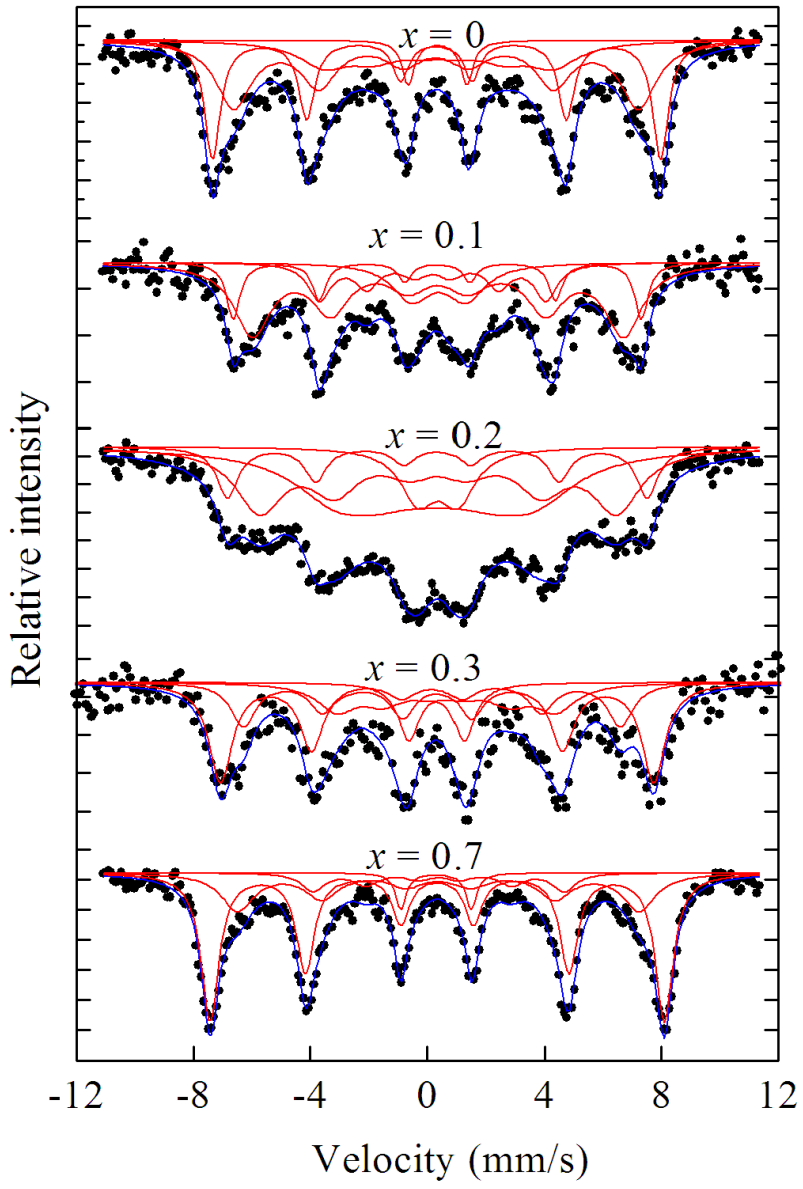

Figure 7.6: Mössbauer spectra for $Mg_xMn_{1-x}Fe_2O_4$ samples annealed at 700 ^oC and measured at $T = 300$ K.

Table 7.3: Isomer shifts (δ), hyperfine fields (H), line widths (LW) and Fe^{3+} fraction (f) on A and B sites for the as-prepared samples of $Mg_xMn_{1-x}Fe_2O_4$ measured at $T = 300$ K.

Sample	δ (mm/s)		H (kOe)			LW (mm/s)		f (%)	
x	δ_A	δ_B	H_A	H_B	H_{3rd}	LW_A	LW_B	f_A	f_B
	± 0.03	± 0.04	± 3	± 2	± 10	± 0.01	± 0.03		
0	0.31	0.30	401	469	239	0.86	0.40	41.4	54.4
0.1	0.45	0.40	213	401	–	1.92	1.32	48.8	37.6
0.2	0.25	0.38	324	402	252	0.82	0.48	30.0	60.0
0.3	0.48	0.34	335	–	–	0.98	0.97	49.1	32.7
0.4	0.34	0.48	415	463	240	0.80	0.34	36.2	52.4
0.5	0.25	0.44	368	440	224	1.27	0.53	40.0	50.6
0.6	0.23	0.34	386	–	–	0.60	2.38	25.5	74.5
0.7	0.41	0.34	408	461	257	0.76	0.37	32.2	21.0
0.8	0.18	0.19	–	–	–	0.63	0.14	66.3	33.7
0.9	0.31	0.35	–	–	–	1.60	0.45	61.8	38.2
1.0	0.44	0.41	375	448	227	0.98	0.52	40.6	25.4

Table 7.4: Isomer shifts (δ), hyperfine fields (H), line widths (LW) and Fe^{3+} fraction (f) on A and B sites for samples annealed at 700 ^{o}C for $Mg_xMn_{1-x}Fe_2O_4$ measured at $T = 300$ K.

Sample	δ (mm/s)		H (kOe)			LW (mm/s)		f (%)		
x	δ_A	δ_B	H_A	H_B	H_{3rd}	LW_A	LW_B	f_A	f_B	$f_{doublet}$
	± 0.04	± 0.07	± 12	± 4	± 15	± 0.01	± 0.03			
0	0.29	0.30	429	475	212	0.72	0.33	41.3	33.2	25.5
0.1	0.36	0.33	393	432	240	0.76	0.27	53.6	15.5	30.9
0.2	0.35	0.33	378	445	213	0.98	0.44	36.0	13.2	40.8
0.3	0.15	0.33	399	459	232	0.51	0.48	21.7	45.8	32.5
0.7	0.37	0.33	426	482	266	0.67	0.37	27.1	59.5	13.6
0.8	0.46	0.32	448	483	238	0.51	0.29	46.8	33.5	19.7

fitted data of isomer shifts, hyperfine fields, line widths and Fe^{3+} population fraction. There is no significant change in isomer shifts with composition, x. This indicates that the $s-$electron density is not significantly affected by Mg concentrations in both annealed and un-annealed samples. A general increase in hyperfine fields with increasing grain size is observed. The reduced values of the hyperfine fields for samples with smaller grains we associate with the collective excitations in small particles as explained in reference [176]. The isomer shifts of Fe^{+3} are expected to lie between 0.1 to 0.5 mm/s while for Fe^{2+} ions between 0.6 to 1.7 mm/s [153]. Our results show isomer shifts that lie between 0.18 to 0.48 mm/s. This indicates that the sextets for all the samples are caused by Fe^{+3} ions only. The line widths, LW for the A site sextets are larger than those for B sites except for the $Mg_{0.6}Mn_{0.4}Fe_2O_4$ sample (see Tables 7.3 and 7.4). The broadening of the A site LW may be caused by the presence of Fe^{+2} [153] or the superparamagnet nature for single-domain nanoparticle in these materials.

7.3.3 Magnetization measurements

The variation of magnetizations as a function of magnetic fields for the as-prepared and annealed samples of $Mg_xMn_{1-x}Fe_2O_4$ are shown in Figures 7.7 and 7.8 respectively. The measurements were recorded at room temperature using a Lakeshore VSM in applied magnetic fields of up to 14 kOe. The magnetic properties such as coercive field (H_C), maximum magnetization (M_m), saturation magnetization (M_S), remanent magnetization (M_R) and squareness were deduced from hysteresis loops. The saturation magnetizations were estimated using the law of approach to saturation given in the form of equation (2.10.1). In Figures 7.9 and 7.10 we show the initial magnetizations as a function of magnetic field. The values of coercive fields, saturation magnetizations, maximum magnetizations, remanent magnetizations, M_R/M_S ratio, high-field susceptibilities and the fit parameter b are given in Table 7.5. The variation of the magnetic parameters with Mg concentration are presented in Figures 7.11 and 7.12.

In Figure 7.13 we shows the hysteresis loops for the $Mg_{0.5}Mn_{0.5}Fe_2O_4$ sample measured at room temperature on samples that had been annealed at different temperatures under Ar atmosphere. We estimated the coercive fields to be 15 Oe, 16 Oe, 12 Oe, 15 Oe and 60 Oe for the as-prepared sample and for samples annealed at 300 ^{o}C, 400 ^{o}C, 500 ^{o}C and 700 ^{o}C respectively. The values of the coercive fields and saturation magnetizations for the annealed samples for $x = 0.5$ are shown in Figure 7.14. The 'S' like shape of the magnetization curves with low coercive fields indicates superparamagnetic behaviour of the fine particles. This relates well with the doublet associated with the paramagnetic nature of the particles that was required to get good fits to the Mössbauer data.

Figure 7.15 shows the variation of the magnetizations as a function of temperature for the $Mg_{0.5}Mn_{0.5}Fe_2O_4$ sample. During field-cooling (FC), the sample was cooled from 350 K to 2 K in the presence of external magnetic fields of 0.05 kOe, 0.20 kOe and 10 kOe. The lower curves are obtained for zero field cooling (ZFC) and the upper curves are for the FC. The magnetization in the FC curve decreases continuously with increasing temperature. The width of the peak in the ZFC curve is associated with particle size distribution. Particles with a particular size

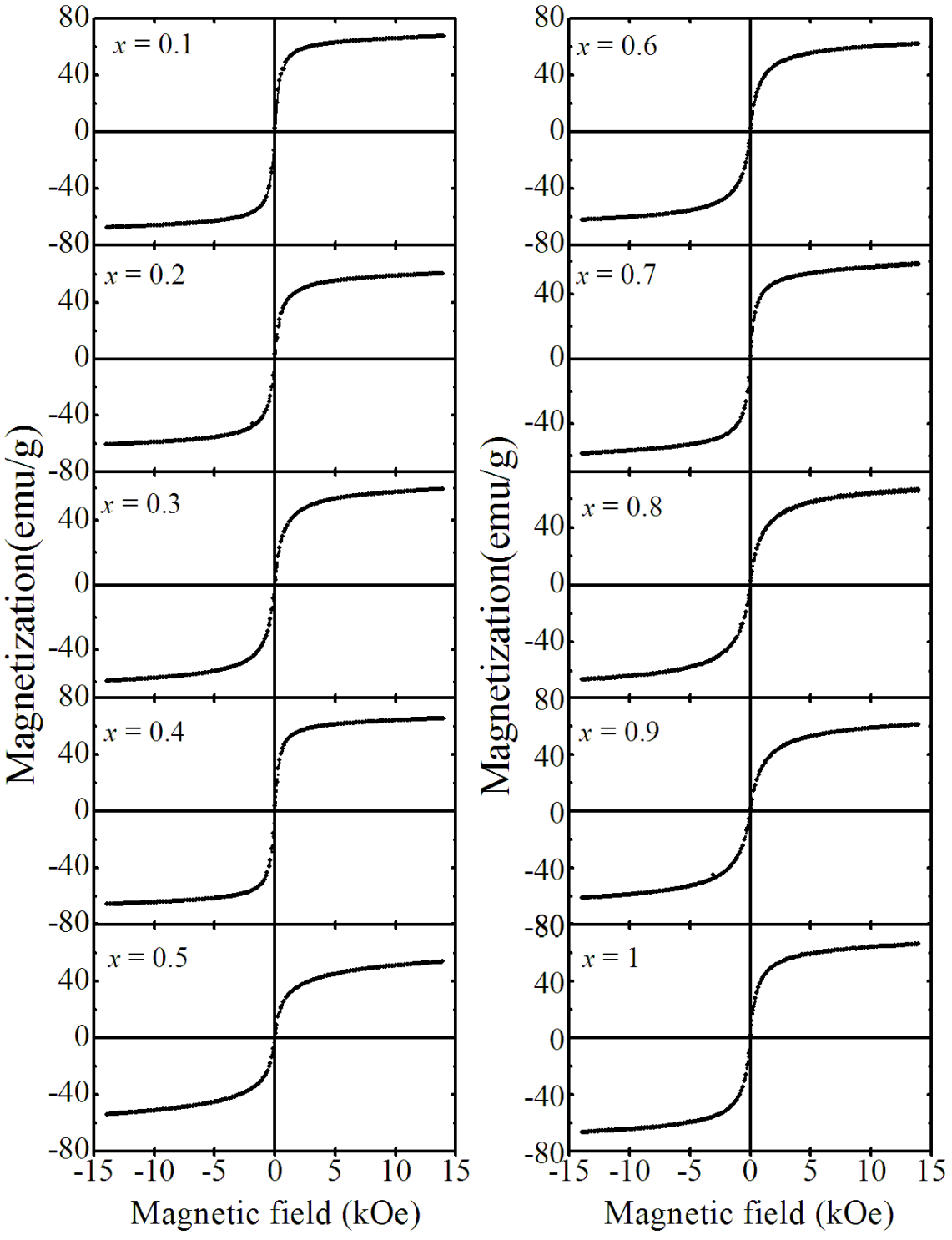

Figure 7.7: Hysteresis loops for the as-prepared samples of $Mg_xMn_{1-x}Fe_2O_4$ measured at 300 K.

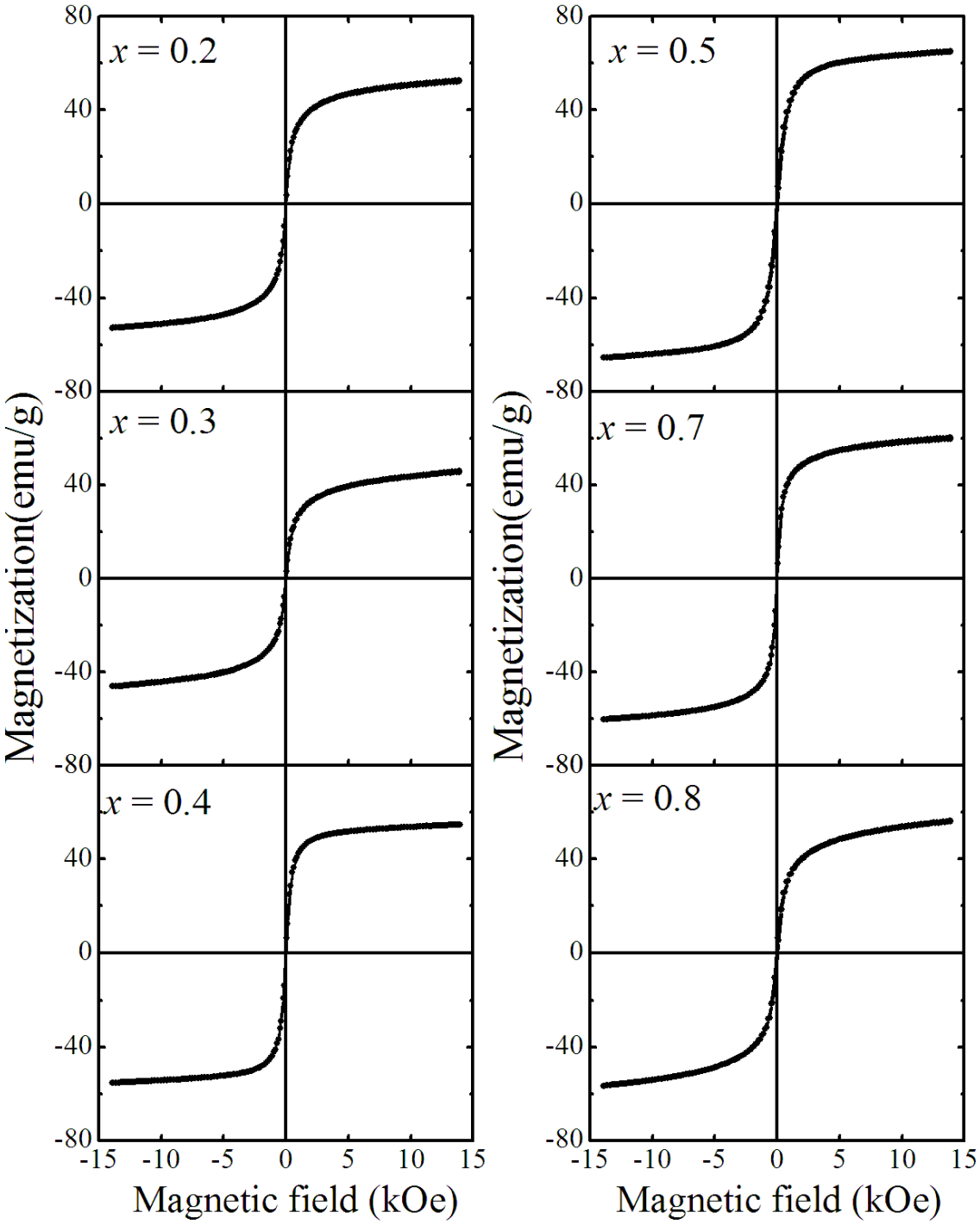

Figure 7.8: Hysteresis loops for $Mg_xMn_{1-x}Fe_2O_4$ samples annealed at 700 ^oC and measured at 300 K.

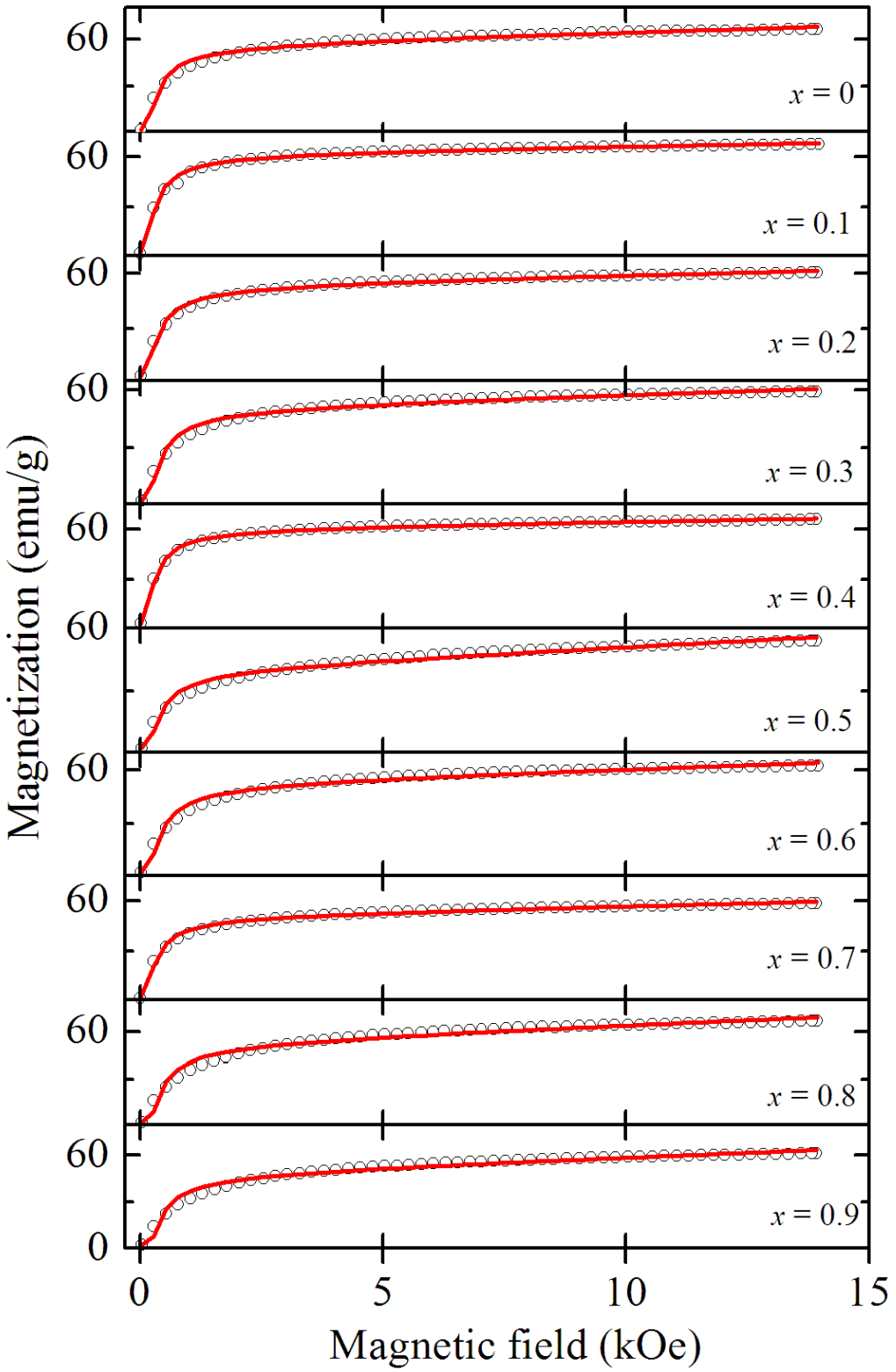

Figure 7.9: Initial magnetizations as a function of magnetic field for the as-prepared samples of $Mg_xMn_{1-x}Fe_2O_4$. The solid lines are the best fit to the data using the formula of approach to saturation given by equation (2.10.1).

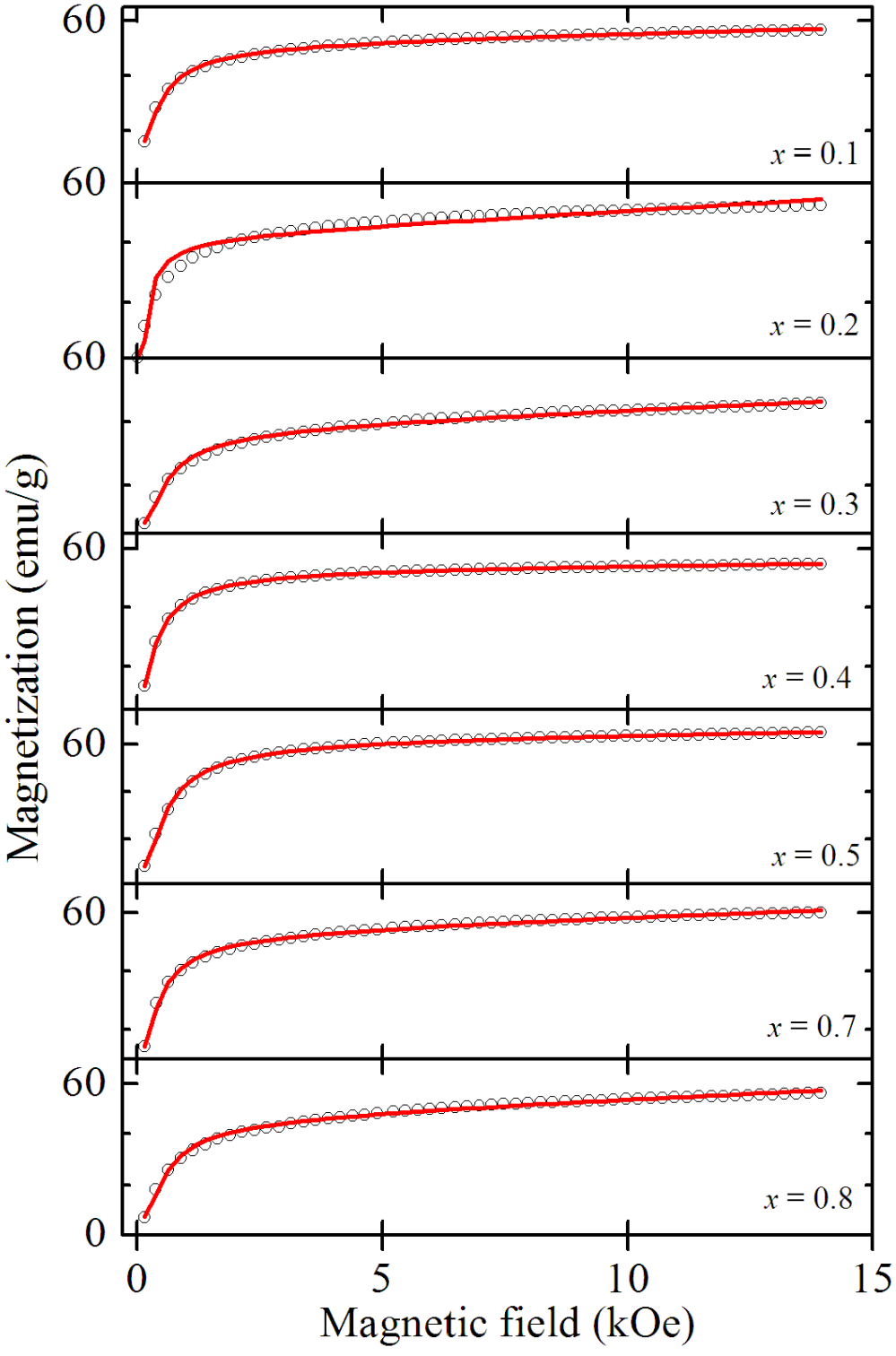

Figure 7.10: Initial magnetizations as a function of magnetic field for the samples annealed at 700 ^{o}C of $Mg_xMn_{1-x}Fe_2O_4$. The solid lines are the best fit to the data using the formula of approach to saturation given by equation (2.10.1).

Table 7.5: Coercive fields (H_C), saturation magnetizations (M_S), maximum magnetizations (M_m), remanent magnetizations (M_R), ratio M_R/M_S and parameters obtained from the empirical law of approach to saturation for the as-prepared and annealed samples of $Mg_xMn_{1-x}Fe_2O_4$ measured at 300 K.

As-prepared x	H_C (Oe) ±2	M_S (emu/g) ±0.5	M_m (emu/g) ±0.1	M_R (emu/g) ±0.2	M_R/M_S ±0.008	b (Oe^{-2}) ±0.0003	χ ±0.06
0	10	56.5	66.5	0.9	0.015	-0.0035	0.86
0.1	14	62.2	67.6	1.3	0.021	-0.0023	0.49
0.2	15	53.5	60.5	0.9	0.017	-0.0054	0.63
0.3	12	50.8	59.2	0.4	0.009	-0.0074	0.76
0.4	18	60.8	66.0	1.7	0.027	-0.0028	0.44
0.5	17	40.2	53.9	0.7	0.018	-0.0075	1.16
0.6	15	52.3	62.2	0.6	0.012	-0.0067	0.89
0.7	12	50.7	58.4	1.2	0.024	-0.0017	0.67
0.8	12	52.6	66.1	0.5	0.009	-0.0083	1.26
0.9	11	48.0	61.3	0.4	0.008	-0.0089	1.17
700 ^{o}C	±2	±0.3	±0.2	±0.2	±0.005	±0.0008	±0.02
0.1	19	52.3	56.5	1.6	0.030	-0.0218	0.41
0.2	12	42.0	52.7	0.9	0.021	-0.0017	0.93
0.3	18	38.4	46.0	1.1	0.029	-0.0314	0.64
0.4	27	53.3	55.0	3.0	0.055	-0.0184	0.16
0.5	60	63.1	65.3	4.9	0.078	-0.0336	0.27
0.7	28	54.0	60.2	2.8	0.053	-0.0203	0.56
0.8	58	47.0	56.5	4.1	0.088	-0.0321	0.83

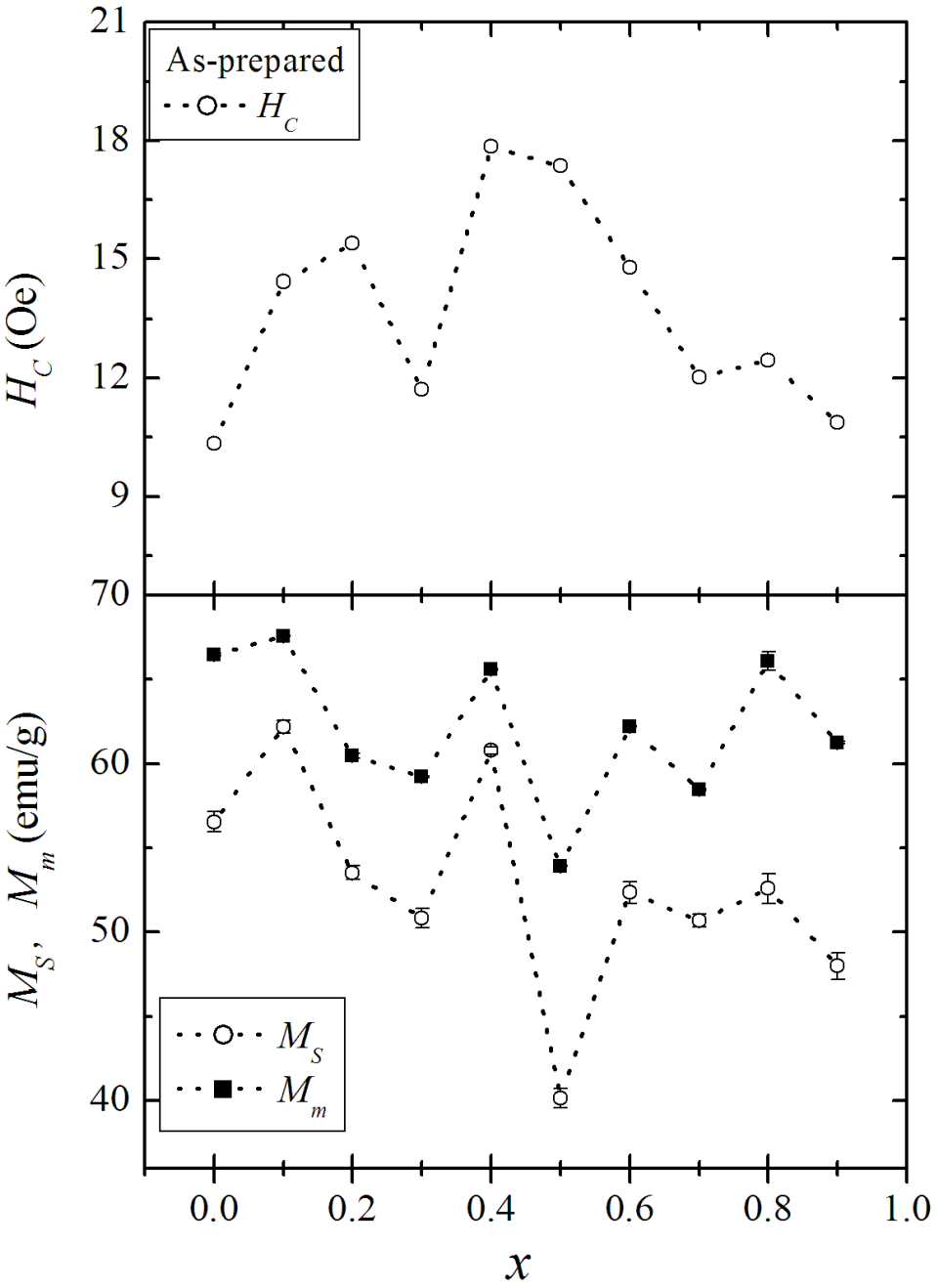

Figure 7.11: Coercive fields, saturation magnetizations and maximum magnetizations for the as-prepared samples of $Mg_xMn_{1-x}Fe_2O_4$.

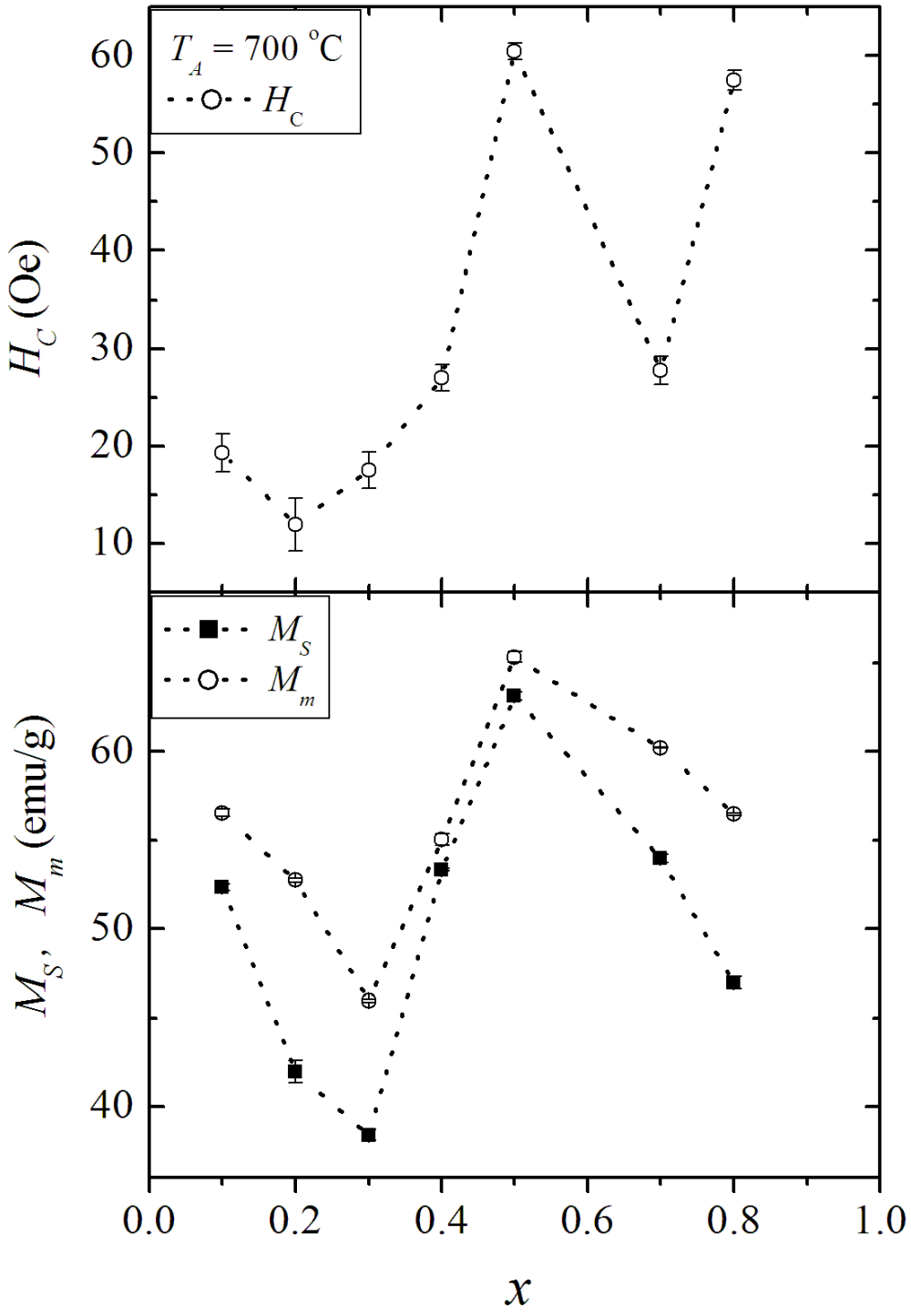

Figure 7.12: Coercive fields, saturation magnetizations and maximum magnetizations for $Mg_xMn_{1-x}Fe_2O_4$ samples annealed at 700 ^{o}C.

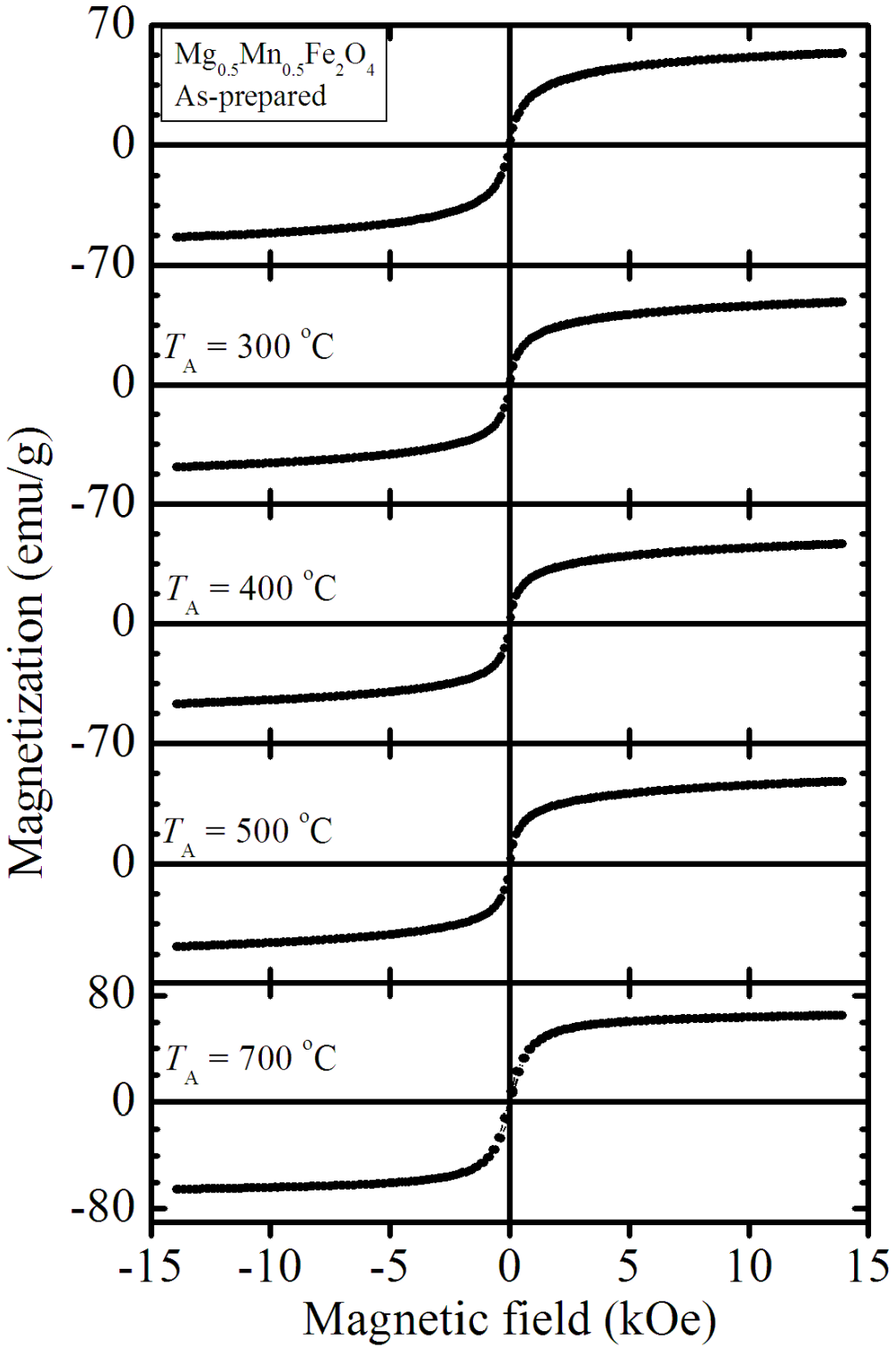

Figure 7.13: Hysteresis loops for $Mg_{0.5}Mn_{0.5}Fe_2O_4$ sample annealed at different temperatures and measured at 300 K.

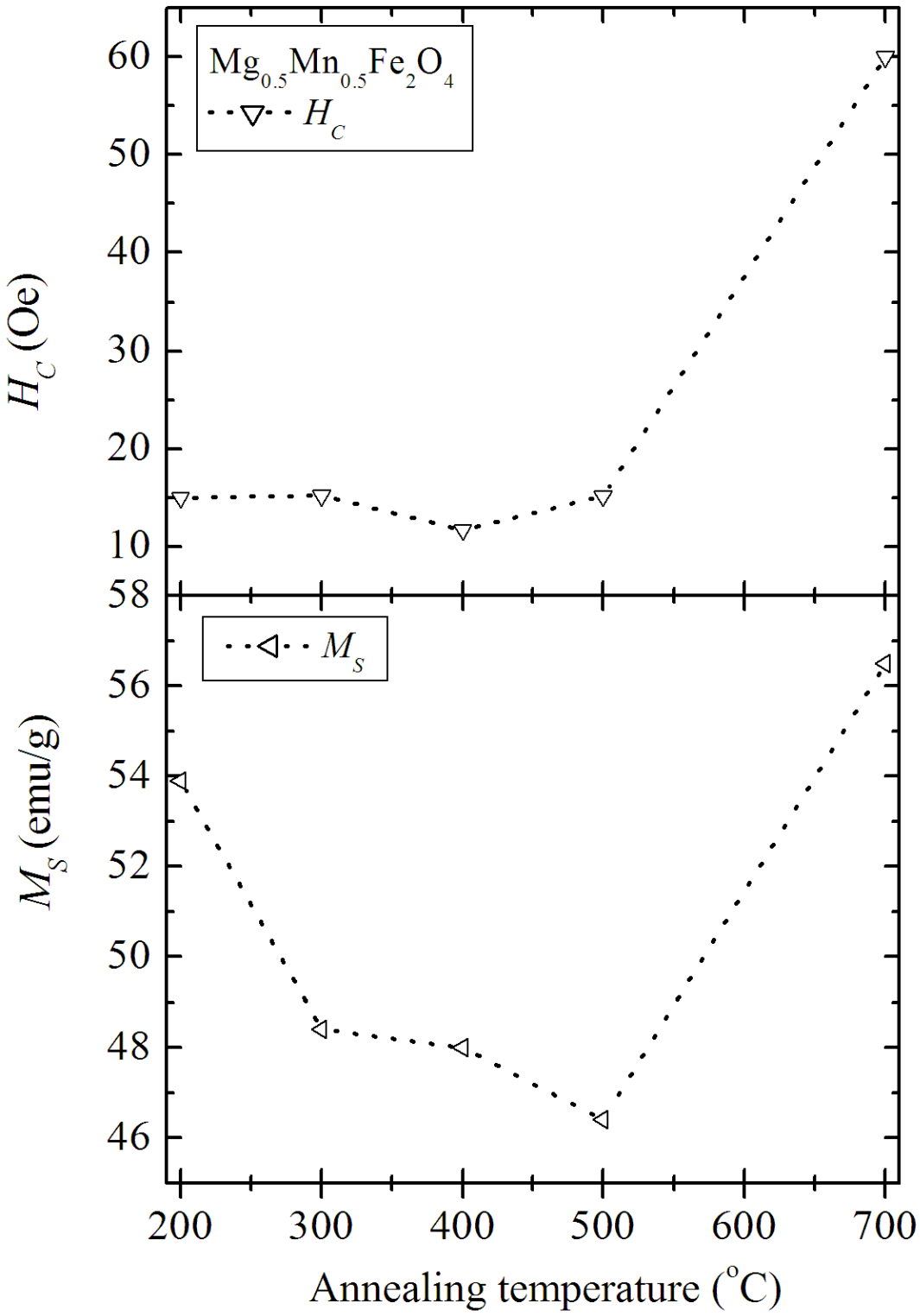

Figure 7.14: Coercive fields and saturation magnetizations for $Mg_{0.5}Mn_{0.5}Fe_2O_4$ sample annealed at different temperatures.

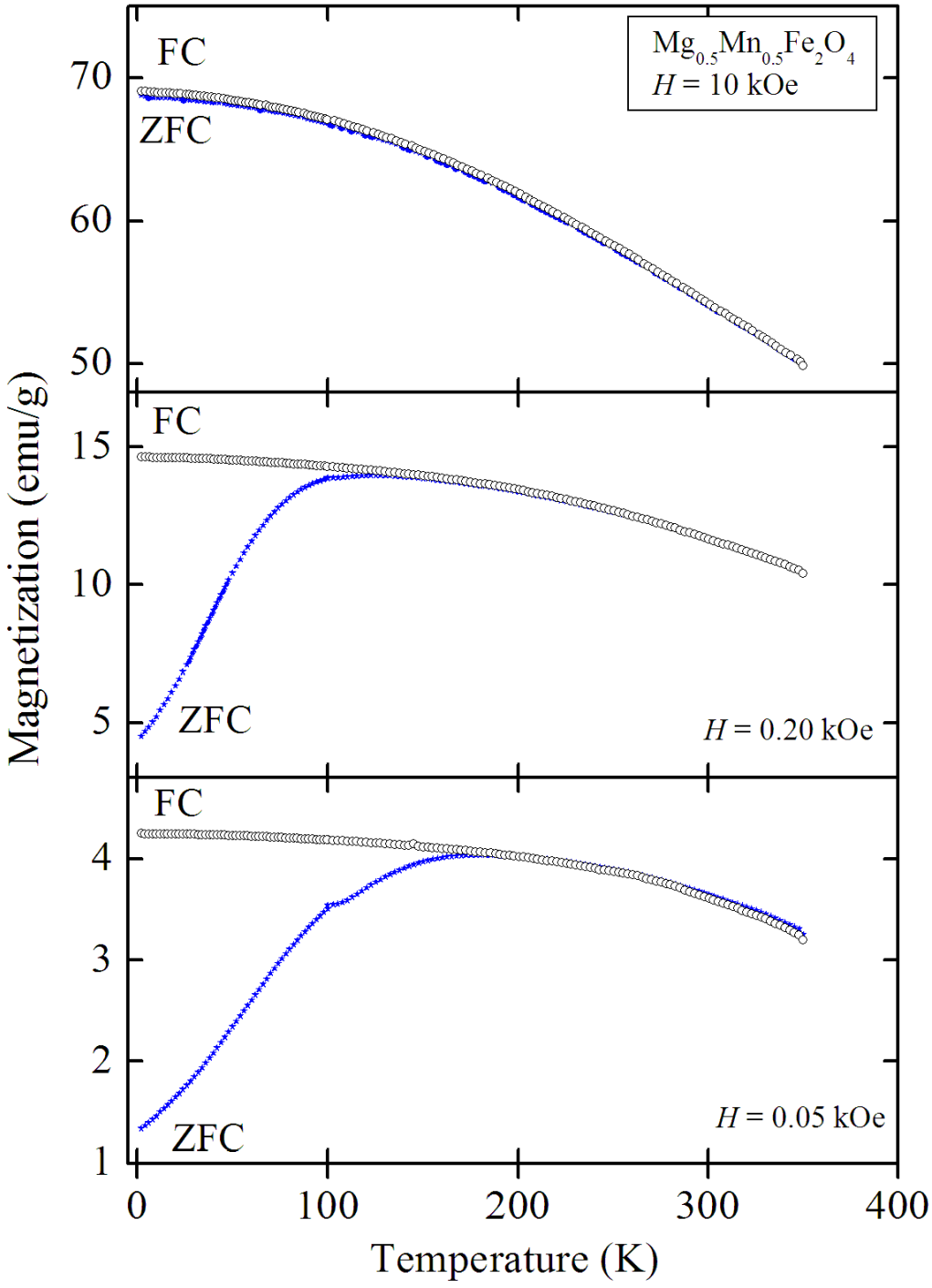

Figure 7.15: Temperature dependence of ZFC and FC magnetizations of $Mg_{0.5}Mn_{0.5}Fe_2O_4$ measured in different static applied magnetic fields.

has a certain blocking temperature. The wide peaks observed in our samples indicate a wide distribution in particle sizes as confirmed by TEM measurements in Figure 7.4. The FC magnetization tends to saturate at low temperatures. The bifurcation temperature is about 200 K at $H = 0.05$ kOe. The ZFC measurements increase gradually with increasing measured temperature up to a blocking temperature (T_B) at low temperature. The increased thermal agitation of the superspins helps the alignment of the spins in the field direction [94]. The blocking temperature at applied static fields of 0.05 kOe and 0.20 kOe are found to be 180 K and 128 K respectively. T_B decreases with the increasing static magnetic field. This difference in T_B has been attributed to the magnetocrystalline anisotropy and $L-S$ coupling. Above T_B, the nanoparticle magnetic spins behave like superparamagnetic particles with fluctuating spins directions due to thermal energy [10].

Figure 7.16 shows the magnetic field dependence of the magnetization curves for the as-prepared $Mg_{0.5}Mn_{0.5}Fe_2O_4$ sample measured at different temperatures. Full saturation is not achieved even in applied magnetic fields of 50 kOe. The values for coercive fields (H_C), saturation magnetizations (M_S), remanent magnetizations (M_R), ratio M_R/M_S and magnetic moment per molecule (μ) obtained from the hysteresis loops are given in Table 7.6. The coercive field, remanent magnetization, ratio M_R/M_S and magnetic moment per molecule decreased with increasing measuring temperature. The increased coercive field at low temperatures is assumed to be due to spin freezing of the nanoparticles. Figure 7.17 shows the temperature dependence of the coercive field and saturation magnetization which have been fitted by the Kneller's law (equation (2.10.2)) [97] and the modified Bloch's law (equation (2.8.6)) [158, 159] respectively as illustrated in Figure 7.18. We attributed this to the confinement effects of the spin-wave spectrum for magnetic clusters.

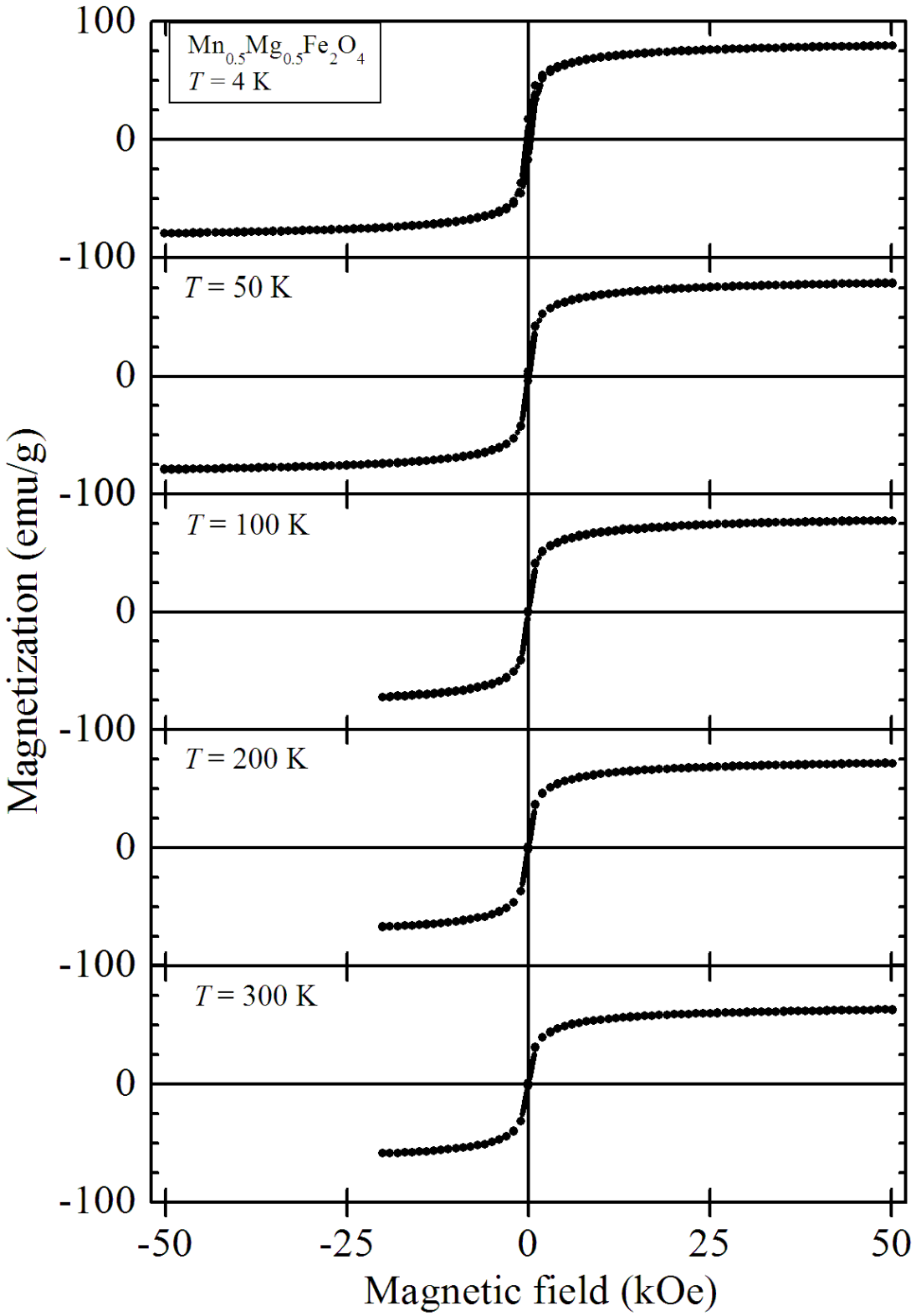

Figure 7.16: Hysteresis loops for $Mg_{0.5}Mn_{0.5}Fe_2O_4$ measured at different temperatures.

Table 7.6: Coercive fields (H_C), saturation magnetizations (M_S), remanent magnetizations (M_R), ratio M_R/M_S and magnetic moment per molecule (μ) for the as-prepared sample of $Mg_{0.5}Mn_{0.5}Fe_2O_4$ measured at different temperatures.

T (K)	H_C (Oe)	M_S (emu/g)	M_R (emu/g)	M_R/M_S	μ (μ_B)
4	208.9	79.65	17.36	0.219	3.07
50	32.8	79.10	3.78	0.048	3.05
100	21.1	77.50	1.32	0.021	3.00
200	18.3	71.75	1.38	0.019	2.77
300	10.5	63.08	0.45	0.006	2.43

7.4 Conclusions

The $Mg_xMn_{1-x}Fe_2O_4$ compounds with particle sizes between 7 nm and 16.3 nm have been produced by the glycol-thermal method at low reaction temperature of 200 ^{o}C. The crystal structure appears to be unstable when samples are at temperatures above 500 ^{o}C in air. The magnetization curves with low values of coercive fields and the broadened Mössbauer spectra provide some evidence for superparamagnetic behaviour of the synthesized samples. Variation of the saturation magnetizations and coercive fields with measuring temperature have been found to follow partly the modified Bloch's law and the Kneller's law respectively.

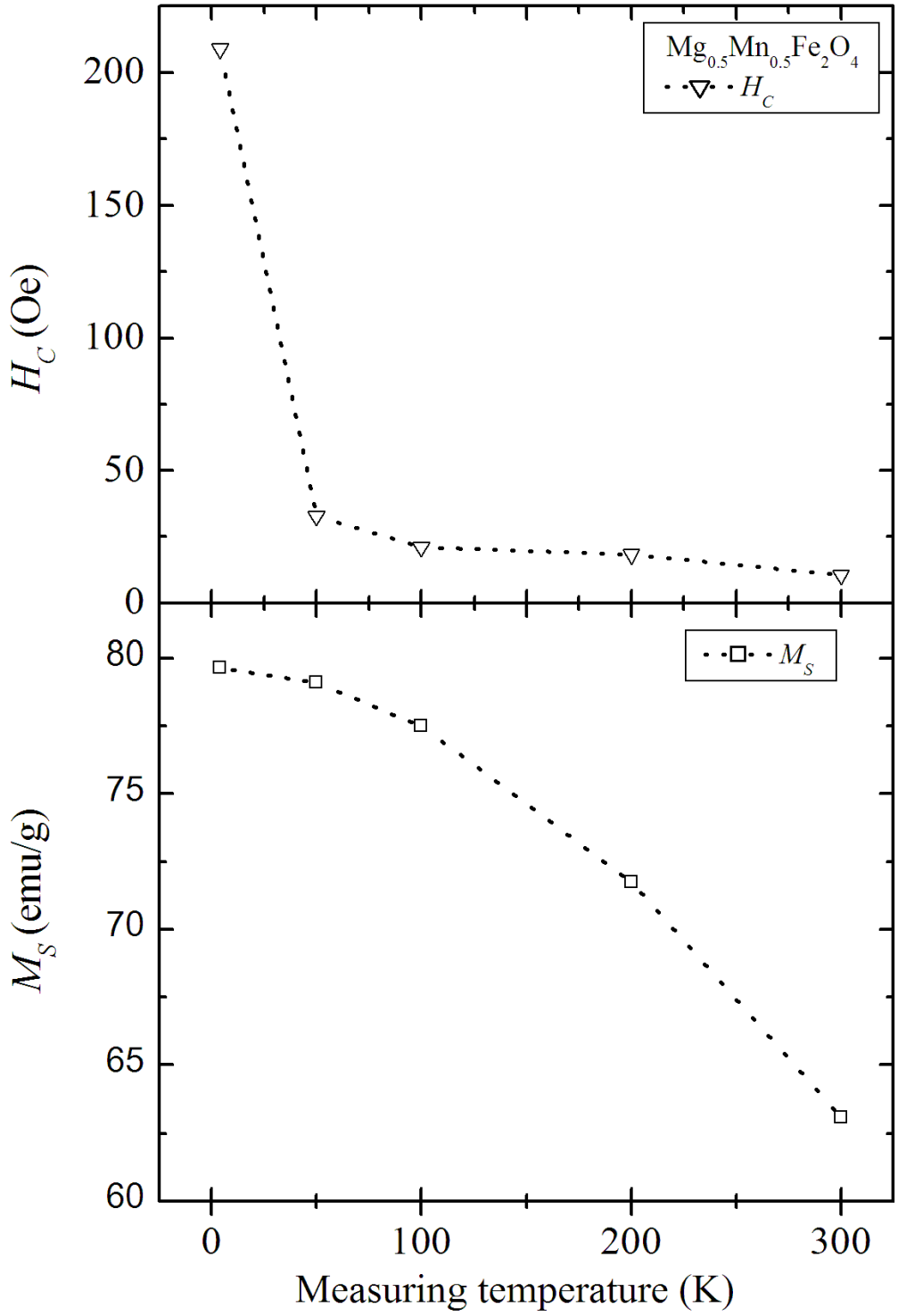

Figure 7.17: Coercive fields and saturation magnetizations for the as-prepared sample of $Mg_{0.5}Mn_{0.5}Fe_2O_4$ measured at different temperatures.

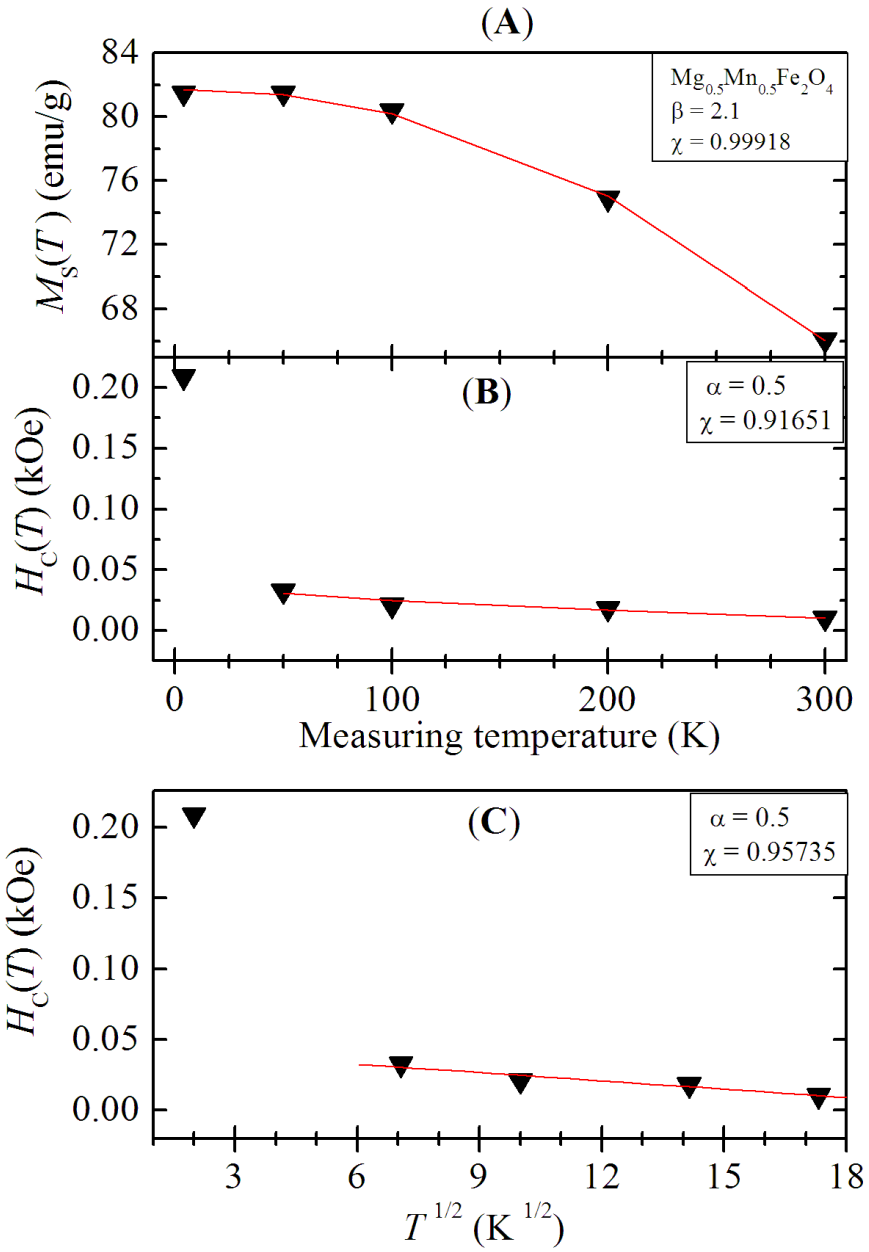

Figure 7.18: Variation of saturation magnetizations and coercive fields with measuring temperature for the as-prepared sample $Mg_{0.5}Mn_{0.5}Fe_2O_4$. The solid lines in: **(A)** follows the Bloch's law, **(B)** follows the Kneller's law and **(C)** follows a linear fit.

Chapter 8

Structure and magnetic properties of $Mg_{0.5}Mn_{0.5}(RE)_{0.1}Fe_{1.9}O_4$ nanoferrites

8.1 Introduction

The properties of ferrites are strongly dependent on a number of factors such as preparation method, annealing process and the type of cations and type of doping atoms distributed amongst the tetrahedral and octahedral sites [177]. Magnetic properties of Mg-Mn ferrites have been studied extensively. Previous substitutions in Mg-Mn ferrites have consisted of replacing of Fe ions by In^{3+} ions to produce compounds with more enhanced permeability [58, 178]. This makes the compounds more suitable for high frequency and magneto-electric applications [58, 76]. The rare earth (RE) atoms are also candidate additives which can be used to modify the properties of ferrites [177]. RE oxides are used in fuel cells, solid electrolytes, phosphors, additives in iron and steel industry, catalysts and biomedical applications [179]. The role of RE ions depends on the effect electronic configuration influenced by localised 4f electrons and larger ionic radii [180]. The magnetic properties can therefore be controlled by substitution in the host spinel structure by RE ions [181]. RE oxides are also good electrical insulators with high electrical resistivity. However, there seems to be a limit to the solubility of RE ions because of their large radii

in the spinel lattice. For $(RE)_x$ with $x \geq 0.2$, secondary phases appear to form on grain boundaries [179, 180, 182]. Following our recent work on $Mg_xMn_{1-x}Fe_2O_4$ nanoferrites [23], we have produced a series $Mg_{0.5}Mn_{0.5}(RE)_{0.1}Fe_{1.9}O_4$ where RE = Ce, Nd, Sm, Eu, Gd, Tb, Dy, Ho, Yb and Lu by glycol-thermal reaction in order to investigate the effect of RE substitutions in $Mg_{0.5}Mn_{0.5}Fe_2O_4$ compound. We intend to investigate how the structure and magnetic properties of the studied materials are affected by changing the atomic radii and electronic configurations of the RE atoms.

8.2 Experimental details

$Mg_{0.5}Mn_{0.5}(RE)_{0.1}Fe_{1.9}O_4$ nanosized ferrites compounds have been synthesis by glycol-thermal method on a Watlow series model PARR 4843 stirred pressure reactor from high-purity metal chlorides following a procedure which we have described earlier in chapter 4 and reported elsewhere in our previous works [17, 18]. In this procedure filtering the precipitate by Whatman glass micofiber GF/F filters important in order to achieve the smallest particle sizes. Powder X-ray diffraction (XRD) measurements were performed on a Phillips diffractometer type PW 1710 using a monochromatic beam of CoK_α radiation. The morphology of the samples were estimated by a Jeol_JEM-2100 high-resolution transmission electron microscopy (HRTEM). A Lakeshore model 735 vibrating sample magnetometer (VSM) was used for magnetic characterization of the samples at room temperature in applied fields of up to about 14 kOe. Zero-field ^{57}Fe Mössbauer spectra were determined using a conventional spectrometer with a 25 mCi ^{57}Co source sealed in Rh matrix and vibrated at constant acceleration. The spectrometer was calibrated by a natural iron foil. All measurements were performed on samples without any subsequent annealing stage.

8.3 Results and discussion

8.3.1 X-ray diffraction and high-resolution transmission electron microscopy measurements

X-ray diffraction was used to investigate the effect of doping by rare earth (RE) elements (Ce, Nd, Sm, Eu, Gd, Tb, Dy, Ho, Yb and Lu) on the structure of the $Mg_{0.5}Mn_{0.5}Fe_2O_4$ ferrite. The as-prepared samples were in the form of powders. Figure 8.1 shows X-ray patterns obtained at room temperature for all $Mg_{0.5}Mn_{0.5}(RE)_{0.1}$-$Fe_{1.9}O_4$ ferrites synthesized. The spectra show single-phase formation with all peaks indexed to the (111), (220), (311), (400), (422), (511) and (440) reflections corresponding to the cubic spinel structure with space group $Fd\tilde{3}m$ [8]. The broad peaks for all the compounds are indicative of nanoparticle sizes of the compounds. No intermediate or additional phases were observed in the synthesized samples. The average grain sizes (D) can be calculated particles from the full-width at half-maximum ($W_{1/2}$) of the (311) XRD peak using the Debye-Scherrer formula (equation (4.1.3)) [17, 18, 62]. The lattice parameters can also be calculated by using Bragg's law and equation (4.1.2). In Table 8.1, we show results of grain sizes (D), lattice parameters (a), X-ray densities (ρ_{XRD}) and microstrains (ε). The grain sizes are found in the range $9-15$ nm. The XRD densities ρ_{XRD} were deduced from X-ray patterns using the equation (4.1.4). The microstrains were also deduced using equation (4.1.5). Pandit et al. [184] have reported comparable results of X-ray densities. In order to test the sensitivity of grain sizes, lattice parameters and microstrains due to rare earth ions, plots of grain size, lattice parameters and microstrains as functions of RE^{3+} 4f electron number are given in Figures 8.2 – 8.4 respectively. The results show increases in grain sizes and lattice parameters for the RE substituted compounds which can be attributed to large RE ions substituting smaller Fe ions. The non-linear behaviour of grain sizes and lattice parameters with RE substitutions appear to be common feature associated with other parameter of RE-based compounds. Slight reduction in the microstrains are observed for all rare earth substitutions exhibited in Figure 8.4.

Figures 8.5 and 8.6 show HRTEM images of $Mg_{0.5}Mn_{0.5}(Ce, Gd)_{0.1}Fe_{1.9}O_4$ com-

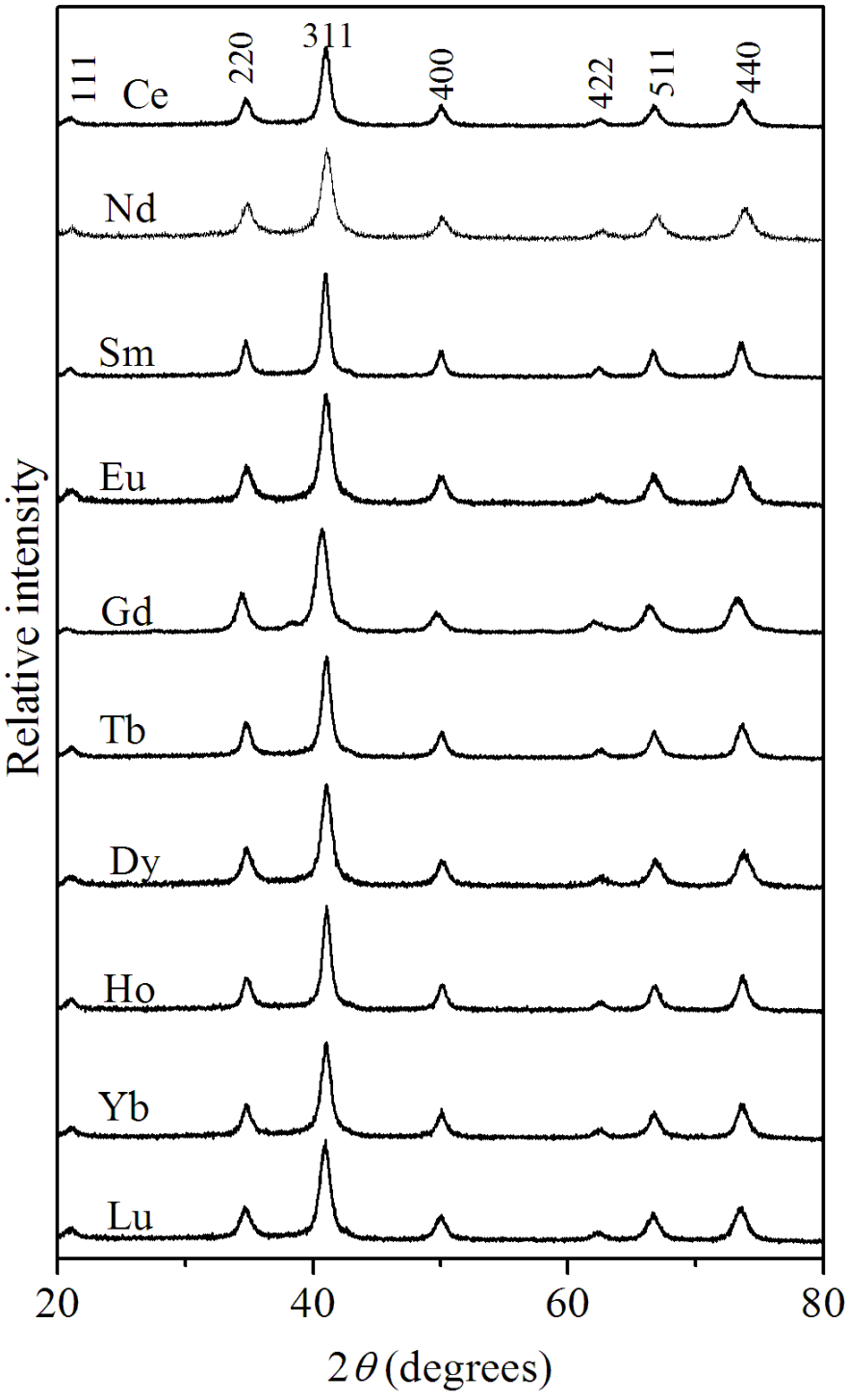

Figure 8.1: X-ray patterns for the as-prepared samples of $Mg_{0.5}Mn_{0.5}(RE)_{0.1}Fe_{1.9}O_4$ nanoferrites.

Table 8.1: Grain size (D), lattice parameter (a), XRD density (ρ_{XRD}) and microstrain (ε) for the as-prepared samples of $Mg_{0.5}Mn_{0.5}(RE)_{0.1}Fe_{1.9}O_4$ nanoferrites.

Sample RE	D (nm) ±0.4	a (nm) ±0.0001	ρ_{XRD} (g/cm^3) ±0.04	ε ±0.00001
0	8.8	0.8404	4.82	0.00142
Ce	11.05	0.8491	4.85	0.00104
Nd	12.55	0.8471	4.90	0.00092
Sm	10.80	0.8468	4.92	0.00106
Eu	9.78	0.8461	4.94	0.00117
Gd	14.29	0.8484	4.90	0.00081
Tb	13.99	0.8465	4.94	0.00082
Dy	11.52	0.8479	4.92	0.00099
Ho	10.39	0.8474	4.94	0.00111
Yb	11.62	0.8477	4.95	0.00099
Lu	10.01	0.8538	4.85	0.00116

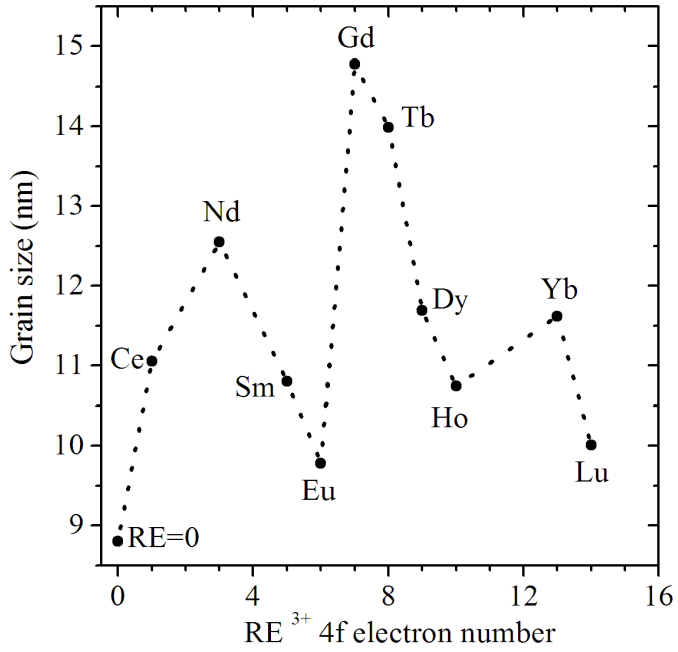

Figure 8.2: Grain sizes (D) of $Mg_{0.5}Mn_{0.5}(RE)_{0.1}Fe_{1.9}O_4$ nanoferrites plotted as a function of RE^{3+} 4f electron number.

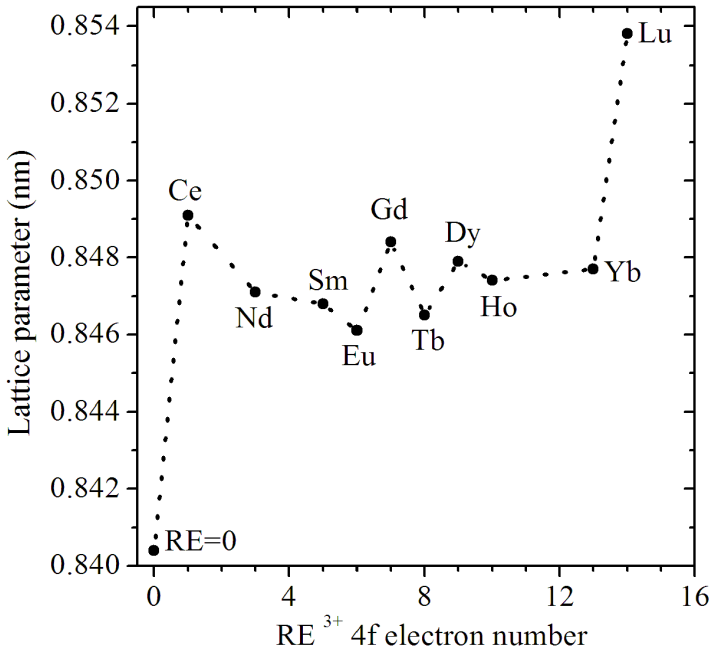

Figure 8.3: Lattice parameters (a) of $Mg_{0.5}Mn_{0.5}(RE)_{0.1}Fe_{1.9}O_4$ nanoferrites plotted as a function of RE^{3+} 4f electron number.

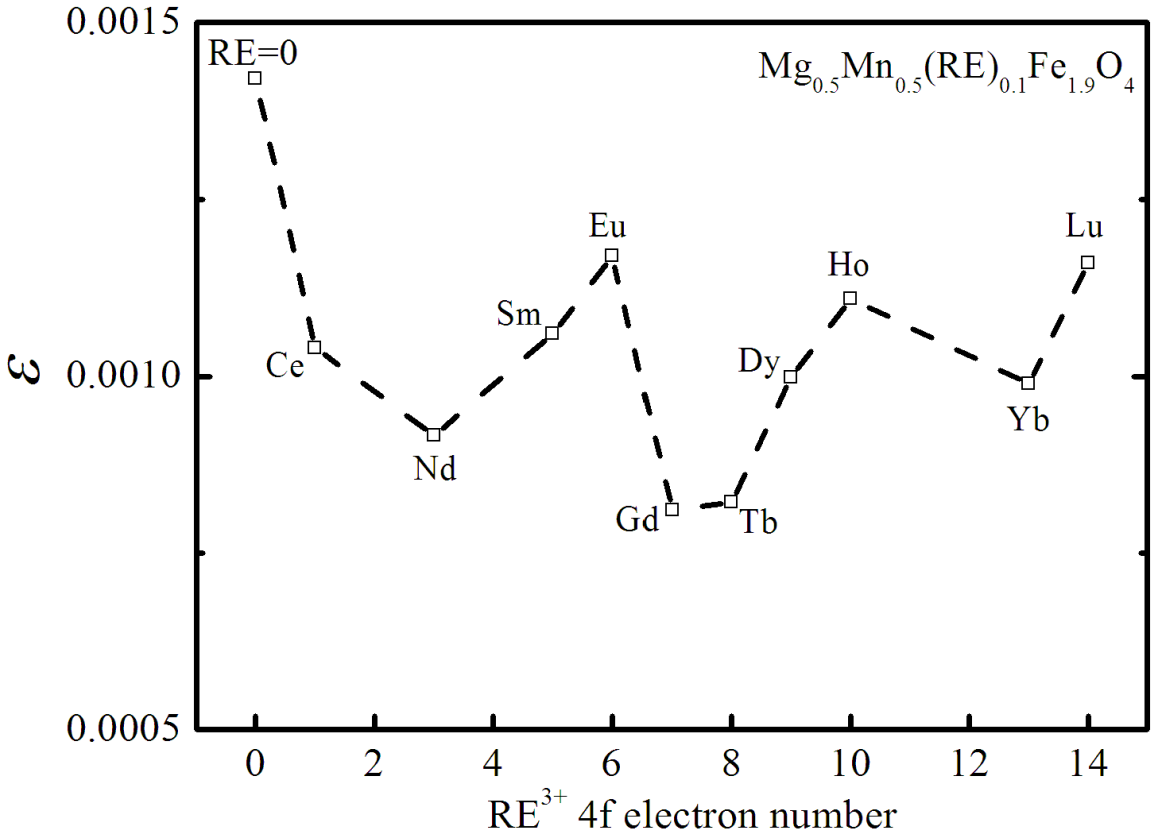

Figure 8.4: Microstrains (ε) for $Mg_{0.5}Mn_{0.5}(RE)_{0.1}Fe_{1.9}O_4$ nanoferrites plotted as a function of RE^{3+} 4f electron number.

pounds which include micrographs and electron diffraction ring patterns images for the as-prepared samples. The low scale image in Figure 8.6 shows the inter-planar distance in the Gd substituted compound. The corresponding lattice parameter of 0.84 nm is obtained from the image which is in agreement with the XRD result in Table 8.1. The electron diffraction ring patterns further confirm that the synthesized samples are nanoparticles with single-phase spinel structure. From the HRTEM micrographs, the nanoparticles appear to be uniformly sized and nearly square in shaped. Some agglomeration also occurs. Similar results have been reported in $NiFe_2O_4$ [62] and $Zn_{0.6}Ni_{0.4}Fe_2O_4$ [96] ferrites.

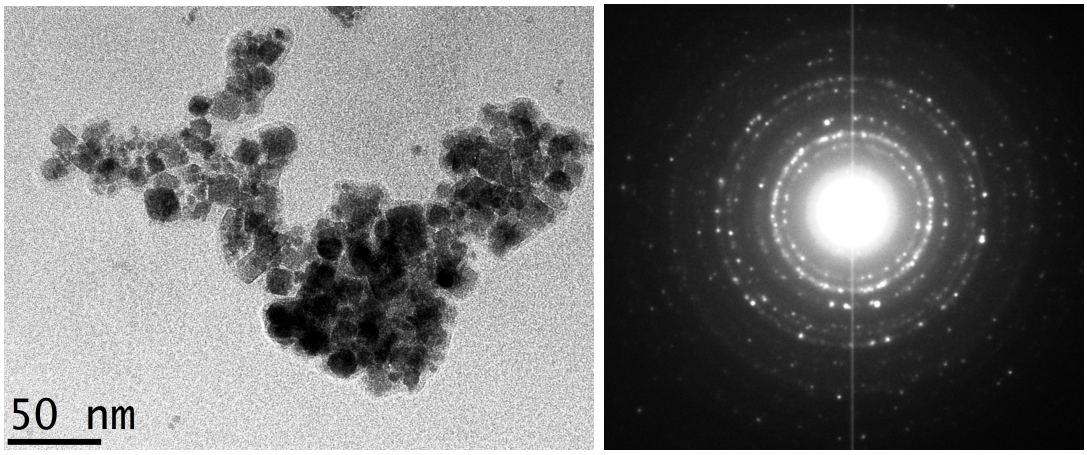

Figure 8.5: HRTEM: (a) Micrograph and (b) Electron diffraction ring pattern images of $Mg_{0.5}Mn_{0.5}Ce_{0.1}Fe_{1.9}O_4$ nanoferrite.

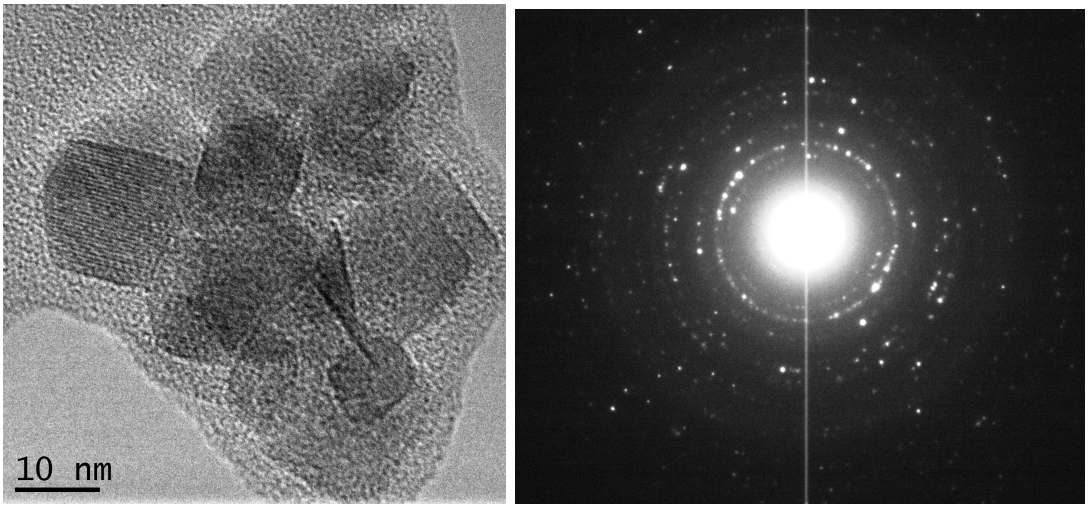

Figure 8.6: HRTEM: (a) Micrograph and (b) Electron diffraction ring pattern images of $Mg_{0.5}Mn_{0.5}Gd_{0.1}Fe_{1.9}O_4$ nanoferrite.

8.3.2 Mössbauer measurements

In Figure 8.7 we show the zero-field room temperature Mössbauer spectrum for the $Mg_{0.5}Mn_{0.5}Fe_2O_4$ compound. The modification of this spectrum due to the rare earth substitutions are indicated by the spectra given in Figure 8.8. Changes in the local environments surrounding Fe^{3+} ions are observed [35]. The spectra show some enhanced ordered magnetic phases at room temperature for Sm, Dy, Eu and Gd substitutions. The remainder of the RE ion substitutions show the on-set of paramagnetic phase, which we can attribute to the weakening of superexchange interactions by RE substitutions. Two sextets and two doublets were used to fit the Mössbauer data. The sextets are associated with Fe^{3+} ions at tetrahedral (A) and octahedral (B) sites of the spinel structure [149]. The doublets describe Fe atoms in paramagnetic states. Higher values of magnetic hyperfine fields have been assigned to B sites and the lower values to A sites. The Mössbauer parameters deduced from the analysis of the spectra are given in Table 8.2. An overall reduction in hyperfine fields on A and B sites is obtained. The substitutions lead to changes in magnetic coupling as reflected by decreases in hyperfine fields [185]. No significant changes in isomer shifts are observed due to $s-$electron charge density of Fe^{3+} by RE substitution.

The $Mg_{0.5}Mn_{0.5}(RE)_{0.1}Fe_{1.9}O_4$ ferrites magnetic interactions can be explained based on Néel's model for inter-sublattice A-O-B, A-O-A and B-O-B interactions. The former two interactions are much weaker and do not have much significant contribution to magnetic ordering. The possible ion interactions amongst A sites and B sites are Fe_A^{3+}-O-Fe_B^{3+}, Fe_A^{3+}-O-Mn_B^{2+}, Mn_A^{2+}-O-Fe_B^{3+}, Fe_A^{3+}-O-$(RE)_B^{3+}$, RE_A^{3+}-O-Fe_B^{3+} and Fe_A^{3+}-O-Mg_B^{3+}. The ferrimagnetic order occurs because of strong exchange interaction of magnetic ions via J_{AB} (A-O-B) [35]. The replacement of Fe^{3+} by RE^{3+} weakens the superexchange Fe_A^{3+}-O-Fe_B^{3+} interactions therefore hyperfine magnetic fields decrease as expected [185].

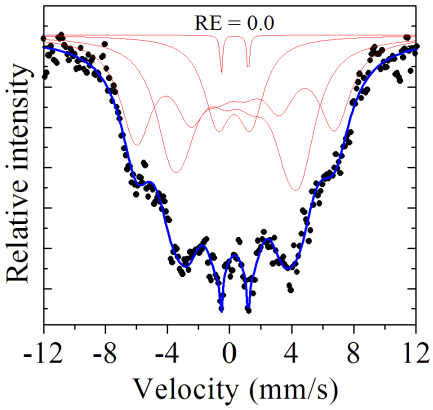

Figure 8.7: Room temperature Mössbauer spectrum of $Mg_{0.5}Mn_{0.5}Fe_2O_4$ nanoferrite.

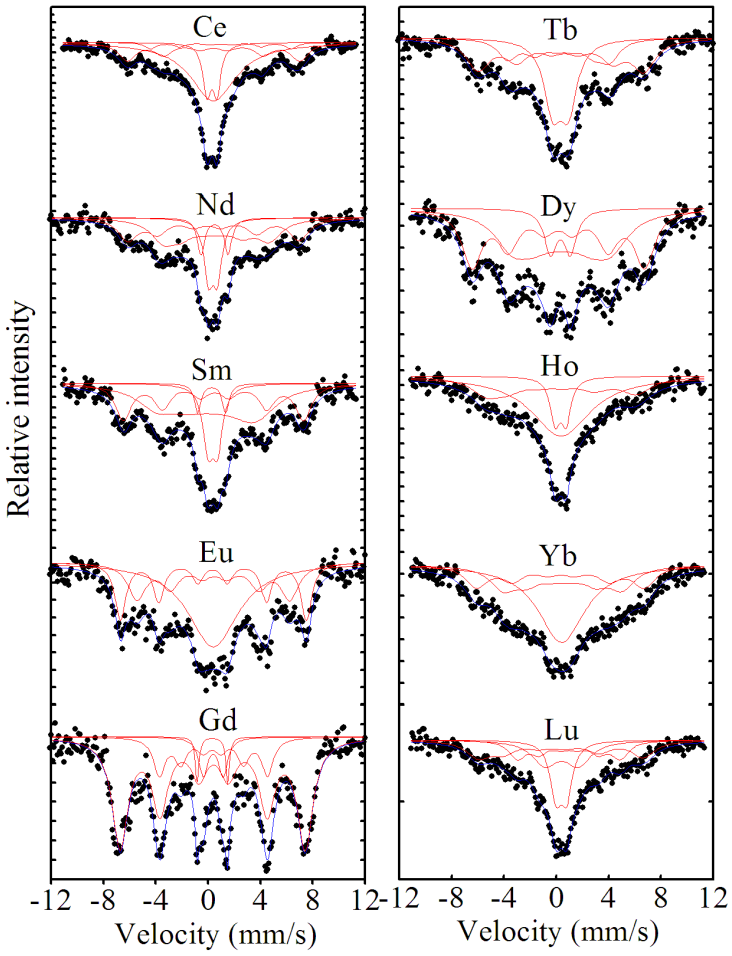

Figure 8.8: Room temperature Mössbauer spectra of $Mg_{0.5}Mn_{0.5}(RE)_{0.1}Fe_{1.9}O_4$ nanoferrites.

Table 8.2: Isomer shifts (δ), hyperfine fields (H), line widths (LW) and Fe^{3+} fraction (f) on A and B sites for the as-prepared $Mg_{0.5}Mn_{0.5}(RE)_{0.1}Fe_{1.9}O_4$ nanoferrites.

	δ (mm/s)		H (kOe)		LW (mm/s)		f (%)	
RE	δ_A ±0.02	δ_B ±0.09	H_A ±16	H_B ±8	LW_A ±0.08	LW_B ±0.01	f_A	f_B
0	0.25	0.44	368	440	1.27	0.53	40.0	50.6
Ce	0.29	0.40	334	409	0.55	0.81	15.3	53.7
Nd	0.44	0.17	252	406	1.10	0.89	38.0	32.3
Sm	0.31	0.45	243	427	1.81	0.73	45.8	31.7
Eu	0.45	0.37	363	441	0.80	0.50	27.1	26.5
Gd	0.40	0.38	256	439	0.50	0.72	17.9	71.5
Tb	0.39	0.49	241	393	0.92	1.10	23.6	43.1
Dy	0.40	0.20	235	409	1.60	0.90	44.5	44.9
Ho	0.33	0.40	356	–	0.50	2.70	31.1	55.9
Yb	0.43	0.32	282	397	1.21	1.05	28.9	24.6
Lu	0.38	0.40	244	390	0.77	1.11	22.5	30.9

8.3.3 Magnetization measurements

In Figure 8.9 we present the hysteresis loops deduced from the magnetization measurements of $Mg_{0.5}Mn_{0.5}(RE)_{0.1}Fe_{1.9}O_4$ nanoparticles at room temperature. The results show evidence of superparamagnetic behaviour of the rare earth substituted compounds as confirmed by Mössbauer analysis. The magnetic properties such as coercive field (H_C), maximum magnetization (M_m), saturation magnetization (M_S) and remanent magnetization (M_R) can be deduced from the narrow hysteresis loops given in Figure 8.9. We observe from the hysteresis loops that the magnetizations are not saturated at 14 kOe because of the presence of surface-spin structure associated with nanoparticles [104]. In Figure 8.10 we show the variations of the initial magnetization curves as a function of magnetic field. The saturation magnetizations were obtained by using the law of approach to saturation based on equation (2.10.1) with average correlation coefficients of at least 0.99. The results of the analysis of the data in Figures 8.9 and 8.10 are given in Table 8.3. Figures 8.11 – 8.13 show the plots of coercive field, maximum magnetization, saturation magnetization and remanent magnetization as a function of the number of RE^{3+} 4f electrons respectively. The highest saturation, maximum and remanent magnetizations are obtained for the Gd substituted sample which also happens to have the largest grain size.

The ratio M_R/M_S is referred to as the squareness of the hysteresis loops. The ratio is approximately 2% and does not change significantly with RE atoms. The magnetic moment per molecule (μ) was obtained by using the formula $\mu = M_0 M_S/5585$ where M_0 is molecular weight in grams [96, 155]. In Table 8.3, we also show the estimated values of M_R/M_S and μ. Clearly various parameters are affected differently by different RE substitutions.

Strong correlation between the Curie temperature T_C and the de Gennes factor G is expected for any series of rare-earth compounds [85]. In a binary series of intermetalic compounds A_xB_{1-x}, the extrapolated spontaneous magnetizations $M_S(T = 0\ \text{K})$ and T_C have been observed [186] to have similar composition dependences related to so called Mathon plots namely

$$M_S^2(0) \propto T_C^2 \propto |x - x_o| \tag{8.3.1}$$

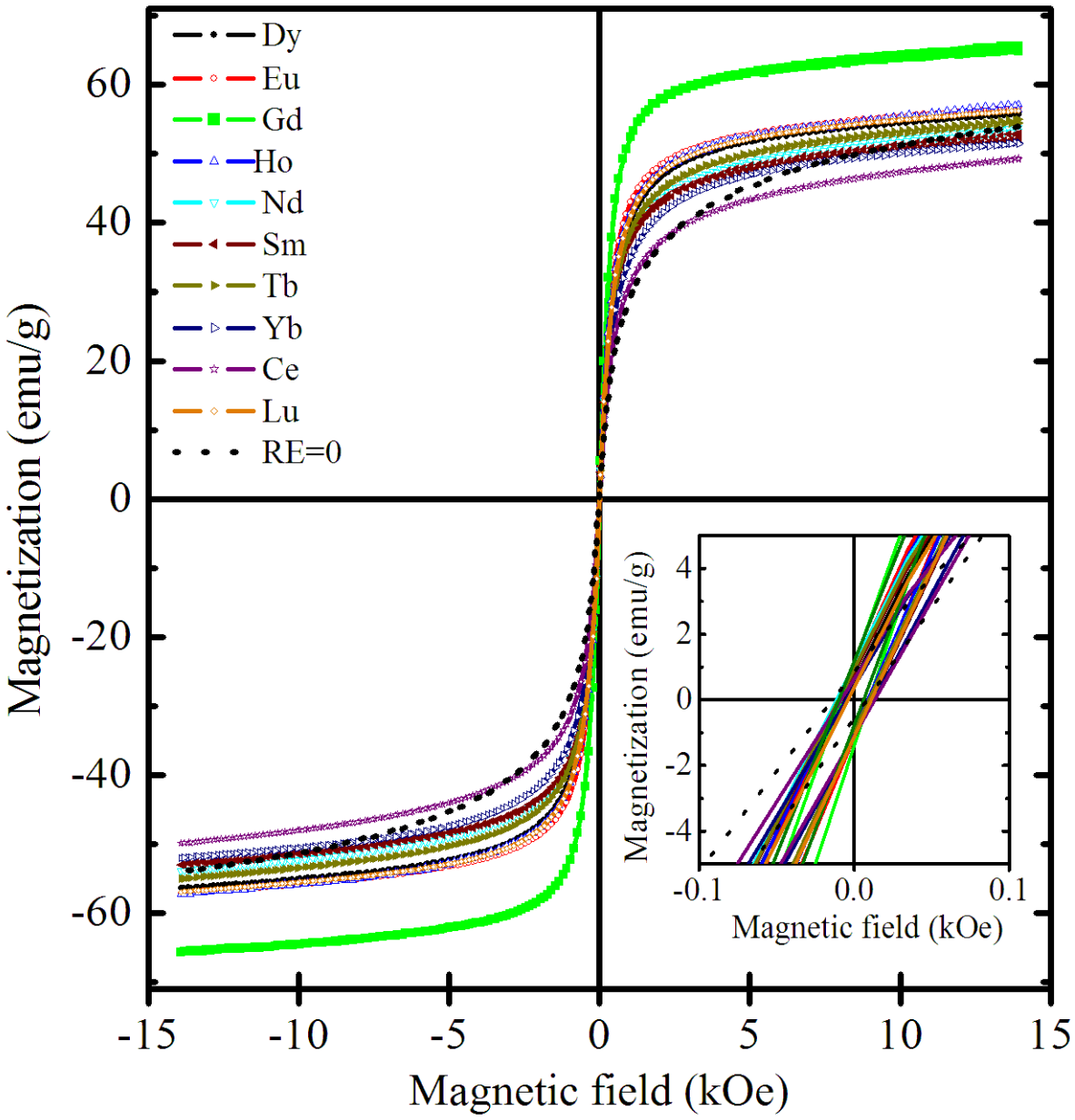

Figure 8.9: Room temperature hysteresis loops of $Mg_{0.5}Mn_{0.5}(RE)_{0.1}Fe_{1.9}O_4$ nanoferrites.

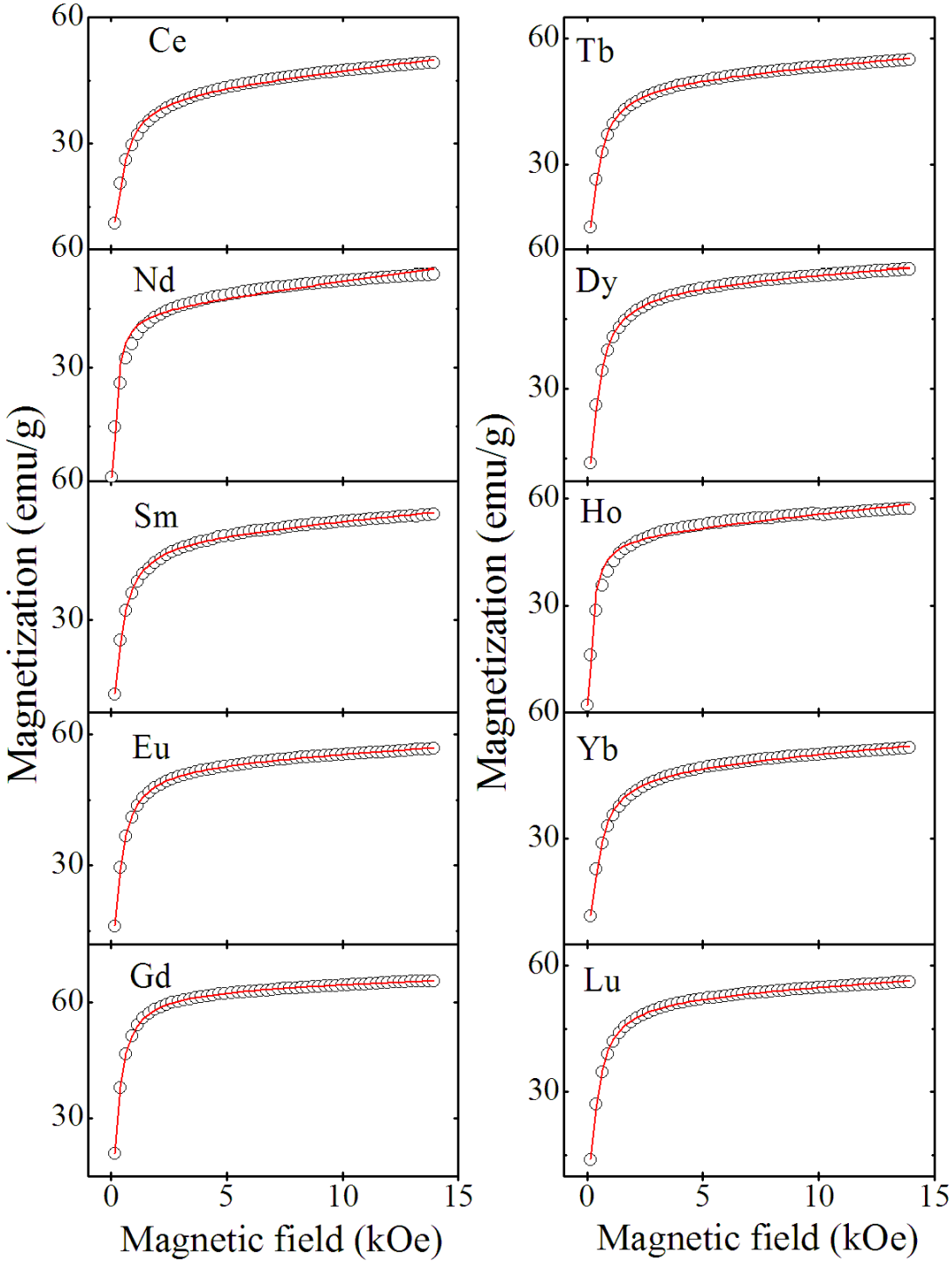

Figure 8.10: Initial magnetizations of $Mg_{0.5}Mn_{0.5}(RE)_{0.1}Fe_{1.9}O_4$. The solid lines are the best fit curves to data based on the empirical law approach to saturation magnetization.

Table 8.3: Coercive fields (H_C), saturation magnetizations (M_S), maximum magnetizations (M_m), remanent magnetizations (M_R), ratio M_R/M_S and magnetic moment per molecule (μ) of $Mg_{0.5}Mn_{0.5}(RE)_{0.1}Fe_{1.9}O_4$ nanoferrites.

Sample RE	H_C (Oe) ±3	M_S (emu/g) ±0.2	M_m (emu/g) ±0.1	M_R (emu/g) ±0.02	M_R/M_S - ±0.003	μ (μ_B) ±0.02
0	17	40.2	53.9	0.70	0.018	1.55
Ce	11	42.3	49.6	0.92	0.022	1.69
Nd	15	44.8	53.8	1.03	0.023	1.80
Sm	12	48.1	53.0	1.00	0.021	1.94
Eu	13	53.5	56.9	1.07	0.020	2.15
Gd	14	63.9	65.8	1.36	0.021	2.58
Tb	14	50.1	55.0	0.96	0.019	2.02
Dy	10	52.6	56.1	0.89	0.017	2.13
Ho	14	49.7	57.2	0.96	0.019	2.01
Yb	13	47.1	51.8	0.78	0.017	1.91
Lu	9	53.0	56.6	0.89	0.017	2.17

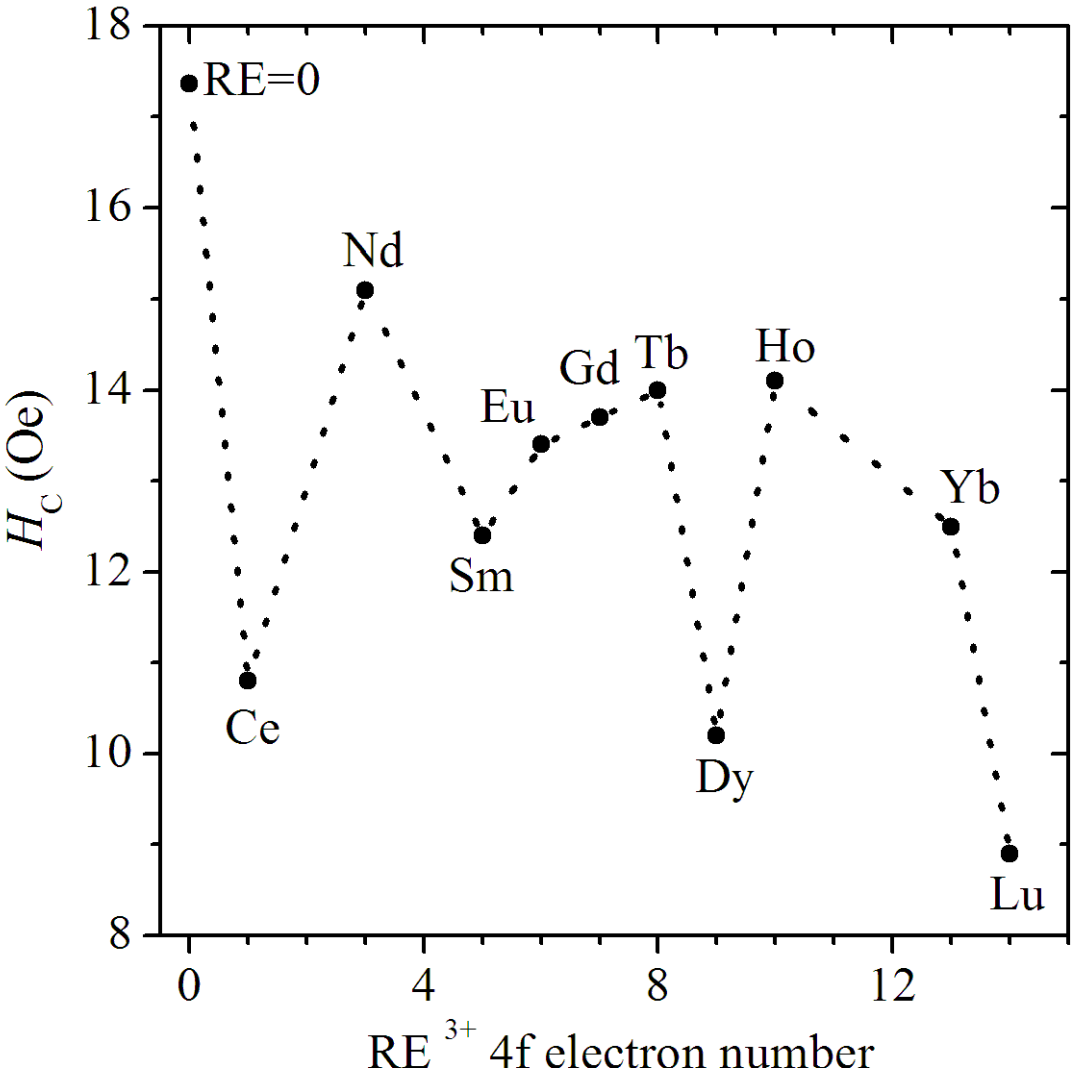

Figure 8.11: Coercive fields (H_C) of $Mg_{0.5}Mn_{0.5}(RE)_{0.1}Fe_{1.9}O_4$ nanoferrites plotted as a function of RE^{3+} 4f electron number.

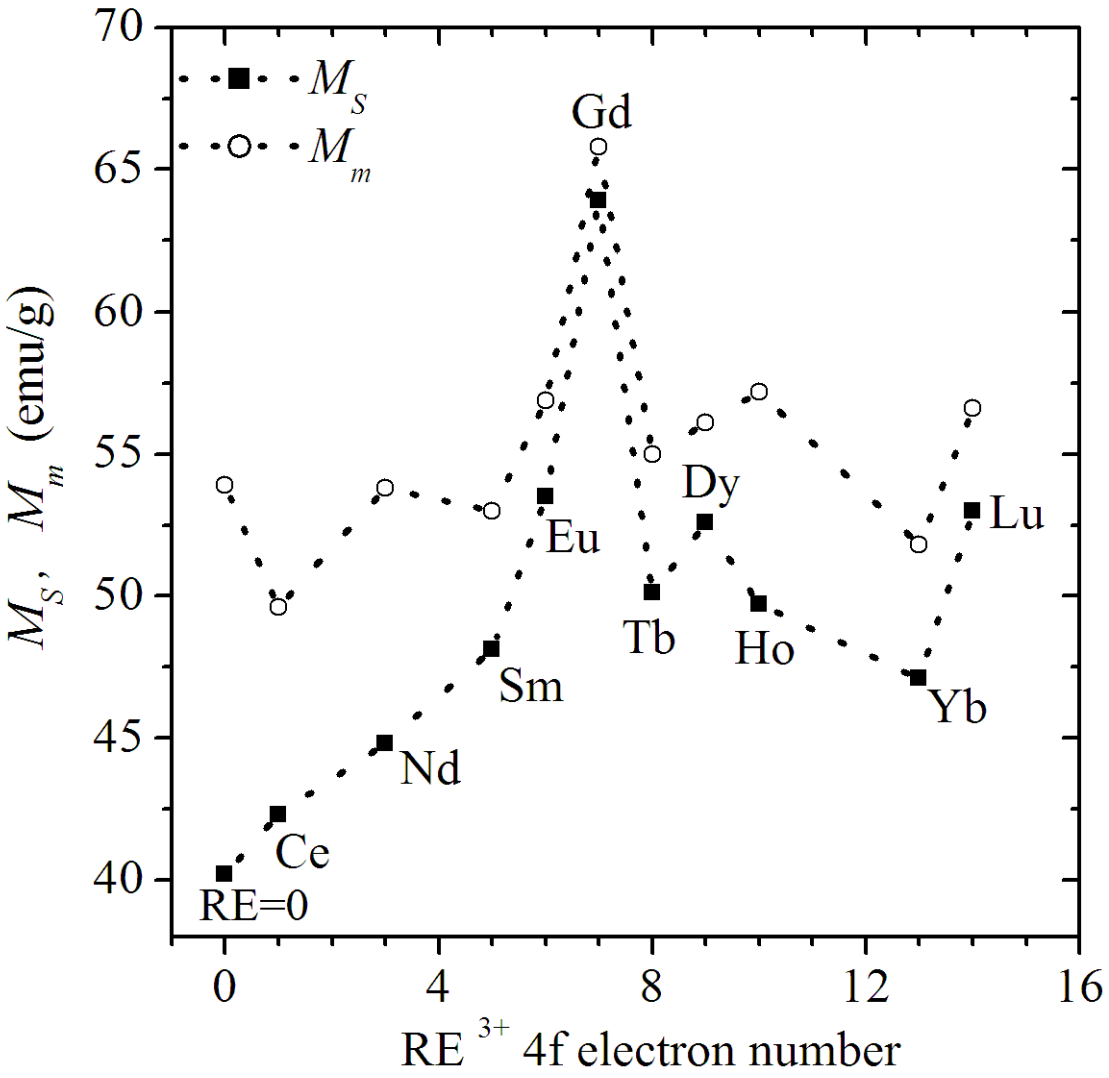

Figure 8.12: Saturation magnetization (M_S) and maximum (M_m) magnetizations of $Mg_{0.5}Mn_{0.5}(RE)_{0.1}Fe_{1.9}O_4$ nanoferrites plotted as a function of RE^{3+} 4f electron number.

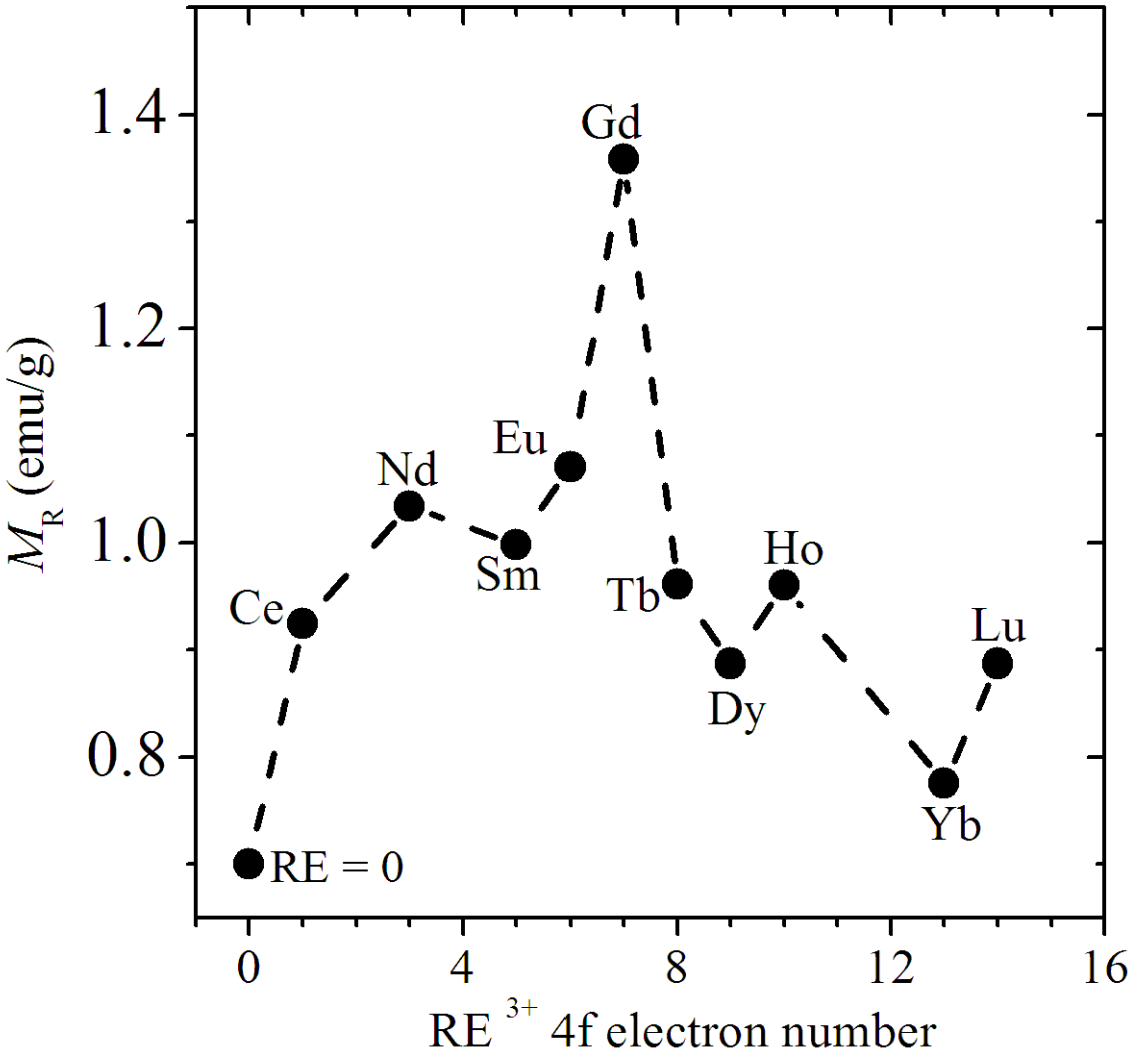

Figure 8.13: Remanent magnetization (M_R) of $Mg_{0.5}Mn_{0.5}(RE)_{0.1}Fe_{1.9}O_4$ nanoferrites plotted as a function of RE^{3+} 4f electron number.

where x_o is a critical concentration. Hence we may assumed that spontaneous magnetizations M_S can also correlate with the de Gennes factor G. We have extended our study to include other correlations with the de Gennes factors. The saturation magnetization (M_S) (in Table 8.3), microstrain (ε) and grain size (D) (in Table 8.1) are plotted as a function of the de Gennes factor $G = (g-1)^2 J(J+1)$ in Figures 8.14, 8.15 and 8.16 respectively. The values of G used have been sourced from [85] which do not include values for Eu^{3+} and Lu^{3+}. Good linear fits to the data with

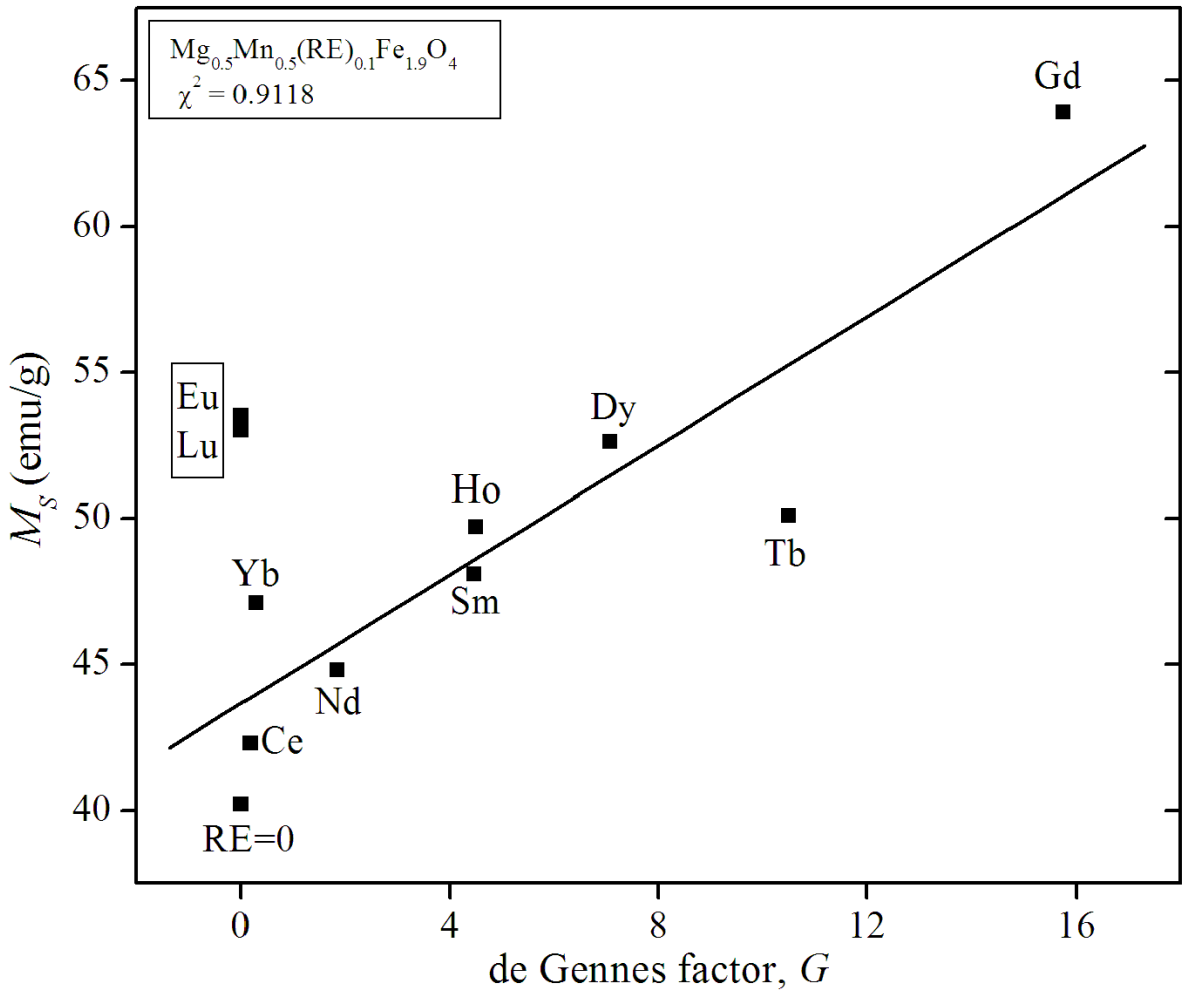

Figure 8.14: Saturation magnetization (M_S) of $Mg_{0.5}Mn_{0.5}(RE)_{0.1}Fe_{1.9}O_4$ nanoferrites plotted as a function of de Gennes factor (G). The fit does not include points corresponding to Eu, Lu and RE = 0.

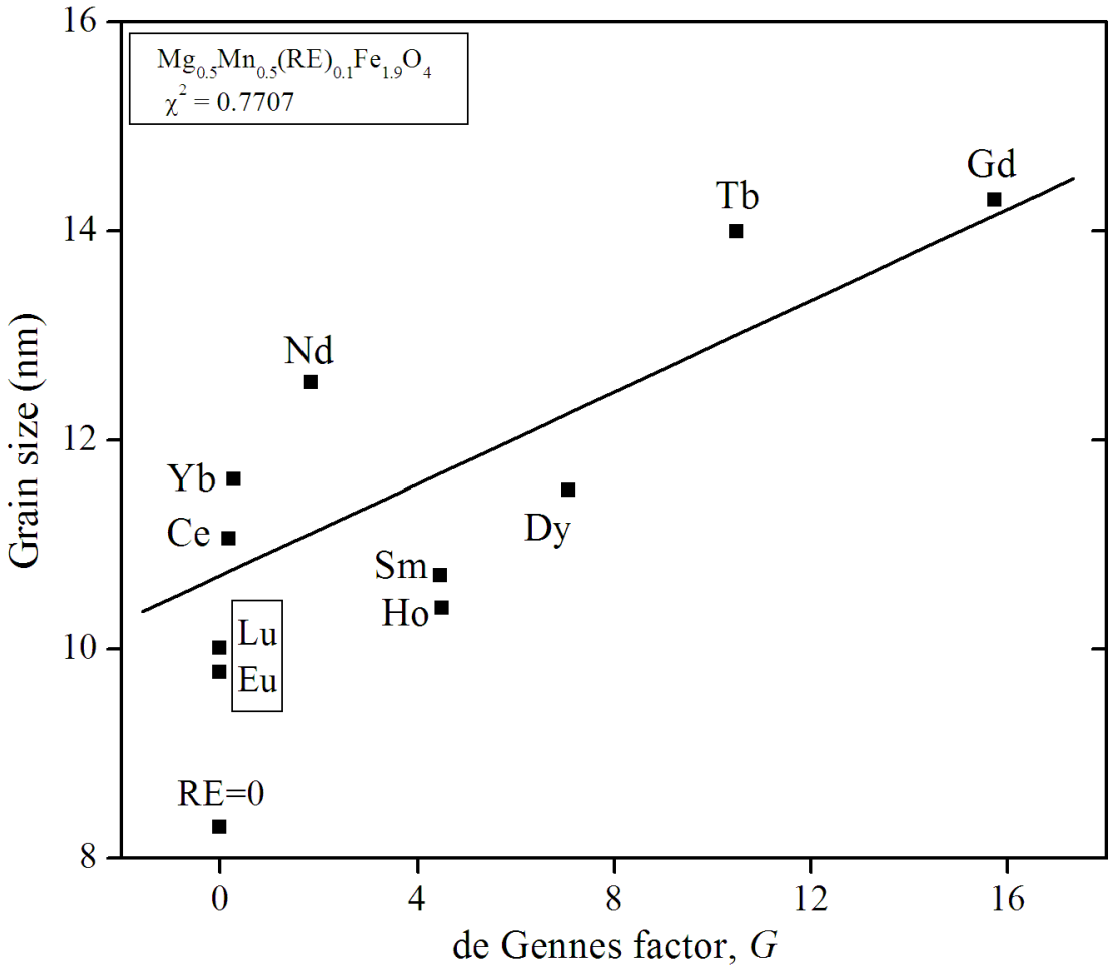

Figure 8.15: Grain size (D) of $Mg_{0.5}Mn_{0.5}(RE)_{0.1}Fe_{1.9}O_4$ nanoferrites plotted as a function of de Gennes factor (G). The fit does not include points corresponding to Eu, Lu and RE = 0.

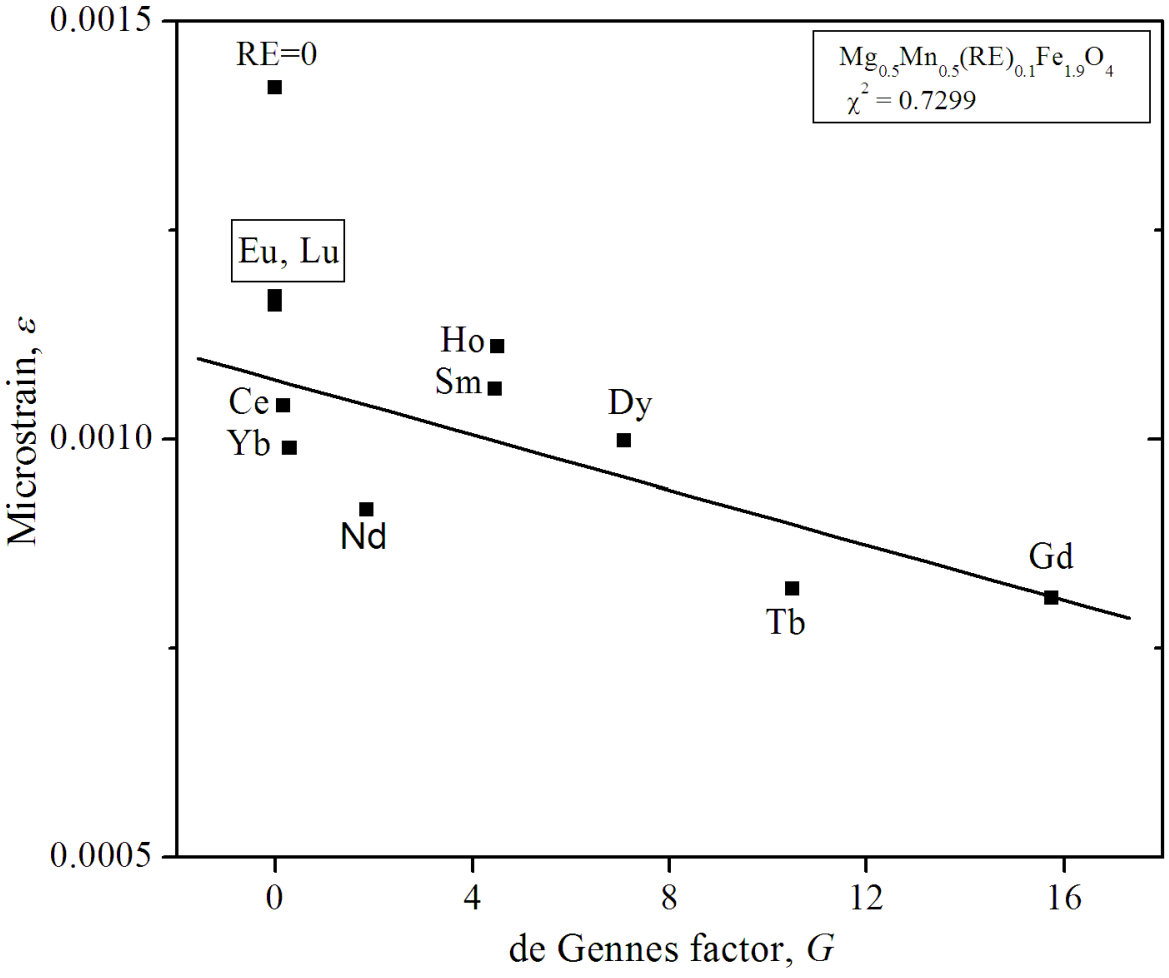

Figure 8.16: Microstrain (ε) of $Mg_{0.5}Mn_{0.5}(RE)_{0.1}Fe_{1.9}O_4$ nanoferrites plotted as a function of de Gennes factor (G). The fit does not include points corresponding to Eu, Lu and RE = 0.

correlation coefficient of about 0.9118 is obtained between M_S and G. This is similar to the expected correlation between T_C and G [85]. We also find reasonable fits to the data with correlation coefficients of about 0.7707 and 0.7299 for grain sizes and microstrains respectively. The correlation of the grain size with G appears to be a unique property of the nano-materials and suggests an intrinsic connection between particle size and the magnetic state of the nano-materials. The incorporation of the rare-earths atoms appears to provide some relief to the strain in the materials. Increased magnetic order seems to favour reduced microstrains. No correlations with the de Gennes factor have been observed for the lattice parameters and the coercive fields.

8.4 Conclusions

Single phase $Mg_{0.5}Mn_{0.5}(RE)_{0.1}Fe_{1.9}O_4$ spinel nanoferrites were successfully synthesized by the glycol-thermal method. Rare earth substitutions lead to the enhancement of grain sizes, lattice parameters and XRD densities. The results show that the microstrains were relieved by substitutions into the parent sample. We associate this with the increased sizes of the rare earth ions. Slight changes to the Mössbauer spectra are observed associated with weakening of the super-exchange interactions. The results show evidence of superparamagnetic behaviour of the synthesized compounds. The substitution by rare earth elements decreases the coercive fields and leads to a significant enhancement of the magnetizations. The highest value of magnetization is obtained by Gd^{3+} substitution. We found correlation between the de Gennes factor and saturation magnetization, grain size and microstrain of the rare-earth substituted compounds. These results suggests strong links with the coupling of the magnetic moments in the compounds.

Chapter 9

General conclusions

Nanoparticles of $Mn_xCo_{1-x}Fe_2O_4$, $(Mg, Sr)_{0.2}Mn_{0.1}Co_{0.7}Fe_2O_4$, $Mg_xMn_{1-x}Fe_2O_4$ and $Mg_{0.5}Mn_{0.5}(RE)_{0.1}Fe_{1.9}O_4$ ferrites with single-phase cubic spinel structure were synthesized directly by the glycol-thermal method at a low reaction temperature of about 200 ^{o}C. In addition, we synthesized the $Mn_{0.5}Co_{0.5}Fe_2O_4$ compound using high-energy ball milling. The samples prepared by the glycol-thermal method appear to be of higher quality than milled samples. Better samples are also obtained from $MnFe_2O_4$ and $CoFe_2O_4$ as starting materials than from metal oxides. The particle sizes, XRD densities and bulk densities of the as-prepared compounds were found between $7 - 16.3$ nm, $4.51 - 5.66$ g cm^{-3} and $2.03 - 4.57$ g cm^{-3} respectively. The porosities of the studied compounds were found to decrease with increasing annealing temperature consistent with increased bulk densities. This can be related to larger grains created during the annealing process at higher temperature. The results show that the micro-strains of the studied samples were relieved by thermal annealing. The crystal structures of $Mn_{0.5}Co_{0.5}Fe_2O_4$ and $Mg_xMn_{1-x}Fe_2O_4$ compounds appear to be unstable after annealing above 500 ^{o}C under air atmosphere which we attribute to the formation of metal oxides. RE- substituted $Mg_{0.5}Mn_{0.5}Fe_2O_4$ samples show increases in grain sizes and lattice parameters.

The magnetic properties derived from magnetization and Mössbauer spectroscopy measurements appear to be sensitive to the microstructure and the doping atoms. Some enhancements of the hyperfine fields are observed for Mn- substituted $CoFe_2O_4$, Mg- substituted $MnFe_2O_4$, RE- substituted $Mg_{0.5}Mn_{0.5}Fe_2O_4$ and Sr- or Mg- sub-

stituted $Mn_{0.3}Co_{0.7}Fe_2O_4$ induced by the substitutions and thermal annealing due to changes in the grain sizes. The $s-$electron charge densities of Fe^{3+} ions at tetrahedral and octahedral sites were not influenced significantly by the substitutions with Mn, Mg and Sr or by sintering. Slight changes to the Mössbauer spectra of the as-prepared RE- substituted compounds were observed which we suspect to be due to the weakening of the super-exchange interactions. The Mössbauer spectra for $Mn_xCo_{1-x}Fe_2O_4$ and (Mg, Sr)$_{0.2}Mn_{0.1}Co_{0.7}Fe_2O_4$ appear closely related and indicate ferrimagnetic behaviour of the compounds. The transition temperature (T_C) for the as-prepared $Mn_xCo_{1-x}Fe_2O_4$ samples can be estimated from the Mössbauer spectra recorded at different temperatures. We expect $T_C > 473$ K for samples with $x = 0$ and 0.5. For samples with $x = 0.1$, 0.2 and 0.6, $423 < T_C < 473$ K. While for $x = 0.3$, $373 < T_C < 423$ K. The magnetization curves of $Mg_xMn_{1-x}Fe_2O_4$ and $Mg_{0.5}Mn_{0.5}(RE)_{0.1}Fe_{1.9}O_4$ with low coercive fields and broadened Mössbauer spectra are indicative of superparamagnetic like-behaviour. No significant changes in the hysteresis loops of the studied compounds are observed with annealing temperature and measuring temperature. The initial magnetizations curves, $M - H$ were found to follow the empirical law for approach to saturation. The values of the saturation magnetizations were deduced from the fits. The coercive fields of the studied compounds are observed to increase with increasing annealing temperature and grain sizes. These results indicate the evolution of the particles from single-domain to multi-domain structure with increasing sintering temperature. The changes in M_S, M_m, M_R and H_C appear to be related to the modifications of the grain sizes and the distortion of the magnetocrystallite anisotropy due to thermal annealing and substitutions by transition metals. The distortion on the surface of the ultra-fine particles due to the interaction of the transition metal ions with the oxygen atoms in the spinel structure may also contribute to the reduction of the saturation magnetization. The slow approach to saturation attributed to the disordered spin configuration at surfaces of magnetic nanoferrites is expected to weaken the exchange coupling. We found correlation between the de Gennes factor and saturation magnetization, grain size and microstrain of rare earth substituted $Mg_{0.5}Mn_{0.5}(RE)_{0.1}Fe_{1.9}O_4$ compounds which suggests strong links with the coupling of the magnetic moments in samples.

Evidence of spin freezing was confirmed by zero-field cooling (ZFC) and field cooling (FC) magnetizations measurements. Spin freezing at low temperature appears to be associated with increased magnetic hardness. Furthermore, our results show evidence of temperature-dependent coercive fields which reveal a clear distinction between $Mn_{0.1}Co_{0.9}Fe_2O_4$, $Mn_{0.5}Co_{0.5}Fe_2O_4$ and $Mg_xMn_{1-x}Fe_2O_4$ as well as between $Mg_{0.2}Mn_{0.1}Co_{0.7}Fe_2O_4$ and $Sr_{0.2}Mn_{0.1}Co_{0.7}Fe_2O_4$. In all cases the coercive field follows Kneller's law of the form $H_C(T) = H_C(0)[1 - (T/T_B)^{\alpha}]$ with $\alpha = 1/2$ usually associated with uniaxial symmetry of the nanoparticles. The temperature dependence of the saturation magnetizations were observed to vary according to the modified Bloch's law of the form $M_S(T) = M_S(0)[1-(T/T_0)^{\beta}]$ with average β equal to 2.34. These results are consistent with the nanoparticle nature of the studied compounds. Spin-glass like behaviour has been observed at low temperature in the two Mn substituted samples, $x = 0.1$ and 0.5. From the FC and ZFC measurements, the state of magnetization appears to be higher in the $Mn_{0.5}Co_{0.5}Fe_2O_4$ sample. The spin freezing at low temperature also appears to be stronger. The distortion of the hysteresis loops at low temperature has been observed which may be attributed to the freezing of the disordered spins state [172]. The distortion may also be attributed to the existence of two types magnetic phases such as antiferromagnetism and ferrimagnetism at the same temperature [173].

The temperature dependence of the resistivity for $Mn_xCo_{1-x}Fe_2O_4$ nanoferrites have been investigated. The resistivity was assumed to be caused by tunnelling effects of electrons between grains. This result has been discussed in the context of the granular nature of the compounds where electrons can tunnel between charged and neutral grains. The resistivity and activation energy of a sample has been found to depend on the annealing temperature and the surface of the pellet that was being probed.

Our investigations have provided us with useful information on the synthesis, structural, electrical and magnetic properties of nanoferrites [17, 18, 19, 20, 21, 22, 23, 24]. Preliminary work is now under-way in our Laboratory to complex some of the nanoferrites with drugs by high-energy ball milling for bioactivity studies [187].

Bibliography

[1] J. Smit and H. P. J. Wijn, *Ferrites*, Philips, Technical Library, (1959) p. 140-154.

[2] P. Hu, H. Yang, D. Pan, H. Wang, J. Tian, S. Zhang, X. Wang and A. Volinsky, J. Magn. Magn. Mater. **322** (2010) 173.

[3] M. U. Rana, T. Abbas and F. A. Khawaja, Mater. Lett. **52** (2002) 389.

[4] I. H. Gul and A. Maqsood, J. Alloys Comps. **465** (2008) 227.

[5] M. J. Iqbal and M. R. Siddiquah, J. Magn. Magn. Mater. **320** (2008) 845.

[6] M. Ashiq, S. Saleem, M. Malana and A. Ur-Rehman, J. Alloys Comps. **486** (2009) 640.

[7] M. A. Ahmed and A. A. El-Khawlani, J. Magn. Magn. Mater. **321** (2009) 1959.

[8] Z. Zi, S. Sun, X. Zhu, Z. Yang, J. Dai and W. Song, J. Magn. Magn. Mater. **321** (2009) 1251.

[9] C. Upadhyay, D. Mishra, H. C. Verma, S. Anand and R. P. Das, J. Magn. Magn. Mater. **260** (2003) 188.

[10] Y. Ichiyanagi, M. Kubota, S. Moritake, Y. Kanazawa, T. Yamada and T. Uehashi, J. Magn. Magn. Mater. **310** (2007) 2378.

[11] X. Liu, W. Zhong, S. Yang, Z. Yu, B. Gu and Y. Du, J. Magn. Magn. Mater. **238** (2002) 207.

[12] B. D. Cullity and C. D. Graham, *Introduction to Magnetic Materials*, second edition, John Wiley & Sons, Hoboken, New Jersey (2009) p. 175-180.

[13] X. Zuo, B. Barbiellini and C. Vittoria, J. Magn. Magn. Mater. **272-276** (2004) 306.

[14] E. C. Snelling, *Soft Ferrites*, second edition, Butterworth & Co. London, UK (1988) p. 1-5.

[15] S. Lee, Y. Chen, C. Ho, C. Chang and Y. Hong, Mater. Sci. Eng. B **143** (2007) 1.

[16] A. Verma and R. Chatterjee, J. Magn. Magn. Mater. **306** (2006) 313.

[17] H. M. I. Abdallah, T. Moyo and J. Z. Msomi, J. Phys.: Conf. Ser. **217** (2010) 012141.

[18] H. M. I. Abdallah, T. Moyo and J. Z. Msomi, J. Supercond. Nov. Magn. **24** (2011) 669.

[19] J. Z. Msomi, H. M. I. Abdallah, T. Moyo and A. Lančok, J. Magn. Magn. Mater. **323** (2011) 47.

[20] H. M. I. Abdallah, T. Moyo and J. Z. Msomi, J. Supercond. Nov. Magn. DOI: 10.1007/s10948-011-1231-4.

[21] H. M. I. Abdallah, J. Z. Msomi, T. Moyo and A. Lančok, J. Supercond. Nov. Magn. DOI: 10.1007/s10948-011-1230-5.

[22] H. M. I. Abdallah, J. Z. Msomi, T. Moyo, J. J. Dolo and A. Lančok, Hyperfine Interac. **203** (2011) 99.

[23] J. Z. Msomi, T. Moyo and H. M. I. Abdallah, J. Supercond. Nov. Magn. DOI: 10.1007/s10948-011-1235-0.

[24] H. M. I. Abdallah, T. Moyo and J. Z. Msomi, IEEE Transac. Magn. submitted 2011.

[25] www.emeraldinsight.com/content_images

[26] B. Viswanathan and V. R. K. Murthy, *Ferrite Materials*, Narosa Publishing House, New Delhi, India (1990) p. 2-23, 25-37.

[27] M. Nasr Isfahani, M. Myndyk, V. Sepelak and J. Amighian, J. Alloys Comps. **470** (2009) 434.

[28] T. Verdier, V. Nachbour and M. Jean, J. Solid State Chem. **178** (2005) 3243.

[29] S.S. Ata-Allah, J. Solid State Chem. **177** (2004) 4443.

[30] J. S. Smart, *Effective Field Theories of Magnetism*, Philadelphia: J. B. Saunders company, London (1966) p. 113-125.

[31] R. P. Moyet, Y Cardona, P. Vargas, J. Silva and O. N.C. Uwakweh, Mater. characterizations **61** (2010) 1317.

[32] P. Tailhades, C. Bonningue, A. Rousset, L. Bouet, I. Pasquet and S. Ledrun, J. Magn. Magn. Mater. **193** (1999) 148.

[33] M. Sugimoto, J. Am. Ceram. Soc. **82** (1999) 269.

[34] M. L. Kahn and Z. J. Zhang, Appl. Phys. Lett. **78** No. 23 (2001) 3651.

[35] A. Lakshman, P. S. V. S. Rao and K. H. Rao, J. Magn. Magn. Mater. **284** (2004) 352.

[36] M. Mouallen-Bahout, S. Bertrand and O. Peña, J. Solid State Chem. **178** (2005) 1080.

[37] O. Caltun, G. Rao, K. Rao, B. Parvatheeswara and C. Kim, J. Magn. Magn. Mater. **316** (2007) e618.

[38] S. Kumar, R. Kumar, S. K. Sharma, V. R. Reddy, A. Banerjee and Alimuddin, Solid state Communications **142** (2007) 706.

[39] S. D. Bahout and P. A. Joy, J. Phys. D: Appl. Phys. **40** (2007) 3263.

[40] R. S. Dunlap, A. Alghamdi, J. W. O' Brien and S. J. Penney, J. Alloys Comps. **365** (2004) 84.

[41] S. Dasgupta, K. B. Kim, J. Ellrich, J. Eckert and I. Manna, J. Alloys Comps. **424** (2006) 13.

[42] C. Rath, K. K. Sahu, S. Anand, S. K. Date, N. C. Mishraand and R. P. Das, J. Magn. Magn. Mater. **202** (1999) 77.

[43] G. B. Ji, S. L. Tang, S. K. Ren, F. M. Zhang, X. B. Gu and Y. W. Gu, J. Cryst. Growth **270** (2004) 156.

[44] D. E. Zhang, X. J. Zhang, X. M. Ni, H. G. Zhang and D. D. Yang, J. Magn. Magn. Mater. **292** (2005) 79.

[45] L. Nalbandian, A. Delimilis, V. T. Zaspalis, E. A. Deliyanni, D. N. Bakoyannkis and E. N. Peleka, Microporous and Mesoporous Mater. **114** (2008) 465.

[46] L. Zhen, K. He, C. Y. Xu and W. Z. Shao, J. Magn. Magn. Mater. **320** (2008) 2672.

[47] D. Bae, S. Kim, H. Lee and K. Han, Mater. Lett. **57** (2003) 1997.

[48] B. Zhou, Y. Zhang, C. Liao and C. Yan, J. Magn. Magn. Mater. **247** (2002) 70.

[49] G. Cerda and S. M. Montemoyor, J. Magn. Magn. Mater. **294** (2005) e43.

[50] K. J. Kim, H. K. Kim, Y. R. Park, and J. Y. Park, J. Magn. Magn. Mater. **304** (2006) e106.

[51] J. Giri, T. Sriharsha, S. Asthana, T. K. G. Rao, A. K. Nigam and D. Bahadur, J. Magn. Magn. Mater. **293** (2005) 55.

[52] C. Hwang, J. Tsai, T. Huang, C. Peng and S. Chen, J. Solid State Chem. **178** (2005) 382.

[53] R. C. Kambale, P. A. Shaikh, N. S. Harale, V. A. Bilur, Y. D. Kolekar, C. H. Bhosale and K. Y. Rajpure, J. Alloys Comps. **490** (2010) 568.

[54] Y. Fu and C. Lin, J Magn. Magn. Mater. **251** (2002) 74.

[55] K. S. Davies, S. Wells, R. V. Upadhyay, S. W. Charley, K. O'Grady, M. El Hilo, T. Meaz and S. Morϕp, J. Magn. Magn. Mater. **149** (1995) 14.

[56] A. B. Gadkari, T. J. Shinede and P. N. Vasambekar, Mater. Chem. Phys. **114** (2009) 505.

[57] X. Qi and D. Wu, J. Magn. Magn. Mater. **320** (2008) 666.

[58] G. Kumar, J. Chand, S. Verma and M. Singh, J. Phys. D: Appl. Phys. **42** (2009) 155001.

[59] S. Son, R. Swaminathan and M. E. McHenry, J. Appl. Phys. **93** No. 10 (2003) 7495.

[60] Y Ahn, E. J. Choi, S. Kim and H. N. Ok, Mater. Lett. **50** (2001) 47.

[61] X. Lin and A. C. S. Samia, J. Magn. Magn. Mater. **305** (2006) 100.

[62] R. Misra, S. Gubbala, A. Kale and W. Jr, Mater. Sci. Eng. B **111** (2004) 164.

[63] S. Singhal, A. N. Gary and K. Chandra, J. Magn. Magn. Mater. **285** (2005) 193.

[64] S. Singhal, A. N. Gary and K. Chandra, J. Magn. Magn. Mater. **306** (2006) 233.

[65] C. M. Hurd, Contemporary Phys. **23** No. 5 (1982) 469.

[66] Z. L. Lu, L. Y. Lv, J. M. Zhu, S. D. Li, X. C. Liu, W. Q. Zou, F. M. Zhang and Y. W. Du, Solid State Communications **137** (2006) 528.

[67] S. Bedanta and W. Kleemann, J. Phys. D: Appl. Phys. **42** (2009) 013001.

[68] B. Aslibeiki, P. Kameli, H. salamati, M. Eshraghi and T. Tahmasebi, J. Magn. Magn. Mater. **322** (2010) 2929.

[69] M. Singh, J. Magn. Magn. Mater. **299** (2006) 397.

[70] W. A. Roshen, J. Magn. Magn. Mater., **312** (2007) 245.

[71] V. Kumar, A. Rana, M. Yadav and R. Pant, J. Magn. Magn. Mater. **320** (2008) 1729.

[72] M. Shobana and S. Sankar, J. Magn. Magn. Mater. **321** (2009) 599.

[73] M. Shobana, S. Sankar and V. Rajendan, J. Mater. Chem. Phys. **113** (2009) 10.

[74] A. Junior, E. Lima and M. Novak, J. Magn. Magn. Mater. **308** (2007) 198.

[75] S. Yanez-Rdriguez, M. Sanchez-Andujar, C. Gomez-Aguirre, J. Mira, M. Senaris-Rodriguez and S. Castro-Garcia, J. Solid State Chem. **182** (2009) 2685.

[76] S. Jigajeni, S. R. Kulkarni, Y. Kolekar, S. B. Kulkarni and P. Joshi, J. Alloys Comps. **492** (2010) 402.

[77] M. Singh and S. P. Sud, Mater. Sci. Eng. B **83** (2001) 180.

[78] I. H. Gul, W. Ahmed and A. Maqsood, J. Magn. Magn. Mater. **320** (2008) 270.

[79] P. Sheng, B. Abeles and Y. Arie, Phys. Rev. Lett. **31** No. 1 (1973) 44.

[80] S. Ge, Y. Liu, L. Xi and C. Li, Phys. Status Solidi **177** (2000) R3.

[81] M. Getzlaff, *Fundamentals of Magnetism*, Springer (2008) p. 1-4, 96-133.

[82] A. P. Guimarães and I. S. Oliveira, *Magnetism and Magnetic Resonance in Solids*, John Wiley & Sons (1998) p. 1-109.

[83] D. Jiles, *Introduction to Solid State Physics*, Champan and Hall, first edition, (1990).

[84] G. F. Dionne, *Magnetic Oxides*, Springer, London, UK, 2009, p. 400-410.

[85] J. M. D. Coey, *Magnetism and Magnetic Materials*, Cambridge University press, UK (2010) p. 218-244.

[86] C. Kittel, *Introduction to Solid State Physics*, John Wiley & Sons, fifth edition, (2005) p. 302-304.

[87] J. S. Blakemore, *Solid State Physics*, second edition, Cambridge University press (1985) p. 436-440.

[88] R. Boča, *Theoretical Fundamental of Molecular Magnetism*, Elsevier (1999) p. 95-100.

[89] J. Solyom, *Fundamentals of the Physics of Solids*, Springer-Verlag, Berlin (2007) p. 450-496.

[90] ar.wikipedia.org/wiki

[91] J. Z. Msomi, *Synthesis, Structural and Magnetic Properties of Bulk and Nano-sized (Zn, Cd, Cu)*$_{0.5}Ni_{0.5}Fe_2O_4$ *and* $NiFe_2O_4$ *Ferrites*, University of KwaZulu-Natal (2007) PhD thesis.

[92] M. Knobel, W. C. Nunes, L. M. Socolovsky, E. De Biasi, J. M. Vargas and J. C. Deardin, J. Nanosci. Nanotechnol. **8** (2008) 2836.

[93] S. P. Gubin, *Magnetic Nanoparticles*, WILEY-VCH Verlag, Weinheim (2009) p. 210-224.

[94] S. Bedanta and W. Kleemann, J. Phys. D: Appl. Phys. **42** (2009) 013001.

[95] M. Jalaly, M. H. Enayati and F. Karimzadeh, J. Alloys Comps. **480** (2009) 737.

[96] M. Sertkol, Y. Köseoğlu, A. Baykal, H. Kavas and A. C. Basaran, J. Magn. Magn. Mater. **321** (2009) 157.

[97] E. Manova, B. Kunev, D. Paneva, I. Mitov, L. Petrov, C. Estournès, C. D'Orlèans, J. Rehspringer and M. Kurmoo, Chem. Mater. **16** (2004) 5689.

[98] T. Moyo, *Lectures notes in Magnetism*, University of KwaZul-Natal.

[99] N. W. Ashcroft and N. D. Mermin, *Solid State Physics*, Holt, Rinehart and Winston (1976) p. 671-681.

[100] N. A. Spaldin, *Magnetic Materials: Fundamentals and Applications*, Cambridge University Press, second edition (2011) p. 22-216.

[101] J. Dyson, Phys. Rev. **102** (1956) 1217.

[102] T. Oguchi, Phys. Rev. **117** (1960) 117.

[103] H. Ibach and H. Lüth, *Solid State Physics: An Introduction to Theory and Experiment*, third edition, Springer-Verlag, Berlin Heidelberg (1990) p. 127-158.

[104] C. Upadhyay, H. Verma, V. Sathe and A. Pimpale, J. Magn. Magn. Mater. **312** (2007) 271.

[105] A. B. Gadkari, T. J. Shinde and P. N. Vasambekar, J. Mater. Sci.: Mater. Electron **20** (2010) 96.

[106] C. Liu, B. Zou, A. J. Rondinone and Z. J. Zhang, J. Am. Chem. **122** (2000) 6263.

[107] J. Stöhr and H. C. Siegmann, *Magnetism from Fundamentals to Nanoscale Dynamics*, Springer-Verlag Berlin Heidelberg (2006) p. 511-521.

[108] D. L. Leslie-Pelecky, Chem. Mater. **8** (1996) 1770.

[109] R. Morjan and S. Prasalovich, *EM4 Magnetic Hysteresis*, Lab version 1.001a, Chalmers University of Technology and University of Göteborg (2003).

[110] W. F. Brown, Phys. Rev. **58** (1940) 736.

[111] I. C. Nlebedim, N. Ranvah, P. I. Williams, Y. Melikhov, J. E. Snyder, A. J. Moses and D. C. Jiles, J. Magn. Magn. Mater. **322** (2010) 1929.

[112] D. P. E. Dickson and F. J. Berry, *Mössbauer Spectroscopy*, Cambridge University Press, Cambridge, UK (2005) p. 1-16.

[113] G. K. Wertheim, *Mössbauer Effect: Principles and Applications*, Academic Press INC., New York, USA (1964) p. 1-35, 47-84.

[114] U. Gonser, *Mössbauer Spectroscopy*, Springer-Verlag, Berlin Heidelberg, Germany (1975) p. 1-48, 98-122.

[115] N. N. Greenwood and T. C. Gibb, *Mössbauer Spectroscopy*, Chapman and Hall, London, UK (1971) p. 46-54.

[116] Y. Chen and D Yang, *Mössbauer Effect in Lattice Dynamics*, Wiley-VCH Verlag GmbH & Co. Weinheim, Germany (2007) p. 1-26, 29-78.

[117] J. Danon, *Lectures on the Mössbauer Effect*, Gordon and Breach, Science Publishers Ltd. London, UK (1968) p. 1-104.

[118] www.serc.carleton.edu

[119] www.parrinst.com

[120] S. R. Elliott, *The Physics and Chemistry of Solids*, John Wiley & Sons, England (1998) p .22.

[121] www.retsch.com

[122] L. Yu, J. Zhang, Y. Liu, C. Jing and S. Chao, J. Magn. Magn. Mater. **288** (2005) 54.

[123] R. Jenkins and R. Snyder, *Introduction to X-ray Powder Diffractometry*, John Willy & Sons, USA (1996) p. 1-95.

[124] D. L. Bish, K. D. Preston, L. W. Finger, R. C. Reynolds Jr, S. A. Howard, D. K. Smith, R. Jenkins, R. Snyder, J. E. Post and R. V. Dreele, *Reviews in Mineralogy: Modern Powder Diffraction*, **20** (1989) p. 1-71.

[125] M. George, A. M. Johna, S. S. Naira, P. A. Joy and M. R. Anantharaman, J. Magn. Magn. Mater. **302** (2006) 190.

[126] Dr James Wesley-Smith, Electrom Microscopy Unit, Westville Campus, UKZN, Durban, South Africa.

[127] D. B. Williams and Carter, *Transmission Electron Microscopy: A textbook for Materials Science*, Springer Science & Business Media, New York, USA (2009) p. 1-37, 141-193.

[128] R. F. Egerton, *Physical Principles of Electron Microscopy: An Introduction to TEM, SEM and AEM*, Springer, New York, USA (2005) p. 1-16.

[129] http://cnx.org/content/m22963/1.5/

[130] W. Burgei, M. J. Pechan, and H. Jaeger, Am. J. Phys. **70** No. 8 (2003) 825.

[131] S. R. Hoon and S. N. M. Willcock, J. Phys. E. Sci. Instrum. **21** (1988) 772.

[132] *Lake Shore 7300 Series VSM Software*, Lake Shore Cryotronics, USA (www.lakeshore.com)

[133] R. Kleiner, D. Koelle, F. Ludwig, and J. Clarke, *Proceedings of IEEE* **92** No. 10 (2004) 1534.

[134] www.nanomagnetics.org

[135] www.mrl.ucsb.edu

[136] www.keithley.com

[137] G. T. Dyoes and T. Farrell, *Electrical Resistivity Handbook*, Peter Peregrinus Ltd., London, UK (992) p. 11-16.

[138] K. S. Dieder, *Semiconductor Material and Devices Characterization*, second edition, John Wily & Sons, New York, USA (1998).

[139] K. Bautista, *Four- Point Probe Operation*, University of Texas and Dallas, first edition, USA (2003) (www.utdallas.edu)

[140] www.sestechno.com

[141] L. Ben Tahar, M. Artus, S. Ammar, L. S. Smiri, F. Herbst, M. J. Vaulay, V. Richard, V. Richard, J. M. Grenẽche, F. Villain and F. Fiẽvet, J. Magn. Magn. Mater. **320** (2008) 3242.

[142] A. Thakur, P. Mathur and M. Singh, J. Phys. Chem. Solid **68** (2007) 378.

[143] B. Haili and J. Enyong, Chinese Science Bulletin **46** No. 7 (2001) 529.

[144] D. Lewis and E. J. Wheeler, J. Mater. Sci. **20** (1969) 681.

[145] J. Frantti, S. Eriksson, S. Hull, S. Iranov, V. Lantto, J. Lapplainen and M. Kakihana, J. European Ceramic Society **24** (2004) 1141.

[146] I. Soibam, S I. Phanjoubam and C. Prakash, J. Alloys Comps. **475** (2009) 328.

[147] K. Roumaih, R. Manapov, E. Sadykkov and A. Pyataev, J. Magn. Magn. Mater. **288** (2005) 267.

[148] J. Z. Msomi and T. Moyo, J. Magn. Magn. Mater. **321** (2009) 1246.

[149] A. M. Gismelseed, K. A. Mohammed, H. M. Widatallah, A. D. Al-Rawas, M. E. Elzain and A. A. Yousif, J. Phys.: Conf. Ser. **217** (2010) 012138.

[150] J. Z. Msomi and T. Moyo, Hyperfine interac. **189** (2009) 151.

[151] C. Kim, W. Kim, S. An and S. Lee, J. Magn. Magn. Mater. **215-216** (2000) 213.

[152] J. Wang, H. Wu, C. Yang and Y. Lin, Mater. Characterization **59** (2008) 1716.

[153] B. P. Rao, P. S. V. Subba Rao, G. V. S Murthy and K. H. Rao, J. Magn. Magn. Mater. **268** (2004) 315.

[154] K. Maaz, A. Mumtaz, S. K. Hasanain and A. Ceylan, J. Magn. Magn. Mater. **308** (2007) 289.

[155] M. Ahmed, J. Magn. Magn. Mater. **322** (2010) 763.

[156] A. Ślawska-Waniewska, P. Didukh, J. M. Greneche and P. C. Fannin, J. Magn. Magn. Mater. **215-216** (2000) 227.

[157] H. Hiroyoshi and K. Fukamichi, Phys. Lett. A **85** No. 4 (1981) 242.

[158] K. Maaz, A. Mumtaz, S. K. Hasanain and M. F. Bertino, J. Magn. Magn. Mater. **322** (2010) 2199.

[159] J. Hochepied, P. Bonville and M. Pileni, J. Phys. Chem. B **104** (2000) 905.

[160] R. S. Devan, C. M. Kanamadi, S. A. Lokare and B. K. Chougule, Smart Mater. Struct. **15** (2006) 1877.

[161] M. A. El Hiti and A. M. Abo El Ata, J. Magn. Magn. Mater. **195** (1999) 667.

[162] M. A. El-Sayed, J. Magn. Magn. Mater. **82** (2003) 583.

[163] S. P. McAlister, A. D. Inglis and P. M. Kayll, Phys. Rev. B **31** (1985) 5113.

[164] P. Didukh, J. M. Greneche, A. Ślawska-Waniewska, P. C. Fannin and L. Casas, J. Magn. Magn. Mater. **242** (2002) 613.

[165] www.ptable.com

[166] P. Muthukumarasamy, T. Nagarjan and A. Narayanasamy, J. Phys. C: Solid State Phys. **15** (1982) 2519.

[167] T. Moyo, J. Phys.: Condens. Matter **8** (1996) 8915.

[168] S. Shukla, K. Jadhav and G. Bichile, J. Magn. Magn. Mater. **195** (1999) 692.

[169] M. Glaragozlou, J. Alloys Comp. **486** (2009) 660.

[170] V. Markovich, I. Fita, A. Wisniewski, G. Jung, D. Mogilyansky, R. Puzniak, L. Titelman and G. Gorodetsky, Phys. Rev. B **81** (2010) 134440.

[171] S. Mϕrup, F. Bodker, P. Hendriksen and S. Linderoth, Phys. Rev. B **52** (1995) 287.

[172] C. Vázquez-Vázquez, M. A. López-Quintela, M. C. Buján-Núñez and J. Rivas, J. Nanopart. Res. **13** (2011) 1663.

[173] F. Gözüak, Y. Köseoğlu, A. Blaykal and H. Kavas, J. Magn. Magn. Mater. **321** (2009) 2170.

[174] C. N. Chinnasamy, A. Narayasanasmy, N. Ponpandian, K. Chattopdhyay, B. Jeyadevan, K. Tohji, K. Nakatsuka, T. Furubayashi and I. Nakatani, Phys. Rev. B **63** (2001) 184108.

[175] R. L. Dhiman, S. P. Taneja and V. R. Reddy, Advanced in Condensed Mater. Phys. **2008** (2008) 7.

[176] S. S. Mϕrup, Hyperfine Interac. **60** (1990) 959.

[177] A. B. Gadkari, T. J. Shinde and P. N. Vasambekar, J. Magn. Magn. Mater. **322** (2010) 3823.

[178] B. S. Chauhan, R. Kumar, K. M. Jadhav and M. Singh, J. Magn. Magn. Mater. **283** (2004) 71.

[179] J. Blanusa, M. B. Antic, A. Kremenovic, A. S. Nikolic, L. Mazzerolles, S. Mentus and V. Spasojevic, Solid State Communications **144** (2007) 310.

[180] E. Ateia, M. A. Ahmed and A. K. El-Aziz, J. Magn. Magn. Mater. **311** (2007) 545.

[181] S. E. Jacobo, S. Duhalde and H. R. Bertorello, J. Alloys Comps. **509** (2011) 966.

[182] E. Rezlescu, N. Rezlescu and P. D. Popa, J. Magn. Magn. Mater. **290-291** (2005) 1001.

[183] G. B. Kadam, S. B. Shelke and K. M. Jadhav, J. Electronic and Electrical Engineering **1** No. 1 (2010) 0976.

[184] A. A. Pandit, A. R. Shitre, D. R. Shengule and K. M. Jadhav, J. Mater. Sci. **40** (2005) 423.

[185] L. Zhao, H. Yang, X. Zhao, L. Yu, Y. Cui and S. Feng, Mater. Lett. **60** (2006) 1.

[186] E. P. Wohlfarth, *Amorphous Metalic Alloys*, Edited by F. E. Lubosrsky (1983) p. 283-299.

[187] M. L. Branham and T. Moyo, European Journal of Pharmaceutics and Biopharmaceutics, submitted for publication (2011) (Manuscript Number: EJPB-D-11-00685).